WAVE ATTENUATION IN PARTIALLY FILLED UNSTEADY PIPE FLOW

by

Nagwa Abd El-Baky Mohamed

B.Sc.(Eng.), M.Sc.(Eng.)

Thesis submitted for the degree of

Doctor of Philosophy

Department of Mechanical Engineering

Brunel University

January 1989

بِسْمِ ٱللَّهِ ٱلرَّحْمَٰنِ ٱلرَّحِيمِ

To my husband, Nabil, and
my children, Dalia and Amr.

ABSTRACT

Much research activity is carried out to reduce water consumption for domestic purposes. This leads to the possibility of reducing the amount of water introduced into building drainage systems. However, an accurate estimation of the flow attenuation within building drainage pipes is of great importance to prevent solid deposition and subsequent blockage.

The research is focused on the field of subcritical flow in partially-filled pipes. Experimental and numerical investigations have been carried out to study the wave attenuation in the following configurations encountered in drainage pipe systems:

i A simple pipe.
ii A pipe subject to one concentrated lateral inflow.
iii A pipe with gate fixed at the downstream section, generating an interaction between wave and backwater profiles.

In the present study the Saint-Venant equations are derived in their general and characteristic forms. A number of numerical procedures for solution of the Saint-Venant equations are reviewed, and the rectangular-grid characteristics method, diffusing scheme and Strelkoff's implicit method are chosen to solve the equations. The stability of the finite-difference methods used is investigated for free-outfall and controlled-outfall boundary conditions.

An experimental installation consisting of 0.105 m diameter uPVC pipe is used to investigate the characteristics of the flow and to form test cases for the numerical methods.

Comparisons between computed and observed depth hydrographs, peak depths and depth variations along the pipe are made for subcritical flow in a pipe of slope 1/300.

The rectangular-grid characteristics method and the diffusing scheme are also applied to supercritical flow. Flow tests are undertaken for supercritical flow in a pipe of slope 1/200 to validate the use of these methods.

The investigation revealed that the attenuation rate of peak depths is affected by the volume of the waves. The implicit method is the most suitable method, dealing efficiently with most problems encountered in drainage pipe systems of flat slope. The diffusing scheme can model the attenuation of supercritical flow within building drainage pipes.

ACKNOWLEDGEMENT

I would like to thank my supervisor **Prof Alan Reynolds**, Head of the Department of Mechanical Engineering, Brunel University, for his invaluable support, guidance and encouragement. I would like also to thank **Prof John Swaffield** of the Department of Building, Herriot Watt University, (formerly of Brunel University), for suggesting the field of research and his guidance and supervision in the first stage of the research. My thanks are also due to **Dr Robin Wakelin** of the Mechanical Engineering Department, Brunel University, for helpful discussions and encouragement in a friendly atmosphere.

The author would like to thank **Prof Mahmood El-Rayes**, Chancellor of El-Minia University, Egypt, and **Prof Maher Abd El-Wahaab**, Dean of the Faculty of Engineering and Technology, El-Minia University, Egypt, for their understanding and support for the author's request for Egyptian Government financial support.

It is a pleasure to express my thanks to my husband **Dr Nabil Kotb** for his support, encouragement, understanding and other kinds of assistance through the years of study.

The financial support of the ORS Award Scheme, Mechanical Engineering Department of Brunel University and Egyptian Government is also gratefully acknowledged.

TABLE OF CONTENTS

page

CHAPTER 5 NUMERICAL METHODS OF SOLUTION FOR THE SAINT-VENANT EQUATIONS 48

NOMENCLATURE

A	Cross-sectional area of flow, m^2
B	Water surface width of channel, m
C^+	Positive characteristic
C^-	negative characteristic
c	Wave speed, m/sec
E	Specific energy of flow, m
Fr	Froude number
g	Acceleration due to gravity, m/sec^2
GL	Gate depth, m
h	Flow depth, m
N	Number of pipe length sections
L	Pipe length, m
P	Wetted perimeter of channel, m
Q	Flow rate, m^3/sec
q	Lateral inflow or outflow per unit length, m^2/sec
R	Hydraulic mean radius, m
S_o	Pipe slope
S_f	Slope of energy grade line
T	Gate width, m
t	Time, sec
v	Local mean velocity, m/sec
x	Distance, positive in initial flow direction, m
Z	Height above datum, m
$\bar{Z}$	The depth of the centroid of water section below

	the water surface at distance x at time t, m
α	Pipe slope, $S_o = \sin\alpha$
Δt	Time increment, sec
Δx	Distance increment, m
θ	$\Delta t/\Delta x$
θ	Weighting factor, Chapter 5
ρ	Fluid density, kg/m^3
γ	Unit weight of fluid, N/m^3
τ_o	Wall shear stress, kN/m^2

Suffixes

A,B,C	Calculated points in an x-t grid at time t^j
c	Critical flow condition
n	Normal flow condition
P	Calculated point in an x-t grid at time t^{j+1}
R,S,S'	Interpolated points in an x-t grid at time t^j

Special Symbols

DIF	Diffusing scheme
RGC	Rectangular-grid characteristics method
SIM	Strelkoff's implicit method
Tfac	Time factor

CHAPTER 1

INTRODUCTION

1.1 General Background

The extreme shortage of water in many parts of the world and the occurrence of successive dry years indicate that water conservation is of paramount importance. This concern has drawn attention to the large amount of water consumed for domestic purposes, which in England and Wales, according to **Rump (1978)**, accounted for 50% of the total water consumption. This fact focused attention on the possibility of reducing domestic water use. Therefore, serious efforts are being made to reduce water consumption in buildings. For example, the Building Research Establishment (BRE) has been engaged in many studies, concerning development of spray-type showers for baths and spray taps in commercial buildings, flush reduction in toilets, and other activities which could contribute greatly to water conservation. In Brunel University, a reduced flush toilet was developed; see **Swaffield, Wakelin** and **Bocarro (1986)** and **Bocarro (1987)**. These improved designs could provide alternatives to the development of additional water resources if applied on a large scale. It is, however, quite clear that such innovations would cause major flow reductions in drains, which in turn would have deleterious effects on drain performance. Therefore the hydraulic performance of drains is the crucial factor which could limit any form of saving; yet so far it has received limited investigation.

Observations of flow in long partially-filled drainage pipes have shown that the shape of an input surge wave is altered during its passage along the system. In the absence of any downstream inflow the surge is observed to attenuate; that is, the depth of water in the pipe decreases and the time taken for the surge to pass any station is seen to increase, indicating a reduced flow rate at any downstream section, see figure 1.1. In the design of drainage systems this flow attenuation can be of great importance, particularly in the context of reduced water consumption. For example, the removal of waste solids discharged into the drainage system is to a large extent dependent on the maintenance of flow depth behind the solid matter during its transportation. Therefore an accurate prediction technique for flow attenuation, able to deal with random inflows along the length of a drain pipe, would be useful in making design decisions.

1.2 Flow Regime

Attenuation is a complex phenomenon and depends upon channel parameters such as pipe size, material and slope. Therefore it would be unrealistic to ignore the effect of these factors on the drain performance. The degree of flow attenuation depends also on the nature of the flow regime within a drainage pipe, whether it is supercritical or subcritical flow. Subcritical flow may occur when the pipe has to be laid very flat to satisfy design constraints. When the pipe is laid steeper, supercritical flow may develop. The principal difference between the two flow regimes is that in supercritical flow waves cannot propagate upstream; whereas in subcritical flow they propagate in both upstream and downstream directions. (Subcritical and supercritical flow are described in detail in Appendix A.) In addition, for subcritical flow an increase in downstream depth, due to the presence of a restrictive device, for example, will be transmitted for a long distance upstream by a so-called backwater curve, see figure 1.2. In supercritical flow, on the other hand, the downstream condition cannot be spread upstream in this way, but the backwater curve will end in a hydraulic jump, as shown in figure 1.2. Thus the flow pattern in a subcritical channel is affected by the downstream conditions; while in a supercritical channel, the flow pattern is dependent fully upon the upstream conditions.

1.3 Attempts to Estimate Attenuation

Until recently, empirical techniques were used to estimate the attenuation effect along drainage pipes. **Burberry (1978)**, for example, studied the attenuation of flushes along underground drainage single pipes and developed an approximate empirical technique to estimate the effect of attenuation at downstream sections. He states that the attenuation of various flushes from a large drainage system could be combined to give a flow rate equal nearly to the mean rate of water delivered at the time at which the flushes emerged. Burberry's investigations revealed that the use of mean flow rate is unsuitable for building drainage; and it would be unrealistic to ignore the importance of attenuation. Thus, according to Burberry, it is important to develop a time-dependent method of estimation to take the effect of attenuation accurately into account. This is essential if the attenuation rate is required to be quantified for separate flushes.

Flow along drainage pipes, in most cases, is unsteady; the flow parameters such as local wave speed, velocity, flow rate, and depth vary with time as a result of changes in system boundary conditions. Hence, a numerical technique based on relatively small time increments and capable of modelling the hydraulic properties of the system would be the best method of estimation.

Flow within drain pipes may be analysed by two partial differential equations which were developed by **Saint-Venant (1870)** to describe unsteady one-dimensional flow. Since the facility of the digital computer has been available, the solution of the Saint-Venant equations has been widely investigated by various numerical methods. The literature records a large number of publications dealing with flow in natural channels. In addition, there are a few publications dealing with flows in storm sewers of large diameter. In the present area of interest the first publications using a numerical analysis technique to predict the depth and flow rate along horizontal sloping drainage-sized pipes were those of **Swaffield (1981) and (1982).** Swaffield solved the Saint-Venant equations by the rectangular-grid teristics '*RGC*' method. A comparison made by Swaffield between calculated and observed waves in a simple pipe of slope corresponding to supercritical flow has suggested that the technique developed is capable of providing data on flow attenuation in long drainage pipes. But more complicated test cases introducing different pipe slopes, materials and diameters are needed to validate the technique in drainage networks.

The technique developed by **Swaffield (1981)** has been extended by **Bridge (1984)** to investigate unsteady wave attenuation in supercritical flow within a single pipe of gradient up to 1/200. Bridge studied also the effect of different junction types on the flow attenuation in the main pipe. Under these circumstances a hydraulic jump may occur upstream of the junction. Bridge's calculations indicated that the end of the water surface profile upstream of the junction decreased over time during the input steady discharge, prior to the arrival of waves generated at the upstream end of the main pipe. Therefore the hydraulic jump position could not be identified accurately. When the *RGC* method is used to analyse such a flow, the flow variables at a grid point such as P in figure 1.3 will be functions of the flow variables at the interpolation points R and S which are located between grid points A and C and C and B at the previous time step. When a linear interpolation technique is used to calculate conditions at R and S, lower depth values than the actual are produced at these points, which underestimates the flow depth value at point P. Thus the depth of the calculated water surface profile is decreased over time.

An attempt has been made by **Standing (1986)** to improve the *RGC* method by using a more complicated interpolation technique for points R and S. This is called the Everett and Newton-Gregory technique and is described in **Spencer et al. (1977)**. A comparison made by Standing of an observed depth hydrograph and calculated depth hydrographs from both linear and Everett and Newton-Gregory interpolation techniques showed that the calculated depth hydrograph using the Everett and Newton-Gregory interpolation technique has a drawdown of the depth prior to the arrival of the wave (this does not occur in practical applications). This obvious error in the calculated flow depth does not encourage one to adopt the Everett and Newton-Gregory interpolation technique in the unsteady flow calculation.

Unfortunately, there is no major study directed to the attenuation of subcritical flow within building-sized drainage pipes. Moreover the only numerical method applied to flow within such pipes is based upon the method of characteristics, which has failed in some applications to provide a meaningful flow prediction.

1.4 Motivation and Objective of the Research

The present study was prompted by the need for an accurate estimation of the attenuation effect in drainage system pipes. From the considerations presented in the previous sections, it can be seen that the subcritical flow regime has not been fully documented. It is also quite clear that no attempt has been made to simulate the effect of attenuation by various numerical methods to identify that which provides the most accurate results.

The objective of the present study is therefore to make some contribution to the understanding of the attenuation of subcritical flow within building-drainage-sized pipes. Hence three of the available numerical techniques were adapted to solve the Saint-Venant equations, and a computer program was developed for each approach. In addition, an experimental programme was carried out to reveal the character of the flow and to form test cases for the numerical techniques. Thus, the depth hydrographs were measured at four locations along the test pipe, and three different configurations were chosen to satisfy the research objectives:

1-A simple pipe.

2-A pipe subject to one concentrated lateral inflow.

3-A pipe with gate fixed at the downstream section, generating an interaction between wave and backwater profiles.

Moreover, some of the techniques developed were applied also to the prediction of supercritical flow parameters.

1.5 Layout of the Thesis

The thesis consists of eight chapters, the first of which is the present introduction. In Chapter 2 the test rig and the experimental apparatus are described. Derivation of the unsteady one-dimensional flow equations' and their characteristic form is reported in Chapter 3. In Chapter 4 free-outfall and controlled-outfall boundary conditions are presented; also the calculation of the initial (steady) flow parameters is described. The solution of the Saint-Venant equations by three numerical methods, with special attention to the effect of changing the grid size, is reported in Chapter 5. Chapter 6 includes a comparison of the stability of the numerical methods, determination of the Manning's n, discussion of the upstream boundary condition and the selection of the observed pipe slopes. The main findings of the current work are presented in Chapter 7, where the computed results are discussed and compared with the experimental data. Chapter 8 reports the conclusions of the present work and suggests some aspects for future work.

CHAPTER 2

EXPERIMENTAL APPARATUS AND INSTRUMENTATION

2.1 Introduction

The object of the experiments is to investigate the depth variations at different sections along the test pipe, in order to reveal the character of the flow, and to provide the means of testing the theoretical predictions.

In the Building Technology Laboratory of Brunel University there existed equipment constructed for research into free-surface flow in pipes. It was decided to use essentially the same rig which had been used by several previous researchers, and not to build anew. Basically the rig consists of a single run of pipe. For different applications a gate can be fixed at the downstream section or a concentrated lateral inflow can be supplied. The flow-depth variations can be recorded at four stations along the test pipe. Differential pressure transducers have been used to measure the flow depth; a description of the data collection system is included in this chapter.

2.2 Test Facility

Figure 2.1 shows the general layout of the rig. The primary test channel is a 13.34 m length of unplasticised PVC transparent pipework of 110 mm nominal diameter (105 mm internal diameter). Some advantages of uPVC pipe are high resistance to a wide range of chemicals, ease of joining, light weight for handling and low cost; more information can be found in **Twort et al. (1974)** and **Burberry (1979)**. The test pipe diameter is that most often found in domestic applications. The pipework was washed and internally cleaned of any dust, dirt and grease which might have remained from previous experiments.

The pipe is fixed along and below a horizontal lightweight heavy-duty aluminium ladder hung on edge from a dexion-angle framework which is clamped to the laboratory roof truss for support. Rubber-lined pipe clamps are introduced at regular intervals through the pipe length in order to fix the pipe to the ladder. There are three turnbuckles, at the pipe entry, middle and exit. The first one is fixed and the other two can be used in altering the pipe slope. A surveyor's level is used to set the pipe slope.

The pipe-support system ensures that the pipe slope remains unchanged over long periods of time; this was found to be true through the present course of study and also by previous researchers such as **Wakelin (1978) and Bridge (1984)**.

During the present work it was observed that the pipe oscillated in the horizontal plane under high discharge values. Therefore additional pipe clamps were introduced to hold the test pipe to vertical dexion-angle framework to obviate any oscillation.

The inflow passes to the test pipe from a tank open to the atmosphere. A Newman 0.55 kW pump having a maximum flow rate of 200 l/min is used to pump the water from the tank and pass it to the pipe through two rotameters of capacity 5-50 l/min and 20-200 l/min. The inflow can be supplied through either of the rotameters. The drainage from the test channel passes back to the original tank.

Figure 2.2 is a schematic diagram showing the concentrated lateral inflow into the main pipe. A SMC 70 W pump having a maximum flow rate of 12 l/min is used to supply the lateral inflow from the main tank. The pumped water passes through a rotameter of capacity 2-20 l/min to a plastic tube leading to a 43 mm diameter section of uPVC pipe. The surface between the main pipe and the lateral inflow pipe is comprised of a circular plate with many holes in it.

The gate configuration used in the present study is shown in figure 2.3; it is made of perspex of 16 mm thickness. The gate height (measuring normal to the pipe bottom) is 35 mm. When its presence is required, it can be inserted in the pipe and fixed to the pipe bottom by two screws.

2.3 Flow Measurements

2.3.1 Steady Flow Measurements

Steady flows were required for all the tests carried out, including those with waves. Three rotameters (Series 2000 made by GEC Marconi Process Control Ltd.) were used. The rotameter's accuracy was investigated by measuring a known volume of water and determining the time taken for it to pass through. The accuracy was found to be within

+6% of the actual flow rate. A similar accuracy range has been reported by **Bridge (1984)**, **Standing (1986)** and **Bainbridge (1986)**. The calibration result indicated that the actual discharge values are always less than the indicated discharge values. This agreed with the accuracy quoted by the manufacture.

2.3.2 Unsteady Flow Measurements

To produce the required inflow hydrograph to the main pipe the flow-control valve (2), see figure 2.1, was used to adjust the steady base flow passing to the test pipe. The flow-control valve (3) was then opened manually to allow the maximum discharge required to pass through it. The valve was then closed gradually until the discharge returned to the base-flow level. At the station 0.6 m from the pipe entry a pressure transducer was connected to a pressure tapping in order to measure the discharge hydrograph to the test pipe. To calibrate the discharge into the test channel a known discharge value was pumped to it and the pressure-transducer output was recorded. Figures 2.4 and 2.5 show the calibration curves for pipe slopes 1/200 and 1/300.

2.4 Measuring the Flow Depth

2.4.1 Pressure Transducers

The flow depth at the instrumented sections of the pipe has been measured by four differential pressure transducers. These were made by the Sangamo Transducer Co.(type P21) for the pressure range 0-35 kN/m^2. Each transducer contains a small metal diaphragm with a small chamber on each side to which the two pressures are connected. The deflection of the diaphragm is monitored by variable reluctance. In this way an electrical output corresponding linearly to the pressure difference across the diaphragm is provided. In the present circumstances this electrical output is a voltage. For the measurements to proceed a pressure tapping is connected to a hole at the pipe bottom at each instrumented section. Then one side of the pressure transducer is connected to the pressure tapping by a plastic tubing. The other side of the transducer is connected to a tube open to the atmosphere. A tap was located upstream of the pressure transducer to allow the tubes to be balanced; i.e., the tube open to the atmosphere was filled to a height at the same horizontal level as the base of the channel. The flow depth can then be determined by measuring the pressure difference produced by the heads of water at the instrumented sections.

2.4.2 Calibration of Pressure Transducers

The pressure transducer calibration is required in order to obtain a relationship between its output and the differential pressure head. At the start of the calibration the pipe was completely drained; that meant the water level in the tube opened to the atmosphere is exactly the same as the water in the tube connected to the pressure tapping and both at the level of the invert of the pipe. Then the output voltage for a known difference in head was recorded. The result was linear and shown in figure 2.6 for one pressure transducer. The calibration procedure was repeated several times; it was found that no change occurred in the relationship between the input and the output.

The linearity, which is a measure of the extent to which the transducer calibration curve over its effective range departs from the best fitting straight line, was found to be approximately 0.3%.

2.4.3 The Accuracy of the Measured Depth

As shown in figure 2.6 the measured flow depth in the pipe is equal to the slope of the calibration line (dh/dv) multiplied by the voltage reading, $h = (dh/dv)\ v$. The maximum error of the voltage reading is dependent upon the voltmeter accuracy, which in the present circumstances is ±0.00005 V. The maximum error of the depth reading in the calibration tube is 0.0005 m. Therefore the worst possible error in dh is ±0.001 m, and in dv is 0.0001 V. The accuracy of the measured depth was found to be ±1.005%; this was found by summing the individual sources of error, for details see **Penny (1974)**.

2.4.4 Investigation of the Pressure Transducer Response

Throughout the present experimental programme an exaggeration of the steepness of the leading edge of the measured wave has been observed (see figure 2.7, for example) compared with computed solutions. This phenomenon had been noted by earlier researchers, for example, **Bridge (1984)**, but not investigated in a quantitative fashion. Therefore a small-scale laboratory investigation into the response of the pressure transducers to a sudden change in pressure was carried out in isolation from the test rig. The general arrangement, which is shown in figure 2.8, comprises a small pressure vessel, part of which contains water. The sudden change of the vessel pressure was supplied from a carbon-dioxide cylinder, a pressure regulator being fitted on the CO_2 line to adjust the maximum pressure which can be used. A Furness digital micromanometer Type MDC FC002 for pressure range 0.01-199.9 mm of water was used to measure the vessel pressure. A plug-cock valve was fitted on the gas line to allow the pressure inputs to rise quickly in the pressure vessel.

The vessel pressure was measured using three of the pressure transducers which were used throughout the present study. The first transducer was connected to the top of the vessel to measure the gas pressure, a short plastic tubing being used to connect the tapping point in the vessel to one of the transducer ports. The second and third transducers were connected to the water-filled part of the vessel; a short plastic tube was used to connect one side of the transducer to the vessel, while a long plastic tube, the same length as that required to connect the transducers to the test rig, connected the third transducer to the vessel. The three pressure transducers were calibrated by applying different known pressure values (these were determined from the digital micromanometer reading) to the pressure vessel and recording the voltage output of the transducers.

The pressure was adjusted, and the valve was then opened and shut quickly to allow the vessel pressure to rise suddenly. The transducers' outputs were recorded using the data-collection system described in the following sections. Figures 2.9 and 2.10 illustrate the results of two tests. These figures show that the pressure transducer which was connected to the vessel by a long plastic tube recorded a steeper edge than the other two transducers. It is also seen that the output of the transducer which is connected to the gas side has fewer fluctuations than the other two which are filled by water. It is clear that the water-filled plastic tubing has an influence on the apparent steepness of the recorded wave form and the fluctuation of the transducers' output signals.

2.5 Data-collection System

The data-collection system is shown in figure 2.11. It consists of several components, each performing an important function in the collection of experimental data of good quality.

A- Pressure Transducer Array

The system allows sixteen pressure transducers to be connected, but as shown in the figure only four were used.

B- Preamplifier

In earlier tests it had been found that the pressure transducer signal has an element of high-frequency noise which affected the accuracy of the results. Hence this unit was built to reduce the noise from the transducers to an acceptable level.

C- Zero-offset Unit

The function of this unit is to adjust the voltage output to zero for a zero differential pressure head. It also contains a channel-selector unit to allow any channel to send signals to the chart recorder for analysis.

D- Computer Control Unit

This unit has been built to allow up to sixteen analogue channels to be time-multiplexed. The output is a signal to a Solarton voltmeter. The operation of this unit is controlled by a program resident in an Apple II computer.

E- The Solarton Voltmeter

The type used is Model 7055 with Type 70554 parallel interface made by Solartron Electronic Group Ltd. The working temperature range is between 0 and 50 °C. It can read from 10 mV to 1000 V D.C. full-scale, with an accuracy of 4/5 or 6 figures. All of the parameters are controllable from the program resident in the Apple II computer. It is possible to control the rate at which the measurements are made by the same program. The maximum sampling rate is about 20-30 msec/sample. However, if n channels are logged, this value will be 30/n msec/sample for each channel.

F- Apple II Computer

The Apple II computer is a standard model with full 48K-RAM and additional switchable 16 K-RAM known as the "language card". A special interface card is fitted in slot three. The interface consists of three peripheral interface adapters, Type 6821. This gives a total of 6x8 bits of data I/O.

2.6 Software

The computer software was written by Mr B.S.T. Marriott who formerly worked as a Research Assistant in the Department of Mechanical Engineering, Brunel University. The role of this software is to record the pressure transducer outputs from the Solartron voltmeter and to produce data suitable for transfer to the main-frame computer or to pass it to a printer.

Several parameters must be introduced to this program before the experimental test starts.

1- Range

The maximum output voltage which is expected is chosen from four given values: 0.01/0.1/1.0/10.0 V.

2- Accuracy

The accuracy which is required in the output data; the maximum accuracy which can be given is 5 digits.

3- Logging Rate

The number of readings per channel per second. This depends on the number of channels logged and the chosen accuracy.

The above parameters were introduced to control the Solartron voltmeter performance.

4- Number of Channels

The number of channel to be logged. The transducers must be connected from channel 1 upwards without gaps. Unused channels should be left open-circuit.

5- Logging Time

The maximum logging time is up to 32 sec. Therefore the test time must be between 1 to 32 sec.

6- File Name

The file name chosen for the output data to identify each test should be less than 32 characters.

7- Test Descriptions

Description of the experimental test to be written with the output data.

Once these parameters have been supplied, automatic logging can be started by pressing the start button at the computer control unit. The output is stored on the computer disc, which can pass it to a printer.

CHAPTER 3

EQUATIONS OF UNSTEADY OPEN-CHANNEL FLOW

3.1 Introduction

Unsteady open-channel flows can be grouped into two types, namely, gradually varied and rapidly varied flow. In one, the changes of depth and velocity take place over a long distance; therefore the curvature of the wave profile is mild, as shown in figure 3.1 (a). Such flow is termed gradually varied flow. For this type of flow the changes occur slowly enough for the effects of the vertical component of acceleration to be negligible in calculating the streamwise acceleration. On the other hand, the role of the channel friction is significant and must be accurately estimated. In the second type of flow, the changes of depth and velocity take place in only a short distance and may, in fact, be quite abrupt; examples are hydraulic jump and hydraulic drop. The curvature of the wave profile is therefore very steep; thus the surface of the profile may become virtually discontinuous, as shown in figure 3.1 (b). In addition, the role of the vertical component of acceleration is of paramount importance when this type of flow occurs, and therefore it must be taken into account.

In the present study, gradually-varied unsteady flow is assumed and can be described by the two partial differential equations established by **Saint-Venant (1870)**. These are the continuity equation and the momentum equation. Besides the restrictions underlying the gradually varied, unsteady, free-surface flow, the following assumptions are made in deriving the equations:

1-Flow is one-dimensional.
2-The flow velocity is uniform over each cross-section and the water surface across the section is horizontal.
3-The pressure at any depth is the hydrostatic pressure.
4-The channel bed slope is sufficiently small for its cosine to be set equal to unity.
5-The effects of boundary friction and turbulence can be modelled using the resistance laws for steady-state flow.

6-Momentum transferred to the flow from any lateral inflow is negligible.

A derivation procedure of the unsteady one-dimensional flow in an open channel will be discussed in detail.

3.2 Continuity Equation

The principle expressed in the continuity equation is the law of conservation of mass. This requires that the mass which moves into a control volume must move out or be stored within. Water is, in the present circumstances, virtually incompressible, and the difference between the inflow and outflow must result in a change in free-surface position. Figure 3.2 shows a control volume enclosing an elemental strip of liquid, where

A = flow area, m^2

v = flow velocity, m/sec

Q = flow discharge, m^3/sec

h = flow depth, m, normal to channel bottom

x = flow direction, parallel to the channel bottom

Δx = an incremental length, m

q = lateral inflow or outflow per unit length, m^2/sec, positive for inflow and negative for outflow

The flow area at section x is A, and at section $x+\Delta x$ it is $A+(\partial A/\partial x)\Delta x$. The mass of water within the control volume is $A \rho \Delta x$. The fluid density ρ being constant for incompressible flow, the rate of mass change within the system can be expressed as

$$\rho \frac{\partial}{\partial t} (A \, \Delta x) \ldots\ldots\ldots\ldots\ldots\ldots\ldots (a)$$

The inflow to the control volume and positive lateral inflow has the following form:

$$Q + q \, \Delta x \ldots\ldots\ldots\ldots\ldots\ldots\ldots (b)$$

The outflow from the control volume is

$$Q + \frac{\partial Q}{\partial x} \Delta x \ldots\ldots\ldots\ldots\ldots\ldots\ldots (c)$$

Then by applying the law of conservation of mass:

inflow (b) - outflow (c) - storage (a) = 0

we obtain

$$Q + q \, \Delta x - Q + \frac{\partial Q}{\partial x} \Delta x - \frac{\partial}{\partial t} (A \, \Delta x) = 0 \ldots\ldots\ldots\ldots\ldots (3.1)$$

Dividing by Δx and rearranging, we have

$$\frac{\partial A}{\partial t} + \frac{\partial Q}{\partial x} = q \qquad \text{(3.2)}$$

On substituting Q = vA in equation 3.2, the continuity equation can be written

$$v\frac{\partial A}{\partial x} + A\frac{\partial v}{\partial x} + \frac{\partial A}{\partial t} = q \qquad \text{(3.3)}$$

Substituting $\partial A = B\partial h$, we finally have

$$vB\frac{\partial h}{\partial x} + A\frac{\partial v}{\partial x} + B\frac{\partial h}{\partial t} = q \qquad \text{(3.4)}$$

3.3 Dynamic (Momentum) Equation

The fundamental principle used in deriving the dynamic equation for unsteady flow in an open channel is Newton's Second Law. This states that the sum of all forces which act on an element of fluid is equal to the time rate of change of the element's momentum in the same direction.

In the present study the assumptions in Section 3.1 are adopted. Figure 3.3 represents the forces acting in the x direction on the incremental volume of the fluid; these are:

1-The gravity force in the flow direction

$$\gamma A \,\Delta x \sin\alpha = \gamma A \,\Delta x\, S_o$$

where $\sin\alpha = S_o$ = channel slope

γ = unit weight of fluid

2-The net hydrostatic force in the x direction due to the hydrostatic pressure

$$-\gamma \frac{\partial h}{\partial x} A \,\Delta x$$

3-The shear force on the wetted area, the resistance term

$$-\tau_o P \,\Delta x$$

where τ_o = wall shear stress

P = mean wetted perimeter of the section

We take the x-momentum transferred from the lateral inflow to be negligible. The time rate of increase of x-momentum within the control volume can be expressed as

$$\partial(\rho A v)\,\Delta x/\partial t$$

At the same time the net efflux of the momentum in the x-direction is

$$\partial(\rho v^2 A)\,\Delta x/\partial x$$

The momentum equation can now be given as

$$\gamma A S_o \Delta x - \gamma \frac{\partial h}{\partial x} A\Delta x - \tau_o P\Delta x = \frac{\partial(\rho A v)\Delta x}{\partial t} + \frac{\partial(\rho v^2 A)\Delta x}{\partial x} \quad .....(3.5)$$

Dividing by $\rho A\Delta x$ and rearranging, we have

$$g\frac{\partial h}{\partial x} + \frac{\tau_o}{\rho R} - gS_o + 2v\frac{\partial v}{\partial x} + \frac{v^2}{A}\frac{\partial A}{\partial x} + \frac{v}{A}\frac{\partial A}{\partial t} + \frac{\partial v}{\partial t} = 0 \quad \ldots.(3.6)$$

The slope of the energy grade line, figure 3.3, as defined by the Chezy equation is

$$S_f = \frac{\tau_o}{\gamma R} \quad \ldots\ldots\ldots\ldots\ldots\ldots\ldots\ldots\ldots\ldots\ldots.(3.7)$$

where R is the hydraulic mean radius, and S_f equals S_o only under steady uniform-flow conditions. Substituting equation 3.7 in equation 3.6, and multiplying equation 3.6 by v/A, we have

$$g\frac{\partial h}{\partial x} + g(S_f - S_o) + v\frac{\partial v}{\partial x} + \frac{\partial v}{\partial t} + \frac{v}{A}q = 0 \quad \ldots\ldots\ldots\ldots\ldots.(3.8)$$

With Q = vA, equation 3.7 can have the form:

$$\left(1-\frac{Q^2B}{gA^3}\right)\frac{\partial h}{\partial x} + \frac{2Q}{gA^2}\frac{\partial Q}{\partial x} + \frac{1}{gA}\frac{\partial Q}{\partial t} + S_f - S_o = 0 \quad \ldots\ldots\ldots\ldots(3.9)$$

More details can be found in **Henderson (1966)** and **Wylie and Streeter (1978)**. Each term in the dynamic equation 3.8 has a physical meaning:

$\partial h/\partial x$	rate of change of depth in the flow direction
S_f	slope of energy grade line

S_o	slope of channel bottom
$v(\partial v/\partial x)$	convective acceleration of flow
$\partial v/\partial t$	local acceleration of flow
vq/A	part of gradient created by the lateral inflow or outflow

Ponce (1982) used the linear stability theory, described in **Lin (1966)**, to investigate the physical mechanisms responsible for wave attenuation in open-channel flow and to identify the terms which caused the dissipation of the free-surface flow wave. Ponce found that the attenuation of the wave is caused by the kinematic terms (S_f and S_o) and the local acceleration term. When the local acceleration is absent or negligible, the attenuation of the wave is caused by the kinematic terms and either or both of the pressure gradient ($\partial h/\partial x$) and the convective acceleration ($v(\partial v/\partial x)$).

The Saint-Venant equations are equations 3.2 and 3.9 with v and h dependent variables and equations 3.4 and 3.8 with Q and h dependent variables. Many forms have been found for the Saint-Venant equations. **Yen (1978)**, for example, does not assume that the cosine of the channel bed slope equals unity, and gives a different form of the equations. Some authors, such as **Barnes (1965)**, **Yevjevich and Barnes (1970)** and **Jolly and Yevjevich (1974)**, have assumed non-uniform velocity distributions and have introduced two velocity coefficients into the equations.

3.4 The Characteristic Form of the Saint-Venant Equations

The continuity and dynamic equations describing unsteady one-dimensional flow in open channels can be expressed in 'characteristic' form in many ways. The technique described below has been developed by Lister (1960) and Fox (1977).

Equations 3.3 and 3.8, with v and h as dependent variables and x and t as independent variables, can be represented in the following forms:

$$F1 = v \frac{\partial A}{\partial x} + A \frac{\partial v}{\partial x} + \frac{\partial A}{\partial t} - q \quad \ldots\ldots (3.10)$$

$$F2 = g \frac{\partial h}{\partial x} + g(S_f - S_o) + v \frac{\partial v}{\partial x} + \frac{\partial v}{\partial t} + \frac{v}{A} q \quad \ldots\ldots (3.11)$$

Combination forms for equations 3.10 and 3.11 can be represented as:

$$F = F1 + \lambda F2 \quad \ldots\ldots (3.12)$$

Then

$$F = \left[\frac{\partial v}{\partial x}(v+\lambda A) + \frac{\partial v}{\partial t}\right]_1 + \lambda B\left[\frac{\partial h}{\partial x}\left(v+\frac{q}{\lambda B}\right) + \frac{\partial h}{\partial t}\right]_2 + g(S_f - S_o)$$

$$+ q\left(\frac{v}{A} - \lambda\right) = 0 \quad \ldots\ldots (3.13)$$

To solve equation 3.13 it is necessary to express it in the form of total derivatives. For the terms in bracket 1 to be a total derivative, dv/dt, we have

$$\frac{dx}{dt} = v + \lambda A \quad \text{.................................} (3.14)$$

Further, for the terms in bracket 2 to be a total derivative, dh/dt, we must have

$$\frac{dx}{dt} = v + \frac{g}{\lambda B} \quad \text{.................................} (3.15)$$

Equating equation 3.14 and 3.15, we obtain

$$\lambda = \pm\sqrt{g/AB} \quad \text{.................................} (3.16)$$

Substituting equation 3.16 into equation 3.15, we have

$$\frac{dx}{dt} = v \pm\sqrt{gA/B} = v \pm c \quad \text{..........................} (3.17)$$

when $c = \sqrt{gA/B}$ = wave speed

Then the characteristic form for the Saint-Venant equations can be written

$$\frac{dx}{dt} = v + c \quad \text{.................................} (3.18)$$

$$\frac{1}{c}\frac{dh}{dt} + \frac{1}{g}\frac{dv}{dt} - S_o + S_f + \frac{q}{gA}(v-c) = 0 \quad \ldots\ldots\ldots\ldots(3.19)$$

$$\frac{dx}{dt} = v - c \quad \ldots\ldots\ldots\ldots(3.20)$$

$$-\frac{1}{c}\frac{dh}{dt} + \frac{1}{g}\frac{dv}{dt} - S_o + S_f + \frac{q}{gA}(v+c) = 0 \quad \ldots\ldots\ldots\ldots(3.21)$$

Equations 3.20 and 3.21 are to be applied on the negative characteristics and equations 3.18 and 3.19 on the positive characteristics. On choosing Q and A as dependent variables, the above equations have the forms:

$$\frac{dx}{dt} = \frac{Q}{A} + c \quad \ldots\ldots\ldots\ldots(3.22)$$

$$\frac{dQ}{dt} - B(\frac{Q}{A} - c)\frac{dh}{dt} = gA(S_o - S_f) - q(\frac{Q}{A} - c) \quad \ldots\ldots\ldots\ldots(3.23)$$

$$\frac{dx}{dt} = \frac{Q}{A} - c \quad \ldots\ldots\ldots\ldots(3.24)$$

$$\frac{dQ}{dt} - B(\frac{Q}{A} + c)\frac{dh}{dt} = gA(S_o - S_f) - q(\frac{Q}{A} + c) = 0 \quad \ldots\ldots\ldots\ldots(3.25)$$

CHAPTER 4

FLOW BOUNDARIES AND INITIAL CONDITIONS

4.1 Introduction

Flow boundary conditions have an important role in solving the two partial differential equations describing unsteady one-dimensional open-channel flow. Definitions for both the upstream and downstream conditions are required. In the present study, the flow hydrograph is considered as the upstream boundary condition. On the other hand, the downstream boundary conditions for subcritical flow were free-outfall or controlled-outfall, depending on the nature of the downstream control section. Derivations of the mathematical models of these conditions are presented in this chapter.

In order that the solution by any numerical method be found, the flow variables, such as velocity, wave speed and depth, must be known along the pipe at time zero. In the present study, a steady uniform flow is assumed for the initial flow calculation. The assumptions of uniform flow, according to **Henderson (1966)**, are that the depth and mean velocity remain the same at all sections along the channel, and the slope of the energy line and channel bottom are the same. In this chapter the normal (uniform) flow depth calculation is reported, and the calculation procedure of the initial water surface profile for subcritical flow is also included.

4.2 Flow Boundary Conditions

4.2.1 Upstream Boundary Condition

At an upstream section of the pipe, 0.6 m from the pipe entry, the observed discharge hydrograph $Q=f(t)$ could be determined; details have been given in Chapter Two. The relationship between Q and t was assumed to be linear within a small time interval Δt; therefore a linear interpolation technique was applied to calculate Q at each time step.

4.2.2 Downstream Boundary Conditions

4.2.2.1 Free-overfall Exit Condition

Subcritical flow is the main area of investigation in the present study. In subcritical flow the flow depth at the conduit exit is found to be the critical depth according to **Chow (1959)**. The critical flow depth will be developed when the flow specific energy is the minimum for a given discharge. The specific energy, which is the energy per unit weight of fluid at the same section measured from the channel bottom as datum, can be expressed as:

$$E_s = h + \frac{Q^2}{2gA^2} \quad \ldots\ldots\ldots\ldots\ldots\ldots\ldots\ldots\ldots\ldots (4.1)$$

where E_s = flow specific energy, m

h = local flow depth, m

Q = local flow discharge, m^3/sec

A = flow area, m^2

For a given discharge two possible alternate depths can occur for a given specific energy except at the critical state, figure 4.1. The necessary condition for a minimum specific energy is $dE_s/dh = 0$; thus

$$\frac{dE_s}{dh} = 1 - \frac{Q^2}{gA^3}\frac{dA}{dh} = 0 \quad \ldots\ldots (4.2)$$

Substituting dA=B dh, where B = flow width, we obtain

$$B\frac{Q^2}{gA^3} = 1 \quad \ldots\ldots (4.3)$$

Equation 4.3 describes the critical flow state. The flow area A and flow width B in this equation are functions of the critical flow depth h_c. Thus equation 4.3 was used to determine the critical flow depth. A bisection method was applied in order to determine the critical flow depth, **Streeter and Wylie (1979)**. The following conditions must be satisfied to justify the use of equation 4.3, **Chow (1959)**:

1-Flow is gradually varied.
2-The channel bed slope is small.
3-The energy coefficient is assumed to be unity.

4.2.2.2 Controlled-outfall Condition

A gate was fixed perpendicular to the flow direction with a horizontal upper edge, at a certain distance from the pipe entry, to be considered as the pipe exit. The gate setting was chosen to ensure that the flow would not attain the full-bore state for the expected maximum discharge.

In order to establish the discharge as a function of the flow depth of the gate, Bernoulli's equation was applied between 1 and 2 in figure 4.2. The following assumptions were made, **Henderson (1966)**:

1-The flow does not contract as it passes over the gate.
2-The pressure is atmospheric across section AB, see figure 4.2.

Then Bernoulli's equation has the form:

$$H + 0 + 0 = \frac{v^2}{2g} + H - y + 0 \quad \text{........................} (4.4)$$

where $v = \sqrt{2gy}$

and $$Q = \int_0^H v \, dA = \int_0^H vTdy \quad \text{.................} (4.5)$$

In the above equation T is the gate width. Equation 4.5 then has the following form:

$$Q = C1 \, H^m \quad \text{.......................................} (4.6)$$

where C1 and m are constants and H is the flow depth over the gate.

For a rectangular channel it is easy to determine this gate relationship between the discharge and the flow depth over the gate. For circular cross-sections it must be developed experimentally. The values of different discharges and depths over the gate were found from experimental tests; then the constants C1 and m in equation 4.6 were found by using Least Squares Method described in **Streeter and Wylie (1979).**

The downstream flow depth, that is, the flow depth just before the gate, can be determined from the following equation:

$$h = H + GL$$

Then

$$h = (Q/C1)^{1/m} + GL \quad \text{...............................} (4.7)$$

where h = flow depth upstream of the gate, m

Q = discharge, m^3/sec

GL = gate depth, m

4.3 Initial Flow Calculations

The initial flow conditions were based on steady uniform flow assumptions. Thus the local discharge was assumed to be the same at all pipe sections. To determine the initial flow conditions, the first step is to determine the flow depth at each node along the pipe; then the flow area, velocity and wave speed can be calculated. For supercritical flow the initial flow depth along the simple pipe was assumed to be the normal flow depth. When a subcritical flow is developed, the initial water surface profile is a drawdown curve between the normal flow depth at the upstream end to the critical flow depth at the downstream end. This profile is called M2 profile, see figure 4.3 (a). The initial water surface profile when a control device is set at the downstream is a backwater curve from a flow depth above the normal at the downstream to the normal flow depth upstream, i.e M1 profile as shown in figure 4.3 (b).

4.3.1 Normal (Uniform) Flow Calculation

A uniform flow will be developed in an open-channel when the resistance to flow is balanced by the gravity force acting on the water in the flow direction. The uniform-flow state may be described by the Chezy formula which is expressed as:

$$v = C\sqrt{RS_f} \quad \text{.......................................(4.8)}$$

where v = flow mean velocity, m/sec

R = hydraulic radius, m

S_f = the slope of the energy line

C = Chezy coefficient

There are numerous empirical equations developed through the years for the Chezy coefficient; perhaps the most widely used formula is the Manning formula, see for example **Reynolds (1974)**:

$$C = R^{1/6}/n \quad \text{.......................................(4.9)}$$

where n is the coefficient of roughness, known as Manning's n. Then equation 4.8 has the following form:

$$v = \frac{1}{n} R^{2/3} S_o^{\frac{1}{2}} \quad \text{.......................................(4.10)}$$

or

$$Q = \frac{1}{n} A R^{2/3} S_o^{\frac{1}{2}} \quad \text{.......................................(4.11)}$$

where Q = discharge, m^3/sec

A = flow cross-sectional area, m^2

Chow (1959), pp 110-114, tabulates suggested values for the Manning's n to cope with different channels. Values between 0.009 and 0.02 are suggested for pipe materials commonly used in building drainage systems. In equation 4.11 both A and R are functions of the normal flow depth, h_n. Thus the flow depth can be found for a given discharge using the bisection technique described by **Wylie and Streeter (1978)**. Satisfying the above equation yields only one value of h; this value should be less than the pipe diameter and greater than zero.

4.3.2 Water Surface-Profile Calculations

To determine the surface profile between the upstream and the downstream ends, the assumptions of gradually varied flow were adopted. These require that the head-loss rate at a given section is given by the Manning formula for the same depth and discharge:

$$S_f = \left(\frac{nQ}{AR^{2/3}} \right)^2 \quad \text{.........} (4.12)$$

The rate of change of energy between sections 1 and 2 in figure 4.4 is equal to the rate of head loss:

$$-\frac{\Delta E}{\Delta L} = S_f \quad \text{.........} (4.13)$$

and

$$\frac{d}{dL}\left[(Z_o - S_o L) + h + \frac{v^2}{2g}\right] = -\left(\frac{nQ}{AR^{2/3}}\right)^2 \text{...........} (4.14)$$

where $(Z_o - S_o L)$ = the elevation of the channel bottom at L, with L measured positive in the downstream direction.

Then

$$S_o - \frac{dh}{dL} - \frac{v}{g}\frac{dv}{dL} = \left(\frac{nQ}{AR^{2/3}}\right)^2 \text{......................} (4.15)$$

Since Q=vA, we have

$$\frac{dv}{dL} A + v\frac{dA}{dL} = 0$$

Which on substituting in equation 4.15, with dA=Bdh, yields

$$L = \int_{h_1}^{h_2} \frac{1 - Q^2 B/gA^3}{S_o - (nQ/AR^{2/3})^2} dh \text{..................} (4.16)$$

where L is the distance between two sections, and h_1 and h_2 are known depths.

In the case under consideration L represents the channel length and h_1 and h_2 represent either normal and critical depths for the free-overall exit condition, or the normal depth and the flow depth upstream of the gate, when the controlled-outfall exit condition applies.

Equation 4.16 can be solved in many ways to give the values of h along the channel; here numerical integration using Simpson's rule, see for example **Streeter and Wylie (1979)**, has been used. This rule states that if

$$L = \int_{h_1}^{h_2} f(h)\, dh \quad \ldots\ldots\ldots\ldots\ldots\ldots\ldots\ldots\ldots\ldots (4.17)$$

The interval between h_1 and h_2 is divided into n equal reaches, normally n=30; then

$$dh = (h_2 - h_1)/n \quad \ldots\ldots\ldots\ldots\ldots\ldots\ldots\ldots\ldots\ldots (4.18)$$

and

$$\Delta L = \frac{1}{3}\, dh \left(f(h_1) + 4f(h_1 + dh(\text{sign})) + f(h_1 + 2dh(\text{sign})) \right)$$

$$\ldots\ldots\ldots\ldots\ldots\ldots\ldots\ldots\ldots\ldots (4.19)$$

This method of integration proceeds in the upstream direction for subcritical flow, i.e.; h_2 represents the downstream depth and L is measured in the upstream direction. For supercritical flow the solution proceeds in the downstream direction; therefore h_2 will be the downstream flow depth and L is measured in the downstream direction. Also 'sign' equals 1 for subcritical flow and -1 for supercritical flow.

Once the flow depth has been calculated along the channel by Simpson's rule, a linear interpolation is applied to calculate the flow depth at each node. Then the flow area, velocity and wave speed are calculated.

CHAPTER 5

NUMERICAL METHODS OF SOLUTION FOR THE SAINT-VENANT EQUATIONS

5.1 Introduction

The literature records a variety of numerical methods applied to open-channel flow equations; those presented here are based upon the integration of the Saint-Venant equations. In principle, these methods are divided into two fundamental groups. The method of characteristics is based upon the characteristic form of the equations, whereas the finite-difference methods are based upon the partial differential equations as originally derived. The finite-difference methods can be classified into two categories - explicit and implicit. The solution is called explicit if arrangements have been made to solve the equtions for the unknowns at one grid point at a time. The solution for any point at time level t^{j+1}, see figure 5.1, is also independent of any points at the same time level. For the implicit methods the solution has to be found by solving a group of equations which includes the unknowns at all grid points at the present time. Furthermore, the unknowns at any grid points at time level t^{j+1}, figure 5.1, are functions of both advanced and previous grid points.

It is found from the literature that certain methods deal more efficiently with one flow regime than the other. For subcritical flow, the evidence indicates that most of the numerical methods can be used, for example, see **Liggett and Cunge (1975)**. On the other hand, there are other factors which may influence the choice of certain methods of solution. These are the type of boundary conditions, channel characteristics and other factors concerning the numerical methods which will be discussed throughout this chapter. Therefore, three numerical schemes, one for each approach, are adopted to solve the unsteady flow equations, namely:

1-rectangular-grid characteristics '*RGC*' method for the method of characteristics,

2-diffusing '*DIF*' scheme for the explicit method, 3-Strelkoff's implicit '*SIM*' method for the implicit method.

For each method a computer program has been written by the author in Fortran 77. A flow chart for each program is given in Appendix B.

In the present chapter a brief history of the method of characteristics and its different schemes is reported in Section 5.2. The solution technique by the *RGC* method and the effect of changing the rectangular grid size on the calculated flow parameters are also included in the same section. In Section 5.3 various schemes of the explicit method are discussed. Details of the *DIF* scheme and the effect of changing the grid size on the predicted depth hydrographs at various pipe sections are presented. The development of the implicit methods and the solution procedures of the *SIM* method are reported in Section 5.4 and the effect of its grid size on the accuracy of the predicted flow depth is also included.

Finally, a concentrated lateral inflow is introduced in part of the present study; thus an equivalent distribution over a certain length of the channel is described in Section 5.5.

5.2 The Method of Characteristics

The method of characteristics has been known for many years; there are various schemes of the method of characteristics available. The first is the characteristics grid method, which was proposed for graphical integration of the shallow-water equations by **Massau (1905)**. In this scheme the grid system is generated by the intersecting characteristic curves in the x-t plane, giving a non-uniform spacing in both x and t. Figure 5.2 shows an example of a generated grid in the x-t plane; the initial characteristic curve may be determined from the initial flow calculations. In order to obtain solutions on a specific rectangular space-time grid, two-dimensional interpolations are required.

The second scheme is the rectangular-grid characteristics '*RGC*' method; in this scheme the dependent variables are functions of the independent variables x and t and the solution at time t^{j+1} depends on the dependent values at the previous time, Figure 5.1. The advantages of this method are that it gives results directly and in a form most needed and usable, for example, the depth and flow hydrographs at selected positions along the channel and the water surface profile at any given time. This scheme also needs less computer storage than the characteristics grid method. **Wylie (1970)**, **Yevjevich and Barnes (1970)**,

Sivaloganthan (1978), **Bridge (1984)** and others have discussed the advantages and disadvantages of both schemes and have concluded that the *RGC* method is the best.

Abbott and Verwey (1970) developed a four-point characteristics method which is suitable for rectangular cross-sections, but needs improvement to cope with other cross-sections.

Due to the advantages of the *RGC* method it has been decided to use it in the present study. The solution by the *RGC* method can be based on the first-order or the second-order approximation in integrating the characteristic form of the Saint-Venant equations. When the first-order approximation is assumed, the non-derivative terms are determined at points R and S, see figure 5.3. For the second-order approximation the non-derivative terms are calculated using points R, S and P. That makes the scheme implicit which leads to great computational difficulties (for more information about the differences between the two approximations see **Standing (1986)**). Therefore the first-order approximation is preferable.

The *RGC* method has been used by previous investigators to predict flow parameters along storm sewer pipes of large diameter; see, for example, **Yevjevich and Barnes (1970)**, **Pinkayn (1972)**, **Sevuk and Yen (1973) and (1982)**. It has also been applied to small-size drainage pipes by **Swaffield (1981)** and **(1982)**, **Bridge (1984)** and **Standing (1986)**.

5.2.1 Rectangular-Grid Characteristics Method

The technique described below is based on **Wylie and Streeter (1978)**. The solution is based upon the characteristic form of the Saint-Venant equations, which are presented in Chapter 3, numbered 3.18 to 3.21.

In figure 5.3 the flow velocity and depth at R and S may be found by a linear interpolation between AC and CB, respectively. Thus four equations along the characteristic lines RP and SP may be written in the following forms:

$$C^{-}\begin{cases} v_P - v_S - g \displaystyle\int_{h_S}^{h_P} \frac{1}{c}\, dh + \int_{t_S}^{t_P} \left[g(S_f - S_o) + \frac{q}{A}(v+c) \right] dt = 0 & \text{..........................(5.1)} \\ x_P - x_S = \displaystyle\int_{t_S}^{t_P} (v-c)\, dt & \text{......................(5.2)} \end{cases}$$

$$C^{+}\begin{cases} v_P - v_R + g \displaystyle\int_{h_R}^{h_P} \frac{1}{c}\, dh + \int_{t_R}^{t_P} [g(S_f - S_o) + \frac{q}{A}(v-c)\, dt = 0 \quad \ldots\ldots\ldots\ldots\ldots\ldots\ldots\ldots (5.3) \\ x_P - x_R = \displaystyle\int_{t_R}^{t_P} (v+c)\, dt \quad \ldots\ldots\ldots\ldots\ldots\ldots\ldots (5.4) \end{cases}$$

The integration must be along the characteristic lines C^{+} and C^{-}; a first-order approximation is assumed to integrate the above equations. The integration of the above equations therefore produces the following set of equations:

$$v_P - v_R + \frac{g}{c_R}(h_P - h_R) + g(S_{f_R} - S_o)\,\Delta t + \frac{q(v_R - c_R)}{A_R}\,\Delta t = 0 \quad \ldots\ldots\ldots\ldots\ldots\ldots\ldots (5.5)$$

$$x_P - x_R = (v_R + c_R)\,\Delta t \quad \ldots\ldots\ldots\ldots\ldots\ldots\ldots\ldots\ldots (5.6)$$

$$v_P - v_S - \frac{g}{c_S}(h_P - h_S) + g(S_{f_S} - S_o)\,\Delta t + \frac{q(v_S + c_S)}{A_S}\,\Delta t = 0 \quad \ldots\ldots\ldots\ldots\ldots\ldots\ldots (5.7)$$

$$x_P - x_S = (v_S - c_S)\,\Delta t \quad \ldots\ldots\ldots\ldots\ldots\ldots\ldots\ldots\ldots (5.8)$$

The flow properties at all grid points A, B, C, ...N+1 can be known from the initial flow calculations which are reported in Chapter 4. While the flow conditions at points R and S can be found from linear interpolation between AC and CB. The solution of equations 5.5 to 5.8 for the unknowns at P depends on the flow regime, i.e., whether it is subcritical or supercritical flow. In subcritical flow influences from downstream sections may propagate to upstream sections. Therefore the flow variables at P are determined by using the positive and negative characteristic lines:

$$\frac{v_C - v_R}{v_C - v_A} = \frac{x_C - x_R}{x_C - x_A} = (v_R + c_R)\frac{\Delta t}{\Delta x}$$

$$\frac{c_C - c_R}{c_C - c_A} = \frac{x_C - x_R}{x_C - x_A} = (v_R + c_R)\frac{\Delta t}{\Delta x}$$

$$\frac{h_C - h_R}{h_C - h_A} = (v_R + c_R)\frac{\Delta t}{\Delta x}$$

and

$$x_P - x_R = (v_R + c_R)\,\Delta t, \quad x_P = x_C$$

The solution of the above equations provide the values of v, c, h at point R:

$$v_R = \frac{v_C + \theta(c_C v_A - v_C c_A)}{1 + \theta(v_C - v_A + c_C - c_A)} \quad \ldots\ldots\ldots\ldots\ldots\ldots(5.9)$$

$$c_R = \frac{c_C(1 - \theta v_R) + \theta c_A v_R}{1 + \theta(v_C - v_A + c_C - c_A)} \quad \ldots\ldots\ldots\ldots\ldots\ldots(5.10)$$

$$h_R = h_C - \theta(v_R + c_R)(h_C - h_A) \quad \ldots\ldots\ldots\ldots\ldots\ldots(5.11)$$

while the conditions at S may be found from a set of similar equations:

$$v_S = \frac{v_C - \theta(v_C c_B - c_C v_B)}{1 - \theta(v_C - v_B - c_C + c_B)} \quad \ldots\ldots\ldots\ldots\ldots\ldots(5.12)$$

$$c_S = \frac{c_C + \theta v_S(c_C - c_B)}{1 + \theta(c_C - c_B)} \quad \ldots\ldots\ldots\ldots\ldots\ldots(5.13)$$

$$h_S = h_C + \theta(v_S - c_S)(h_C - h_B) \quad \ldots\ldots\ldots\ldots\ldots\ldots(5.14)$$

where $\theta = \Delta t / \Delta x$,

In supercritical flow, the flow velocity is greater than the wave speed, and there is no influence of the downstream sections at upstream sections. Thus the negative characteristic PS becomes positive and lies between A and C; both PS' and PR have positive slopes. The following set of equations determines the flow variables at S' for supercritical flow:

$$v_{S'} = \frac{v_C(1 - \theta c_A) - \theta v_A v_C}{1 + \theta(v_C - v_A + c_A - c_C)} \quad \ldots\ldots\ldots\ldots\ldots\ldots(5.15)$$

$$c_{S'} = \frac{c_C + \theta v_{S'}(c_A - c_C)}{1 + \theta(c_A - c_C)} \quad \ldots\ldots\ldots\ldots\ldots\ldots(5.16)$$

$$h_{S'} = h_C - \theta(h_C - h_A)(v_{S'} - c_{S'}) \quad \ldots\ldots\ldots\ldots\ldots(5.17)$$

Thus the flow conditions at the internal nodes at time level t^{j+1} can be determined from equations 5.5 to 5.8.

In this scheme Δx can be chosen and Δt, for stability reasons, must satisfy the Courant condition; see **Courant, Isaacson and Ress (1952)**:

$$\Delta t \leq \Delta x/(v+c)_{max} \quad \ldots\ldots\ldots\ldots\ldots\ldots\ldots\ldots\ldots\ldots(5.18)$$

where Δt = time increment, sec

Δx = distance increment, m

v = local flow velocity, m/sec

c = local wave speed, m/sec

5.2.2 Upstream Boundary Condition

In supercritical flow the inflow profile alone determines the flow depth at the upstream end. Once the discharge value is determined at the first grid point from the flow hydrograph $Q=\int(t)$, it can then be solved with the equation which describes the normal flow depth and has the following form:

$$1 - \frac{(nQ)^2}{A^2 R^{2/3} S_o} = 0 \quad \ldots\ldots\ldots\ldots\ldots\ldots\ldots\ldots\ldots\ldots (5.19)$$

where Q = flow discharge, m^3/sec

A = flow cross-sectional area, m^2

R = hydraulic radius, m

n = Manning's coefficient

S_o = pipe slope

where both A and R are functions of the normal flow depth h_n and the suitable values for n can be found in **Chow (1959)**. Equation 5.19 may be solved at each time step by the bisection technique for h with known Q.

In subcritical flow the downstream conditions may have an effect on the upstream conditions; therefore the flow hydrograph $Q=f(t)$ is solved with the negative characteristics for the flow depth at the first grid point:

$$Q = f(t) = v_1 A_1$$

After rearranging the negative characteristic equation 5.7, we have:

$$v_1 = K4 + K3\ h_1$$

where $K3 = g/cs$

and $$K4 = vs - \frac{g}{cs} hs - g(Sf_S - S_o)\Delta t - \frac{q(vs + cs)}{As} \Delta t$$

Then

$$Q(t) = A_1 (K4 + K3\ h_1)$$

where $A_1 = f(h_1)$; finally the above equations have the following form:

$$Q(t) - A_1 (K4 + K3\ h_1) = 0 \quad \ldots\ldots\ldots\ldots\ldots\ldots\ldots\ldots (5.20)$$

Equation 5.20 is then solved for the value of h_1.

5.2.3 Downstream Boundary Conditions

In supercritical flow the flow conditions at the downstream boundary point can be determined from the equations applicable at internal nodes. Therefore no special arrangements are required.

In subcritical flow, when the free-outfall boundary condition was assumed, the downstream flow depth may be defined as a critical depth. Hence equation 4.3, which is reported in Chapter 4, can be solved with the positive characteristic, equation 5.5, for the unknowns at the downstream boundary. Equation 5.5 has then the following form:

$$v_{N+1} = K2 - K1\ h_{N+1}$$

where $K1 = g/c_R$

and $$K2 = v_R + \frac{g}{c_R} h_R - g(S_{f_R} - S_o)\ \Delta t - \frac{q(v_R - c_R)}{A_R}\ \Delta t$$

and equation 4.3 has the following form after it has been rearranged:

$$\frac{Q^2}{gA^3{}_{crit}}\ B_{crit} = 1$$

Finally the downstream boundary becomes:

$$[A_{N+1}(K2-K1\ h_{N+1})]^2 \frac{B_{N+1}}{gA^3_{N+1}} - 1 = 0 \quad\ldots\ldots\ldots\ldots\ldots(5.21)$$

This equation again may be solved by the bisection technique for the flow depth at the downstream end, when A and B are functions of the downstream flow depth h_{N+1}.

For the controlled-outfall boundary condition, an empirical equation has been found to describe the discharge-depth relationship at the downstream section, equation 4.7 which is given in Chapter 4. Hence the solution procedure can be achieved as described above for the free-outfall boundary condition using equation 4.7 instead of equation 4.3.

5.2.4 Effect of Grid Size on the Predicted Waves

The differences between computed and observed waves have numerous sources. One of these is the possible systematic error in computational procedures. Therefore the effect of the size of the grid on the computed wave accuracy will be examined. The two important parameters describing a depth hydrograph are the peak depth h_P and the time to peak depth T_P as shown in figure 5.4 (a). In consequence, the effect of different grid sizes on the calculated depth hydrographs will be examined by considering these parameters. For the discharge hydrographs, the predicted peak flow rate Q_p and the time to peak flow t_p will be also examined.

The *RGC* method has the specified distance interval Δx, and specified time interval Δt. If N is the number of sections along the channel and L is the channel length, then:

$$\Delta x = L/N$$

To determine Δx from the above equation, N may be chosen as any number. Presumably smaller Δx will provide more accurate flow prediction, but more computing time will be required.

Figures 5.5 to 5.7 demonstrate the effect of changing the grid on the calculated subcritical flow parameters. Figure 5.5 illustrates an observed inflow hydrograph entering a test pipe having a subcritical slope of 1/300 and the calculated flow hydrographs at three positions along the pipe. This graph represents the effect of increasing the number of pipe sections N from 10 to 30 and 40. The results show that as the number of pipe sections increases the time to peak flow rate t_p decreases. This is because the conditions at P in figure 5.3 are calculated from the flow conditions at R and S, resulting from iterpolation between A, B and C, i.e.; they are affected by the conditions at those points. However, any change in the flow conditions upstream will be recorded later for smaller Δx than for larger Δx. It is clear from the graph also that smaller Δx will produce higher flow rate. Although the change between 10 and 30 pipe sections is significant, that between 30 and 40 is nearly negligible. This indicates that the solution is approaching asymptotic values.

Figure 5.6 shows the effect of changing the number of pipe sections on the predicted depth hydrographs. The conclusions of this figure are the same as those based on the calculated flow hydrographs.

The calculated time interval is restricted by the Courant condition described by equation 5.18 to insure that the characteristic lines lie through Δx. To determine the effect of smaller Δt on the computed depth hydrographs, Δt may be determined as:

$$\Delta t = \Delta x / Tfac\ (v+c)_{max}$$

where Tfac is a time factor equal or greater than one.

Figure 5.7 illustrates the effects of smaller Δt on the calculated depth hydrographs. In this graph the upstream inflow hydrograph was the same as in figure 5.5 and N = 30 is selected. The values of Tfac are 1, 3 and 4. The comparisons indicate that decreasing the time increment Δt decreases the calculated peak depth h_P and increases time to peak depth T_P, i.e.; the wave becomes flatter.

The effect of changing the grid size on the calculated supercritical flow parameters have been demonstrated in figures 5.8 to 5.10 for pipe slope 1/200. The effects of different Δx and Δt remain as described above for subcritical flow. Smaller Δx will cause higher peak flow rate and peak depth and less time to peak flow or peak depth, and smaller Δt will predict lower peak depth and more time taken to peak depth.

5.3 Explicit Method

The explicit methods involve solution point-by-point from one time level to the next. Various explicit schemes have been developed, such as the Leap-Frog scheme, Lax-Wendroff scheme and diffusing scheme. The Leap-Frog scheme uses centred differences in both x and t, as shown in figure 5.11, as follows:

$$\frac{\partial f}{\partial t} = \frac{f_i^{j+1} - f_i^{j-1}}{2 \Delta t}$$

$$\frac{\partial f}{\partial x} = \frac{f_{i+1}^{j} - f_{i-1}^{j}}{2 \Delta x}$$

and

$$f_{(x,t)} = f_i^j$$

where f represents any variable.

The solution obtained by this scheme is a saw-tooth line, since the points where the dependent variables are computed are alternately odd or even.

Numerical experiments show that for steady flow the real solution is given at the even points of the grid, **Koren and Kuchment (1967).** Envelopes of values computed at the odd points of a grid are higher than the real solution if a positive wave is introduced at the left boundary, while they seem to be lower for a negative wave. Smoothing the results can avoid this, but the solution's accuracy suffers. A stability and accuracy analysis for the scheme can be found in **Liggett and Cunge (1975)**, who show that the solution can suffer damping if the Courant condition is satisfied exactly. This scheme is prone to instability for the type of boundary conditions encountered in storm-sewer flow, according to **Sivaloganthan (1980).**

The second scheme is the Lax-Wendroff scheme. This was developed by **Lax (1957)** and **Lax and Wendroff (1960)** and was applied to the open-channel unsteady flow equations by **Houghton and Kasahara (1968), (1969)**. The scheme includes a second-order derivative for the approximation of the variables at the grid points. The finite-difference scheme approximation may be developed using Taylor series. The boundary values of the dependent variables must be computed with the method of characteristics, **Sevuk and Yen (1973)**. The scheme is stable and can be used in flood routing through storm drains, but requires some particular programming considerations and adjustment in the case of supercritical flow, according to **Yevjevich and Barnes (1970)**.

The third and simplest explicit scheme is the diffusing one. The stability analysis for the *DIF* scheme shows that the Courant condition must be satisfied through the calculation, see for example **Liggitt and Cunge (1975)**. This scheme has been used by many authors dealing with open-channel flows, particularly in partially filled pipe flow, for example, in storm-sewers by **Yevjevich and Barnes (1970)** and **Sivaloganthan (1980)**. The scheme predicts depth and discharge histories with acceptable accuracy, as suggested also by **Sivaloganthan (1980)** for flows with concentrated lateral inflows.

From the previous discussion the *DIF* scheme was chosen in the present study to solve the Saint-Venant equations by an explicit method for its stability and simplicity.

5.3.1 The Diffusing Scheme

The x and t derivatives can be expressed for the diffusing scheme as follows, see figure 5.12 (a):

$$\frac{\partial f}{\partial x} = \frac{f_{i+1}^{j} - f_{i-1}^{j}}{2\,\Delta x}$$

$$\frac{\partial f}{\partial t} = \frac{f_{i}^{j+1} - \dfrac{f_{i+1}^{j} + f_{i-1}^{j}}{2}}{\Delta t}$$

The Saint-Venant equations can be expressed in the following form, which is suitable for the explicit solution scheme, see **Liggett (1968)**. The continuity equation is

$$\frac{\partial A}{\partial t} + \frac{\partial Q}{\partial x} = q \quad \text{......................................}(5.22)$$

and the dynamic equation is

$$\frac{\partial Q}{\partial t} + \frac{\partial F}{\partial x} = E \quad \text{......................................}(5.23)$$

where $F = (Q^2/A) + gA\bar{Z}$

$E = gA(S_o - S_f)$

Replacing the x and t derivatives in equations 5.22 and 5.23, we have:

$$\frac{A_i^{j+1} - \dfrac{A_{i+1}^j + A_{i-1}^j}{2}}{\Delta t} + \frac{Q_{i+1}^j - Q_{i-1}^j}{2\Delta x} = q_i^j \quad ....(5.24)$$

and

$$\frac{Q_i^{j+1} - \dfrac{Q_{i+1}^j + Q_{i-1}^j}{2}}{\Delta t} + \frac{F_{i+1}^j - F_{i-1}^j}{2\Delta x} = E_i^j \quad .....(5.25)$$

For the unknowns A and Q, the above equations can be written

$$A_i^{j+1} = \frac{A_{i+1}^j - A_{i-1}^j}{2} - \frac{\Delta t}{2\Delta x}(Q_{i+1}^j - Q_{i-1}^j) + \Delta t q_i^j \quad .....(5.26)$$

$$Q_i^{j+1} = \frac{Q_{i+1}^j - Q_{i-1}^j}{2} - \frac{\Delta t}{2\Delta x}(F_{i+1}^j - F_{i-1}^j) + \Delta t E_i^j \quad ...(5.27)$$

Equations 5.26 and 5.27 have been used to determine the flow depth and discharge at the internal nodes at time level t^{j+1}, when the flow conditions at time level t^j

have been determined from the initial-flow calculation described in Chapter 4.

5.3.2 Boundary Condition Calculations

All explicit schemes are unsuitable for calculations at boundary points, **Sevuk and Yen (1973) and Sivaloganthan (1980).** For example, in the subcritical flow regime the methods fail to represent the downstream condition; hence these methods could be unstable in this case. However, the explicit schemes can be applied at the interior points and the method of characteristics at the upstream and downstream grid points.

5.3.2.1 Upstream Boundary Condition

Figure 5.12 (b) presents the upstream and downstream boundaries for supercritical and subcritical flow. In the supercritical flow regime the dependent variables at the upstream point must be defined. If the inflow hydrograph is given, then the upstream flow depth can be calculated as in Section 5.2.2. In subcritical flow the negative characteristic equation, equation 3.25 in Chapter 3, is applied along the backward characteristic line PS. Expressed in the finite-differences form it is

$$\frac{Q_1^{j+1} - Q_S^j}{\Delta t} - \left[\frac{Q}{A} + \sqrt{\frac{gA}{B}}\right]_S^j + \frac{A_1^{j+1} - A_S^j}{\Delta t} =$$

$$\left[gA(S_o - S_f) - q\left(\frac{Q}{A} + \sqrt{\frac{gA}{B}}\right)\right]_S^j \quad \ldots\ldots\ldots\ldots\ldots\ldots\ldots\ldots (5.28)$$

The flow variables at point S were calculated using a linear interpolation procedure between i=1 and i=2 at time level $t=t^j$. The flow hydrograph is known at the upstream point; Q_1 can be determined from it. Equation 5.28 can be solved for A_1; then h_1 may be calculated.

5.3.2.2 Downstream Boundary Condition

The calculation procedure at the downstream grid point is dependent upon the flow regime, as shown in figure 5.12. If the flow condition is subcritical, the positive characteristic equation, equation 3.23, can be applied along the forward characteristic RB. Expressing this equation in finite-difference form gives

$$\frac{Q_{N+1}^{j+1} - Q_R^j}{\Delta t} - \left[\frac{Q}{A} - \sqrt{\frac{gA}{B}}\right]_R^j \frac{A_{N+1}^{j+1} - A_R^j}{\Delta t} =$$

$$\left[gA\ (S_o - S_f) - q\left(\frac{Q}{A} - \sqrt{\frac{gA}{B}}\right)\right]_R^j \quad \ldots\ldots\ldots\ldots\ldots\ldots\ldots\ldots (5.29)$$

Another equation linking the unknowns at the downstream point is required to be solved simultaneously with the above equation for Q_{N+1} and A_{N+1}. For free-outfall the equation linking the flow discharge and depth can be expressed as

$$Q_{N+1}^{j+1} = \left(\sqrt{\frac{gA^3}{B}}\right)_{N+1}^{j+1} \qquad \text{.............................(5.30)}$$

For controlled-outfall the equation linking the flow discharge and depth is

$$Q_{N+1}^{j+1} = C1(h_{N+1}^{j+1} - GL)^m \qquad \text{............................(5.31)}$$

where C1 and m are constants known from the experiment and GL is the gate length.

The downstream variables for the supercritical flow regime can be found by solving the positive and negative characteristics, or by applying the explicit finite-difference scheme to the Saint-Venant equations, which is more practical. However, the downstream boundary conditions are found by introducing the following explicit form of x and t derivatives into Saint-Venant equations:

$$\frac{\partial f}{\partial x} = \frac{f_{N+1}^{j} - f_{N}^{j}}{\Delta x}$$

$$\frac{\partial f}{\partial t} = \frac{f_{N+1}^{j+1} - f_{N+1}^{j}}{\Delta t} \qquad \text{.............................(5.32)}$$

where f represents any variable, and N+1 refers to downstream grid point.

5.3.3 Effect of Grid Size on the Predicted Waves

Figure 5.13 demonstrates the effect of increasing the number of pipe sections N on the predicted depth hydrographs for subcritical flow. The inflow hydrograph was the same as in figure 5.5, and the number of pipe sections used is 20, 40 and 50. The figure shows that the time to peak depth T_P decreases when the number of pipe sections increases. These results were expected because the x derivatives were determined using the grid points at the previous time step; therefore any change in the flow conditions at the upstream will be recorded later downstream for smaller Δx than for larger Δx. This continues until the numerical solution approaches asymptotic values; the change of grid size then will not affect the predicted waves. It is also clear from the figure that with smaller Δx the value of peak depth decreases; the obvious change occurs at the grid points near to the upstream section, while there is no significant effect further downstream.

The effect of reducing the time step on the calculated depth hydrographs is shown in figure 5.14. The conclusion from this figure is that reducing the time step will reduce the peak flow depth h_P and increase the time to peak depth T_P, as the front wave becomes flatter.

Figures 5.15 and 5.16 present the effect of changing Δx and Δt on the calculated supercritical flow parameters; it has been found to be the same as that on subcritical flow parameters.

5.4 Implicit Method

The implicit methods were developed because of the limitations in choosing Δt when using explicit methods. **Richtmyer (1957)** published the first description of an implicit scheme and applied it to heat-propagation problems. The scheme was applied later to open-channel flow equations.

Preissmann's implicit method was then developed and published by **Preissmann (1960)** and **Preissmann and Cunge (1961)**. This method provided 2(N+1) algebraic equations for 2(N+1) unknowns; this system of equations may be solved at any time step by the double-sweep method. This method was applied to the open-channel flow equations by **Cunge and Wegner (1964)**, **Chaudhry and Contractor (1973)**, **White and Price (1975)** and many others. Also **Quinn (1972)** used it to model the Detroit River connecting lakes St. Clair and Erie. He found that the system had a strong stability when $0.6 \leq \theta \leq 1.0$. Normally in this method the system can be stable between $0.5 \leq \theta \leq 1.0$, according to **Wylie (1972) and Wylie and Streeter (1978)**, for example.

In this method the finite-difference form takes the form:

$$f(M) = \theta\left(\frac{f_i^{j+1} + f_{i+1}^{j+1}}{2}\right) + (1-\theta)\left(\frac{f_i^{j} + f_{i+1}^{j}}{2}\right)$$

$$\frac{\partial f(M)}{\partial x} = \frac{\theta(f_{i+1}^{j+1} + f_i^{j+1}) + (1-\theta)(f_{i+1}^{j} - f_i^{j})}{\Delta x}$$

$$\frac{\partial f(M)}{\partial t} = \frac{(f_i^{j+1} + f_{i+1}^{j+1}) - (f_i^{j} - f_{i+1}^{j})}{2\Delta t}$$

where f is any variable and θ is a weighting factor, see figure 5.17. When the above forms are applied to the Saint-Venant equations, the result will be 2N non-linear algebraic equations in 2(N+1) unknowns. The boundary conditions at each end of the system provide the two necessary equations. The Newton-Raphson procedure can be used to transform these equations to a set of linear equations; then these equations can be solved by any method to provide the values of the unknowns.

Amein and Fang (1970) introduced a four-point centroid implicit method, i.e; $\theta=0.5$ as shown in figure 5.17, and applied it to the Saint-Venant equations to analyse long-term flows in long river reaches. **Amein and Chu (1975)** then looked for a simpler formula and used $\theta=1$, which leads to a simpler solution. The scheme is still stable.

Other schemes have been suggested, such as the six-point implicit method, see **Sevuk and Yen (1973)**.

Vasiliev, Godunov, et al (1963) and **Vasiliev, Temnoeva and Shugrin (1965)** published a different implicit scheme known as Vasiliev's implicit scheme. This scheme applies at the interior grid points and the finite-difference version of the characteristic form of the Saint-Venant equations is applied at the upstream and downstream grid points.

Strelkoff (1970) presented an implicit scheme and applied it to solve the Saint-Venant equations. His scheme is similar to Vasiliev's. Strelkoff's implicit method produces a set of linear equations which can be solved for the unknowns. This makes this scheme simpler than the schemes producing non-linear equations. A stability investigation using Fourier series is carried out by Strelkoff and showed that the scheme becomes fully implicit when the resistance term S_f is evaluated at time level t^{j+1}, see figure 5.1; therefore the scheme is unconditionally stable and Δt and Δx can be chosen independently. Strelkoff's implicit method was applied to storm-sewer pipe flows by **Sivaloganthan (1980)**, and it produced acceptable flow prediction. It is also recommended by Sivaloganthan for flows with concentrated lateral inflow.

In the present study Strelkoff's implicit method has been chosen to solve the Saint-Venant equations by the implicit method.

All implicit finite-difference schemes were found to be unconditionally stable; see, for example, **Sevuk and Yen (1973)**. Thus the method progresses much faster in time, and the convergence of a solution is the only factor which may limit the maximum value of Δt.

5.4.1 Strelkoff's Implicit Method

In this method the x-derivatives are evaluated on time level t^{j+1}, see figure 5.18, and have the following forms:

$$\frac{\partial f}{\partial x} = \frac{f_{i+1}^{j+1} - f_{i-1}^{j+1}}{2\Delta x}$$

and t-derivatives

$$\frac{\partial f}{\partial t} = \frac{f_i^{j+1} - f_i^{j}}{\Delta t}$$

where f can be any variable.

The solution starts by introducing the above x and t-derivatives into the Saint-Venant equations, equations 3.2 and 3.9. The result will be a pair of algebraic equations for each node containing six unknowns. However, the system will contain N-2 pairs of equations for the interior points, involving 2N unknowns, plus four more equations, two known boundary conditions and the backward and forward characteristics equations for the entry and exit points. In fact, this system can be made linear if the coefficients in the original equations are evaluated on time level t^j.

Expressing equations 3.2 and 3.9 in the finite-difference form, we have:

$$\frac{Q_{i+1}^{j+1} - Q_{i-1}^{j+1}}{2\Delta x} + B_i^j \frac{h_i^{j+1} - h_i^j}{\Delta t} = q_i^{j+1} \quad \ldots\ldots\ldots\ldots\ldots\ldots(5.33)$$

and

$$gA_i^j\left(1-\frac{Q^2 B}{gA^3}\right)_i^j \frac{h_{i+1}^{j+1} - h_{i-1}^{j+1}}{2\Delta x} + \left(\frac{2Q}{A}\right)_i^j \frac{Q_{i+1}^{j+1} - Q_{i-1}^{j+1}}{2\Delta x} + \frac{Q_i^{j+1} - Q_i^j}{\Delta t}$$

$$= gA_i^j S_o - gA_i^j (S_f)_i^j - gA_i^j \left(\frac{\partial S_f}{\partial Q}\right)_i^j (Q_i^{j+1} - Q_i^j) - gA_i^j \left(\frac{\partial S_f}{\partial h}\right)_i^j (h_i^{j+1} - h_i^j)$$

$$\ldots\ldots\ldots\ldots\ldots\ldots\ldots\ldots\ldots\ldots\ldots\ldots(5.34)$$

For simplicity the above equations may be written as:

$$K_i^j Q_{i+1}^{j+1} - K_i^j Q_{i-1}^{j+1} + L_i^j h_i^{j+1} = M_i^j \quad \ldots\ldots\ldots\ldots\ldots\ldots\ldots(5.35)$$

and

$$N_i^j Q_{i+1}^{j+1} + P_i^j Q_i^{j+1} - N_i^j Q_{i-1}^{j+1} + W_i^j h_{i+1}^{j+1} + R_i^j h_i^{j+1} - W_i^j h_{i-1}^{j+1} = S_i^j$$

$$\ldots\ldots\ldots\ldots\ldots\ldots\ldots\ldots\ldots\ldots\ldots\ldots(5.36)$$

with superscripts omitted, equations 5.35 and 5.36 become

$$K_i Q_{i+1} - K_i Q_{i-1} + L_i h_i = M_i$$

and

$$N_i Q_{i+1} + P_i Q_i - N_i Q_{i-1} + W_i h_{i+1} + R_i h_i - W_i h_{i-1} = S_i$$

where

$$K_i = \frac{1}{2\,\Delta t} \quad , \quad L_i = \frac{B_i^j}{\Delta t} \quad , \quad M_i = q_i^{j+1} + \left(\frac{B_i^j}{\Delta t}\right)h_i^j \quad ,$$

$$N_i = Q_i^j / \Delta x \;, \quad P_i = \frac{1}{\Delta t} + \left[gA\left(\frac{\partial S_f}{\partial Q}\right)\right]_i^j \;, \quad R_i = \left[gA\left(\frac{\partial S_f}{\partial h}\right)\right]_i^j \;,$$

$$W_i = \left[\frac{gA}{2\Delta x}\left(1 - \frac{Q^2 B}{gA^3}\right)\right]_i^j = \left[\frac{(c^2 - v^2)B}{2\Delta x}\right]_i^j \quad , \text{ and}$$

$$S_i = \frac{Q_i^j}{\Delta t} + gA_i^j\left(S_o - S_f + \frac{\partial S_f}{\partial Q}Q + \frac{\partial S_f}{\partial h}h\right)_i^j$$

5.4.1.1 Upstream Boundary Conditions

At the upstream end the scheme needs two equations. The first equation is the backward characteristic, equation 3.25. The total derivatives have been replaced by the equivalent partial derivatives in this equation, see Vasileiv, Glandyshev and Sudobicher (1965); we have:

$$\left[\frac{\partial Q}{\partial t} + (v-c)\frac{\partial Q}{\partial x}\right] - B(v+c)\left[\frac{\partial h}{\partial t} + (v-c)\frac{\partial h}{\partial x}\right] = gA(S_o - S_f) - q(v+c) \qquad \text{.....................................(5.37)}$$

Expressing equation 5.37 in finite-difference form and omitting the superscripts, we have

$$E_1 Q_2 + F_1 Q_1 + G_1 h_2 + H_1 h_1 = J_1$$

where $E_1 = \frac{(v-c)_1^j}{\Delta x}$, $G_1 = \frac{B_1^j (v^2 - c^2)_1^j}{\Delta x}$

$$F_1 = \frac{1}{\Delta t} \frac{(v-c)_1^j}{\Delta x} + gA_1^j [\frac{\partial S_f}{\partial Q}]_1^j ,$$

$$H_1 = \frac{[B(v+c)]_1^j}{\Delta t} + \frac{[B(v^2-c^2)]_1^j}{\Delta x} + g[A\frac{\partial S_f}{\partial h}]_1^j$$

$$J_1 = gA_1^j [S_o - S_f + Q(\frac{\partial S_f}{\partial Q}) + h(\frac{\partial S_f}{\partial h}))]_1^j - q_1^{j+1} (v+c)_1^j$$

$$+ \frac{Q_1^j}{\Delta t} - \frac{[B(v+c)h]_1^j}{\Delta t}$$

The second equation which is needed at the upstream limit can be developed from the discharge hydrograph at the upstream section, and can be written in the form

$$D_1 Q_1 + T_1 h_1 = W_1 \quad \text{.................................(5.38)}$$

Where $D_1 = 1$, $T_1 = 1$ and W_1 is the discharge value at the upstream section at time level t^{j+1}.

5.4.1.2 Downstream Boundary Conditions

The forward characteristic equation will have the following form after the total derivatives are replaced by the equivalent partial derivatives:

$$\left[\frac{\partial Q}{\partial t} + (v+c)\frac{\partial Q}{\partial x}\right] - B(v-c)\left[\frac{\partial v}{\partial t} + (v+c)\frac{\partial h}{\partial x}\right] = gA(S_o - S_f) - q(v-c)$$

$$\ldots\ldots\ldots\ldots\ldots\ldots\ldots\ldots\ldots\ldots\ldots\ldots(5.39)$$

By expressing equation 5.39 in finite-difference form, simplifying and omitting the superscripts we obtain:

$$E_{N+1}Q_N + F_{N+1}Q_{N+1} + G_{N+1}h_N + H_{N+1}h_{N+1} = J_{N+1} \quad .....(5.40)$$

where $E_{N+1} = \dfrac{(v+c)^j_{N+1}}{\Delta x}$, $G_{N+1} = \dfrac{[B(v^2-C^2)]^j_{N+1}}{\Delta x}$,

$$F_{N+1} = \frac{1}{\Delta t} + \frac{(v+c)^j_{N+1}}{\Delta x} + gA^j_{N+1}\left[\frac{\partial S_f}{\partial Q}\right]^j_{N+1}$$

$$H_{N+1} = \frac{[B(v-c)]^j_{N+1}}{\Delta t} - \frac{[B(v^2-c^2)]^j_{N+1}}{\Delta x} + g\left[A\frac{\partial S_f}{\partial h}\right]^j_{N+1}$$

$$J_{N+1} = g\left[A\left(S_o - S_f + Q\frac{\partial S_f}{\partial Q} + h\frac{\partial S_f}{\partial h}\right)\right]^j_{N+1} + \frac{Q^j_{N+1}}{\Delta t} - \frac{[B(v-c)h]^j_{N+1}}{\Delta t} - q^{j+1}_{N+1}(v-c)^j_{N+1}$$

As for the first grid point the scheme needs two equations at the exit section. The first is equation 5.40 and the second is the equation linking the flow depth and discharge at the exit section; this depends upon the flow regime and the nature of the exit section.

For the free-outfall condition, equation 4.3 is applied at the downstream section. Differentiating it we have:

$$\frac{dQ}{dt} = [\frac{3gA^2}{2Q} - \frac{Q}{2B}\frac{dB}{dh}]\frac{dh}{dt}$$

Expressed in the finite-difference form and rearranged this is

$$D_{N+1}Q_{N+1} + T_{N+1}h_{N+1} = W_{N+1}$$

$$\text{where} \quad D_{N+1} = 1, \; T_{N+1} = -[\frac{3gA^2}{2Q} - \frac{Q}{2B}\frac{dB}{dh}]^{j}_{N+1}$$

$$W_{N+1} = T_{N+1}h^{j}_{N+1} + Q^{j}_{N+1}$$

For the controlled-outfall boundary condition the depth-discharge relationship has been described by equation 4.7. This takes the following form after differentiation it with respect to t:

$$\frac{dQ}{dt} = C_1 \; m(h-GL)^{m-1}\frac{dh}{dt} \quad \text{..........................(5.42)}$$

Expressing this in the finite-difference form, omitting superscripts and rearranging, we have:

$$F_{N+1}Q_{N+1} + T_{N+1}h_{N+1} = L_{N+1} \quad \ldots\ldots\ldots\ldots\ldots\ldots\ldots (5.43)$$

where $F_{N+1} = 1, \quad T_{N+1} = -C_1\ m(h^j_{N+1}-GL)^{m-1}$

$$L_{N+1} = T_{N+1}h^j_{N+1} + Q^j_{N+1}$$

The above system contains 2(N+1) linear equations in 2(N+1) unknowns which can be solved with high accuracy by using a double-sweep method, according to **Strelkoff (1970)**. The solution procedures for the above equations by the double-sweeep method are reported in Appendix C.

5.4.2.3 Effect of Grid Size on the Calculated Waves

Figure 5.19 presents the influence of different grid sizes on the calculated depth hydrographs for subcritical flow. The inflow hydrograph in figure 5.5 was the upstream boundary condition. The values of $\Delta t/\Delta x$ were chosen to examine the method for Δt values greater than, nearly equal to, and less than the size of Δt which is required by the Courant condition. The results are illustrated at three locations along the pipe. The method remains stable for different values of $\Delta t/\Delta x$. Also the predicted depth hydrographs from smaller Δt have higher peak depth values. On the other hand there is no change for the time taken to attain the peak depth.

5.5 Equivalent Distribution of Concentrated Lateral Inflow

The symbol "q" in the Saint-Venant equations represents the lateral inflow per unit length; here the concentrated lateral inflow provided from the pipe bottom has been replaced by an equivalent triangular distribution over the adjoining few distance steps. **Sivaloganthan (1981)** developed this technique and tested it for distribution over two and four distance steps. He found that the difference between the computed waves when the concentrated lateral inflow was distributed over two or four distance steps was negligible away from the lateral inflow section and quite small near to it. However, according to Sivaloganthan, distribution over further distance steps can be made without losing a high degree of accuracy.

Figure 5.20 illustrates triangular distributions of a lateral inflow over two and four distance steps. If x=xL is the centre line of the concentrated lateral inflow QL, and the distribution is made over two distance steps, then the value of q in the Saint-Venant equations is given as:

$$q = 0 \qquad (xL+\Delta x) \le x \le xL$$

$$q = \frac{QL}{(\Delta x)^2}\,(x - (xL-\Delta x)) \qquad (xL-\Delta x) < x \le xL$$

$$q = \frac{QL}{(\Delta x)^2}\,((xL+\Delta x) - x) \qquad xL < x < (xL+\Delta x)$$

CHAPTER 6

VALIDATION

6.1 Introduction

In the present study three of the numerical methods were chosen to solve the Saint-Venant equations. For each method the finite-difference forms of the governing equations, together with the appropriate boundary conditions, were coded into a computer program to predict one-dimensional unsteady free-surface flow in pipes with circular cross-sections. Prior to predicting the main flow of interest to the present study, testing was performed to examine the stability of the numerical methods; this is reported in Section 6.2.

A few tests were also carried out in order to:

i Evaluate Manning's n from the observed results; this is reported in Section 6.3;

ii Check the correctness of the assumption of the upstream boundary conditions; see Section 6.4;

iii Select the observed pipe slopes; this will be discussed throughout Section 6.5.

6.2 Investigation of the Stability of the Numerical Methods

6.2.1 Introduction

The equations that are actually solved are the finite-difference equations. Stability, according to **O'Brien, Moton and Sidney (1950)**, is then related to the difference between the exact solution of the difference equations and the numerical solution of these equations; this difference may be called the "round-off" error. Stability can then be defined in terms of the growth of this error, **Smith (1985)**. For the Saint-Venant equations there are no methods of determining sufficient conditions for stability, see for example **Strelkoff (1970)**. Therefore it is quite common to investigate the necessary, and not sufficient, conditions for stability by the Fourier-series method based on the technique of **Von Neumann (1963)**. This type of investigation is usually carried out to discard unstable schemes or to provide the necessary conditions for the others to remain stable. This type of investigation has been reported for the methods used in the present study by a large number of authors, for example, see **Gunaratnaln and Perkins (1970)**. The sufficient stability condition of a numerical scheme for a given class of problems can be examined only by a numerical experiment. **Richtmyer (1962)** stated that "when instabilities develop in the numerical solution of partial differential equations, they appear as oscillations of rather short wave length and initially small amplitude". Therefore if a numerical scheme applied to a certain problem is unstable, an error introduced at any stage of the solution will grow with time, i.e.; the wave amplitude will increase. Hence, in the present study, stability of a numerical method has been tested by adding a large error to the flow depth throughout the channel length under a steady input discharge. If the numerical method is stable, it will approach the steady-state profile with time.

The stability of the *RGC*, *DIF* and *SIM* methods was examined for controlled-outfall and free-outfall boundary conditions. The initial water-surface profiles were calculated using the equations of gradually-varied flow and solved by Simpson's rule, as described in Chapter 4. The upstream flow depth was the normal flow depth. The downstream flow depth for controlled-outfall was determined from the stage-discharge relationship at x = 11.0 m, which was found experimentally in the form:

$$Q = 0.143(h-GL)^{1.31} \quad \text{.............................(6.1)}$$

where Q = discharge, m^3/sec

h = downstream flow depth, m

GL = gate depth = 0.035 m

For the free-outfall boundary condition the discharge-depth relationship was described by equation 4.3, which gives the critical flow state.

6.2.2 Controlled-Outfall Boundary Condition

In this section the initial water-surface profile was calculated for the following data:

steady discharge	= 0.0002 m^3/sec (12 l/min)
pipe diameter	= 0.105 m
pipe length	= 11.0 m
pipe slope	= 1/300
Manning's n	= 0.009

Then the stability of *RGC, DIF, SIM* methods was investigated by assuming that the initial backwater surface profile is a straight line between 0.02 m at the upstream end to 0.042 m at the downstream end, so that a large error was introduced at each pipe section. The calculated flow depths given by the *RGC, DIF* and *SIM* methods at six locations along the pipe were then plotted versus time; they are presented in figure 6.1. It is clear from the figure that the three methods remain stable. The solution by the *RGC* and *DIF* methods required more time than the *SIM* method to approach the steady-state depth.

6.2.3 Free-Outfall Boundary Condition

Here the stability of the numerical methods used in the present study is examined for the free-outfall boundary condition. The following data were used to determine the initial water surface profile for subcritical flow:

steady discharge = 0.0002 m^3/sec
pipe diameter = 0.0105 m
pipe length = 30 m
pipe slope = 0.001
Manning's n = 0.009

To examine stability, three assumptions were made for the initial water surface profile:

1-The flow depth along the pipe is a straight line between 0.03 m at the upstream end (this value is greater than the normal flow depth) and 0.015 m at the downstream end (this is greater than the critical flow depth).
2-The flow depth is 0.01 m along the pipe, which is less than the critical flow depth.
3-The flow depth equals 0.03 m along the pipe.

When the first assumption was applied, the three numerical methods remained stable and approached the steady-state depth, approximately, after 150 seconds of simulation. The calculations' progress at six pipe sections is shown in figures 6.2, 6.3 and 6.4 for the *RGC, DIF* and *SIM* methods, respectively.

For the second assumption the *RGC* and *DIF* methods approached the steady-flow depth at all pipe sections with the same accuracy; figure 6.5 shows the calculated depth versus time given by the *RGC* method. Despite the fact that the calculated flow depths given by the *SIM* method did not approach the steady-state depth at most pipe sections, the solution remained stable as shown in figure 6.6.

Finally, the initial water-surface profile was set to be as in the third assumption, and again, the results given by the *RGC* and *DIF* methods approached the true depth values at all pipe sections. Figure 6.7 illustrates the progress of the depth calculation by the *RGC* method. Figure 6.8 shows the calculation results of the *SIM* method. The solution by this method approached the steady-state depth at all locations except x = 24.0 m and x = 30.0 m, although it remained stable at all pipe sections. The behaviour of the *SIM* method could be attributed to the manner of discretization of the equations at the downstream boundary.

6.2.4 Conclusion

Stability tests were carried out for the *RGC, DIF* and *SIM* methods when the downstream boundary conditions were controlled-outfall and free-outfall. The three methods were found to be stable; therefore they can be applied to the problems of the present interest. Hence the validity (which is the extent to which computed results match observed results) of these methods is the most important factor in selecting the best method for each problem. This will be investigated in Chapter 7.

6.3 Calculation of Manning's n

The Manning formula was used in the present study to determine the normal flow depth and the slope of the energy grade line S_f. The Manning formula (**Powell (1960)** has thrown some light on the history of this formula) was chosen for its wide use in the field and for its mathematical simplicity, see for example **Ragan (1965)**, **Swaffield (1982)** and **Sivaloganthan (1981)**. The Manning's n which is characteristic of the surface roughness can be expressed as:

$$n = \frac{AR^{2/3}S_o^{1/2}}{Q} \quad \ldots\ldots\ldots\ldots\ldots\ldots\ldots\ldots\ldots\ldots\ldots\ldots (6.2)$$

where A = flow area = $f(h)$, m^2

R = mean flow hydraulic radius = $f(h)$, m

S_o = pipe slope and slope of energy grade line S_f for uniform flow

Q = flow discharge, m^3/sec

The Manning's n was calculated at pipe slopes 1/300 and 1/200. A known steady flow was passed to the uPVC pipe and the depth of flow was measured at three locations at the middle of the pipe (x = 6.6 m, x = 7.4 m and x = 8.2 m), which were chosen to ensure that uniform flow was established. In this case the flow depth at the three locations was the same. Then for each pair of known discharge and depth values the roughness coefficient "n" was determined from equation 6.2. An average value of 0.009 was found for Manning's n.

6.4 Verification of the Upstream Boundary Condition

In the computer programs the upstream flow depth was assumed to be the normal flow depth. This assumption was made for the initial flow calculation and for the unsteady-flow calculation for supercritical flow. To validate this assumption, known steady discharge values were passed to the uPVC pipe and the corresponding upstream flow depths were measured. These were found to be approximately the same for pipe slopes 1/200 and 1/300. The normal flow depth was then calculated for each discharge value. The measured upstream flow depth was found to be less than the normal flow depth for both slopes as shown in figure 6.9. Furthermore, it is expected that as the pipe slope becomes steeper the normal-depth assumption will provide an upstream flow depth which is less than that observed. Therefore the normal-depth assumption could lead to inaccurate flow prediction at the upstream end of the pipe. Hence the known discharge values were plotted against the corresponding measured upstream flow depth. The result is shown in figure 6.10. The Least Squares procedure was then used to fit the results by a second-order equation. An empirical relationship was then established between the upstream flow depth and discharge.

Once the flow depth was known at the upstream end, it was necessary for the calculation to proceed to establish where the normal flow depth will be achieved. For this, the gradually varied flow equation was used to calculate the depth profile from the upstream flow depth until the normal depth is achieved; this equation is:

$$\frac{dh}{dL} = \frac{S_o - (nQ/AR^{2/3})^2}{1 - (Q^2B/gA^3)} \qquad \text{......................(6.3)}$$

where h = flow depth, m

L = distance along the channel, m

B = flow width, m

An iterative method of numerical integration, the trapezoidal method, has been used to integrate the above equation, see **Prasad (1970)**. This method has been chosen because the computations can proceed downstream or upstream as the application requires for both subcritical flow and supercritical flow. This method states that

$$h_{i+1} = h_i + \Delta h$$

and if $h = f(L)$, then

$$h_{i+1} = h_i + \Delta h = h_i + (dh/dL)\,\Delta L$$

and if ΔL is very small, then small or negligible error will be introduced by assuming that dh/dL varies linearly, therefore

$$h_{i+1} = h_i + 0.5\left[\left(\frac{dh}{dL}\right)_i + \left(\frac{dh}{dL}\right)_{i+1}\right]\Delta L \quad\ldots\ldots\ldots\ldots\ldots\ldots (6.4)$$

It has been found that the normal flow depth is achieved in about one metre from the first tapping point indicating the establishment of the uniform-flow state, the exact point depending on the pipe slope and flow rate.

6.5 Selection of the Required Pipe Slopes

6.5.1 Calculation of Critical Pipe Slope

A simple calculation using the pipe configurations, roughness and the range of the available discharge values has been carried out to determine the critical pipe slope. The critical flow depth for each discharge value was calculated, and the normal flow depth for different pipe slopes was determined. (Calculation procedures for critical and normal flow depths are reported in Chapter 4.) The critical pipe slope was found to be 1/260, as shown in figure 6.11. Therefore a pipe slope greater than 1/260 will provide supercritical flow regime and a lesser slope will provide subcritical flow.

6.5.2 Subcritical and Supercritical Pipe Slopes

An experimental investigation was carried out to select suitable pipe slopes. The object of this investigation is to select subcritical pipe slopes which ensure that the discharge-voltage relationship at the first tapping point, which is reported in Chapter 2, is not affected by the pipe slope. Four pipe slopes were chosen, 1/500, 1/400, 1/350 and 1/300. The observed sections are located at x = 0.0, x = 6.6 m, x = 7.4 m and x = 8.2 m.

Figures 6.12 to 6.14 are examples of the observed depth hydrographs for pipe slopes 1/500, 1/400 and 1/350, respectively. It is clear from the figures that a backwater curve appeared at x = 0.0 and responded to the rise in the flow depth. The figures also show that the increase of the flow depth due to the backwater effect and the time of the appearance of the backwater curve are affected by the pipe slope. For flatter pipe slopes a greater increase of the flow depth and an earlier backwater effect are observed. Thus for the present study pipe slopes of 1/500, 1/400 and 1/350 are rejected.

For pipe slope 1/300 and x = 0.0 figure 6.15 (a) presents in the upper graph the measured discharge hydrograph and the smooth curve fitted to it, and in the lower graph the depth hydrograph. This figure shows that the flow parameters are not affected by the downstream flow conditions. From this fact this pipe slope was selected to provide the observed results for subcritical flow. Figure 6.15 (b) presents the observed depth hydrographs at the other three locations.

A pipe slope of 1/200 was chosen to provide the required data for the supercritical flow regime and a representation of one test is shown in figures 6.16 (a) and 6.16 (b). For the convenience of the reader only the smoothed curve of the observed discharge hydrograph is represented, see the upper graph of figure 6.16 (a).

CHAPTER 7

RESULTS AND DISCUSSION

7.1 Introduction

In this chapter detailed measurements of subcritical flow in a circular cross-section uPVC pipe of slope 1/300 are presented and discussed. The flow discharge was measured at an upstream section of the pipe (x = 0.0). The flow depth was measured at four locations along the pipe, one at x = 0.0. The Apple logging system described in Chapter 2 was used to record simultaneously the data required to calculate the depth hydrographs over a period of 32.0 sec. These data are compared with corresponding predictions given by the numerical methods described in Chapter 5. The comparison between measured and predicted waves is presented in three different ways. First, waves in the form of depth hydrographs are compared over 32 sec. Secondly, the observed variations of peak-depth versus distance and time are compared with corresponding predictions. Finally, the depth changes along the pipe length are presented.

In the figures, for the sake of clarity, only the predicted depth hydrograph at x = 0.0 given by one of the methods is presented, since the predicted depth hydrographs from the other two methods fell very close to it and the observed hydrographs. In the figures also, for better representation and clarity, the depth changes along the pipe length predicted by only one of the methods of solution are presented for comparison with the experiments.

In computing, values of 0.009 for Manning's n and 0.105 m for the pipe diameter were used. The time step for the *SIM* method was sufficiently small to ensure that enough details of the inflow hydrograph have been fed to the computer model, see **Price (1974)**. For the other two methods the time step was determined from the Courant condition with time factor "Tfac" equal to unity.

This chapter contains five sections, the first of which is the present introduction. Section 7.2 presents the results of the wave attenuation along the uPVC pipe of subcritical slope 1/300; therefore the downstream boundary condition is considered to be a free-outfall. The results and discussion for a more complicated case - this is when the the channel under study is subject to one concentrated lateral inflow - are reported in Section 7.3. Following this are the results and discussion for the controlled-outfall boundary condition, which are presented in Section 7.4. In this section the influence of the backwater process on the attenuation of the wave is considered. Finally, comparison between the observed waves which are measured in the uPVC pipe of supercritical slope 1/200 and those predicted by the *RGC* and *DIF* methods are discussed in Section 7.5.

7.2 Wave Attenuation for Subcritical Flow in a Simple Pipe

These tests were performed to compare the observed and predicted waves along the test channel of subcritical slope 1/300. The length of channel under study was 12.74 m and the observed sections were at distances of 0.0, 6.6, 7.4 and 8.2 m. Three tests were carried out to allow the effect of decreasing the peak flow on the attenuation of the waves to be studied. In computing, values of 30 pipe sections (Δx = 0.4247 m) for the first and second tests and 40 pipe sections (x = 0.3185 m) for the third test were chosen.

7.2.1 Comparison of Observed and Predicted Waves

Figures 7.1 (a) to 7.1 (c) give the first set of results. The inflow hydrograph is shown in the upper graph of figure 7.1 (a), has a base flow of 0.000183 m^3/sec and peak flow of 0.002417 m^3/sec. The observed depth hydrographs and the calculated depth hydrographs by the *RGC, DIF* and *SIM* methods are presented in figure 7.1 (b). The hydrographs calculated by any of the methods have the same features as the observed hydrographs. But the measured hydrographs have a steeper leading edge than those predicted, an observation which is corroborated by **Bridge (1984)** and **Standing (1986)**. The figure shows also the time lag between the observed and calculated maximum depths.

Figure 7.1 (c) compares measured and predicted peak depths versus time and distance. It is apparent from the figures that the predicted peak-depth variations versus time and distance by the *DIF* and *RGC* methods are very close in shape and value. The figure shows that the observed peak depth at x = 8.2 m is higher than that predicted. Figure 7.1 (d) presents a comparison between the calculated depth changes by the *RGC* method and those observed at four points along the pipe. The initial surface water profile shows the upstream flow depth, which is less than the normal flow depth and also shows the exit flow depth, which is the critical flow depth. The difference between the observed and the calculated depth at the wave arrival is clear at time = 13.38 sec.

The inflow hydrograph for the second test is given in the upper graph of figure 7.2 (a); this shows that the base flow is 0.000242 m^3/sec and the peak flow is 0.002137 m^3/sec. Since the results predicted by the *RGC* and *DIF* methods are so close, only the results predicted by the *RGC* method are considered for this test. Figure 7.2 (b) shows the predicted depth hydrographs given by the *SIM* and *RGC* methods and those observed. The figure shows that at each distance the attenuation of the wave with time is predicted more accurately by the *SIM* method than by the *RGC* method. At the same time the depth hydrographs predicted by the *RGC* method have a steeper leading edge than the calculated hydrographs by the *SIM* method. Figure 7.2 (c) illustrates the measured and calculated peak-depth response versus time and distance. Generally, the peak depths decrease along the pipe, and they are correctly predicted by the two methods. The time lag between predicted and observed peak depths is also notable from this graph. Figure 7.2 (d) illustrates the observed and calculated flow depths along the pipe for the *SIM* method. The agreement between the observed and predicted waves is good except near wave arrival.

The third test is shown in figures 7.3 (a) to 7.3 (d). The inflow hydrograph, which is given in the upper graph of figure 7.3 (a), has a base flow of 0.000217 m^3/sec and peak flow equals 0.00125 m^3/sec. In this test the calculation is carried out to demonstrate the difference between the waves predicted by the *RGC* and *DIF* methods. The measured and calculated depth hydrographs at distances 6.6 m, 7.4 m and 8.2 m are shown in figure 7.3 (b). The figure shows that the depth hydrographs predicted by the two methods are in agreement with the observed hydrographs. It also indicates that the *DIF* scheme predicts a longer time to peak depth than does the *RGC* method. Figure 7.3 (c) shows the peak-depth variations versus time and distance. The figure indicates that the peak depth predicted by the *DIF* scheme near the upstream end of the pipe is higher than that predicted by the *RGC* method; then away from the upstream effect both methods predict approximately the same results. The depth changes along the pipe are illustrated in figure 7.3 (d).

7.2.2 General Remarks and Conclusion

From the previous discussion of the measured and computed results it is found that the observed depth hydrographs always have a steeper leading edge than that given by any of the numerical methods. Investigation of this matter carried out in Chapter 2 revealed that an exaggeration of the steepness of the leading edge of the observed hydrographs is recorded by the pressure transducer, due to the use of a long water-filled plastic tube to connect the pressure transducer to the tapping point at the pipe bottom.

It is also found that the rate of decrease of the wave peak with distance (or time) is affected by the volume of the wave; this agrees with the findings of **Ackers and Harrison (1965)**. It is observed that an increase in the volume of the wave reduces the rate of decrease of the peak depth with distance. This is clearly seen in figures 7.1 (a) and 7.3 (a): the inflow hydrographs have approximately the same shape and base flow, but in the first hydrograph the wave has more volume (nearly three times that of the second wave), and it was found that at x = 6.6 m the peak depth becomes 85% of the peak depth at x = 0.0; while for the second wave it becomes 96% of the peak depth at x = 0.0.

From the previous discussion, all of the numerical methods have shown a measure of agreement compared with the experimental data. Therefore any of them can be used to provide a description of the flow.

7.3 Wave Attenuation in Subcritical Flow in a Pipe with One Concentrated Lateral Inflow

In this section the main uPVC pipe is provided with a concentrated lateral inflow from the pipe bottom as reported in Chapter 2. Therefore the response to the unsteady input flow from the upstream end of the main pipe and the concentrated lateral inflow from the perforated pipe section along the pipe can be investigated experimentally and theoretically. The centre-line of the perforated section, where the concentrated lateral inflows have been fed into the test pipe, is at x = 7.7 m. The observed sections are located at distances of 0.0, 6.6 m, 7.4 m and 8.2 m, unless different values are reported. In computing, a number of pipe sections equal to 30 is used, unless a different number is reported.

Initially, when no lateral inflow is introduced into the pipe, the water-surface profile is a drawdown curve from the normal flow depth to the critical flow depth at the pipe exit. Then when a concentrated lateral inflow is first introduced into the main pipe (during the period of steady-inflow from the upstream end of the main pipe), there is a rise in the flow depth upstream of the lateral inflow section; this process gives rise to the backwater effect just upstream of the the inflow section.

7.3.1 Effect of Different Lateral Inflow Distributions on the Accuracy of the Predicted Waves

In the Saint-Venant equations the lateral inflow has been expressed by the symbol "q" (this is reported in Chapter 3) which represents the lateral inflow per unit length. Thus the local inflow provided from the pipe bottom should be distributed over certain length of the channel, so it can be used in the Saint-Venant equations. Two cases are used in the present study based on **Sivaloganthan's (1981)** technique (see Chapter 5) as follows:

i The concentrated lateral inflows are distributed over two distance steps.

ii The concentrated lateral inflows are distributed over four distance steps.

The effect of these distributions on the accuracy of prediction is investigated in the following test and calculation. The inflow hydrograph for this test is given in the upper graph of figure 7.4 (a); the base flow is 0.000167 m^3/sec and the peak flow is 0.0016 m^3/sec. The concentrated lateral inflow "QL" is given by

$0.0 \le \text{time(sec)} \le 3.0 \qquad QL(m^3/sec) = 0.0$

$3.0 < \text{time(sec)} \le 4.0 \qquad 0.0 \le QL(m^3/sec) \le 0.0001$

$4.0 < \text{time(sec)} \le 32.0 \qquad QL(m^3/sec) = 0.0001$

The comparisons between the observed and calculated waves are made at three locations very close to the lateral inflow (x = 6.86 m, x = 7.62 m and x = 8.2 m) to test the greatest possible difference of the two cases of distribution on the accuracy of the predicted waves. The calculation is then carried out by the *SIM, DIF* and *RGC* methods. This reveals that, when the concentrated lateral inflow is distributed over two distance steps, the solution by the *SIM* method is not stable. However, it becomes stable when the concentrated lateral inflow is distributed over four distance steps.

The solution by the *DIF* scheme is stable when either of the two distributions is used. The computations also revealed that the differences in the predicted depth hydrographs at x = 6.86 m and x = 7.62 m produced in both distributions were insignificant. At x = 8.2 m the differences were less than 3%.

The *RGC* method produces a stable solution when either of the two distributions is used. The predicted depth hydrographs, when the two patterns of lateral inflow are used, are compared with the measured depth hydrographs in figure 7.4 (b). At x = 6.86 m and x = 8.2 m a higher peak depth is produced when a distribution over four distance steps is used. The solution for the two cases failed to produce the double peak values of the observed hydrograph at x = 7.62 m. Generally, the figure shows that the solution for the first case is closer to the experiments.

7.3.2 Comparison of Measured and Predicted Waves

The inflow hydrograph for the first set of results is presented in the upper graph of figure 7.5 (a); the base flow is 0.000167 m^3/sec and the peak flow is 0.002 m^3/sec. The concentrated lateral inflow is given as:

$0.0 \le time(sec) \le 2.0$ $QL(m^3/sec)=0.0$

$2.0 < time(sec) \le 3.0$ $0.0 \le QL(m^3/sec) \le 0.0001$

$3.0 < time(sec) \le 32.0$ $QL(m^3/sec) = 0.0001$

In computing, the lateral inflow was distributed over four distance steps. Figure 7.5 (b) is a comparison between the observed depth hydrographs and the depth hydrographs calculated by the *SIM*, *DIF* and *RGC* methods. The measured depth hydrographs at x = 6.6 m and x = 7.4 m demonstrate the backwater effects of the lateral inflows. The hydrograph at x = 7.4 m has double peak values, the second peak of the hydrograph being higher than the first peak. When the wave is introduced from the upstream end of the main pipe, it travels down the pipe causing the first peak. It is suggested that the passage of the wave over the lateral inflow section gives rise to a reflected wave which propagate upstream and causes the second peak of the hydrograph. This transitional backwater effect is well predicted by the *SIM* method. Generally, the waves predicted by the *SIM* method are in better agreement with the measured depth hydrographs than are those from the other two methods.

The peak-depth variations versus time and distance are illustrated in figure 7.5 (c). It is clear from the figure that the peak depth increases dramatically in the neighbourhood of the local inflow section. The figure shows that near the lateral inflow section the predicted peak depths given by the *DIF* method are too low, while the peak depths predicted by the other two methods are in better agreement with those observed. The difference apparent between the measured and predicted peak-depth variations versus time is due to the time lag between them, as clearly seen in the previous figure. The depth changes along the pipe are illustrated in figure 7.5 (d). This figure shows the complicated shape of the free-surface flow in the presence of the lateral inflow compared to the shape for the simple pipe case: see figures 7.1 (d), 7,2 (d) and 7.3 (d). The propagation of the backwater curve is also clear from the figure.

The second test is illustrated in figures 7.6 (a) to 7.6 (d). The inflow hydrograph is presented in figure 7.6 (a). This has a base flow 0.000217 m^3/sec and peak flow 0.00124 m^3/sec. The concentrated lateral inflows were the same as in the preceding test. The predicted waves were obtained by solving the Saint-Venant equations by the *RGC* and *DIF* methods. In this test the *RGC* method failed to predict a solution when the lateral inflow was distributed over two distance steps. The *DIF* scheme produced a stable solution when the lateral inflow was distributed over two or four distance steps; no significant difference was found between the two solutions. However, distribution over four distance steps is used in the present test.

Figure 7.6 (b) compares of the calculated and measured depth hydrographs. The measured hydrographs show that as a result of the presence of the lateral inflow the backwater effect appears twice at distances 6.6 m and 7.4 m. It is also clear that the depth hydrograph at x = 7.4 m has a double maximum. The figure shows that the *RGC* method produces results in better agreement with the observed values at distances 7.4 m and 8.2 m, and the *DIF* scheme predicts the best results at x = 6.6 m. The peak-depth changes with time and distance are shown in figure 7.6 (c). This figure shows clearly the time lag between the observed and predicted depths. It also shows that the maximum peak-depth values increase at and around the lateral inflow section, while in a simple pipe the peak depths decrease in the downstream direction as the wave attenuates: see figures 7.1 (c), 7.2 (c) and 7.3 (c). The depth variations along the pipe calculated by the *DIF* scheme and the observed variations are illustrated in figure 7.6 (d).

In the upper graph of figure 7.7 (a) the input inflow hydrograph for the last set of data is given. In this graph the base flow is 0.000217 m^3/sec and the maximum flow is 0.00212 m^3/sec. The concentrated lateral inflow is given as:

$0.0 \le time(sec) \le 3.0$ $QL(m^3/sec) = 0.0$

$3.0 < time(sec) \le 4.0$ $0.0 \le QL(m^3/sec) \le 0.0001$

$4.0 < time(sec) \le 32.0$ $QL(m^3/sec) = 0.0001$

In computing, the concentrated lateral inflow is distributed over four distance steps. Figure 7.7 (b) is a comparison between the observed and predicted depth hydrographs for the three numerical methods. The observed hydrographs show the general trend which is described in figures 7.5 (b) and 7.6 (b). Again the *SIM* method has been able to produce more acceptable results than the other two methods. Figure 7.7 (c) shows that the peak depths predicted by the *DIF* method are too low around the lateral inflow section. The figure also demonstrates the characteristics of the peak depth variations versus time and distance, which increase upstream of the lateral inflow section then decrease downstream of the pipe. Finally the changes of the flow depth along the pipe are illustrated in figure 7.7 (d).

7.3.3 The Effect of Increasing the Lateral Inflow on the Depth of the Free-Surface Flow

Figures 7.8 (a) and 7.8 (b) show the effect of increasing the concentrated lateral inflow until it is equal to the steady base flow. Figure 7.8 (a) shows the measured input hydrograph and the depth hydrograph at x = 0.0. A steady concentrated lateral inflow equal to the steady base flow in the main pipe is introduced for 32 sec. Figure 7.8 (b) illustrates the measured depth hydrographs at distances of 6.6 m, 7.4 m and 8.2 m. It is clear from the figure that the depth of the free-surface flow has a marked fluctuation during the steady-inflow period; the flow depth, for example, at x = 7.4 m reached a minimum value of 17 mm and maximum value of 40 mm. It is clear also from the figure that the fluctuation of the flow depth started to decrease after the passage of the wave.

7.3.4 General Remarks and Conclusion

From the results in the previous pages, the following remarks and conclusions can be drawn:

1-The observed waves have a steeper leading edge than those predicted by any of the numerical methods; this was discussed in Section 7.2.3.

2-The concentrated lateral inflows cause a backwater curve in the upstream direction. This effect is significant and cannot be ignored. The backwater effect could cause a double peak hydrograph, as clearly seen in figures 7.6(b) and 7.7 (b).

3-The characteristics of the peak-depth changes depend primarily on the backwater effect; thus the maximum depth can occur at any position along the drain pipe. It is seen in figure 7.5 (b) that at x = 7.4 m the second peak of the observed hydrograph is higher than the first peak.

4-When the concentrated lateral inflow is approximately equal to the discharge at the main pipe, the position of the free-surface fluctuates widely.

5-The rate of attenuation of the wave peak with distance has the same characteristics as in a simple pipe ; an increase in the volume of the wave decreases the rate of lowering of the peak depth value, see figures 7.5 (b) and 7.6 (b).

6-The results predicted by the *SIM* method are in better agreement with the observed values than those from the other two methods; that is, the backwater effect and the peak depth values are well predicted. Therefore the *SIM* method is considered to be superior in predicting flow attenuation in subcritical flow with concentrated lateral inflows.

7.4 Wave Attenuation for Subcritical Flow when the Exit Section is Obstructed by a Gate

The flow response to the arrival of waves generated at the upstream end of the pipe when the water passage was obstructed by a gate at the downstream end is studied in this section. For pipe slope 1/300, the gate was at x = 11.07 m and the downstream stage-discharge relationship was found at x = 11.0 m. This is given in Chapter 6.

Figures 7.9 (a) to 7.11 (c) show three sets of experimental and computed results. These examine the validity of the proposed numerical methods in predicting the flow parameters. At the beginning of each set the input discharge hydrograph is given. The measured and predicted depth hydrographs are shown at distances of 0.0 m, 6.6 m, 8.2 m and 11.0 m. In computing, a value of 30 pipe sections (i.e., Δx = 0.3667 m) is used.

7.4.1 Comparison of Measured and Predicted Waves

For the first set of results the base flow is 0.00025 m^3/sec and peak flow is 0.0025 m^3/sec, as shown in the upper graph of figure 7.9 (a). Figure 7.9 (b) presents comparisons of the measured depth hydrographs and the depth hydrographs predicted by the *SIM, DIF* and *RGC* methods. The figures show that through the steady-state period the depth hydrograph predicted by the *DIF* method recorded a significant increase of the initial depth values at all sections. The depth predicted by the *RGC* method also has an increase which is notable at the downstream section then gradually decreases in the upstream direction. The depth predicted by the *SIM* method remains constant through the steady-state period. It is quite clear from the figures that the observed wave has a steeper leading edge than that predicted. It is also apparent from the figure that a backwater curve is propagated in the upstream direction, as a result of the presence of the gate. The backwater effect consists of a rise in depth upstream of the gate accompanied by a change in velocity which propagates upstream until it attenuates and dies away. This process is quite noticeable in the hydrographs observed at x = 6.6 m and x = 8.2 m.

In computing, the *SIM* method is the one which predicts the backwater effect with greatest accuracy. This is demonstrated, for example, at x = 8.2 m, observed at 24.52 seconds and predicted at 24.75 seconds. As an overall view it can be said that the depth hydrographs predicted by the *SIM* method match the observed hydrographs more accurately than do those from the other two methods.

Figure 7.9 (c) shows the characteristics of the peak-depth variations versus distance and time. In this figure the observed and computed depth variations are compared. The comparison between the observed and calculated peak-depth variations along the pipe presents a measure of agreement. The depth changes along the pipe length predicted by the *SIM* method are compared with the experiments and are illustrated in figure 7.9 (d). In this figure the initial water-profile calculations and the upstream and downstream boundary conditions are shown. The effect of the wave as it travels down the pipe is also evident. Generally, the agreement between the predicted and observed results is good.

In the second test, the peak flow is reduced to 0.001667 m^3/sec; the inflow hydrograph is given in the upper graph of figure 7.10 (a), which has a base flow 0.000217 m^3/sec. In this test the *DIF* method was eliminated from the comparison because it has been seen to predict a significant increase of the initial depth through the steady-state period. Therefore figure 7.10 (b) compares the observed depth hydrographs and the depth hydrographs predicted by the *RGC* and *SIM* methods. It is seen from the figure that the depth calculated by the *RGC* method still recorded an increase of the initial depth through the steady-state period and this is more noticeable at x = 11.0 m. At x = 11.0 m the wave predicted by the two methods is too low. It is also clear from the figure that the backwater effect is observed at x = 8.2 m and x = 6.6 m at times equal to 29.26 sec and 25.52 sec, respectively. The agreement between the observed and predicted backwater effect by the *SIM* method is quite adequate. The ability of the two methods to predict the peak depth is demonstrated in figure 7.10 (c). Figure 7.10 (d) illustrates the propagation of the surge wave down the pipe. The initial surface profile was calculated by the gradually varied flow equation described in Chapter 4, which compares well with the observed values.

The third set of results are presented in figures 7.11 (a) to 7.11 (d). The input discharge hydrograph has a peak value of 0.0012 m^3/sec; it is given in figure 7.11 (a). The *SIM* method was used to predict the flow parameters. The observed and calculated hydrographs are shown in figure 7.11 (b). The predicted depth hydrographs are in agreement with those observed except at wave arrival, where there is a time lag between the predicted and observed waves. The predicted maximum depth is also less than the observed at $x = 11.0$. Figure 7.11 (c) presents the peak depth changes with time and distance, the figure shows that the measured peak depth increases with time and distance; it also shows that the predictions of the *SIM* method have the same trend as the measured values. The characteristics of the peak-depth variations are affected by the presence of the gate. The variations of the measured and the calculated flow depth along the pipe are illustrated in figure 7.11 (d); this variation is accurately predicted by the *SIM* method.

7.4.2 General Remarks and Conclusion

In the last few pages a comparison has been made between the observed and computed waves of subcritical flow when the exit boundary condition is one of controlled outfall. This comparison leads to the following conclusions:

1-The observed wave again has a steeper leading edge than that calculated, as reported in Sections 7.2 and 7.3.

2-The peak depth predicted by any of the methods is low at the exit section. It is felt that this is because the stage-discharge relationship is found from steady-state tests and used as a downstream boundary condition for the unsteady flow tests. After the passage of the wave to the test pipe, the flow depth upstream of the gate reached a certain value, then due to the presence of the gate a backwater curve propagates in the upstream direction until the steady-state flow was established. At this time the flow depth upstream of the gate will be less than the value recorded at the moment of passage of the flow, i.e., for a certain discharge value, the steady flow depth (which is used to establish the depth-discharge relationship) is less than the unsteady flow depth (which is actually measured in the depth hydrographs).

3-The *DIF* and *RGC* methods, as used in the present study, are not suitable for the evaluation of the unsteady flow parameters when the initial water surface profile is a backwater profile determined by a controlled-outfall exit condition.

4-The *SIM* method is the most suitable method to model the attenuation of flow which contains a backwater effect.

5-In the case under consideration, the peak depths increase with time and distance. The rate of increase in peak depth is affected by the volume of the wave. The investigations revealed that an increase in the volume of the wave reduces the rate of increase of the maximum depth with distance. An example of this is presented in figures 7.9 and 7.10. In figure 7.9 the peak depth at distances 6.6 m, 8.2 m and 11.0 m exceeds the peak depth at x = 0.0 by 1.06%, 1.17% and 1.53% respectively. When a reduction of the wave volume is made, as shown in figure 7.10, the rate of increase the peak depth becomes 1.23%, 1.36% and 1.79% of its value at x = 0.0 at the same distances.

7.5 Wave Attenuation in Supercritical Flow

In the present study the Saint-Venant equations are solved by three numerical methods which are coded in computer programs. In previous sections of the present chapter a comparison between the observed waves in subcritical flow and values predicted by the *RGC, DIF* and *SIM* methods was made. In the present section a comparison between the observed waves in supercritical flow and values predicted by the *RGC* and *DIF* methods is carried out. No attempt was made to model the attenuation of supercritical flow by the *SIM* method. This is because the evidence indicates that this method is not appropriate for this type of flow; see for example **Liggett and Cunge (1975)**. A relationship is also required between the flow depth and the discharge at the downstream boundary, **Price (1974)**, in order for the solution by this method to progress; for supercritical flow this relationship must be found experimentally.

In this section the measured waves are those produced in the uPVC pipe of supercritical slope 1/200. The length of the pipe under study is 12.74 m, and the observed sections are at distances 0.0, 6.6 m, 7.4 m and 8.2 m. In computing, values of 30 pipe sections for the first and second tests and 40 pipe sections for the third test were taken.

7.5.1 Comparison of Observed and Predicted Waves

The upper graph of figure 7.12 (a) shows the input inflow hydrograph of the first set of results; this shows a base flow of 0.000217 m^3/sec and peak flow of 0.0018 m^3/sec. Figure 7.12 (b) compares measured and calculated depth hydrographs at distances of 6.6 m, 7.4 m and 8.2 m. The predicted depth hydrographs for the two methods have the same features as the observed hydrographs. The difference between the predicted hydrographs is that the *DIF* method predicts a longer time to peak depth t_P. The peak-depth changes versus time and distance are shown in figure 7.12 (c). It is clear from the figure that the peak depths versus time and distance predicted by the two methods are very close in value and general trend, and they also have the same features as the measured values. The flow depth variations along the pipe at different times are illustrated in figure 7.12 (d). The initial flow depth is less than the normal at the upstream section then gradually increases to the normal flow depth through a small distance; it then remains equal to the normal flow depth through the length of the channel. The lag between the observed and predicted waves is also clear at time = 14.0 sec.

Figures 7.13 (a) to 7.14 (b) compare observed and predicted depth hydrographs given by the *DIF* and *RGC* methods for two different input inflow hydrographs. The degree of agreement and conclusion are the same as for figure 7.12 (b).

7.5.2 Conclusion

In the present section three tests have been carried out to examine the ability of the *DIF* scheme to model attenuation in supercritical flow. The flow parameters computed by the *DIF* scheme are compared with those predicted by the *RGC* method and also with the observed flow parameters. The comparisons revealed that the *DIF* scheme is capable of providing a stable and satisfactory description of the attenuation of waves in supercritical flow in circular cross-section building-drainage pipes.

CHAPTER 8

CONCLUSIONS AND FUTURE WORK

8.1 Conclusions

The novel features of the investigation reported here are as follows:

1-It provides a comprehensive investigation (experimental and numerical) of the attenuation of waves in subcritical flow within building-drainage size pipes. The effect of decreasing the wave volume on the rate of the attenuation is studied for some of the configurations encountered in drainage pipe systems. These are:

a) A simple pipe.

b) A pipe subject to one concentrated lateral inflow.

c) A pipe with gate fixed at the downstream section, generating an interaction between wave and backwater profiles.

2-A laboratory investigation is carried out to identify the reason for the exaggeration of the steepness of the leading edge of the measured waves, a problem noted but not investigated by **Bridge (1984)**.

3-The high-frequency noise of the output from the pressure transducers noted in **Bridge (1984)** and **Standing (1986)** is investigated. A preamplifier unit was built and connected to the data-collection system; also the pipe-supporting system is improved by adding additional pipe clamps to prevent any oscillation in the horizontal plane. These improvements contribute to the accuracy of the pressure transducers' output signals.

4-The *RGC*, *DIF* and *SIM* methods are adopted to simulate the attenuation of waves for the problems under investigation, in order to identify the best method for this class of problems.

5-The effects of changing the grid size on the predicted depth hydrographs are investigated. The stability of the finite-difference methods used is investigated for free-outfall and controlled-outfall boundary conditions.

6-**Sivaloganthan (1981)** developed a new technique for modelling concentrated lateral inflows and applied it to storm-sewers pipe flow. In the present study, this technique is applied for concentrated lateral inflow in building-drainage pipe flow.

7-To contribute to the knowledge of the attenuation of waves in circular cross-section building-drainage size pipe comparisons between measured and predicted waves are made in three different ways: depth hydrographs, variations of peak-depth versus distance and time, and depth changes along the pipe length.

Several conclusions have been reached from the present study and they are summed up as follows:

1-For free-outfall boundary condition the peak depths decrease down the channel as the wave travels. The rate of decrease of the wave peak with distance or time is affected by the volume of the wave. Decreasing the volume of the wave increases the rate of which the peak-depth decreases with distance or time. A study carried out by **Swaffield and Marriott (1979)** shows that the transport of solids through drainage systems is dependent on flow depth. Therefore, the conclusion reached in the present study contributes positively to the water conservation ideas; namely, that a certain reduction of the wave volume can be made without affecting the peak depth values at different downstream positions.

2-The concentrated lateral inflows have a significant effect on the drain performance, and can cause double peak hydrographs, due to the propagation of the backwater profile in the upstream direction.

3-For controlled-outfall boundary condition, the peak depth increases in the downstream direction. An increase in the volume of the wave reduces the rate of increase in peak depth with distance and time.

4-It is found that the water-filled plastic tube which connects the pressure transducer to the tapping point in the pipe bottom has a significant influence on the steepness of the measured waves.

5-The main conclusion from the comparison of observed and computed waves in subcritical flow is that the implicit method is the most suitable prediction method, and can deal efficiently with most problems encountered in drainage pipe systems, such as wave interaction with backwater profiles. The initial backwater surface profile, for example, remains unchanged during the passage of the steady discharge, while the other two methods recorded some change. The solution by this method also predicts the backwater effect, which results from the presence of the gate or the lateral inflow, in good agreement with the experiments, while such agreement is not reached using the other methods.

6-The comparison between the flow parameters for supercritical flow predicted by the *DIF* method and those measured shows that the *DIF* scheme is capable of providing an adequate description of the attenuation of waves in supercritical flow within building-drainage pipes.

7-The investigation revealed that the size of the rectangular solution grid has an influence on the predicted depth hydrographs. The investigation shows that for the *RGC* and *DIF* methods a decrease in Δx decreases the time taken to peak depth (i.e., produces a steeper wave front) and increases the peak depth value; while a decrease in Δt produces a flatter wave, i.e., increases the time taken to peak depth and decreases the peak depth value. For the *SIM* method a decrease in $\Delta t/\Delta x$ increases the peak depth, but no change occurs for the time taken to the peak depth.

8.2 Recommendations for Future Work

1-The present study shows the significant effect of concentrated lateral inflows on the drain performance. Further study should be carried out to investigate the backwater effects on the wave propagation when the drain is subject to more than one lateral inflow.

2-Consideration should be given to the occurrence of full-bore flow as a result of wave interaction with increased depth zones. This case may be developed within the laboratory test rig by increasing the gate height to produce a full-bore flow upstream of the gate. Numerical modelling can be then carried out to solve the equations of continuity and motion for one-dimensional unsteady flow in an open channel and the corresponding equations for closed conduit flow to investigate the propagation of the full-bore flow interface upstream.

3-As shown in Chapter 7, and especially in the case of a simple pipe, the predicted depth hydrographs match the observed hydrographs, except at wave arrival. The observed hydrographs have a steeper leading edge than those predicted by any of the numerical methods. This leads to a difference between the measured and predicted time of peak-depth. The evidence discussed in Chapter 2 shows that the measurement technique exaggerates the steepness of the wave front. However, improvement to the measurement technique should be introduced in order to measure the leading edge of the wave more accurately.

4-The effect of using different resistance models (such as Darcy-Weisbach equation and Colebrook-White equation) on the accuracy of the predicted flow parameters should be examined. Also more research should be carried out to develop unsteady resistance models.

5-Improvement to the depth-discharge relationship upstream of the gate should be made by applying a different approach based on dimensional or other considerations in the establishment of this relationship.

Finally, the outcome of the present study can provide useful tools for designers. The *SIM* method displayed a better agreement with the experiments; therefore it can be used to calculate the pipe diameter required for different drainage systems. The *SIM* method can be also extended to meet the requirements of design for building-drainage networks of flat slope.

REFERENCES

Abbot, M.B. and Verwey, A. (1970)
"Four-point method of characteristics", Proc. Amer. Soc. Civ. Eng. 96, J. Hyd. Div. HY12, pp. 2549-2564, December.

Ackers, P. and Harrison, A.J.M. (1964)
"Attenuation of flood waves in part-full pipes", Proc., I.C.E., 28, pp. 361-382, July.

Amein, M. and Chu, H.L. (1975)
"Implicit numerical modelling of unsteady flows", Proc. Amer. Soc. Civ. Eng. 101, J. Hyd. Div. HY6, pp. 717-731, June.

Amein, M. and Fang, C.S. (1970)
"Implicit flood routing in natural channels", Proc. Soc. Civ. Eng. 96, J. Hyd. Div. HY12, pp. 2481-2500, December.

Bainbridge, K.P. (1986)
"The confluence of open-channel flow at pipe junctions", M.Phil Thesis, Brunel University, Uxbridge, Middlesex, England.

Barnes, A.H. (1965)
"Predictability of free-surface profiles for steady non-uniform flow in a circular cross-section", Ph.D. Dissertation, Dept. of Civil Eng., Colorado State University.

Bocarro, R.A (1987)
"Water conserving WC design for developing countries", Ph.D. Thesis, Brunel University, Uxbridge, Middlesex, England.

Bridge, S. (1984)
"A study of unsteady flow wave attenuation in partially filled pipe networks", Ph.D. Thesis, Brunel University, Uxbridge, Middlesex, England.

Burberry, P.J. (1978)
"Water economy and the hydraulic design of underground drainage", Proc. Seminar on Drainage Design, Brunel University, Paper C3, 12 pages, May.

Burberry, P.J. (1979)
"Environment and services", Batsford Halsted, London, 360 pages.

Chaudhry, Y.M. and Contractor, D.N. (1973)
"Application of the implicit methods to surges in open channels" Wat. Res. Res., 9(6), pp. 1605-1612, December.

Chow, V.T. (1959)
"Open-Channel Hydraulics", McGraw-Hill International, 680 pages.

Courant, R., Isaacson, E. and Ress, M. (1952)
"On the solution of non-linear hyperbolic differential

equations by finite differences", Comm. Pure and App. Math., 5, pp. 243-255.

Cunge, J.A. and Wegner, M. (1964)
"Integration numerique des equations d'ecoulement de Barre de Saint Venant par un schema implicit de differences finies, La Houille Blanche, No.1, pp. 33-39.

Fox, J.A. (1977)
"Hydraulic analysis of unsteady flow in pipe networks", MacMillan, London, 216 pages.

Gunaratnaln, D.J. and Perkins, F.E. (1970)
"Numerical solution of unsteady flows in open channels", Report No. 127, Hydrodynamics Laboratory, MIT, 260 pages, July.

Henderson, F.M. (1966)
"Open channel flow", MacMillan, New York, Book, 522 pages.

Houghton, D.D. and Kasahara, A. (1968)
"Nonlinear shallow fluid flow over an isolated ridge", Comm. Pure and App. Math. xxI, No.1, January.

Jolly, J.P. and Yevjevich, V. (1974)
"Simulation accuracies of gradually varied flow", Proc. Amer. Soc. Civ. Eng. 100, J. Hyd. Div. HY7, pp. 1011-1030, July.

Kasahara, A. and Houghton, D.D. (1969)
"Nonlinear mountain flow", Part I, National Center for Atmospheric Research, Part 43, pp. 103-130.

Koren, V.I. and Kuchment, L.S. (1967)
"Numerical integration of de Saint Venant's equations with explicit schemes when computing the unsteady flow in rivers", Trudy G.N.I., No.8.

Lax, P.D. (1957)
"Hyperbolic systems of conservation laws II", Comm. Pure Appl. Math., 10, pp. 537-566.

Lax, P.D. and Wendroff, B. (1960)
"Systems of conservation laws", on Pure and Appl. Math., 13, pp. 217-237.

Liggett, J.A. (1968)
"Mathematical flow determination in open channels" Proc. Amer. Soc. Civ. Eng. 94, J. Eng. Mech. Div. EM4, pp. 947-963.

Liggett, J.A. and Cunge, J.A. (1975)
"Numerical method of solution of the unsteady flow equations", Unsteady flow in open channels, 1, Water Resources Publications, Fort Collins, Colarado.

Lin, C.C. (1966)
"The theory of hydrodynamic stability", 1st ed., The Cambridge University Press, London, England, 305 pages.

Lister, M. (1960)
"The numerical solution of hyperbolic partial differential equations by the method of characteristics", Mathematica, Methods for Digital Computers, Ralston, A. and Wilf, H.S. eds., John Wiley and Sons Inc., New York, pp. 165-179.

Massau, J. (1905)
"L'integration graphique des equations aux derivees parcielles", Assoc. Ingenieurs Sortis des Ecoles Speciales de Gand, Annales, 4, pp. 65-80.

O'Brien, G.C., Moton, A.H. and Sidney, K. (1950)
"A study of the numerical solution of partial differential equations", J. Math. and Phy., 29, pp. 223-251.

Penny,R.K. (1974)
"The experimental method, a text for students of engineering and science", Longman, London, 179 pages.

Pinkayn, A.M. (1972)
"Routing storm water through a drainage system", Proc. Amer. Soc. Civ. Eng. 98, J. Hyd. Div. HY1, pp. 123-135, January.

Ponce, V.M. (1982)
"Nature of wave attenuation in open channel flow", Proc. Amer. Soc. Civ. Eng. 108, J. Hyd. Div. HY2, pp. 257-261, February.

Powell, R.W. (1960)
"History of Manning's formula", J. Geophysical Research, 65, No.4, pp. 1310-1311, April.

Prasad, R. (1970)
"Numerical method of computing flow profiles", Proc. Amer. Soc. Civ. Eng. 96, J. Hyd. Div. HY1, pp. 75-86, January.

Price, R.K. (1974)
"Comparison of four numerical methods for flood routing", Proc. Amer. Soc. Civ. Eng. 100, J. HYd. Div. Hy7, pp. 879-899, July.

Preissmann, A. (1960)
"Propagation des intumescences dans les canaux et rivieres", 1st Congres de l'Assoc. Francaise de calcul, Grenoble, Printed 1961, pp. 433-442.

Preissmann, A. and Cunge, J.A. (1961)
"Tidal bore calculation on an electronic computer", Intumescences, Societe Hydrotechnique De France", La Houille Blanche, No.5, pp. 588-596, October.

Quinn, F.H. and Wylie, E.B. (1972)
"Transient analysis of the Detroit river by the implicit method", Wat. Res. Res., 8(6), pp. 1461-1469.

Ragan, R.M. (1965)
"Synthesis of hydrographs and water surface profiles for

unsteady open channel flow with lateral inflows", Ph.D. Thesis, Cornell University, Water Resources Center, Ithaca, New York.

Reynolds, A.J. (1974)
"Turbulent flows in engineering", Wiley-Interscience, London (etc), 462 pages.

Richtmyer, R.D. (1957)
"Difference methods for initial-value problems", Interscience Tracts in pure and applied Mathematics, 4, Wiley (Interscience), New York.

Richtmyer, R.D. (1962)
"A survey of difference methods for non-steady fluid dynamics", ACAR Technical Notes 63-2, National Center for Atmospheric Research, Boulder, Colorado.

Rump, M.E. (1978)
"Current work at BRE on water conservation", Proc. Seminar on Drainage Design, Brunel University, Paper C1, 19 pages.

Saint-Venant, A.J.C.B. (1870)
"Elementary demonstration of the propagation formula for a wave or transitory wave in a prismatic channel and remarks on the propagation of sound and light, on hydraulic jumps and also on the distinction between

rivers and torrents", Comptes rendus des seances de l'Academie des sciences, 71, pp. 186-195.

Sevuk, A.S. and Yen, B.C. (1973)
"A comparative study on flood routing computation", Proc. Int. Symp. River Mech, 3, Bangkok, pp. 275-290, January.

Sevuk, A.S. and Yen, B.C. (1982)
"Sewer network routing by dynamic wave characteristics", Proc. Amer. Soc. Civ. Eng. 109, J. Hyd. Div. HY3, pp. 379-398, March.

Sivaloganthan, K. (1978)
"Flood routing by characteristic methods", Proc. Amer. Soc. Civ. Eng. 104, J. Hyd. Div. HY7, pp. 1075-1091, July.

Sivaloganthan, K. (1980)
"Numerical computation of flow in storm water sewers", Ph.D. Thesis, University of London, England.

Sivaloganthan, K. (1980)
"Routing of steep discharge hydrographs in open channels", Proc. Inst. Civ. Engrs, 69, Part 2, pp. 845-853, September.

Sivaloganthan, K. (1981)
"Storm sewer flow computations", Proc. Instn. Civ. Engrs, 71, Part 2, pp. 513-522, June.

Smith, G.D. (1985)
"Numerical solution of partial differential equations, finite difference methods", 3rd ed., Clarendon, Oxford, 337 pages.

Spencer, A.J.M. et al. (1977)
"Engineering Mathematics", Van Nostrand Reinhold, New York, 536 pages.

Standing, K.M. (1986)
"Surge generation as an aid to water conserving building drainage design", Ph.D. Thesis, Brunel University, Uxbridge, Middlesex, England.

Streeter, V.L. and Wylie, E.B. (1979)
"Fluid mechanics", 7th ed., McGraw-Hill, New York, 562 pages.

Strelkoff, T. (1970)
"Numerical solution of Saint-Venant equations", Proc. Amer. Soc. Civ. Eng. 96, J. Hyd. Div. HY1, pp. 223-253, January.

Swaffield, J.A. (1981)
"An initial study of the application of the numerical method of characteristics to unsteady flow analysis in partially filled gravity drainage sized pipes", NBSIR 81-2308, US Department of Commerce, July.

Swaffield, J.A. (1982)
"Application of the method of characteristics to predict attenuation in unsteady partially filled pipe flow", NBSIR 82-2478, US Department of Commerce, March.

Swaffield, J. A. and Marriott, B.S.T. (1979)
"An investigation of the effect of reduced volume w.c. flush on the transport of solids in above ground drainage systems" CIB W62 meeting, Brussels.

Swaffield, J.A., Wakelin, R.H.M. and Bocarro, R.A. (1986)
"Low flush volume WC design for developing countries", paper presented at the CIB W62 Seminar, Copenhagen, Denmark, May.

Twort, A.C., Hoather, R.C. and Law, F.M. (1974)
"Water supply", Edward Arnold Publishers, London, 478 pages.

Vasiliev, O.F., Godunov, S.K., et al (1963)
"Numerical method of computation of wave propagation in open channels; application to the problem of floods", Dokl. Akad. Nauk. SSSR, 151, No.3.

Vasiliev, O.F., Temnoeva, T.A., and Shugrin, S.M. (1965)
"Numerical method for the calculation of unsteady flows in open channels", Izv. Akad. Nauk SSSR, Mechanics, No.2, pp. 17-25.

Von Neumann, J. (1963)
"First report on the numerical calculation of flow problems", Paper No.19, John Von Neumann collected works. A. H. Taub, General Editor, v, Pergamon Press, pp. 664-712.

Wakelin, R.H.M. (1978)
"A study of the transport of solids in hospital's above ground drainage systems", Ph.D. Thesis, Brunel University, Uxbridge, Middlesex, England.

White, W.R. and Price, R.K. (1975)
"The design of storm water drainage channels using mathematical model technique", Proc. Inst. Civ. Engrs., 59, Part 2, pp. 91-102, March.

Wylie, E.B. (1970)
"Unsteady free-surface flow computations", Proc. Amer. Soc. Civ. Eng. 96, J. Hyd. Div. HY11, pp. 2241-2251, November.

Wylie, E.B. (1972)
"Transient analysis of the Detroit River by the implicit method", Wat. Res. Res., 8, No.6, pp. 1461-1469, December.

Wylie, E.B. and Streeter, V.L. (1978)
"Fluid transients", McGraw-Hill, New York, 384 pages.

Yen, B.C. (1978)
"Hydraulic instabilities of storm sewer flow", Proc. International Conference on Urban Storm Drains, Southampton University, Southampton, Pentch Press, London, pp. 282-293, April.

Yevjevich, V. and Barnes, A.H. (1970)
"Flood routing through storm drains", Part I, Hydrology Paper No.43, Colorado State University, Fort Collins, Colorado, November.

Yevjevich, V. and Barnes, A.H. (1970)
"Flood routing through storm drains", Part II, Hydrology Paper No.44, Colorado State University, Fort Collins, Colorado, November.

Yevjevich, V. and Barnes, A.H. (1970)
"Flood routing through storm drains", Part III, Hydrology Paper No.45, Colorado State University, Fort Collins, Colorado, November.

Yevjevich, V. and Barnes, A.H. (1970)
"Flood routing through storm drains", Part IV, Hydrology Paper No.46, Colorado State University, Fort Collins, Colorado, November.

APPENDIX A

SUBCRITICAL AND SUPERCRITICAL FLOW

Flow in open channels can be defined by reference to the values of Froude number Fr which is the ratio of the stream velocity to the wavespeed, **Henderson (1966)**, i.e.;

$$Fr = v / \sqrt{gh} \qquad \text{(A.1)}$$

where v = mean flow velocity, m/sec

$\sqrt{gh}$ = wavespeed for rectangular channels, m/sec

However, if Froude number Fr is less than unity, i.e.; the wave velocity is greater than the flow velocity, the flow regime will be subcritical. In this type of flow effects from downstream are propagated to the upstream sections.

Supercritical flow will be developed when the Froude number Fr is greater than unity; that means the flow velocity becomes greater than the wavespeed, therefore no such effect from the downstream sections may propagate to the upstream sections.

APPENDIX B

FLOW CHARTS OF THE NUMERICAL METHODS

B.1 Flow Chart Of the *RGC* Method

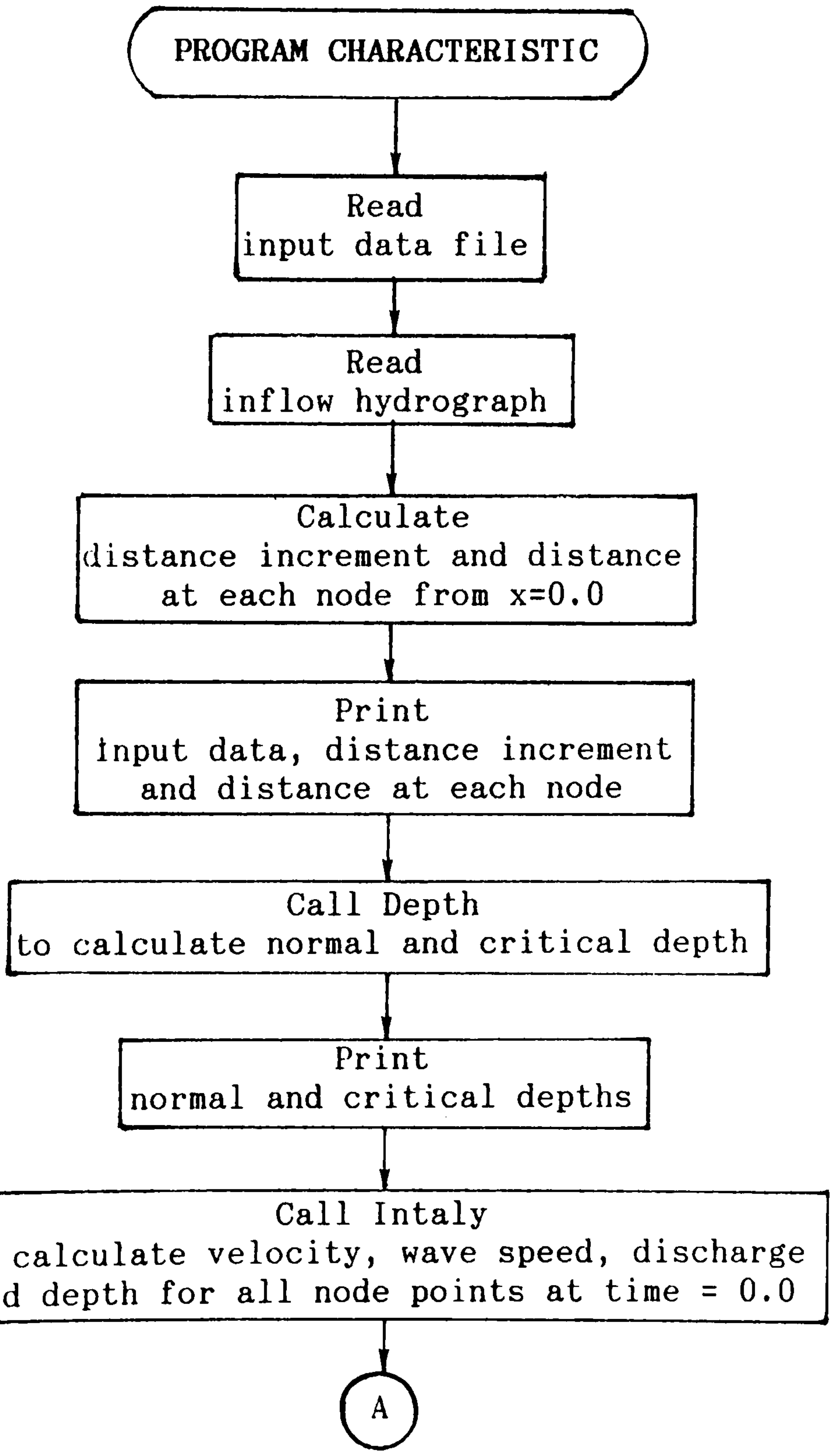

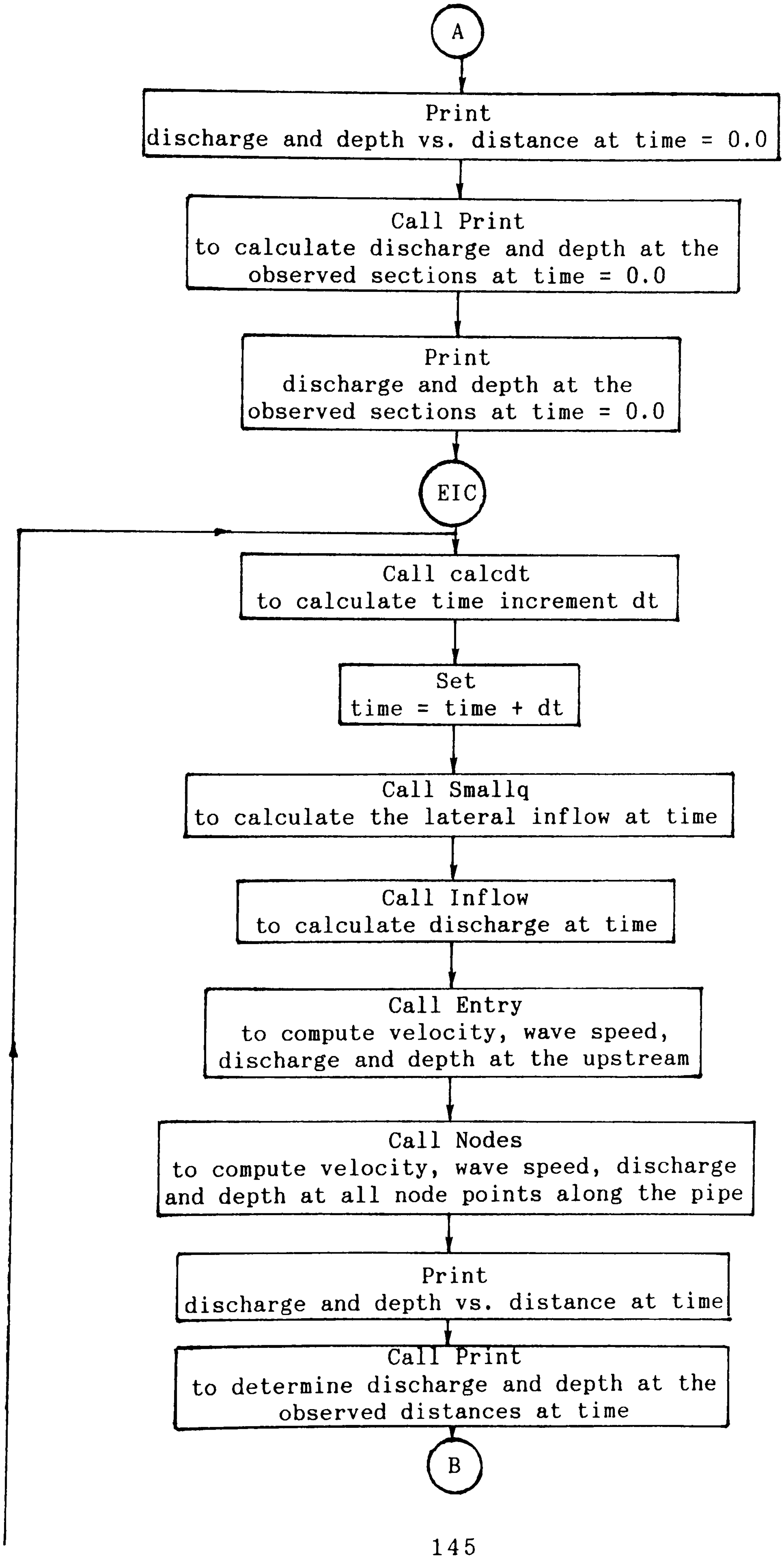
A
Print
discharge and depth vs. distance at time = 0.0
Call Print
to calculate discharge and depth at the observed sections at time = 0.0
Print
discharge and depth at the observed sections at time = 0.0
EIC
Call calcdt
to calculate time increment dt
Set
time = time + dt
Call Smallq
to calculate the lateral inflow at time
Call Inflow
to calculate discharge at time
Call Entry
to compute velocity, wave speed, discharge and depth at the upstream
Call Nodes
to compute velocity, wave speed, discharge and depth at all node points along the pipe
Print
discharge and depth vs. distance at time
Call Print
to determine discharge and depth at the observed distances at time
B

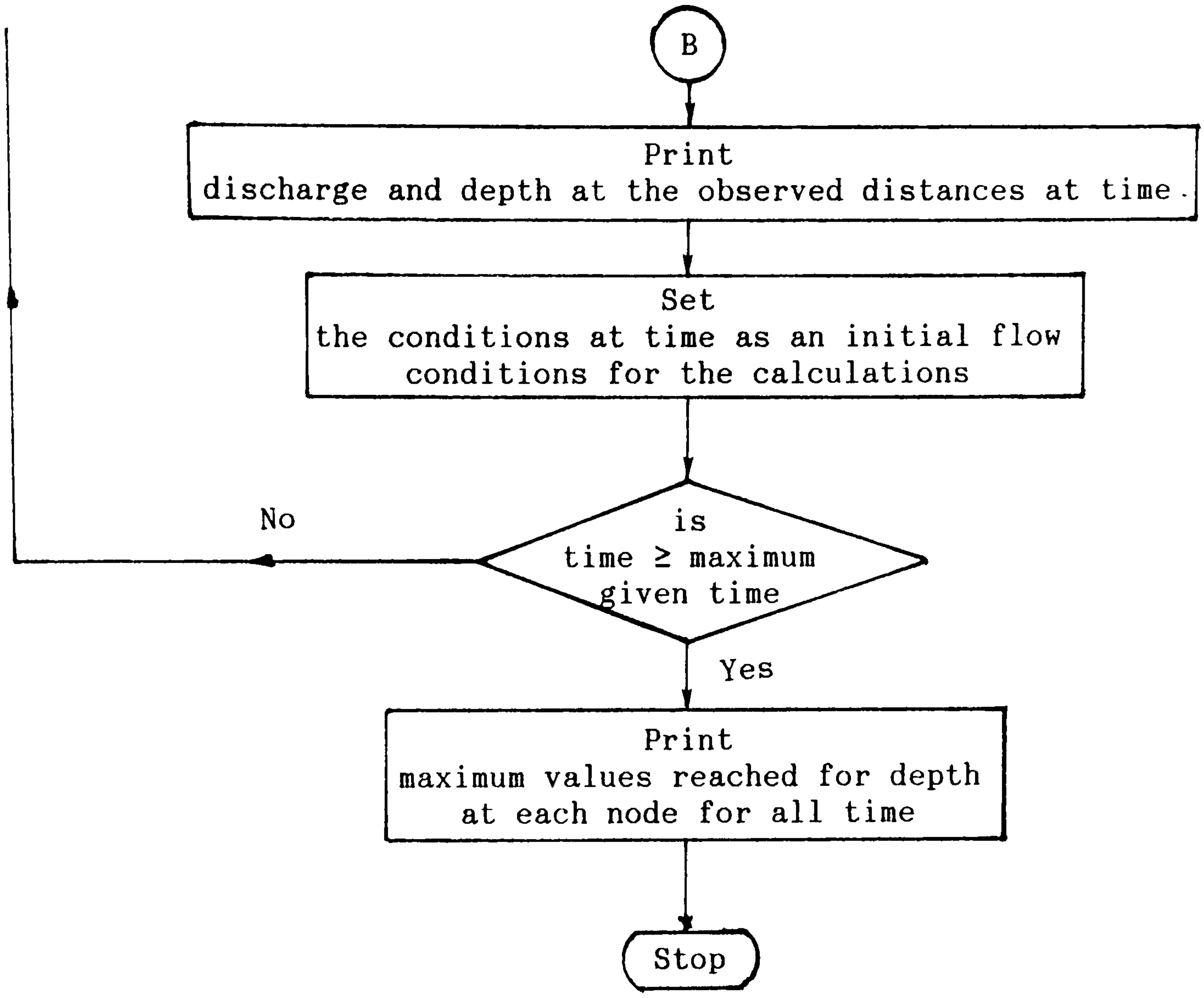

B.2 Flow Chart of the *DIF* method

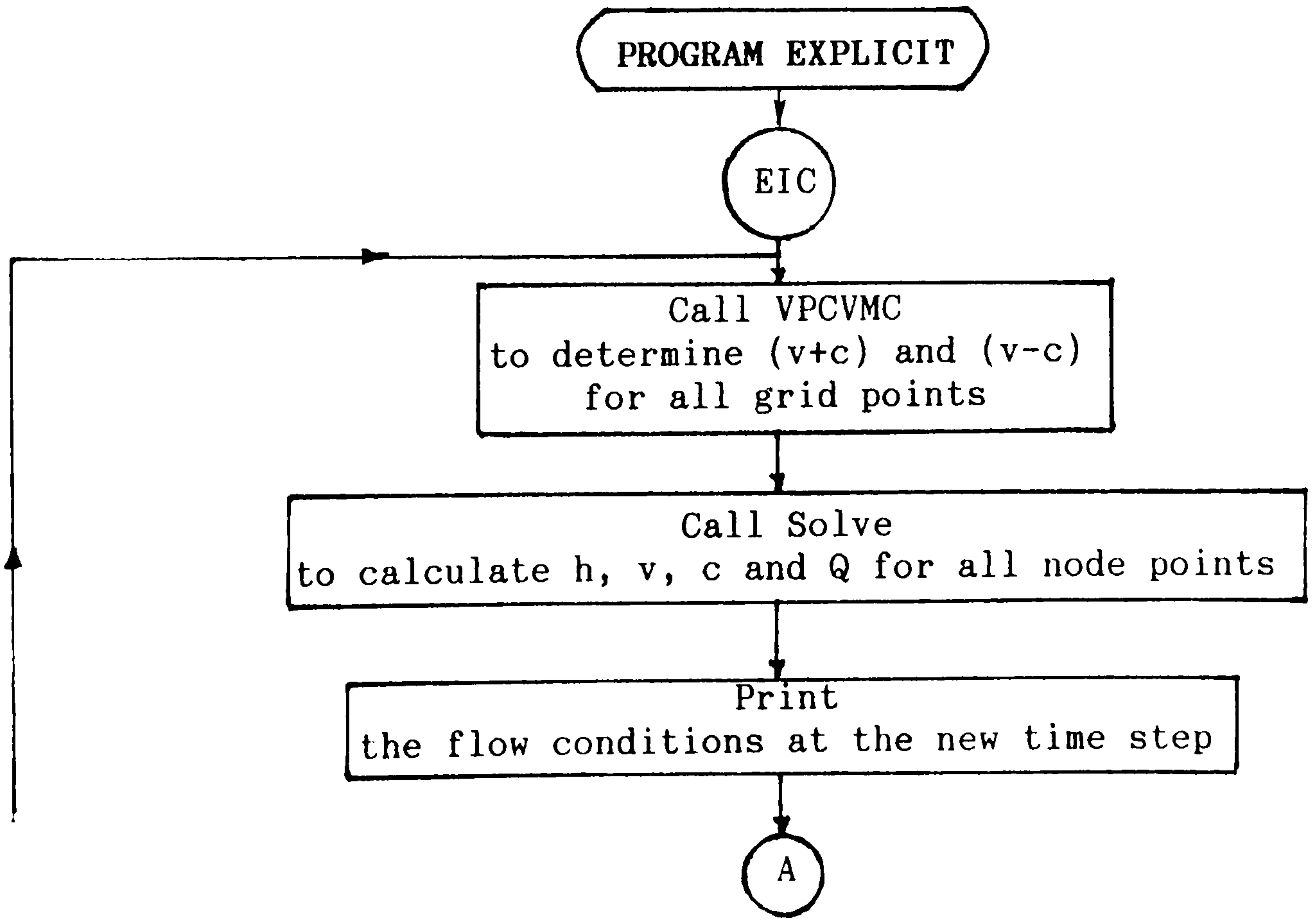

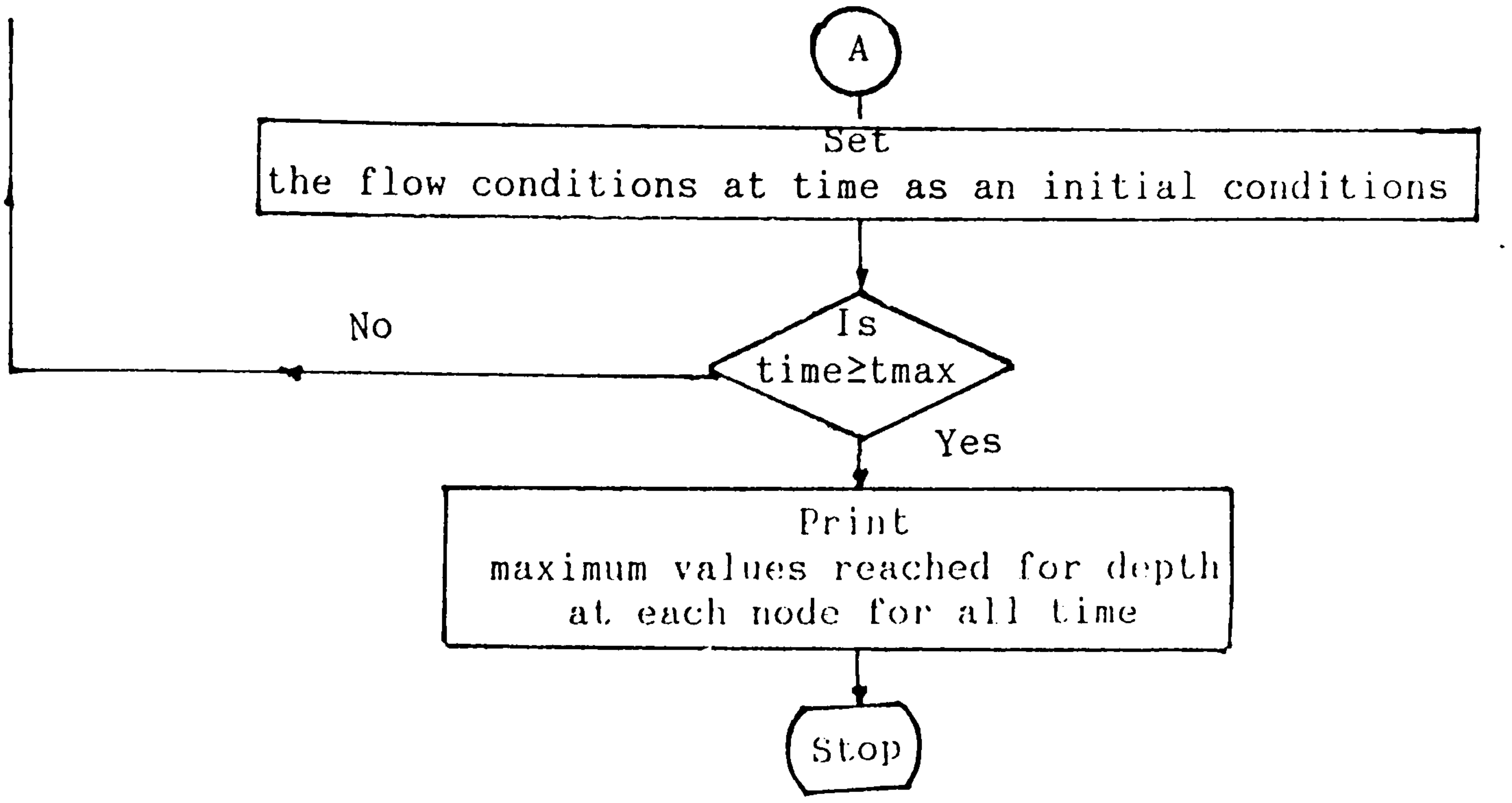
A
Set
the flow conditions at time as an initial conditions
Is
time≥tmax
No
Yes
Print
maximum values reached for depth
at each node for all time
Stop

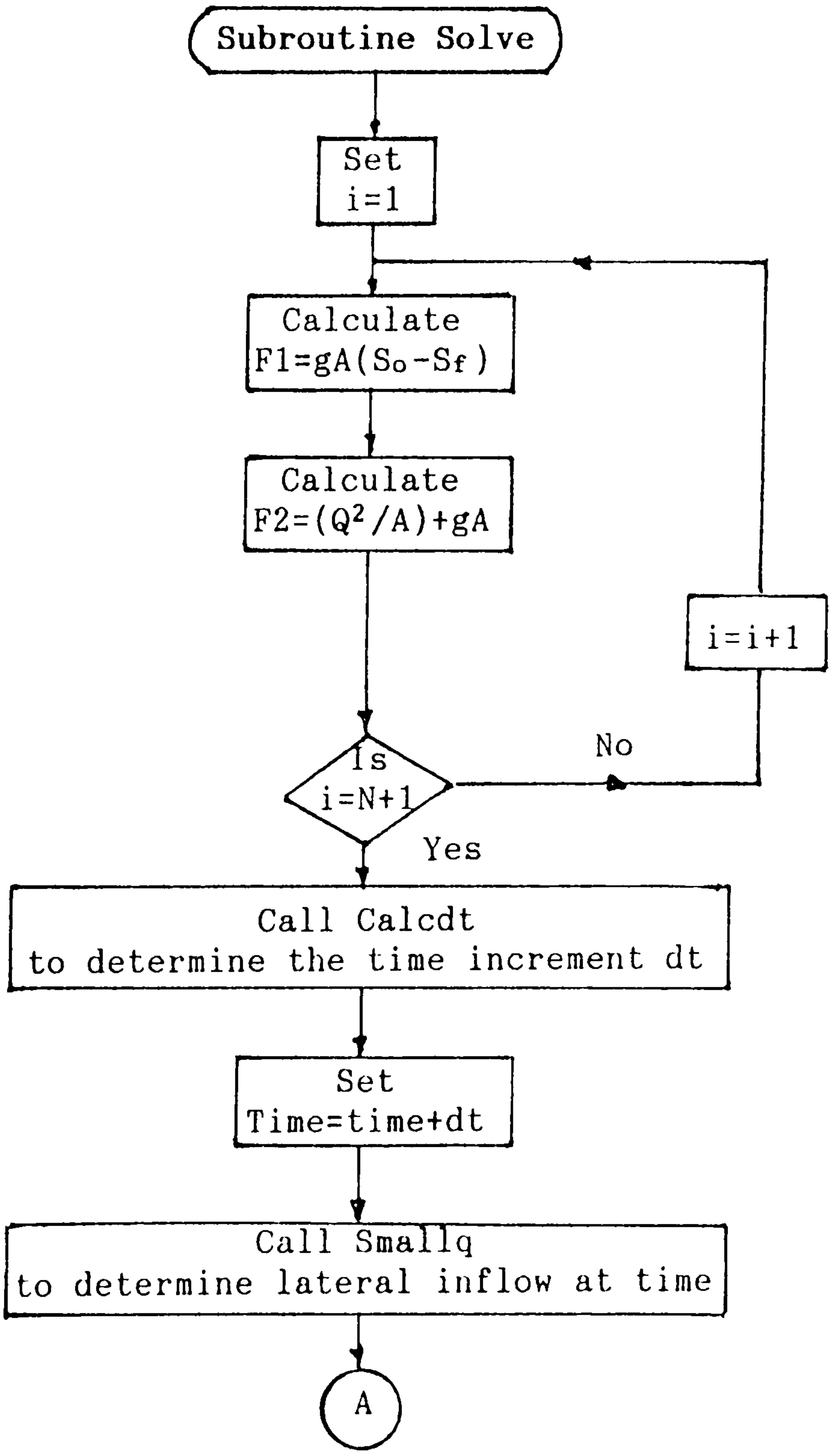
Subroutine Solve
Set
i=1
Calculate
F1=gA(So-Sf)
Calculate
F2=(Q²/A)+gA
i=i+1
Is
i=N+1
No
Yes
Call Calcdt
to determine the time increment dt
Set
Time=time+dt
Call Smallq
to determine lateral inflow at time
A

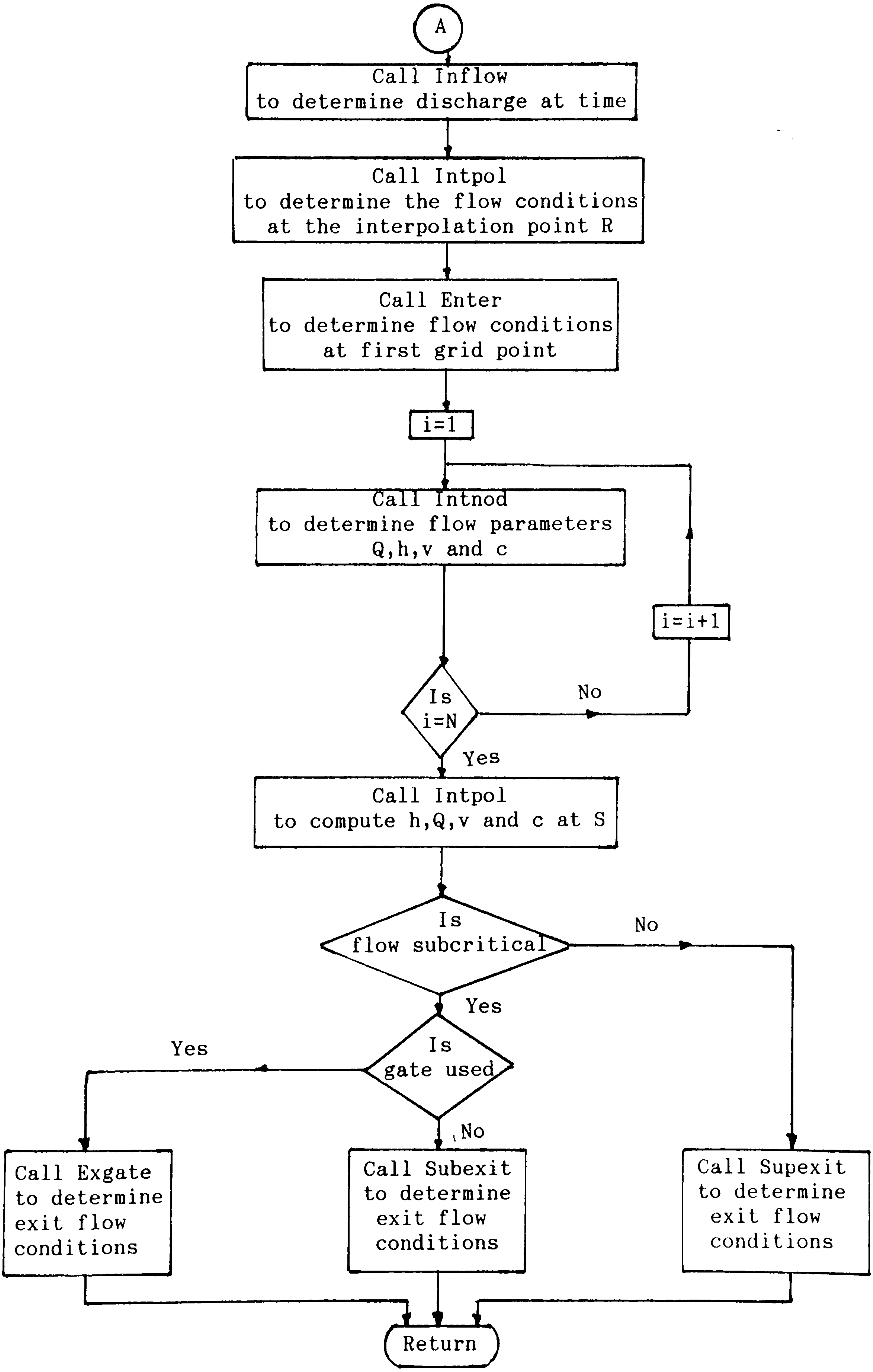
A
Call Inflow
to determine discharge at time
Call Intpol
to determine the flow conditions
at the interpolation point R
Call Enter
to determine flow conditions
at first grid point
i=1
Call Intnod
to determine flow parameters
Q,h,v and c
i=i+1
Is
i=N
No
Yes
Call Intpol
to compute h,Q,v and c at S
Is
flow subcritical
No
Yes
Is
gate used
Yes
No
Call Exgate
to determine
exit flow
conditions
Call Subexit
to determine
exit flow
conditions
Call Supexit
to determine
exit flow
conditions
Return

B.3 Flow Chart of the *SIM* method

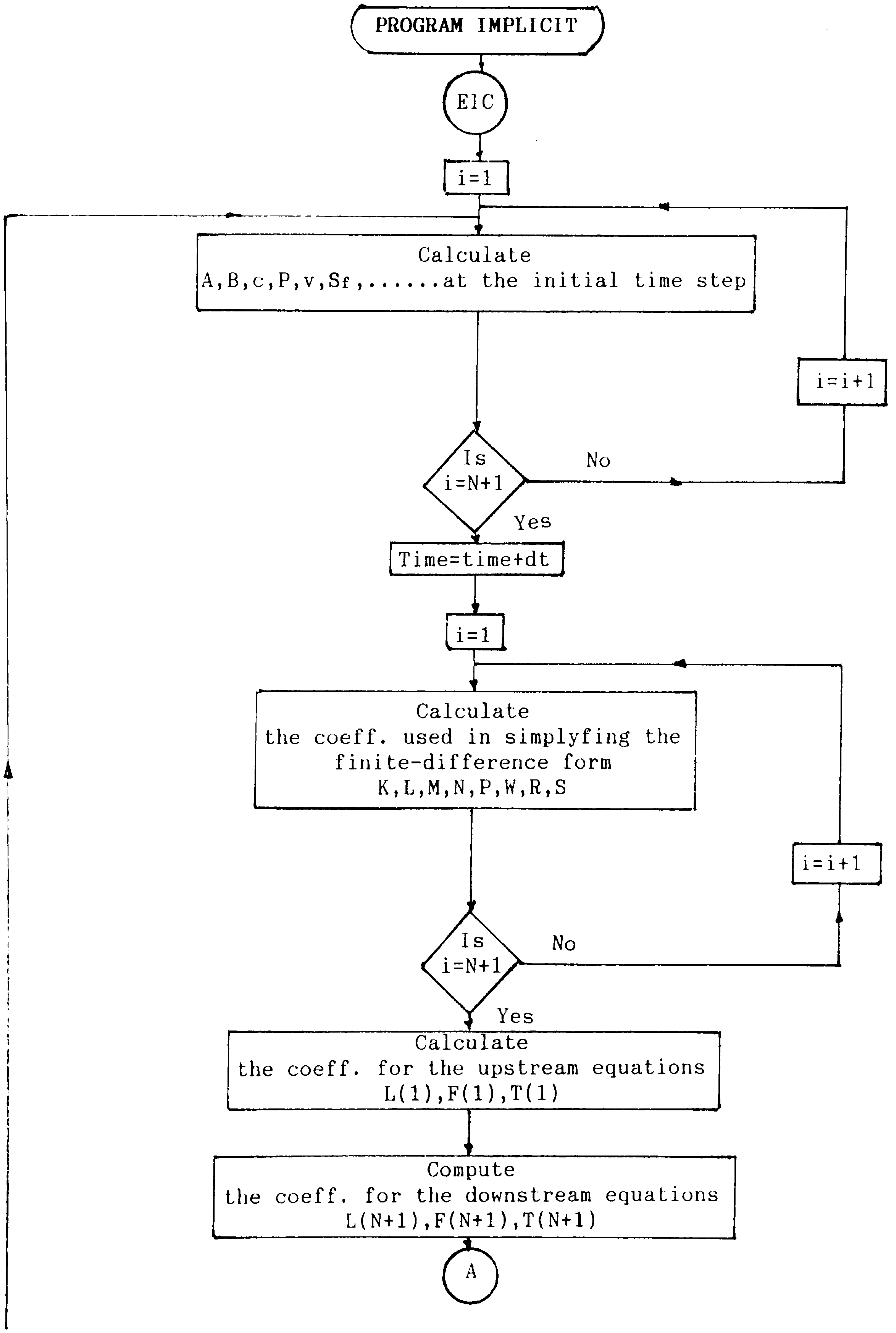

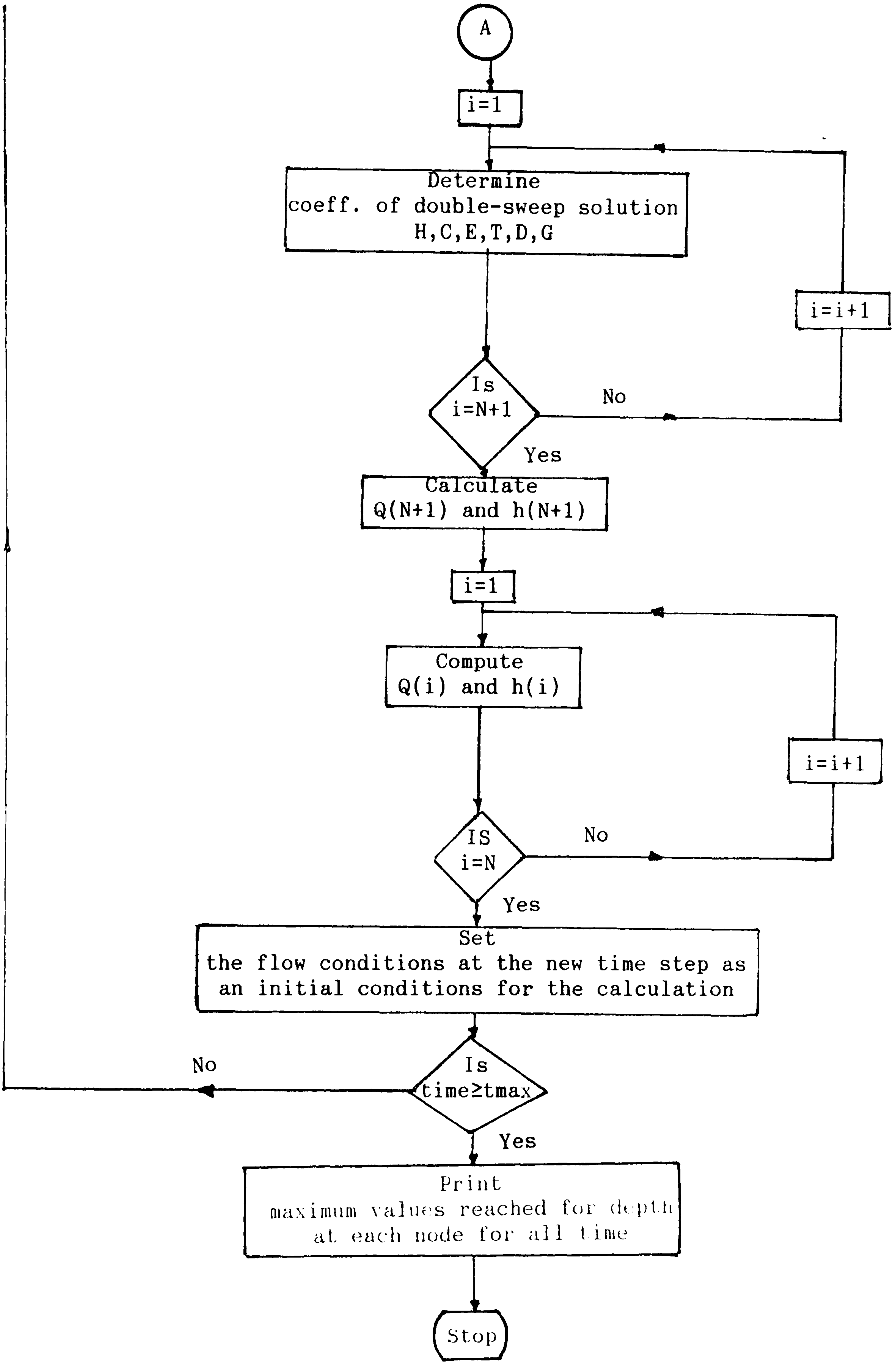
A
i=1
Determine coeff. of double-sweep solution H,C,E,T,D,G
i=i+1
Is i=N+1
No
Yes
Calculate Q(N+1) and h(N+1)
i=1
Compute Q(i) and h(i)
i=i+1
IS i=N
No
Yes
Set the flow conditions at the new time step as an initial conditions for the calculation
No
Is time≥tmax
Yes
Print maximum values reached for depth at each node for all time
Stop

APPENDIX C

SOLUTION BY DOUBLE-SWEEP METHOD

Equations 5.35 and 5.36 with superscripts omitted have the following form:

$K_iQ_{i+1} - K_iQ_{i-1} + L_ih_i = M_i$ ....(C.1)

$N_iQ_{i+1} + P_iQ_i - N_iQ_{i-1} + W_ih_{i+1} + R_ih_i - W_ih_{i-1} = S_i$
........................(C.2)

We assume that

$h_i = H_i + T_iQ_{i+1} + C_ih_{i+1}$ (a)

and

$Q_i = D_i + E_iQ_{i+1} + G_ih_{i+1}$ (b)

Then h_{i-1} and Q_{i-1} have the following form

$h_{i-1} = H_{i-1} + T_{i-1}Q_i + C_{i-1}h_i$ (c)

and

$Q_{i-1} = D_{i-1} + E_{i-1}Q_i + G_{i-1}h_i$ (d)

Equations C.1 and C.2 have the following form

$$h_i = \frac{M_i}{L_i} + \frac{K_i}{L_i} Q_{i-1} - \frac{K_i}{L_i} Q_{i+1} \quad \ldots\ldots\ldots\ldots\ldots\ldots\ldots\ldots (C.3)$$

$$Q_i = \frac{S_i}{P_i} + \frac{N_i}{P_i} Q_{i-1} + \frac{W_i}{P_i} h_{i-1} - \frac{N_i}{P_i} Q_{i+1} - \frac{W_i}{P_i} h_{i+1} - \frac{R_i}{P_i} h_i$$

$$\ldots\ldots\ldots\ldots\ldots\ldots\ldots\ldots\ldots (C.4)$$

Substituting for Q_{i-1} from equation (d) into equation C.3,

$$(1 - \frac{K_i}{L_i} G_i)h_i = (\frac{M_i}{L_i} + \frac{K_i}{L_i} D_{i-1}) + \frac{K_i E_{i-1}}{L_i} Q_i - \frac{K_i}{L_i} Q_{i+1}$$

$$\ldots\ldots\ldots\ldots\ldots\ldots\ldots\ldots (C.5)$$

Substituting for Q_{i-1}, h_{i-1} in equation C.4, we have

$$(1 - \frac{N_i}{P_i} E_{i-1} - \frac{W_i}{P_i} T_{i-1})Q_i = (\frac{S_i}{P_i} + \frac{N_i}{P_i} D_{i-1} + \frac{W_i}{P_i} H_{i-1})$$

$$- \frac{N_i}{P_i} Q_{i+1} - \frac{W_i}{P_i} h_{i+1} + (\frac{N_i}{P_i} G_{i-1} + \frac{W_i}{P_i} C_{i-1} - \frac{R_i}{P_i})h_i \quad \ldots (C.6)$$

We assume that

$Y1 = (1 - (N_i/P_i)E_{i-1} - (W_i/P_i)T_{i-1})$

$Y2 = ((L_i/K_i) - G_{i-1}$, $\quad Y3 = N_i G_{i-1} + W_i C_{i-1} - R_i$

$Y4 = S_i + N_i D_{i-1} + W_i H_{i-1}$, $\quad Y5 = (M_i/K_i) + D_{i-1}$

Then equations C.5 and C.6 become

$$Y2K_i h_i = K_i Y5 + K_i E_{i-1} Q_i - K_i Q_{i+1} \quad \ldots\ldots\ldots\ldots\ldots\ldots (C.7)$$

$$Y1Q_i = Y4 - N_i Q_{i+1} - W_i h_{i+1} + Y3h_i \quad \ldots\ldots\ldots\ldots\ldots\ldots (C.8)$$

Rearranging equation C.7, we have

$h_i = (Y5/Y2) + (E_{i-1}/Y2)Q_i - (1/Y2)Q_{i+1}$

Eliminating h_i from equation C.8, we have

$$(Y1\ Y2 - Y3\ E_{i-1})Q_i = (Y4\ Y2 + Y3\ Y5) - (Y3 + Y2\ N_i)Q_{i+1} - Y2\ W_i\ h_{i+1} \quad \ldots\ldots\ldots\ldots\ldots\ldots\ldots (C.9)$$

Elimination of Q_i from equations C.7 and C.8 gives

$$(Y2\ Y1 - E_{i-1}\ Y3)h_i = (Y5\ Y1 + Y4\ E_{i-1}) - (N_i\ E_{i-1} + Y1)\ Q_{i+1} - E_{i-1}W_i h_{i+1} \quad \ldots\ldots\ldots (C.10)$$

Comparing equation (a) with equation C.10, and equation (b) with equation C.9, we have

$H_i = (Y5\ Y1 + Y4\ E_{i-1})/(Y2\ Y1 - E_{i-1}\ Y3)$

$C_i = (E_{i-1}\ W_i)/(Y2\ Y1 - E_{i-1}\ Y3$

$E_i = (Y3 + Y2\ N_i)/(Y1\ Y2 - Y3\ E_{i-1})$

$T_i = (E_{i-1}\ N_i + Y1)/(Y2\ Y1 - E_{i-1}\ Y3$

$D_i = (Y2\ Y4 + Y3\ Y5)/(Y1\ Y2 - Y3\ E_{i-1})$

$G_i = -((Y2\ W_i)/(Y1\ Y2 - Y3\ E_{i-1}))$

A similar procedure is carried out to solve the upstream and downstream equations for h(1), Q(1), h(N+1) and Q(N+1).

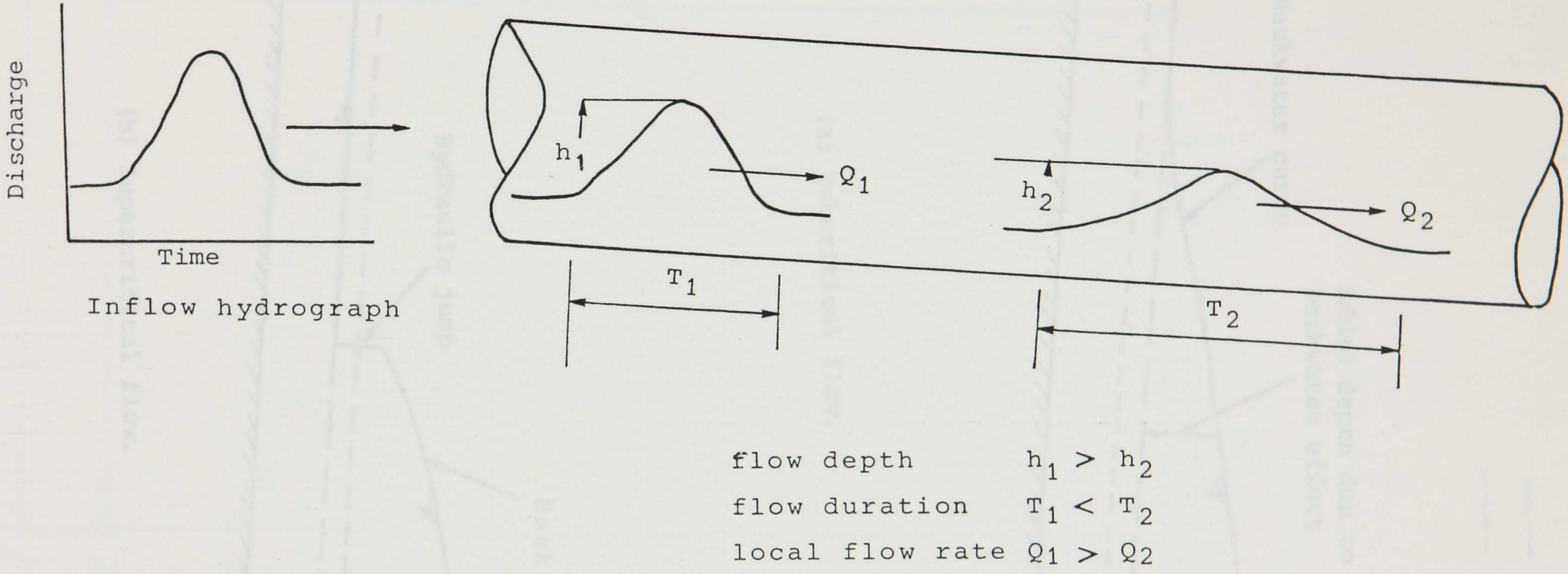

Figure 1.1 Wave attenuation in partially filled unsteady pipe flow.

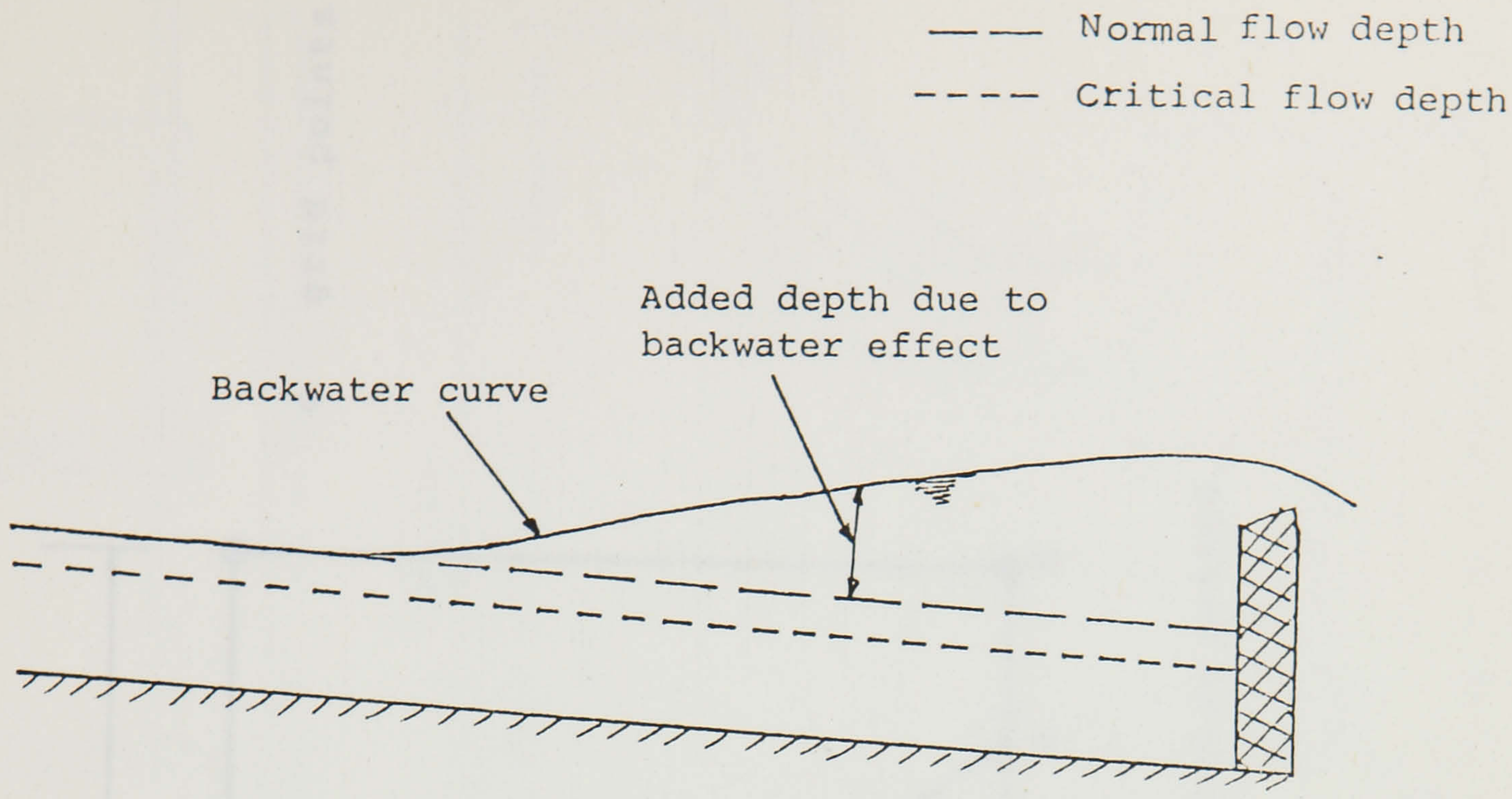

(a) Subcritical flow.

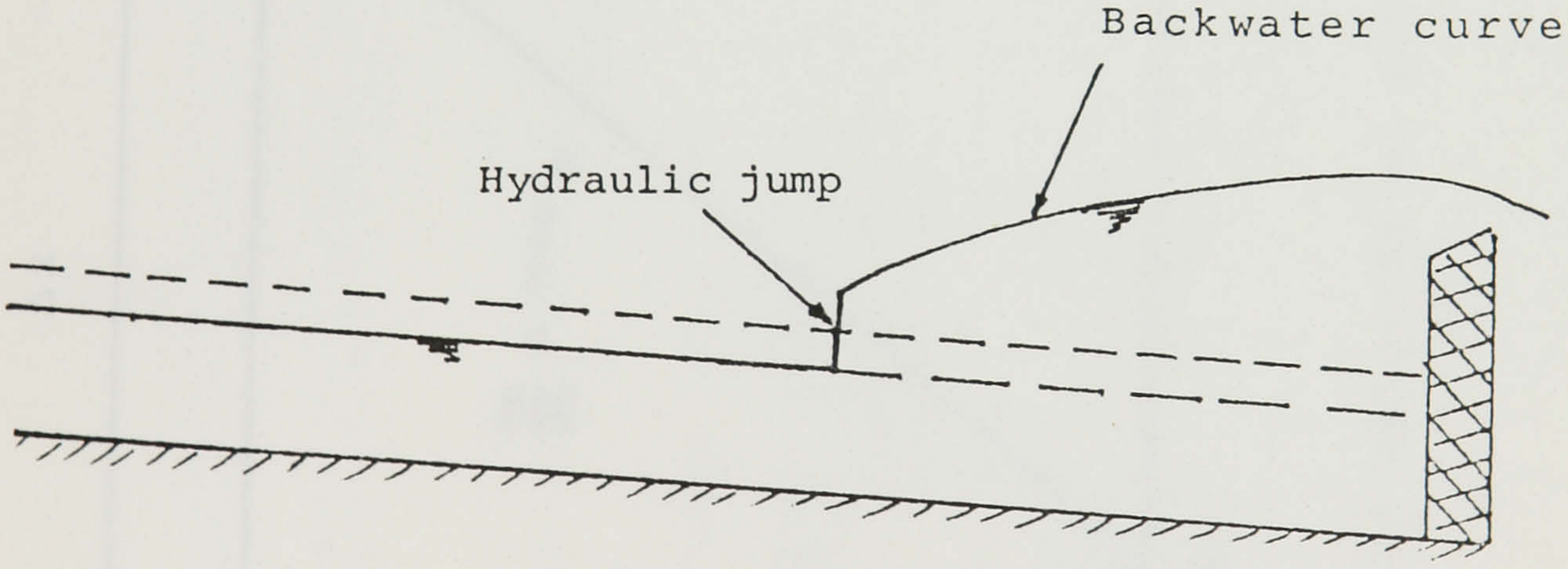

(b) Supercritical flow.

Figure 1.2 Principle differences of subcritical and supercritical flow.

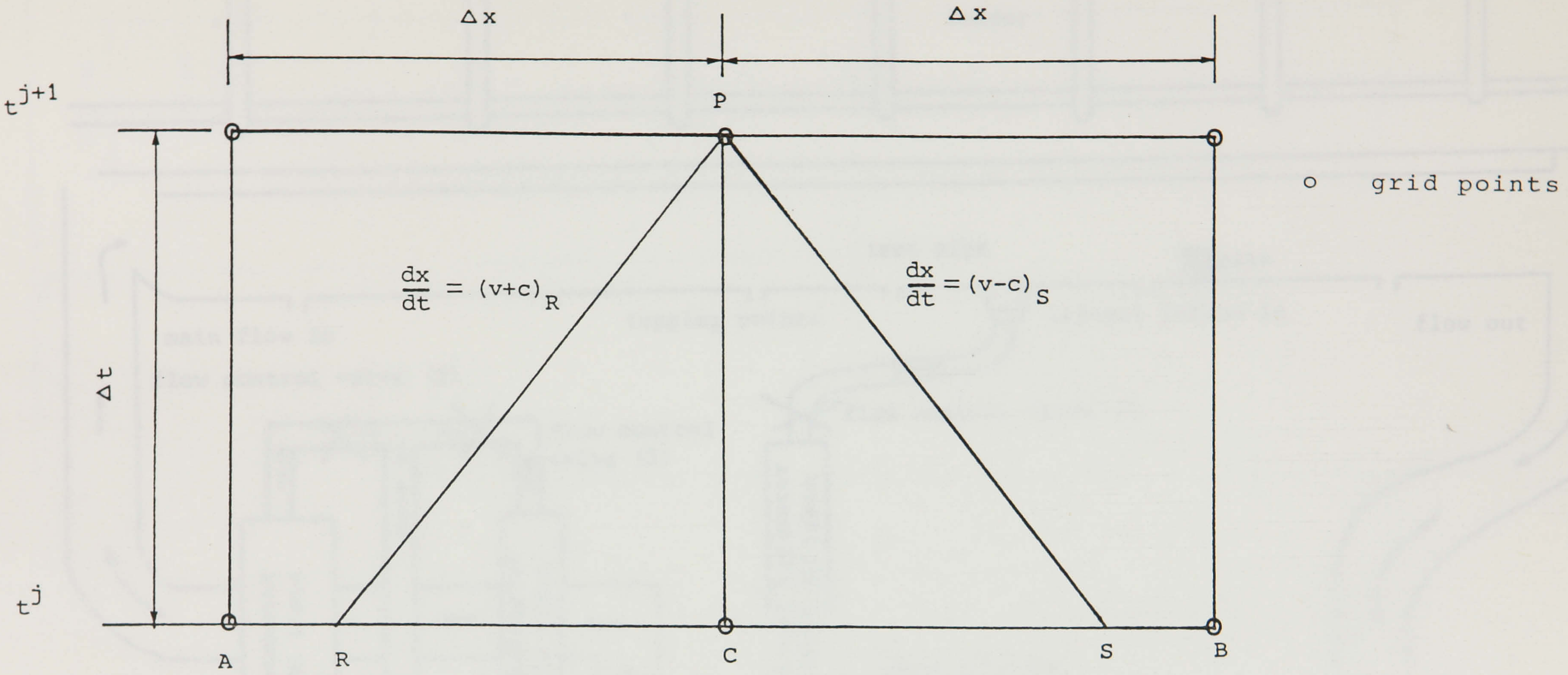

Figure 1.3 Grid solution of rectangular-grid characteristics method.

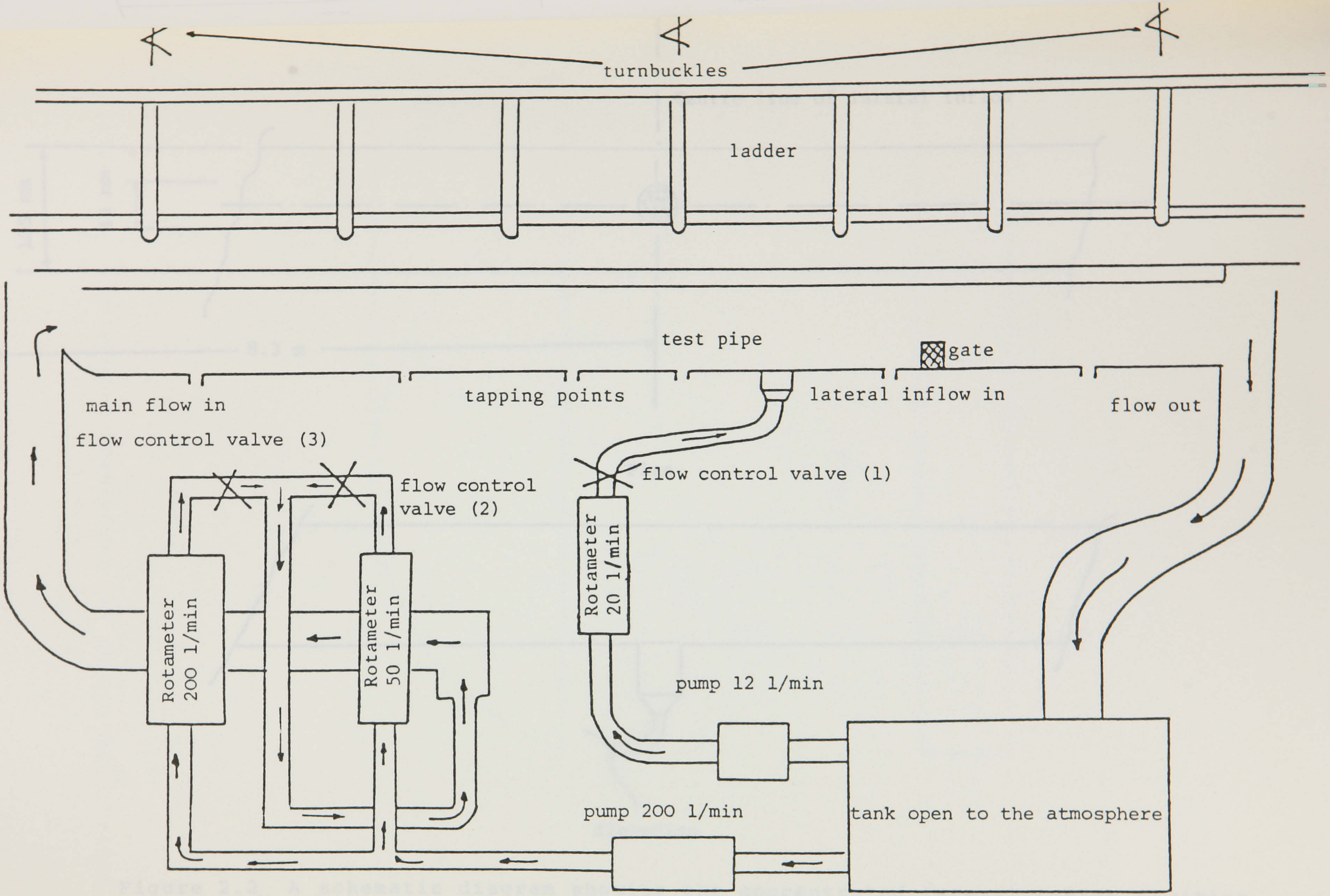

Figure 2.1 A schematic diagram of the test facility.

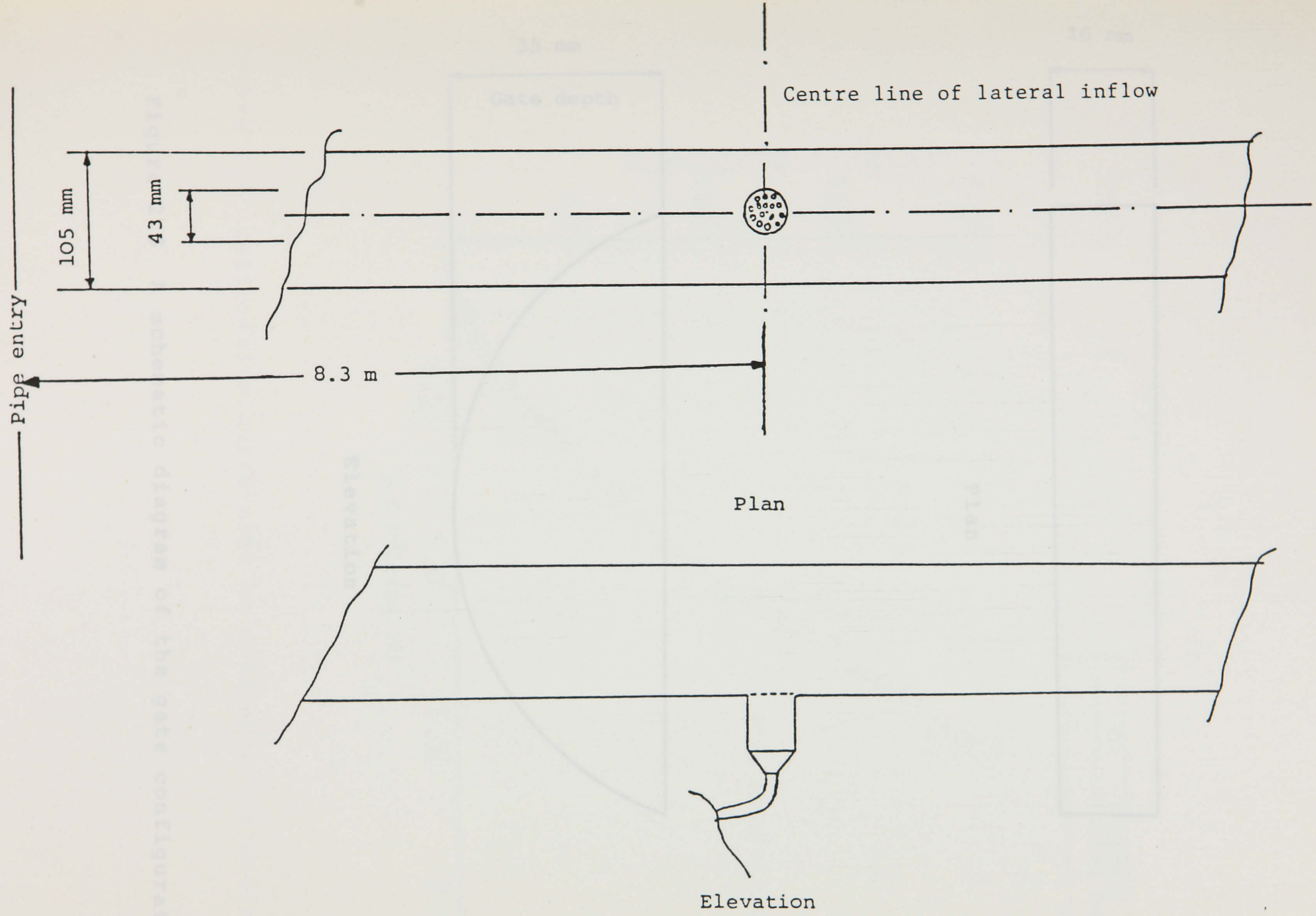

Figure 2.2 A schematic diagram showing the concentrated lateral inflow position.

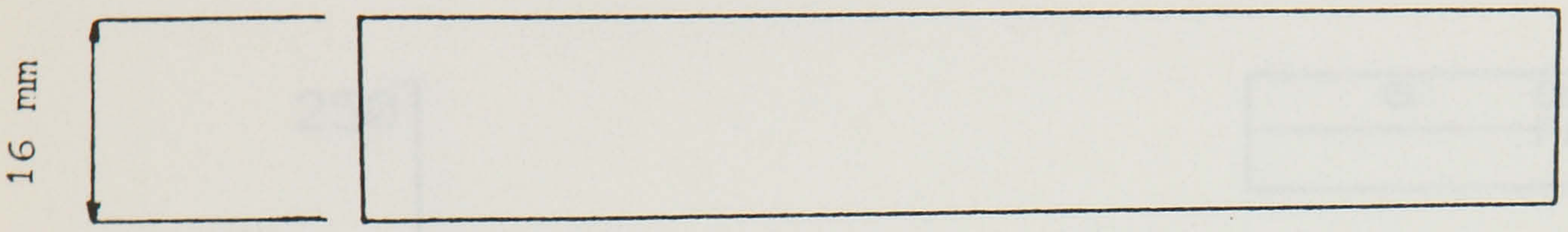

Plan

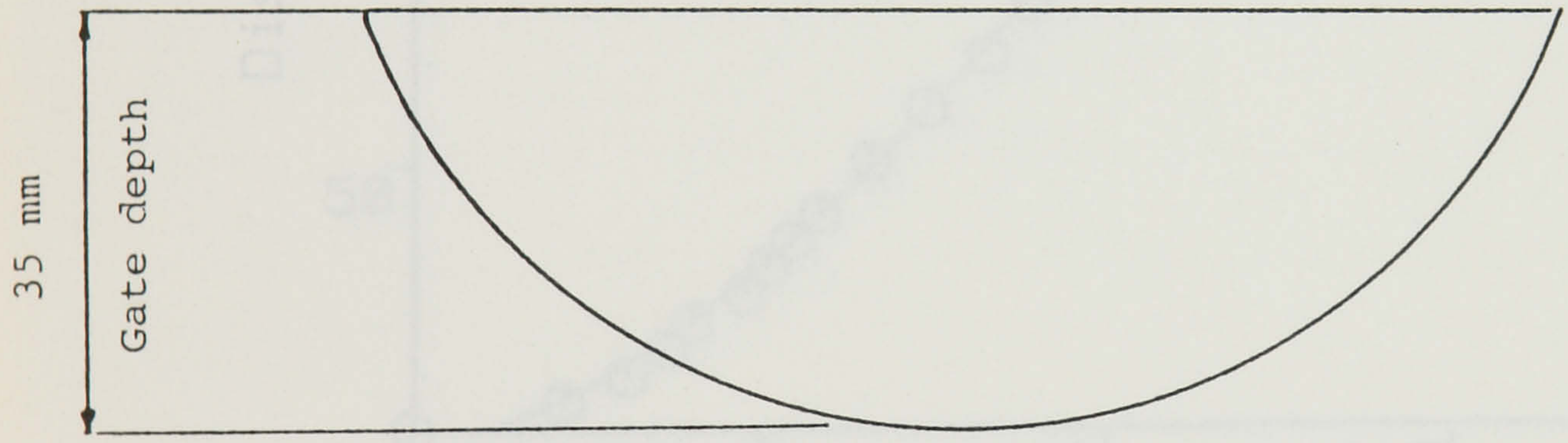

Elevation

Figure 2.3 A schematic diagram of the gate configuration.

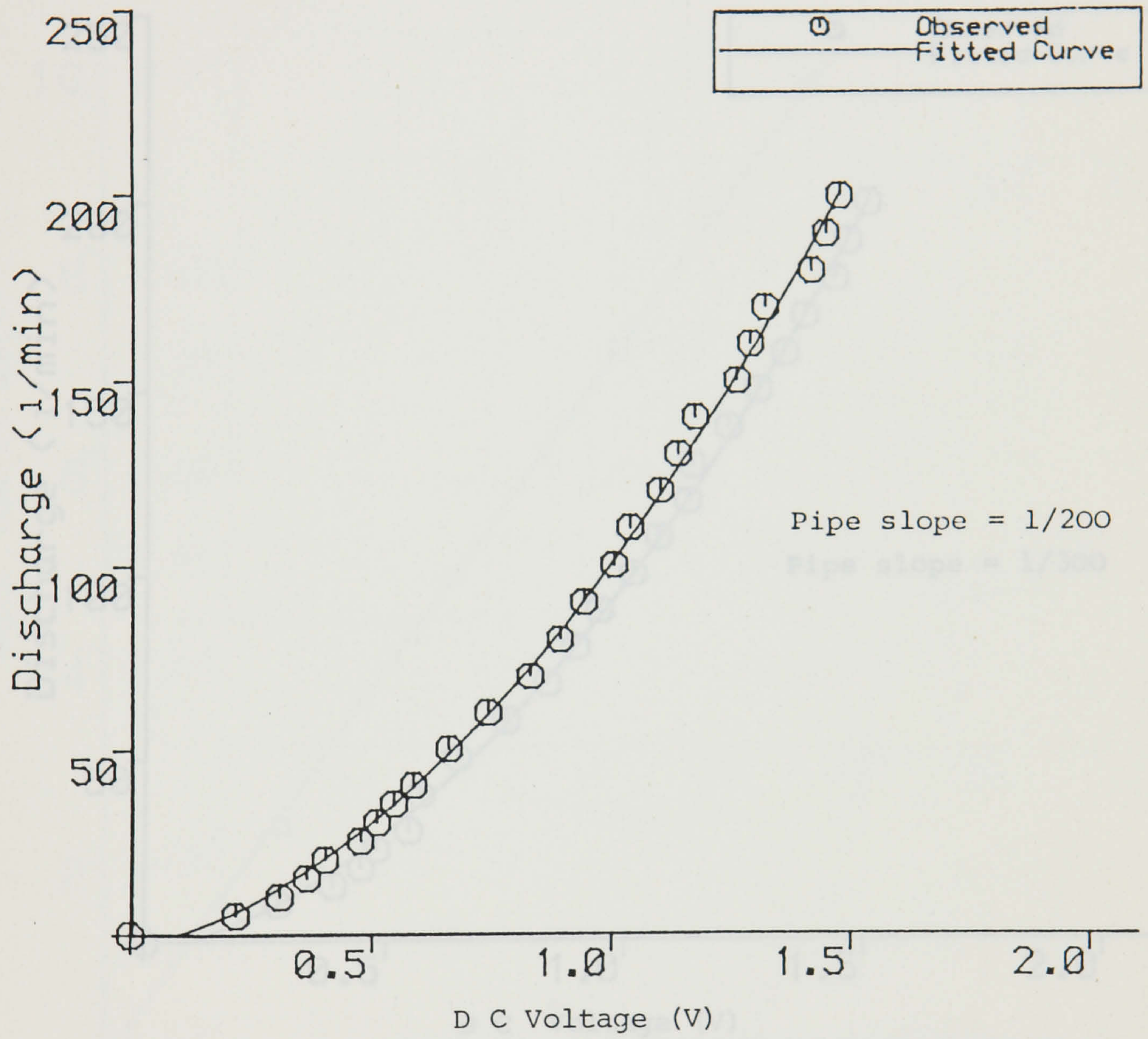

Figure 2.4 Calibration curve used to determine the unsteady flow.

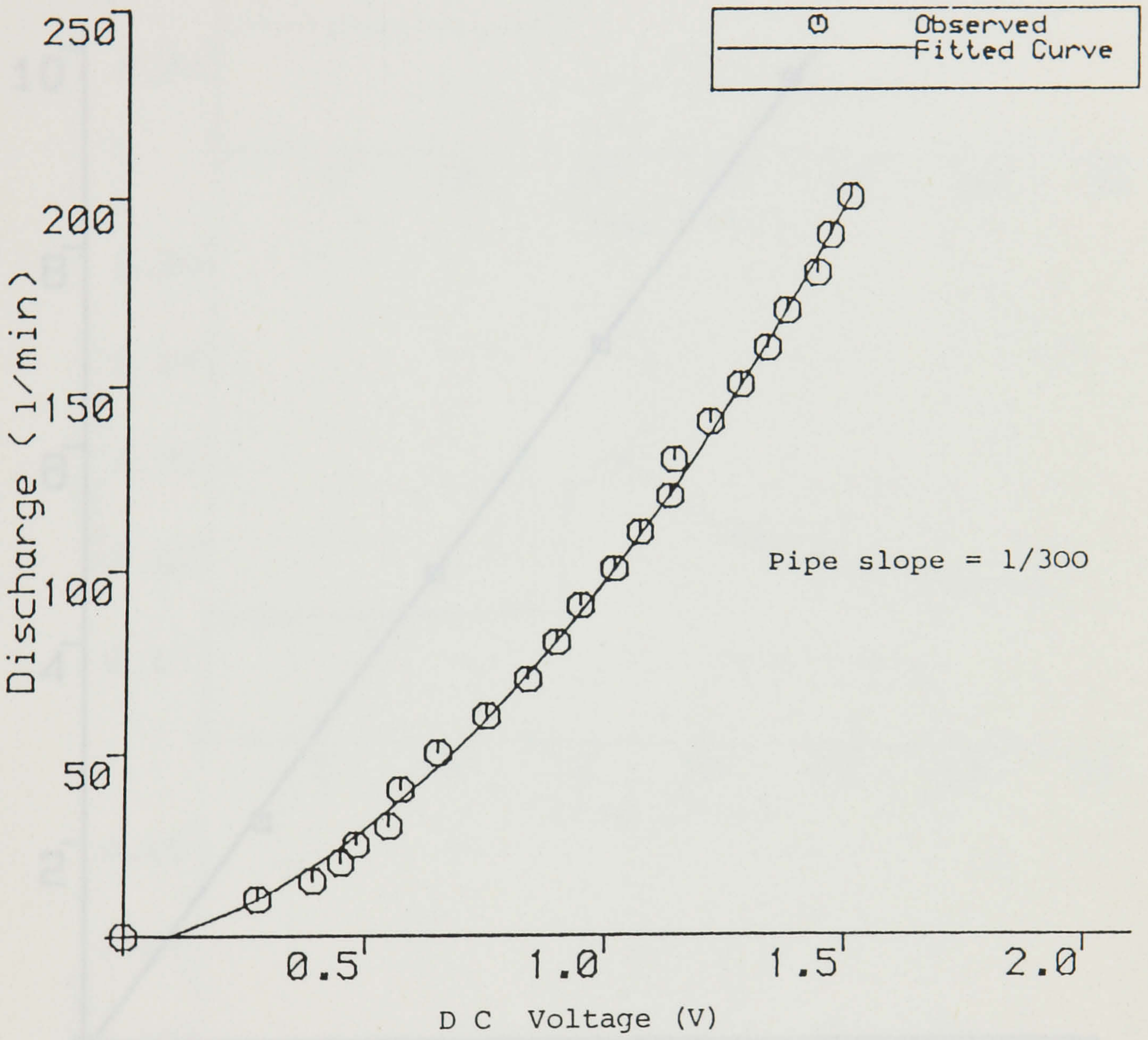

Figure 2.5 Calibration curve used to determine the unsteady flow.

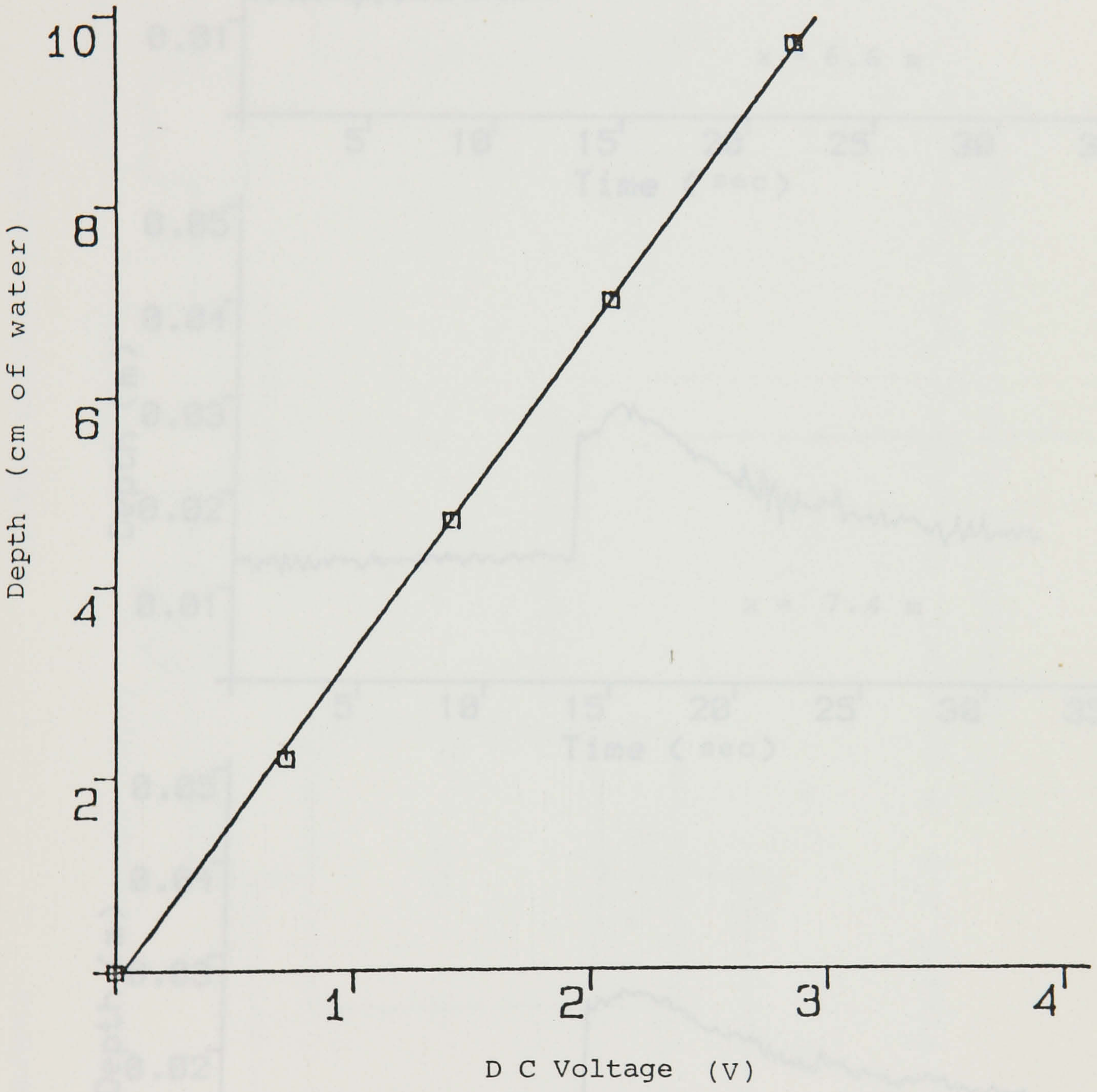

Figure 2.6 Typical calibration line used to determine the flow depth.

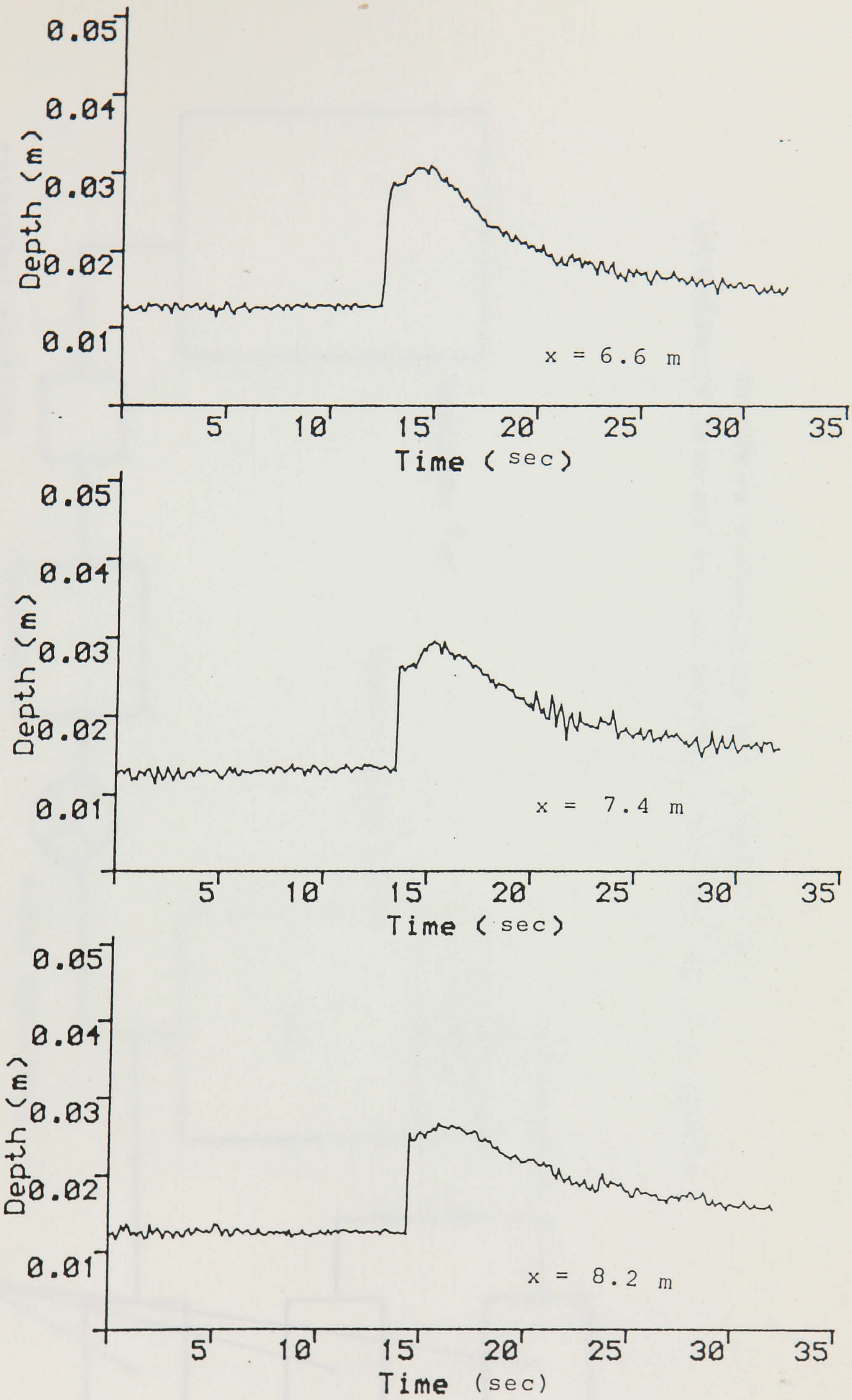

Figure 2.7 Observed depth hydrographs.

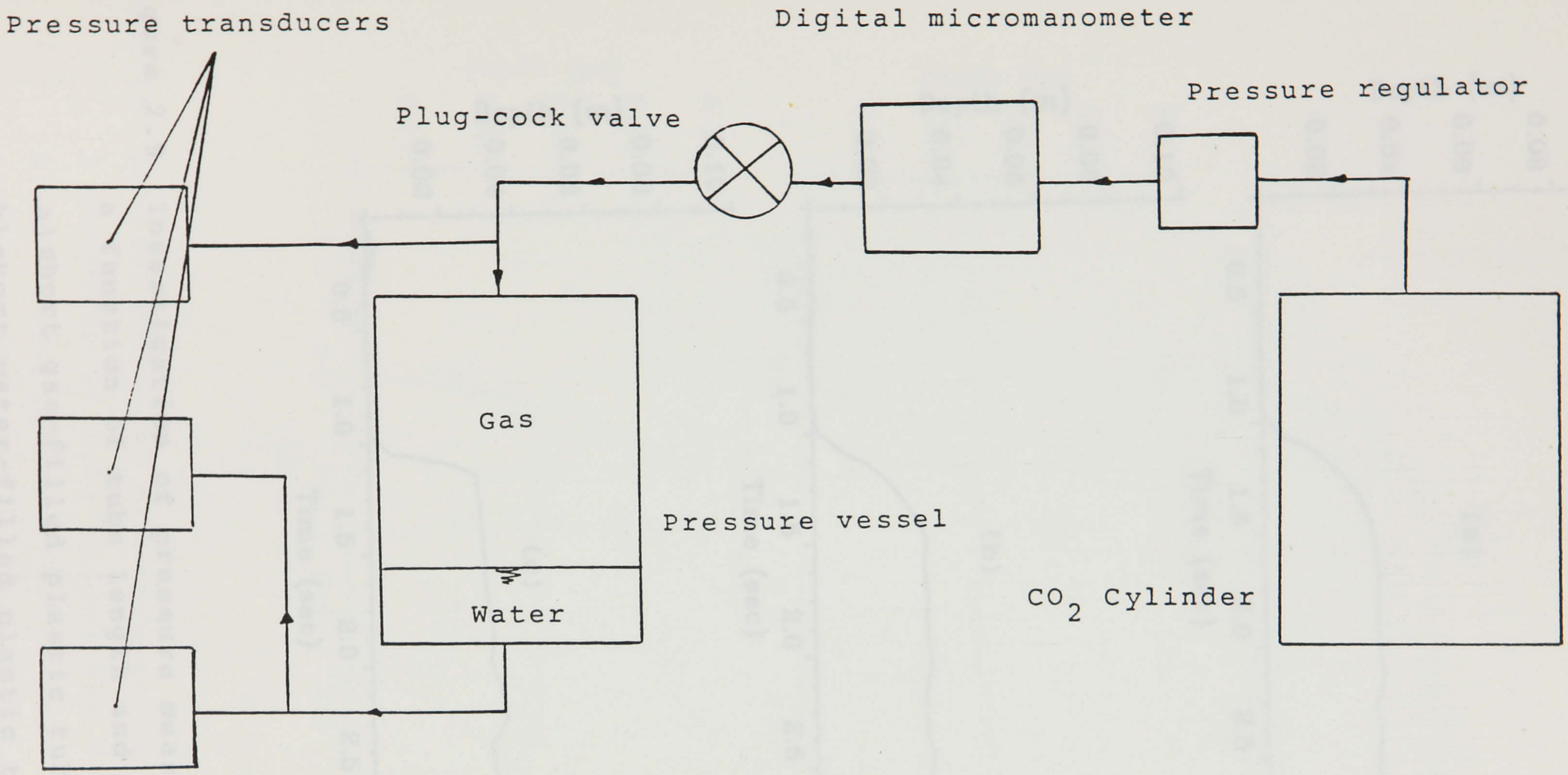

Figure 2.8 A schematic diagram of the general arrangement for testing the transducers response.

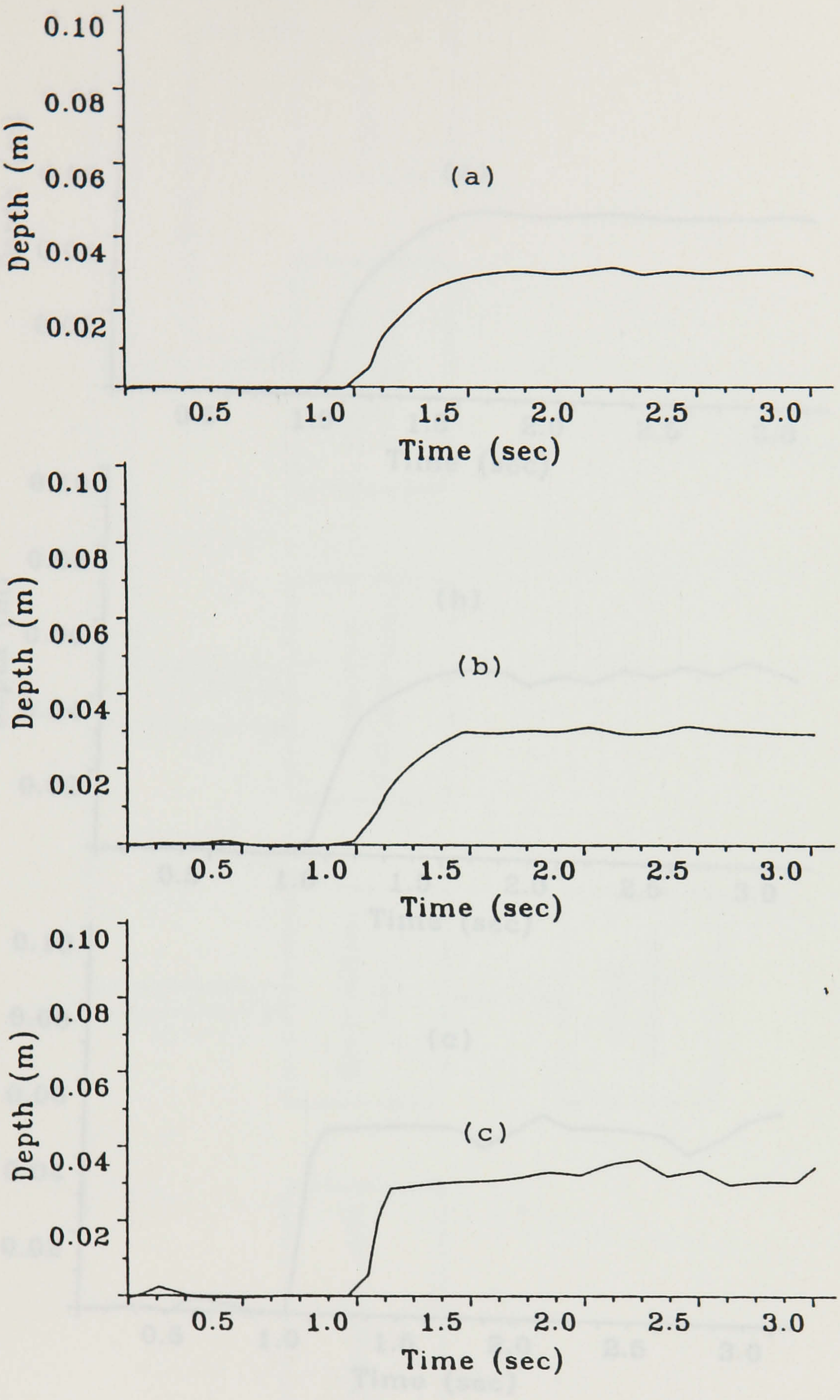

Figure 2.9 Investigation of pressure measurements as a function of tube length and fluid.

a) short gas-filled plastic tube

b) short water-filled plastic tube

c) long water-filled plastic tube

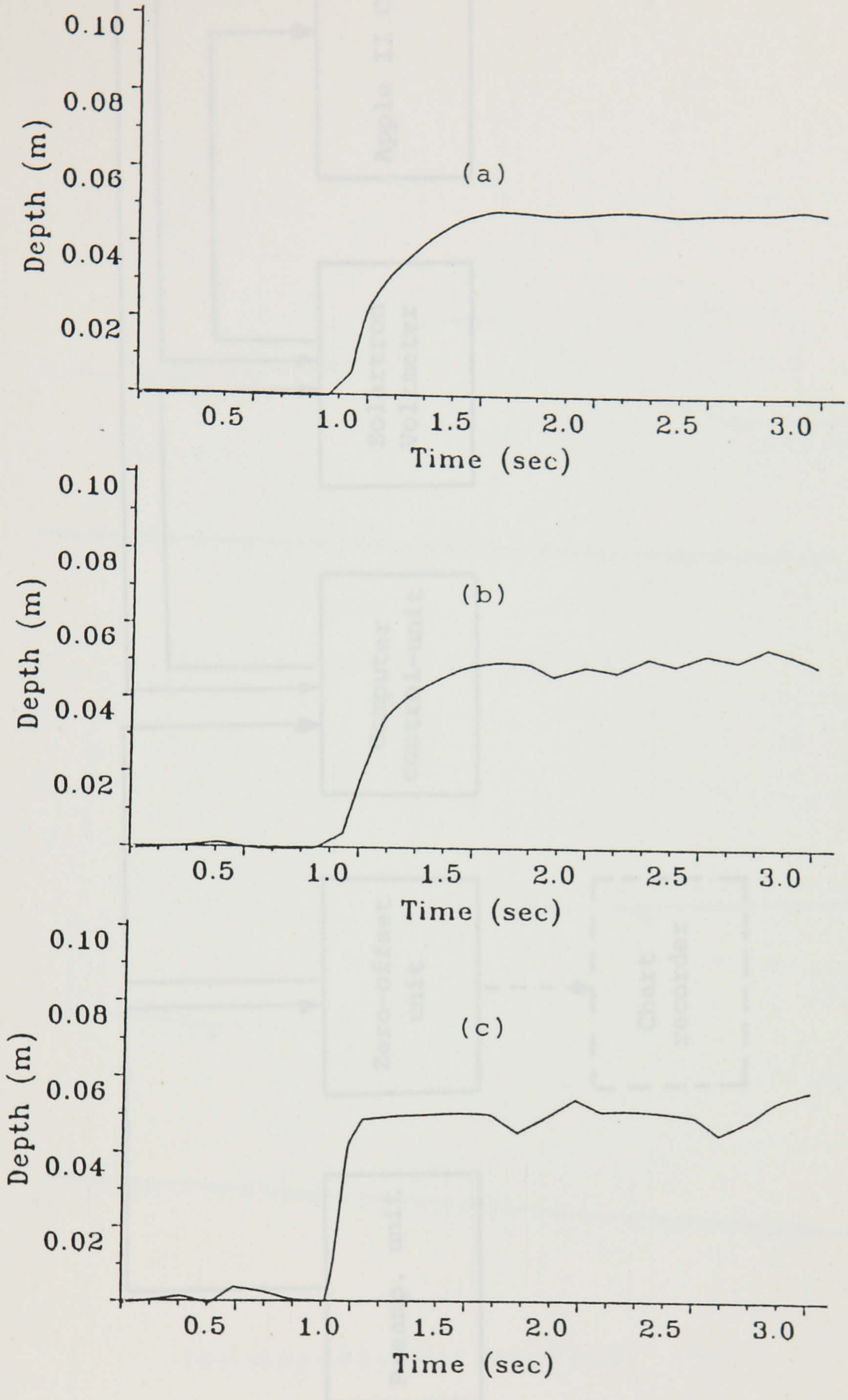

Figure 2.10 Investigation of pressure measurements as a function of tube length and fluid.

a) short gas-filled plastic tube

b) short water-filled plastic tube

c) long water-filled plastic tube

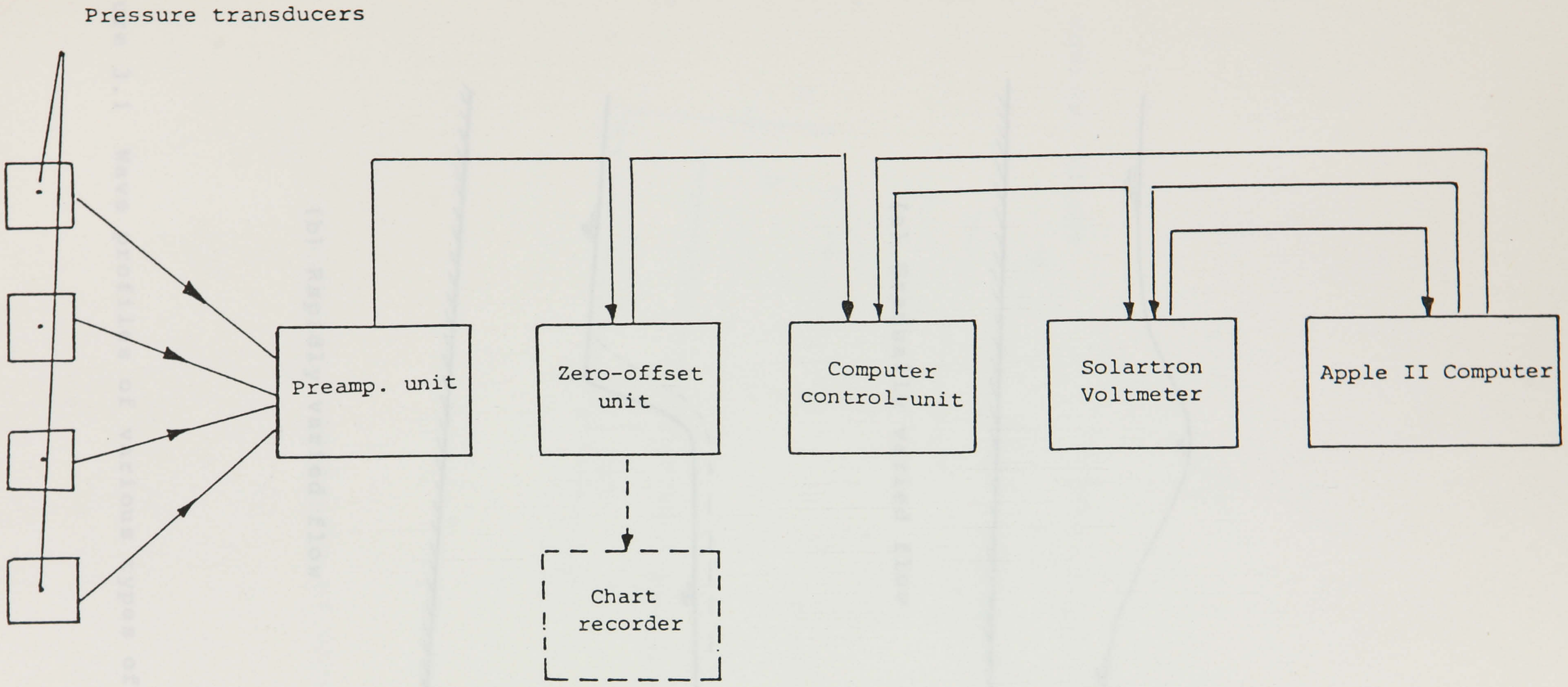

Figure 2.11 General schematic diagram of the data-collection system.

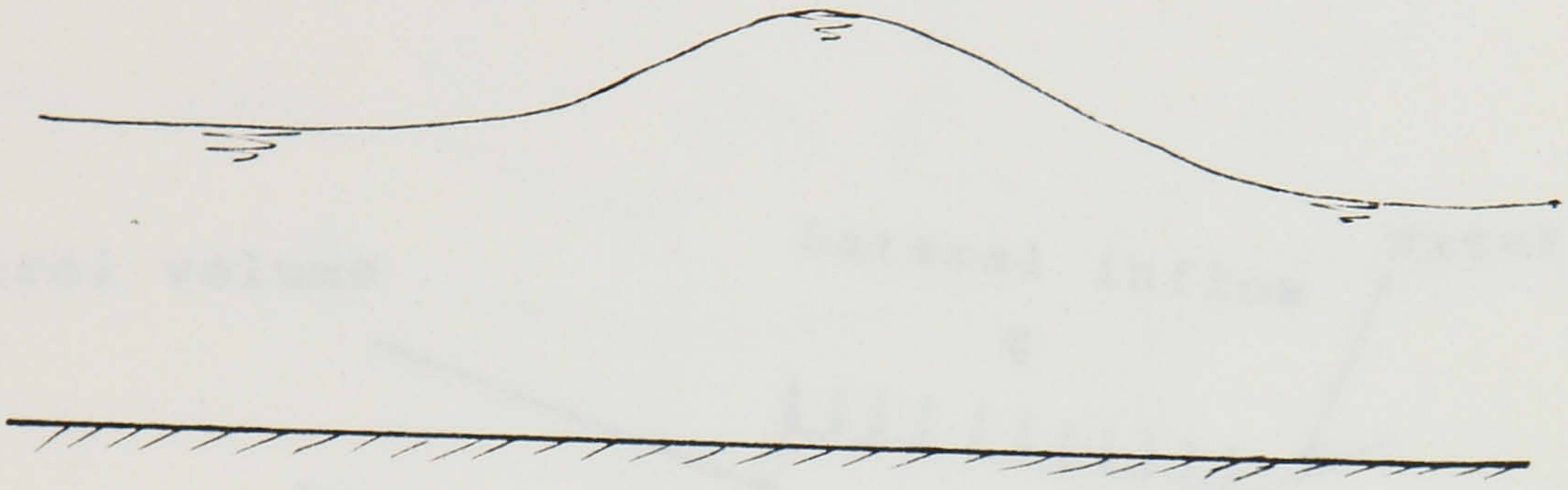

(a) Gradually varied flow

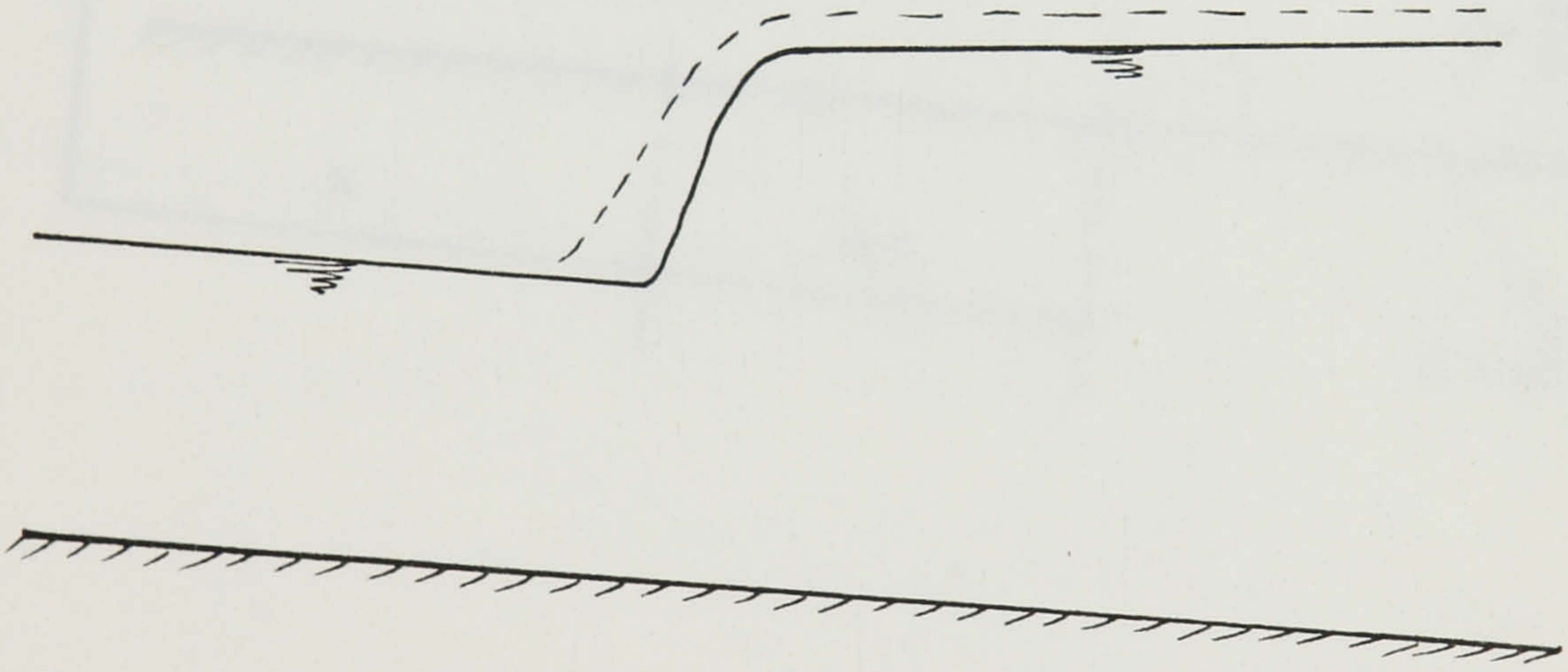

(b) Rapidly varied flow

Figure 3.1 Wave profiles of various types of open-channel flow.

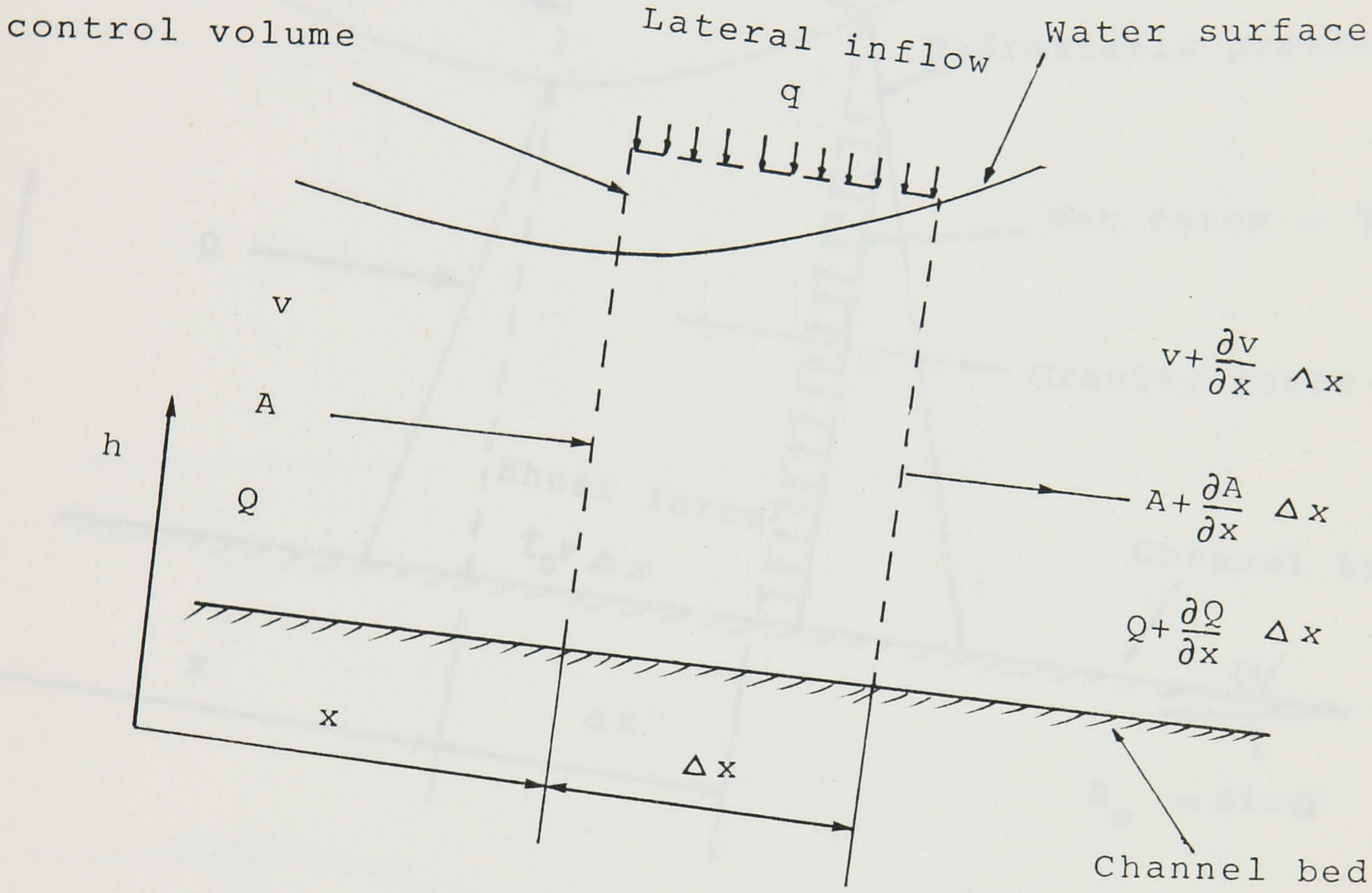

Figure 3.2 Continuity of flow.

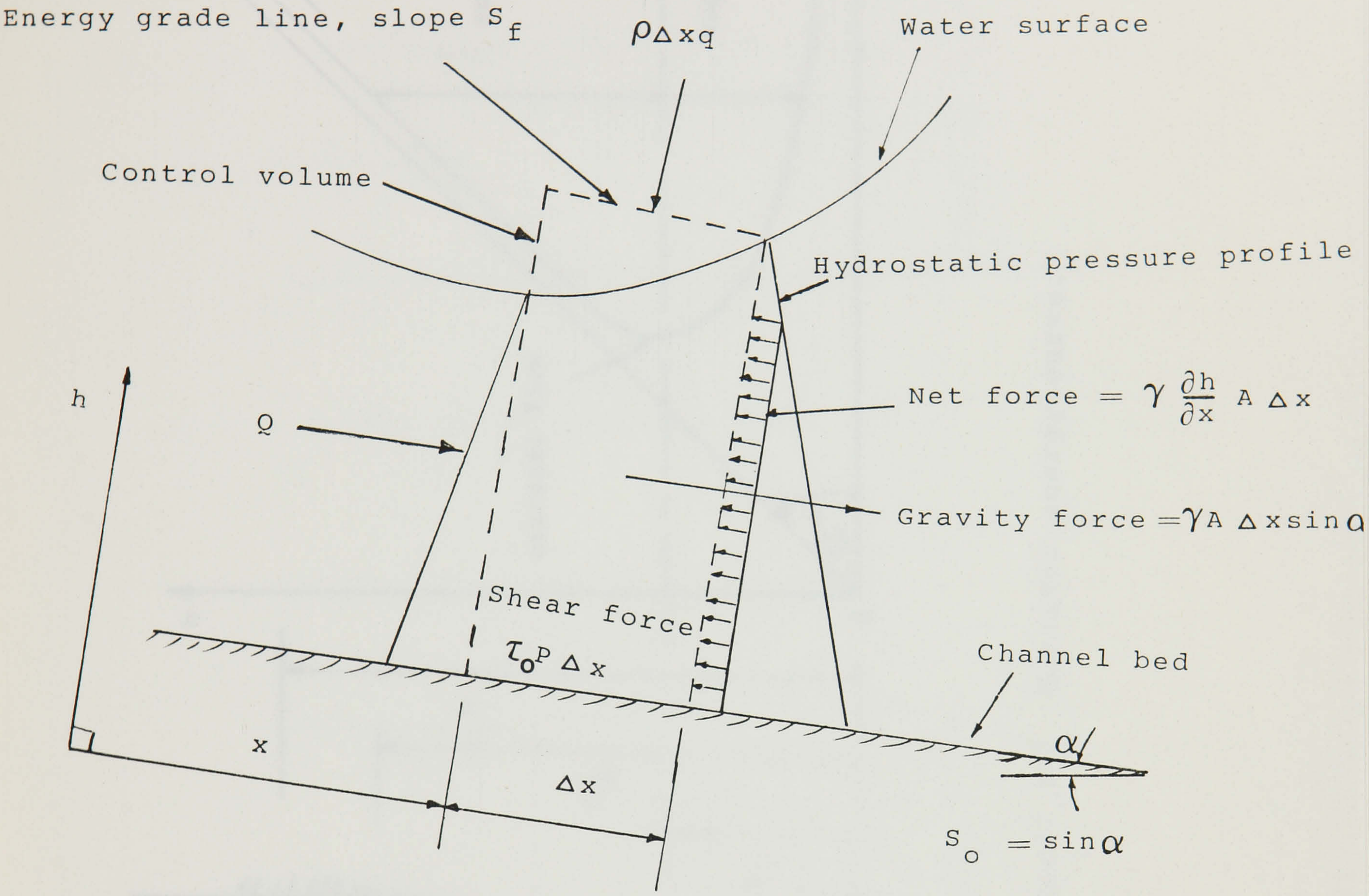

Figure 3.3 Momentum balance in flow direction.

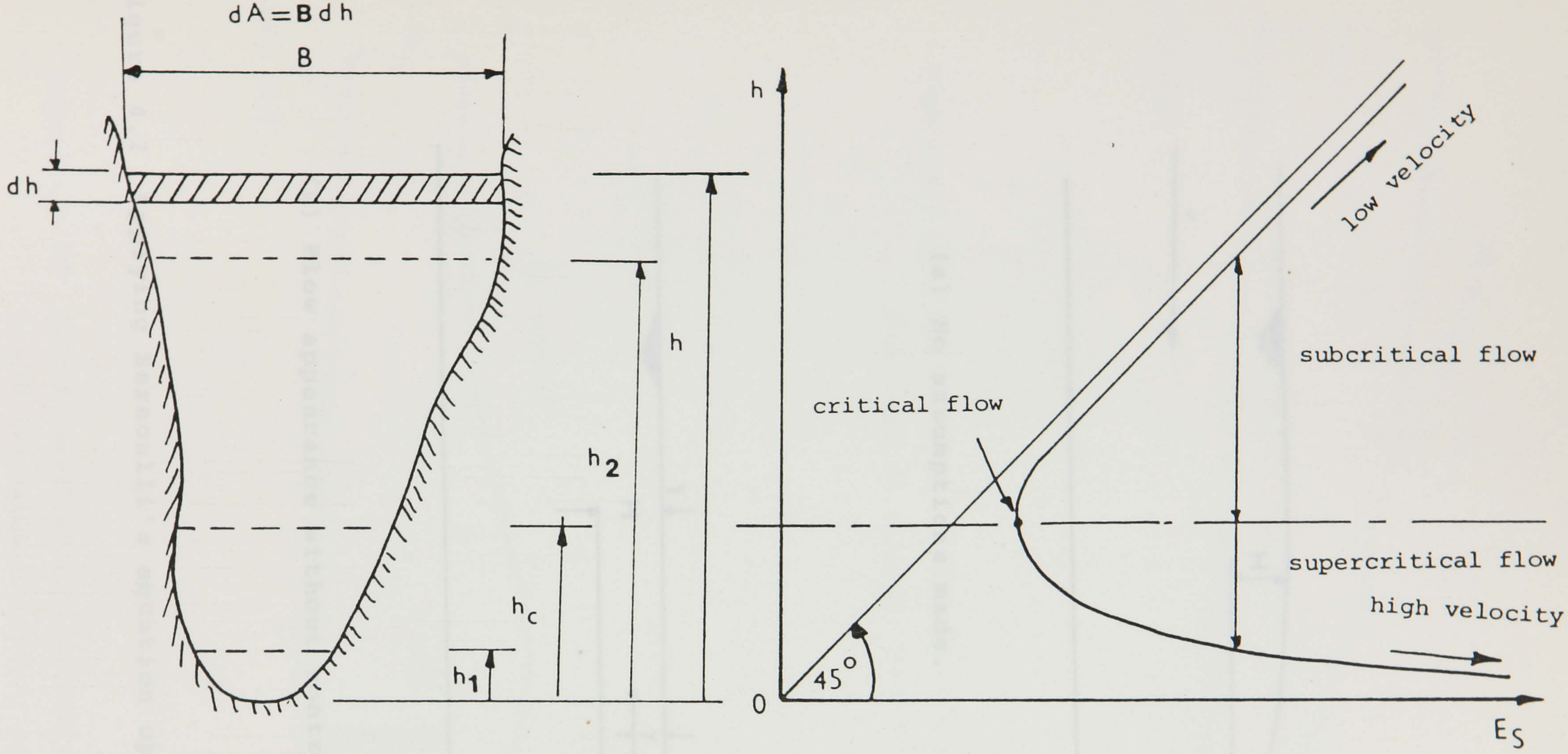

Figure 4.1 Specific-energy curve.

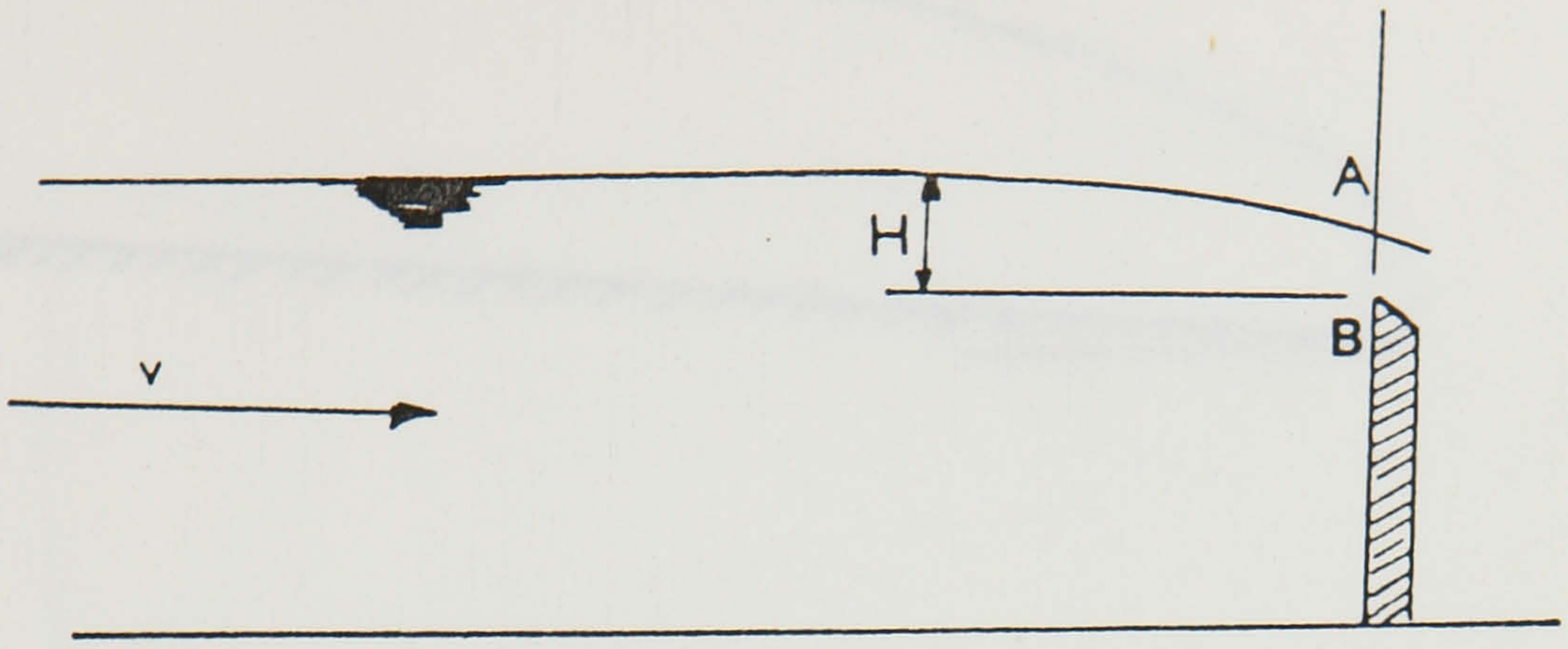

(a) No assumptions made.

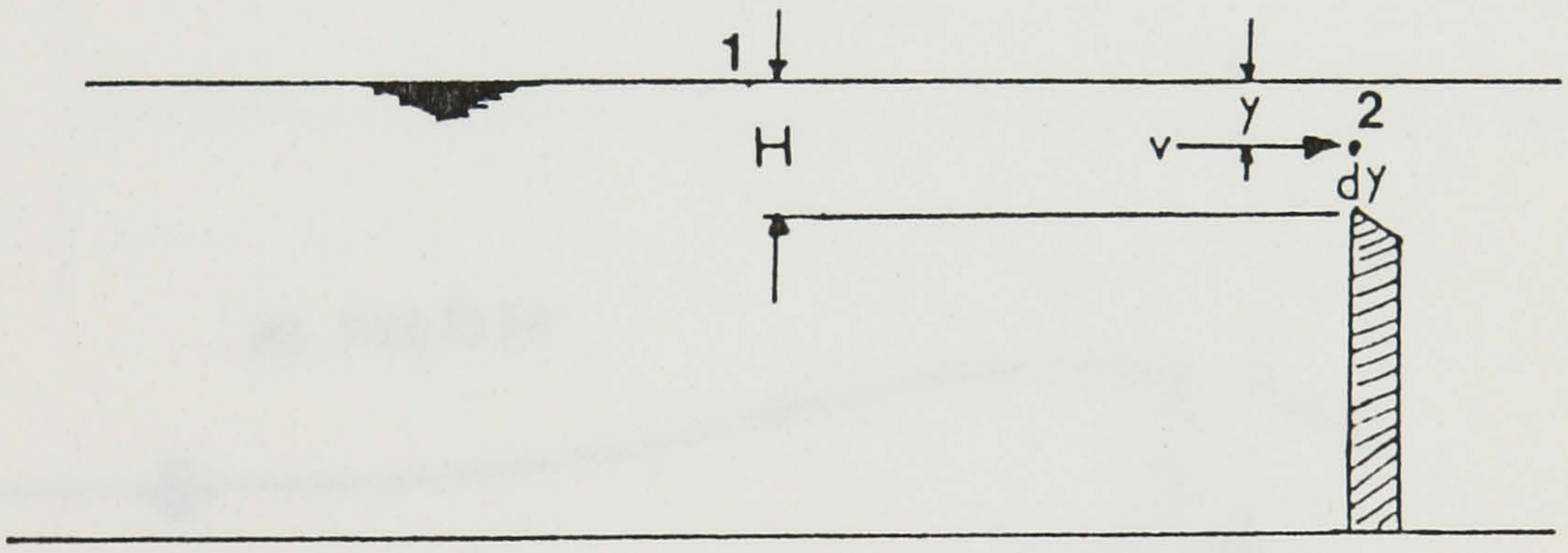

(b) Flow appearance without contractions.

Figure 4.2 Applying Bernoulli's equation upstream of the gate.

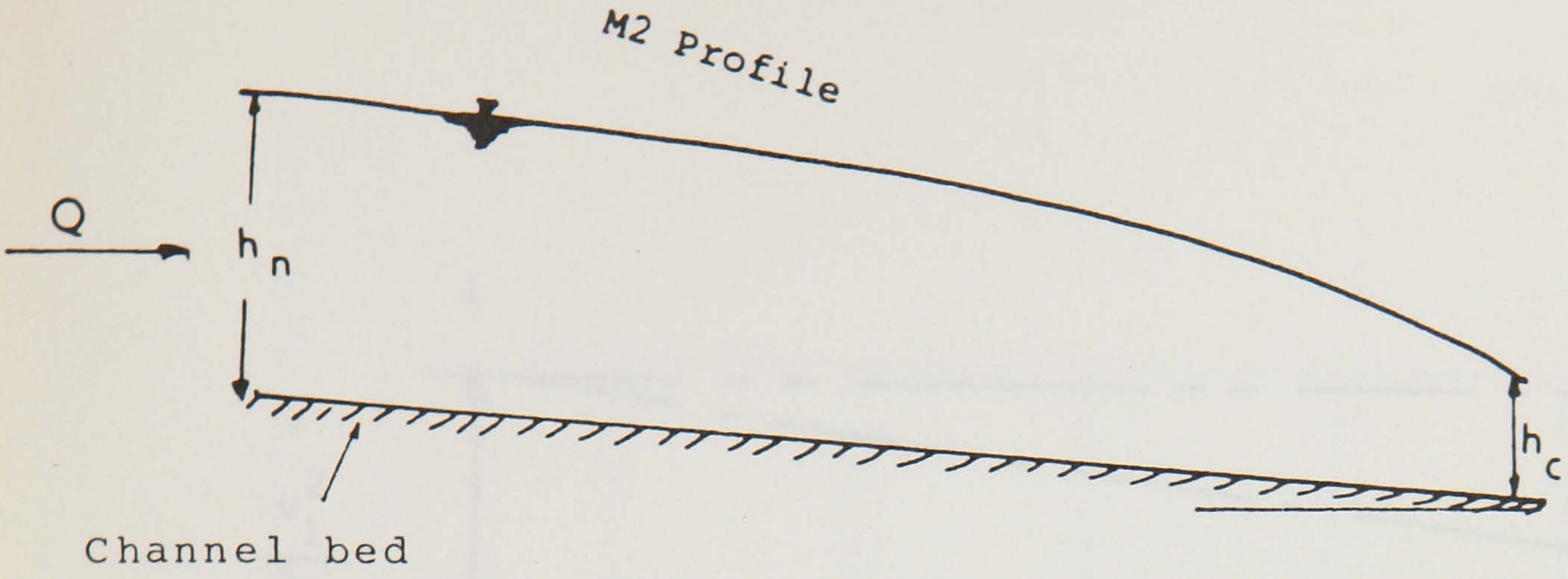

Figure 4.3 (a) Initial water surface profile for free-overfall boundary condition.

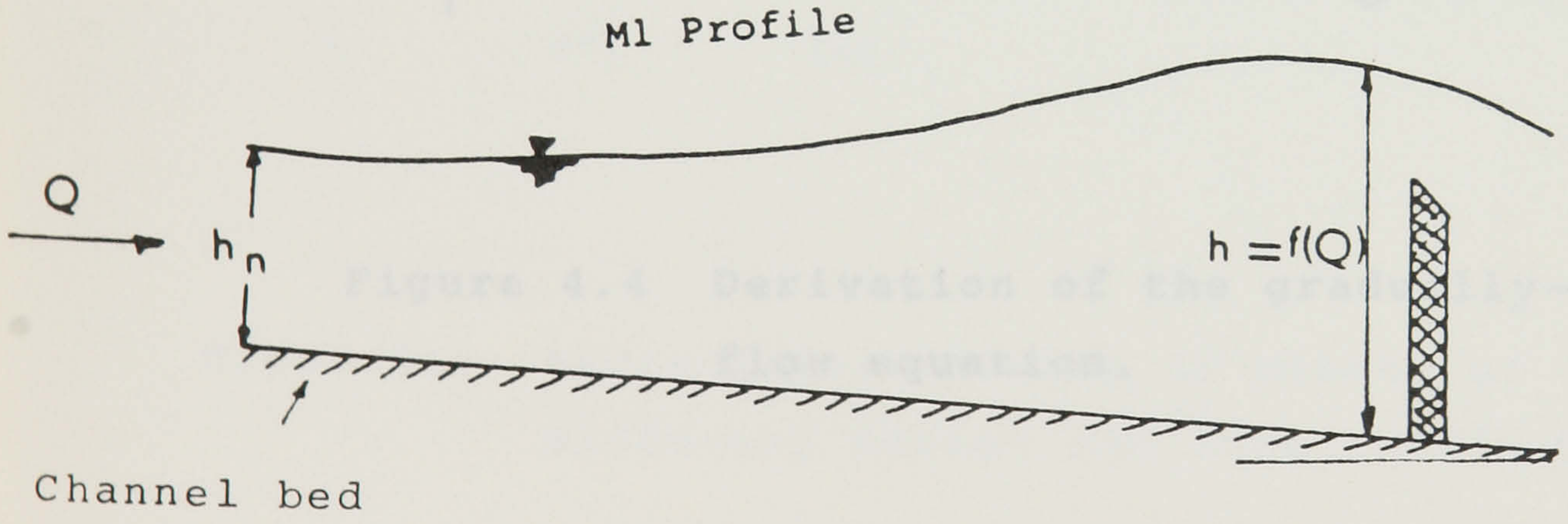

Figure 4.3 (b) Initial water surface profile for controlled-outfall boundary condition.

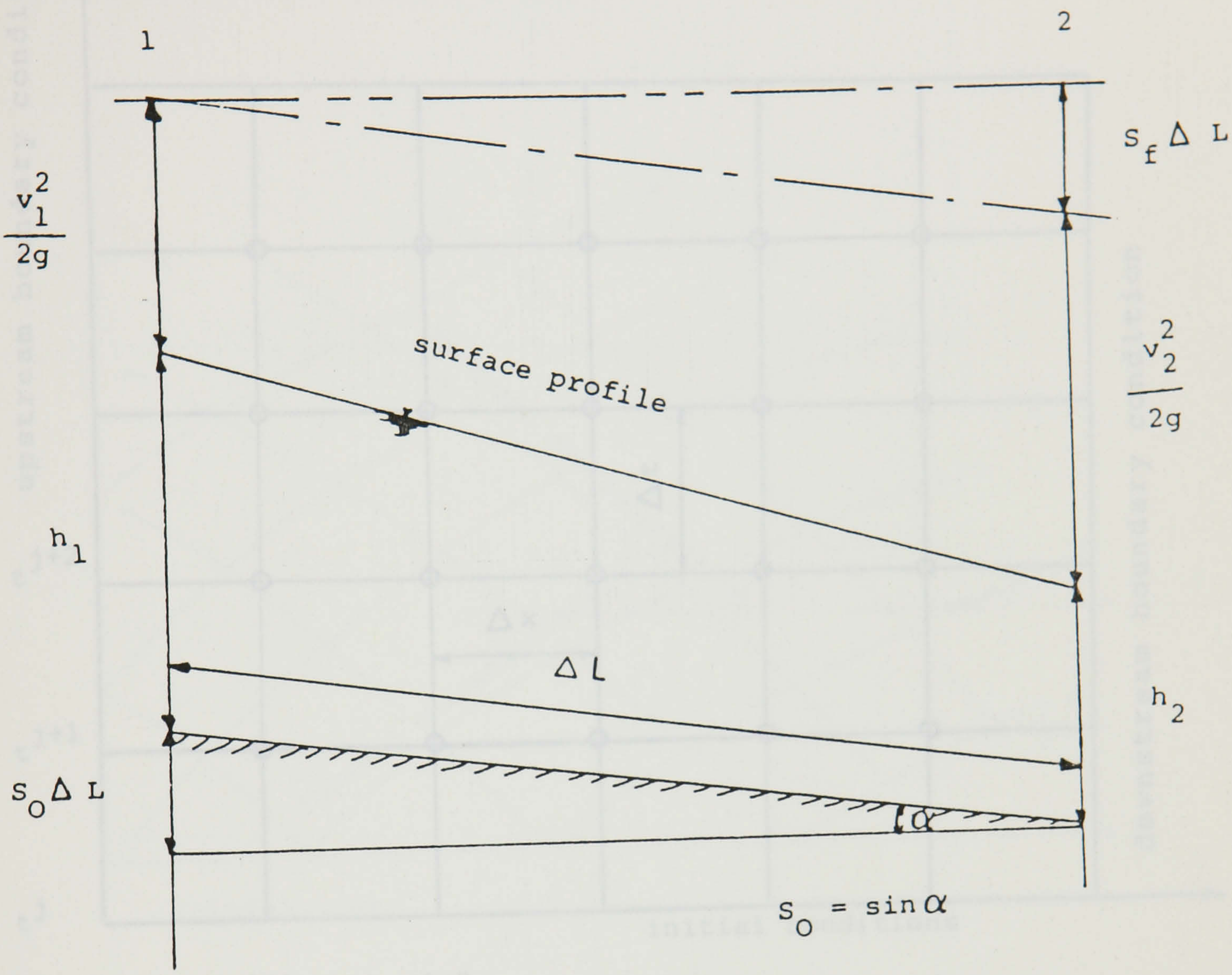

Figure 4.4 Derivation of the gradually-varied flow equation.

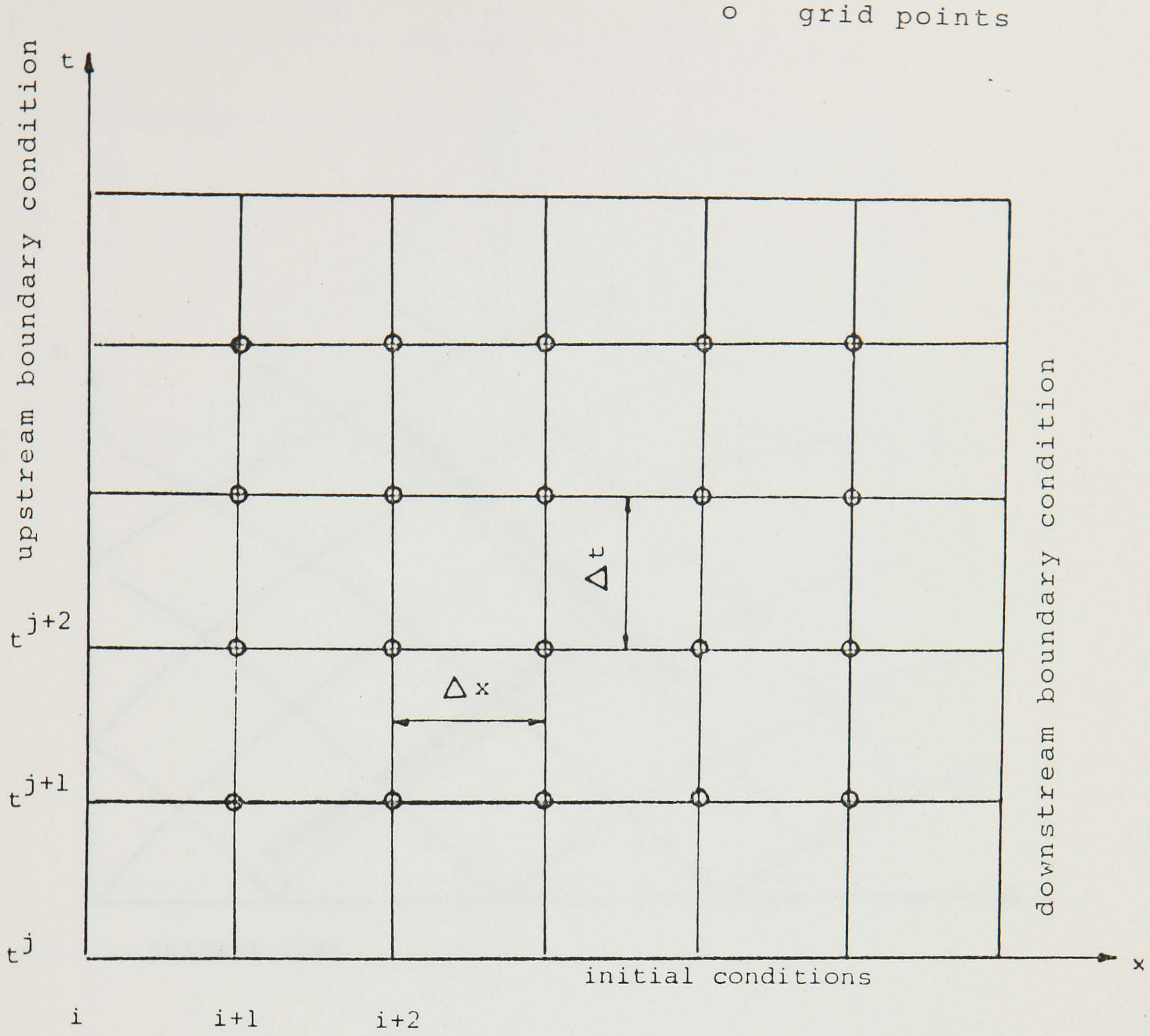

Figur 5.1 Rectangular network of method of characteristics, diffusing scheme and Strelkoff's implicit method.

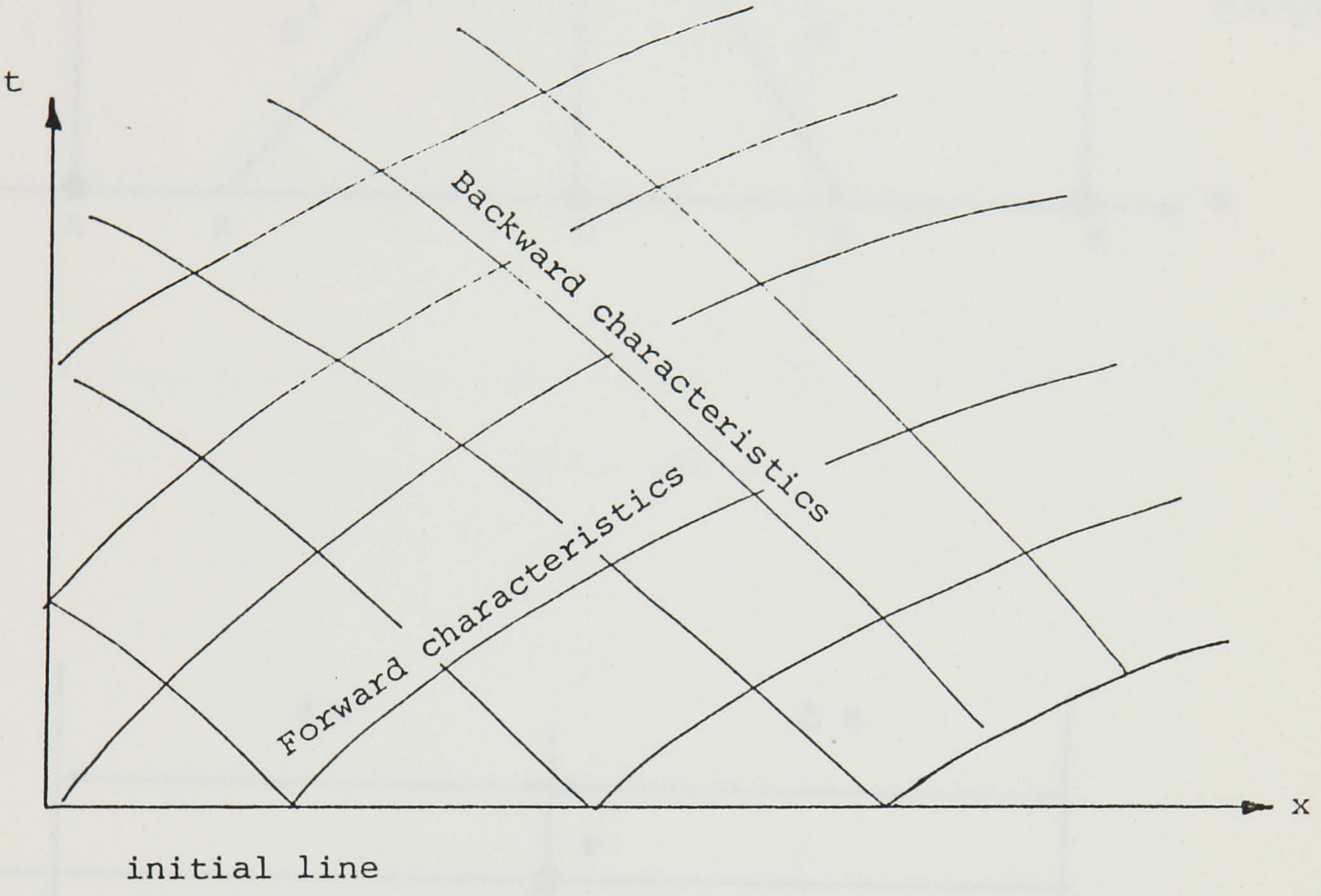

Figure 5.2 Characteristics in x,t-plane.

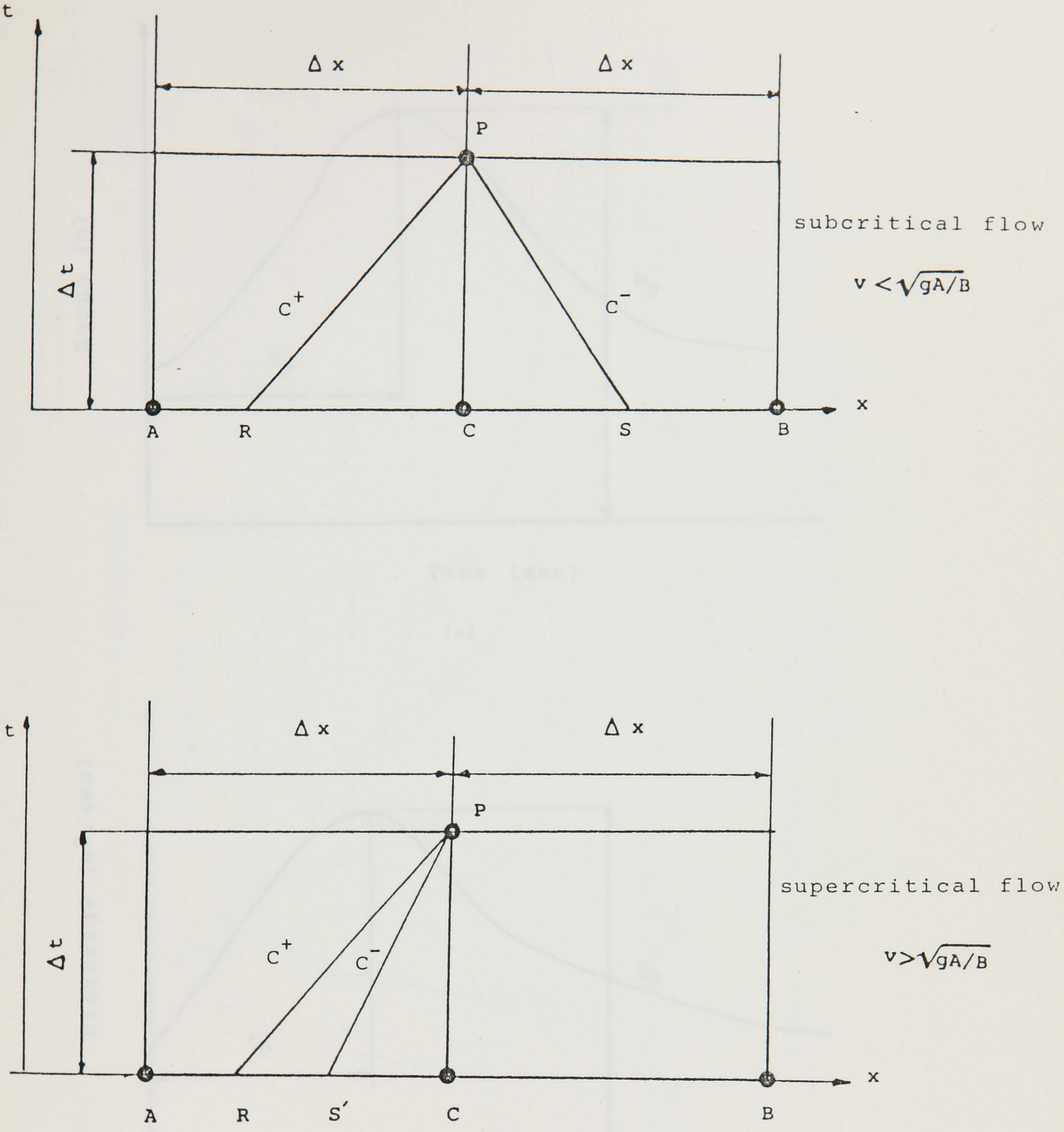

Figure 5.3 Grid solution for the rectangular-grid characteristics method.

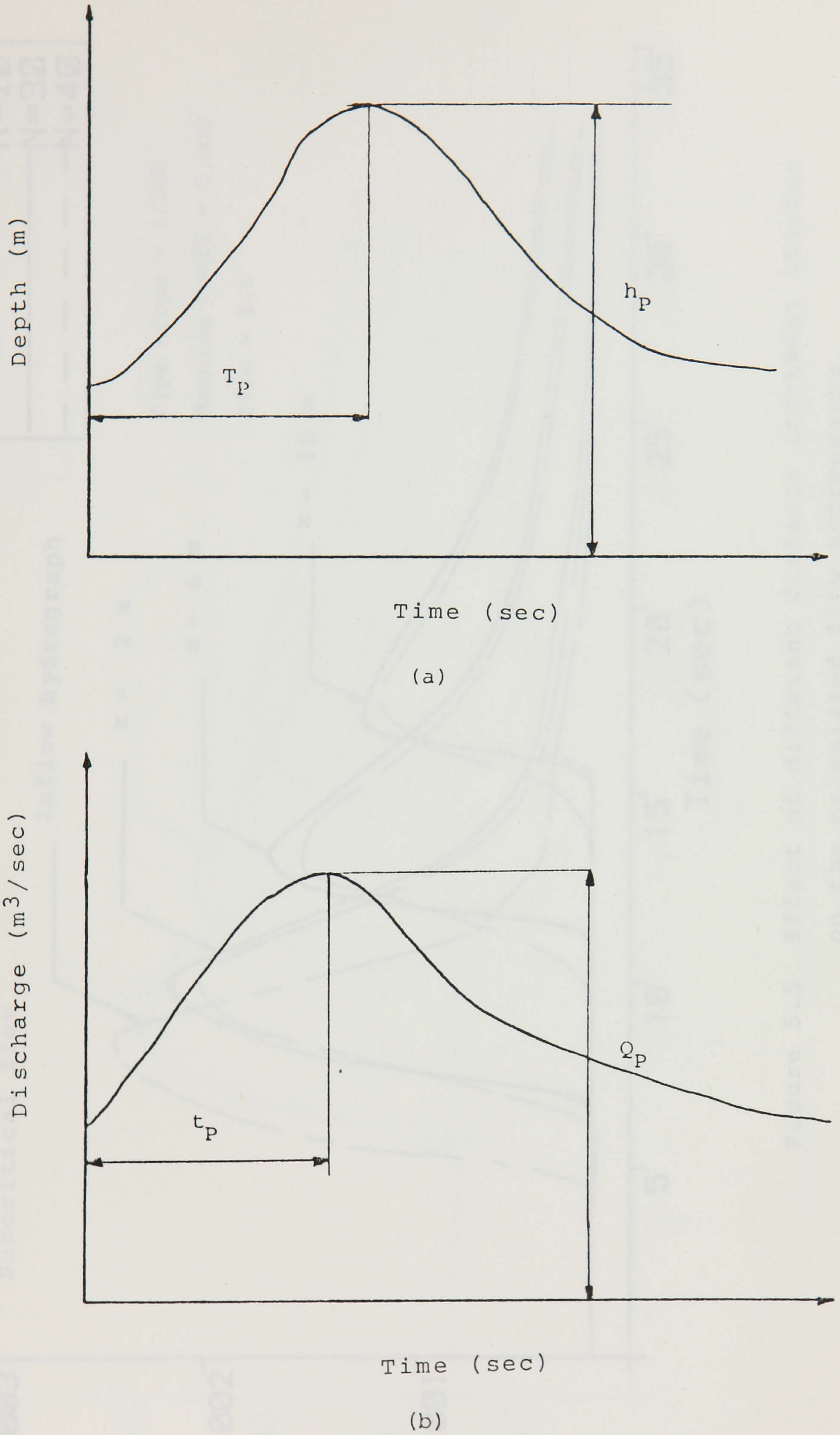

Figure 5.4 Parameters of depth and flow hydrographs.

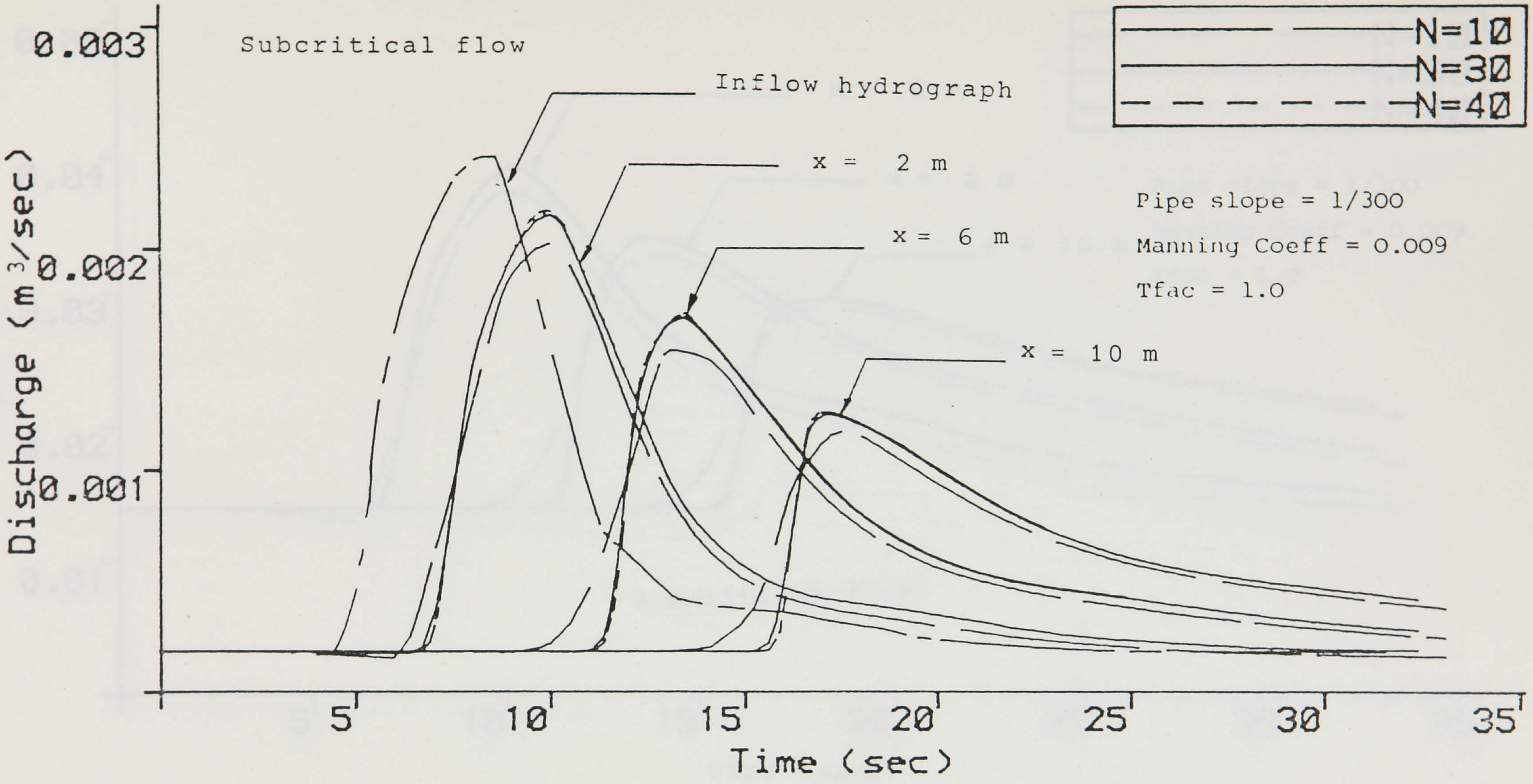

Figure 5.5 Effect of different distance increment lengths on the calculated flow hydrographs.

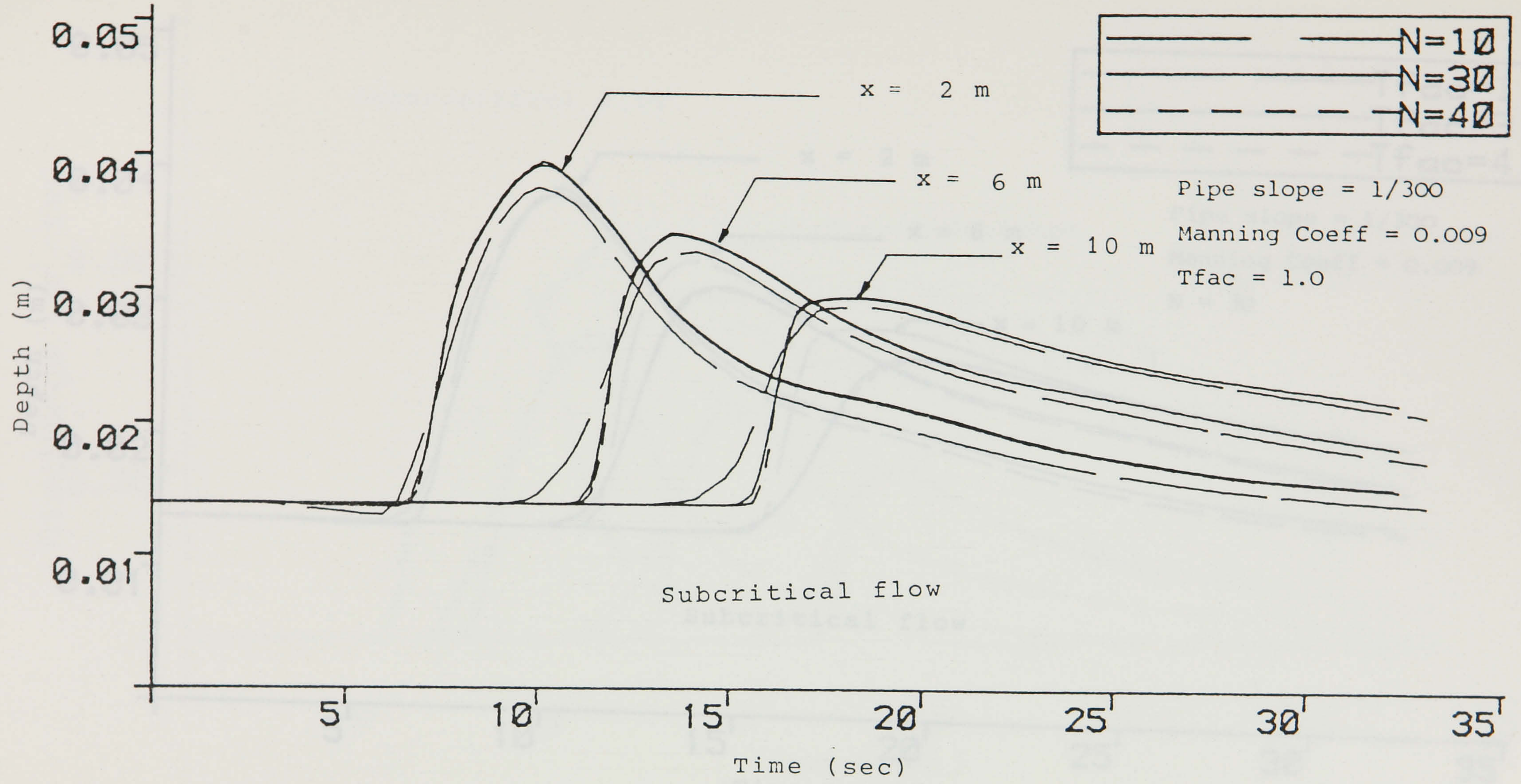

Figure 5.6 Effect of different distance increment lengths on the calculated depth hydrographs.

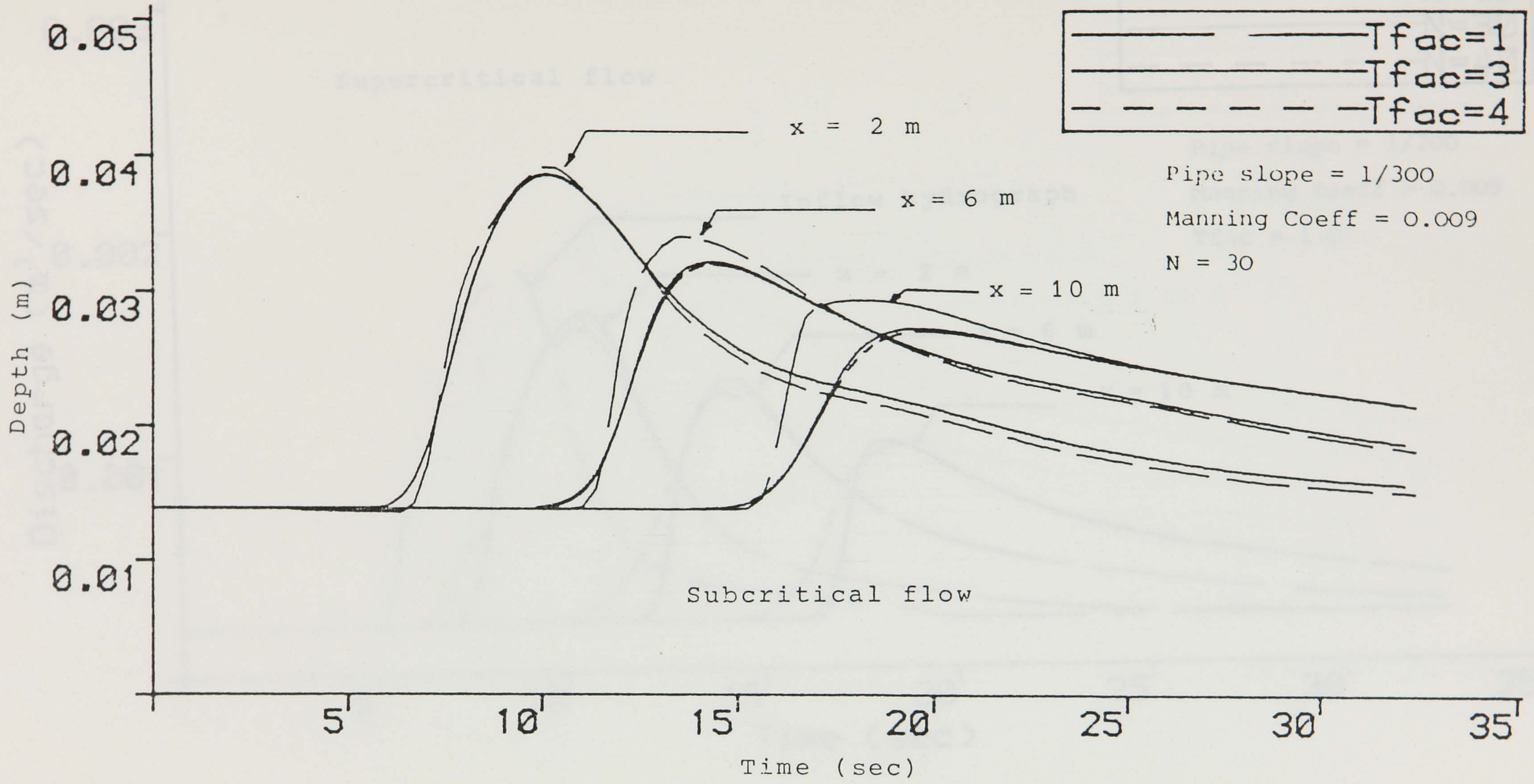

Figure 5.7 Effect of changing the time increment on the calculated depth hydrographs.

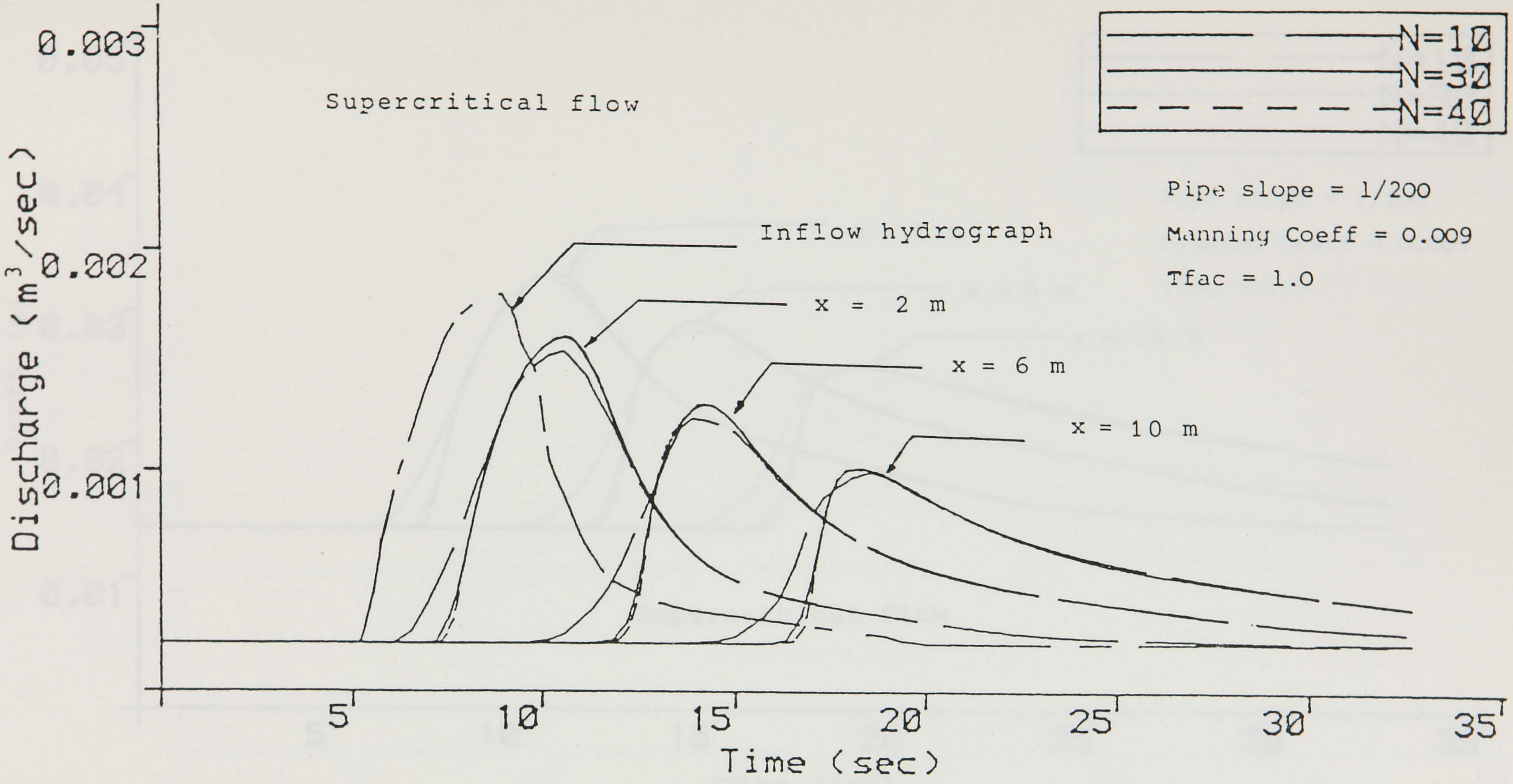

Figure 5.8 Effect of different distance increment lengths on the calculated flow hydrographs.

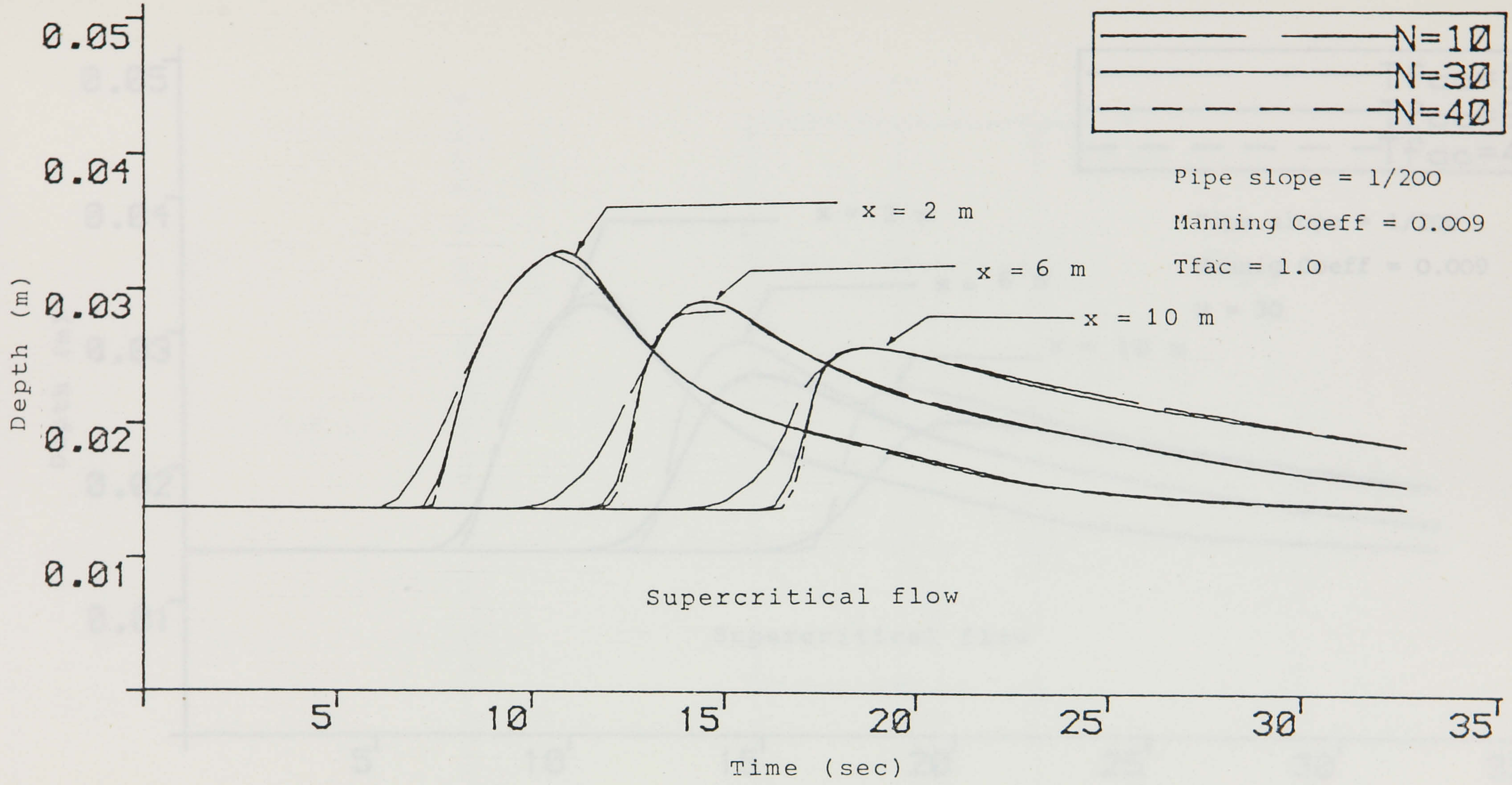

Figure 5.9 Effect of different distance increment lengths on the calculated depth hydrograph.

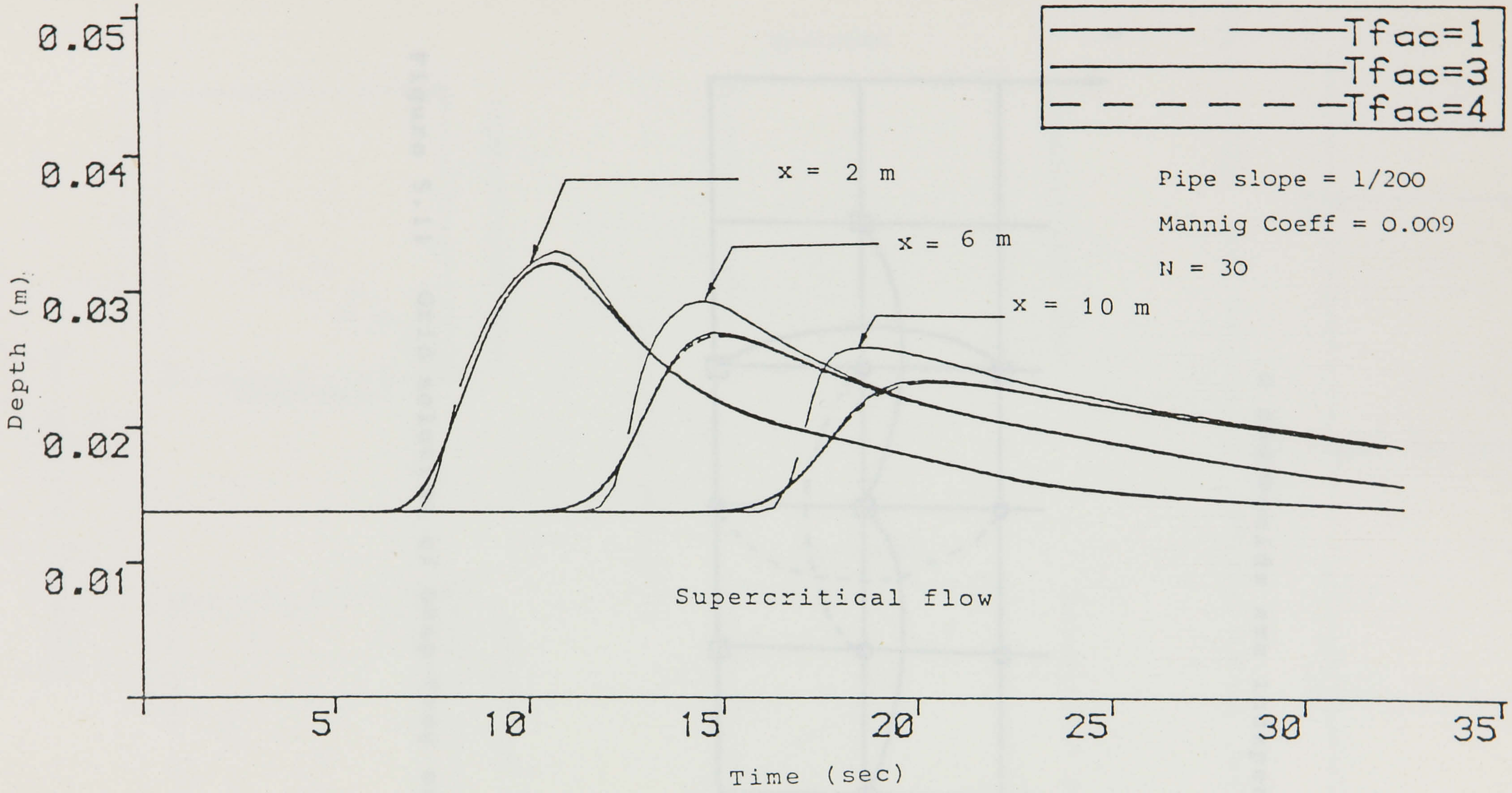

Figure 5.10 Effect of changing the time increment on the calculated depth hydrographs.

○ and □ grids are independent

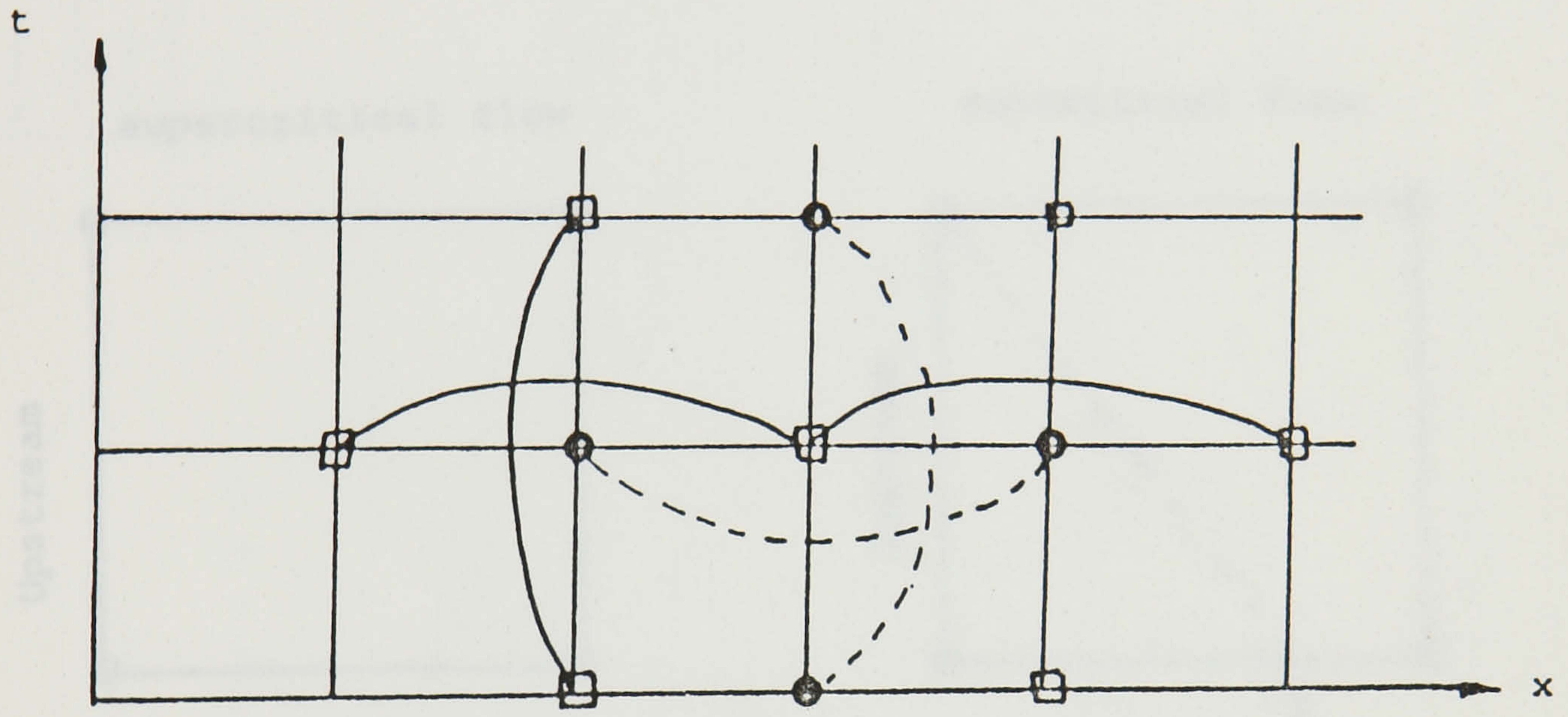

Figure 5.11 Grid solution of Leap-Frog scheme.

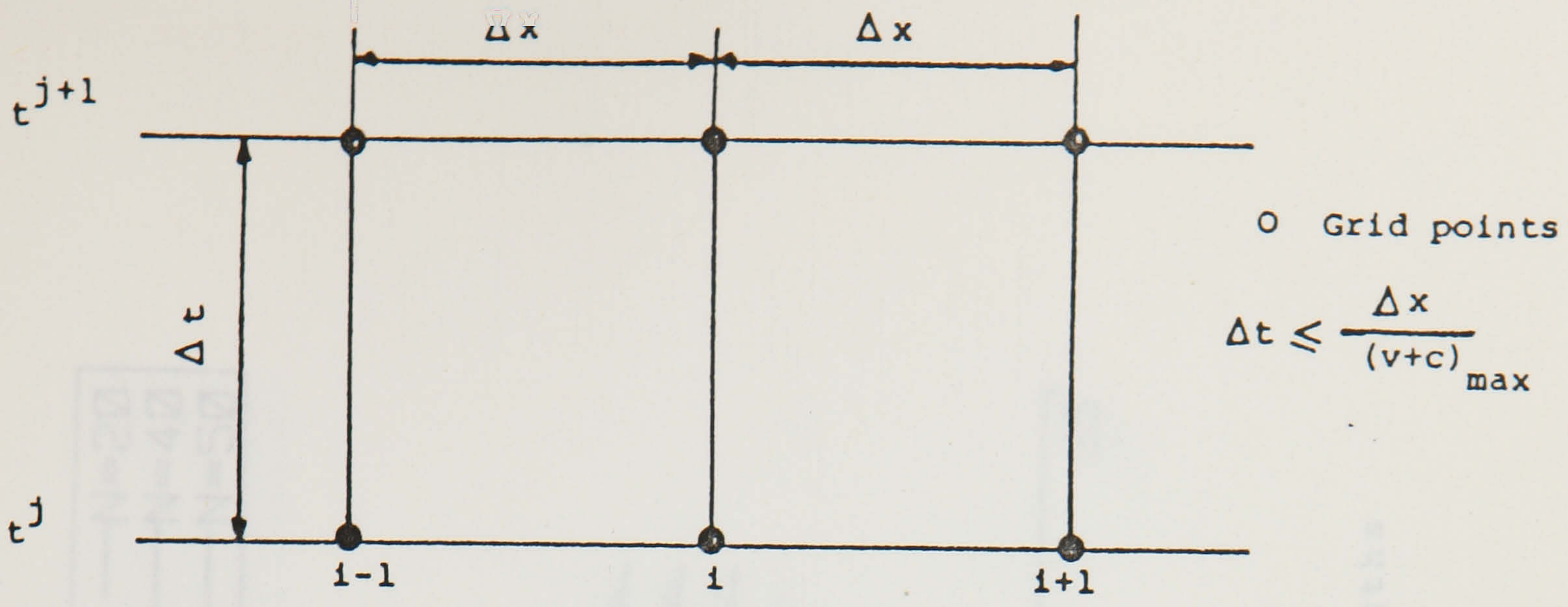

Figure 5.12(a) Grid solution of diffusing scheme (internal nodes).

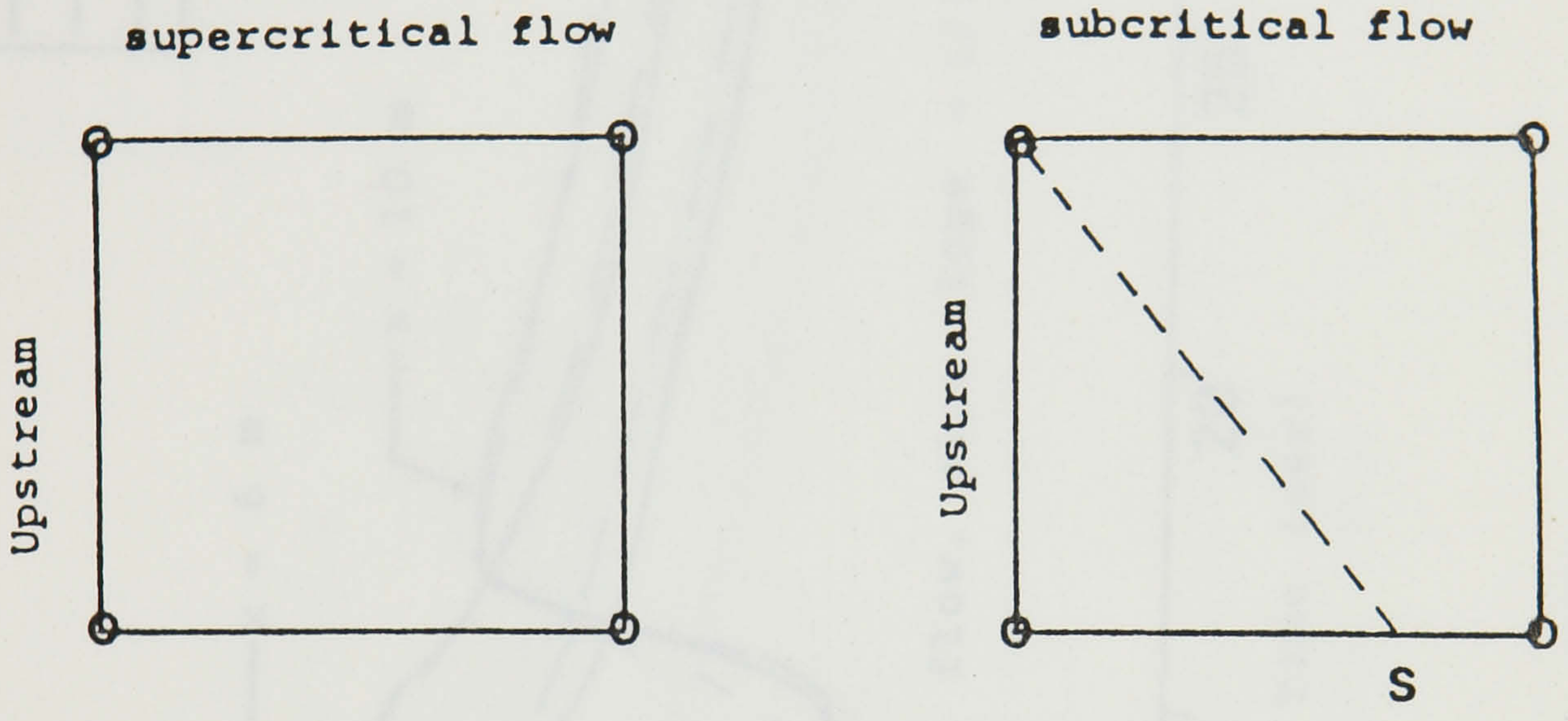

Upstream boundary

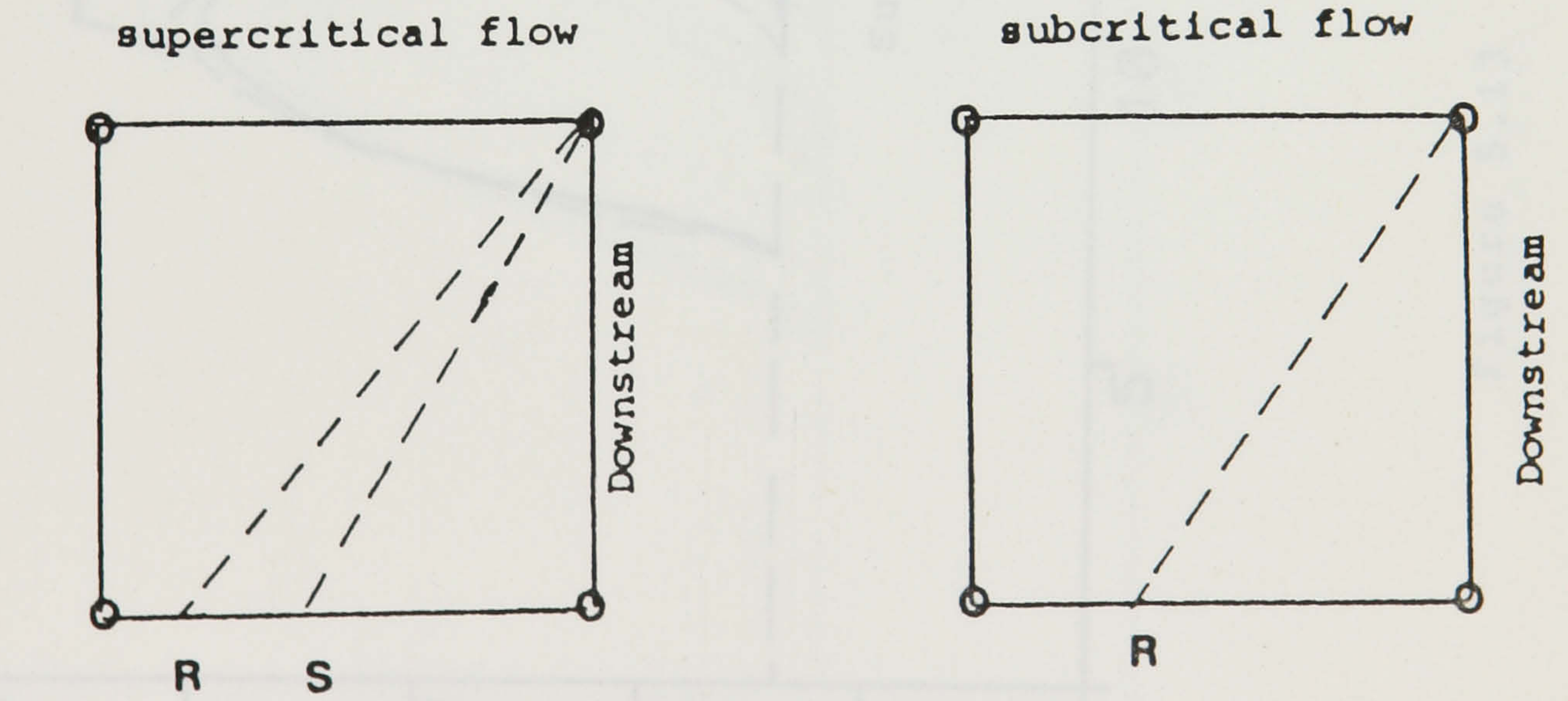

Downstream boundary

Figure 5.12(b) Boundary calculations of diffusing scheme.

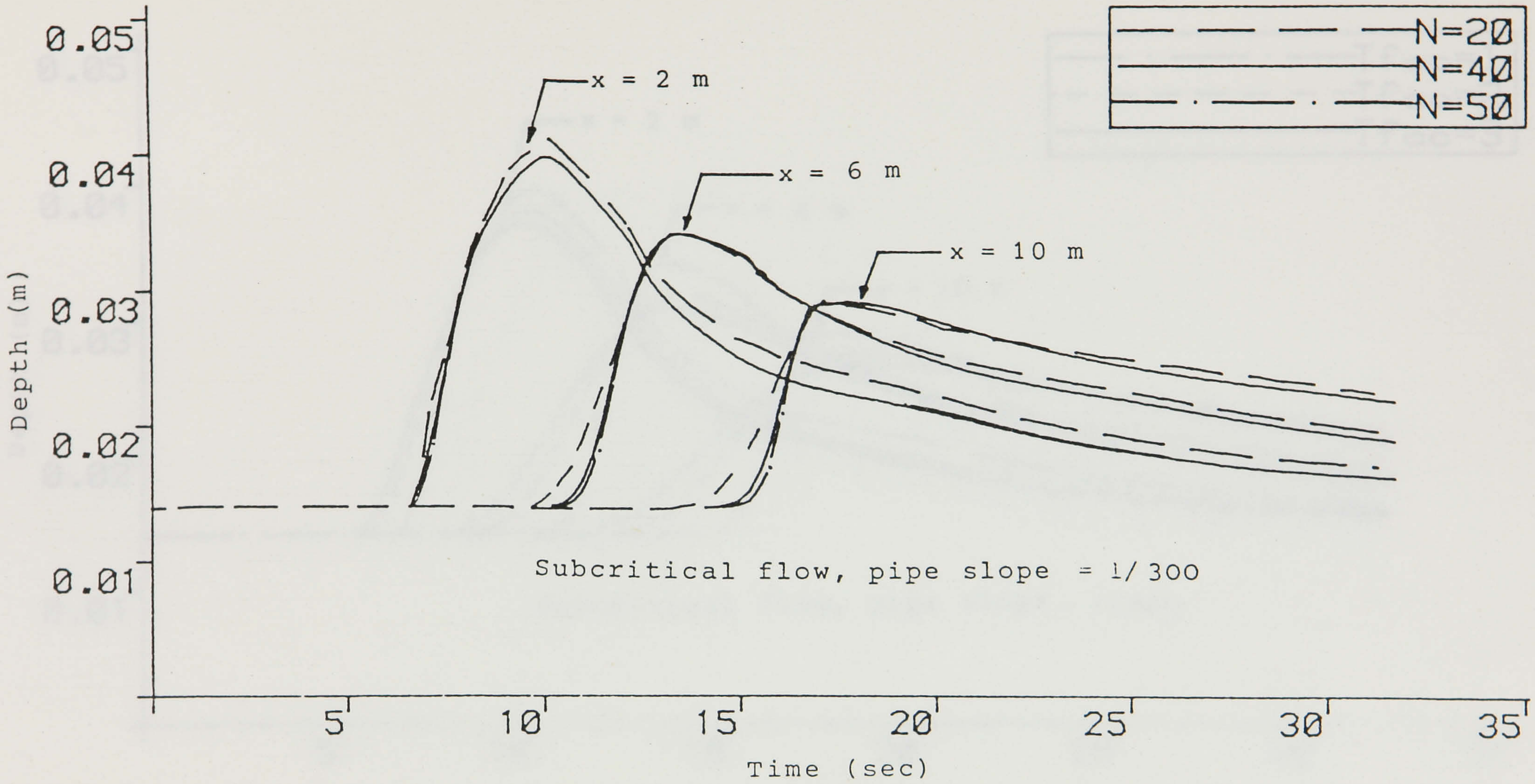

Figure 5.13 Effect of different distance increment lengths on the calculated depth hydrographs.

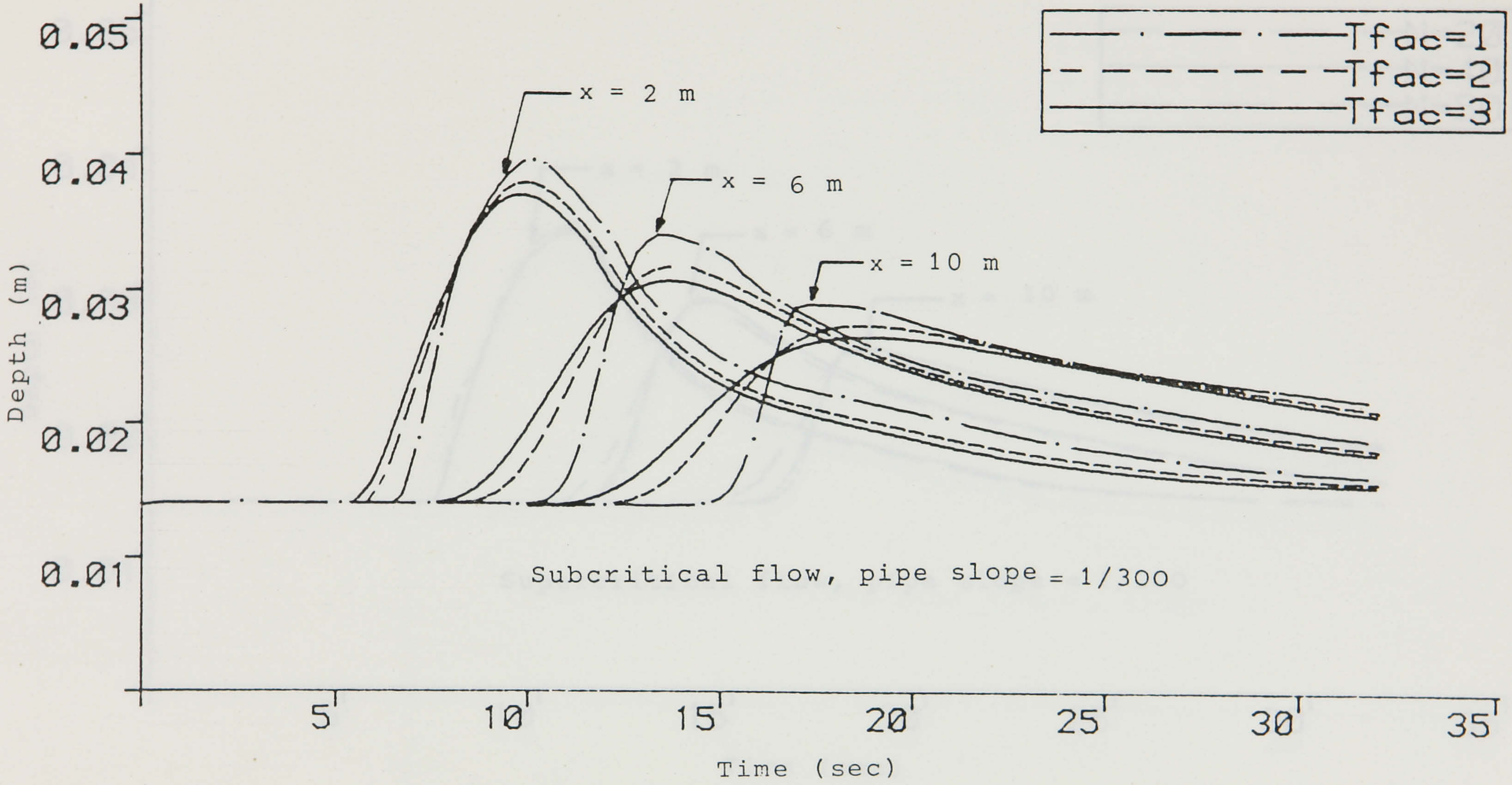

Figure 5.14 Effect of different time steps on the calculated depth hydrographs.

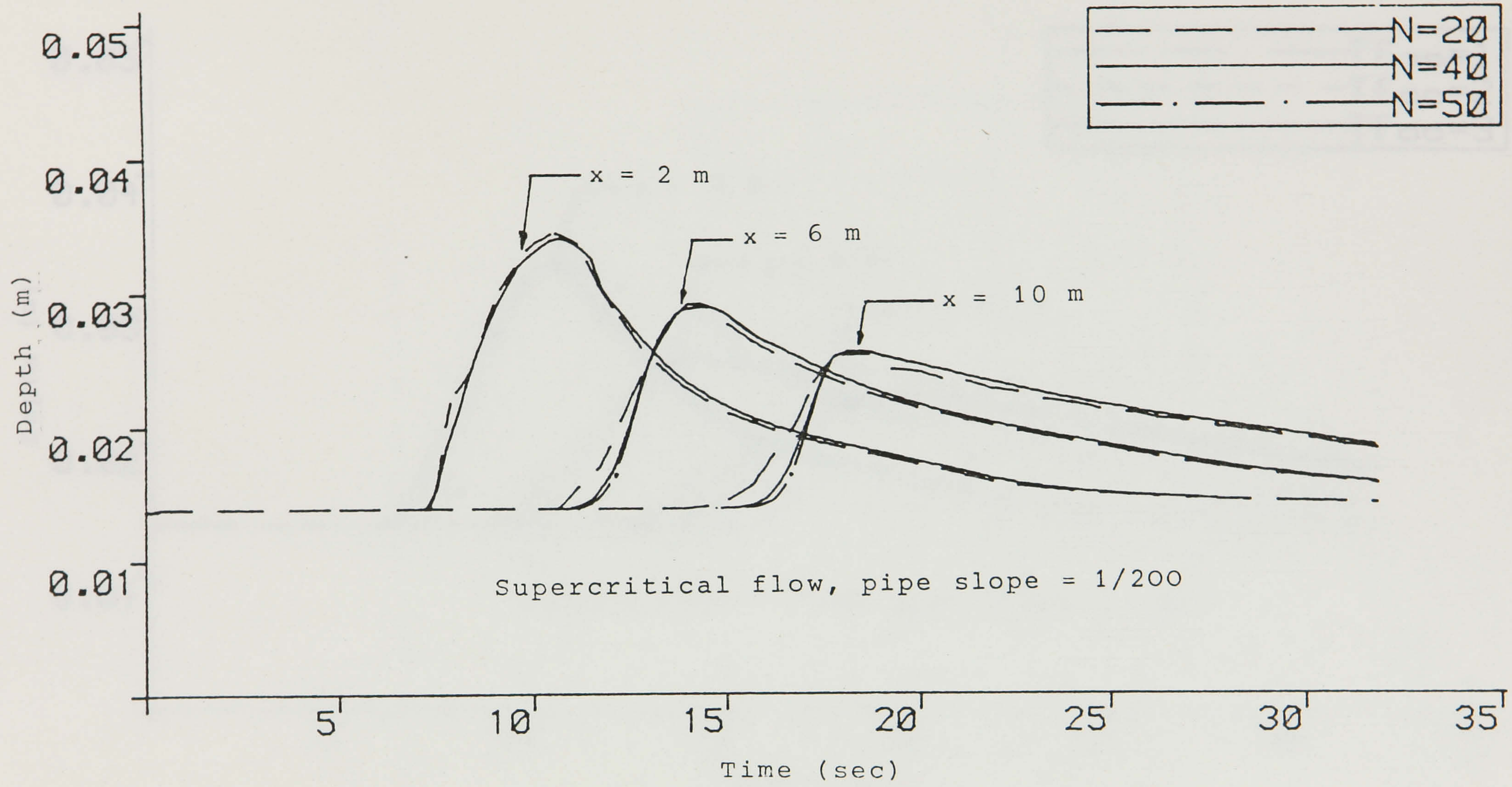

Figure 5.15 Effect of different distance increment lengths on the calculated depth hydrographs.

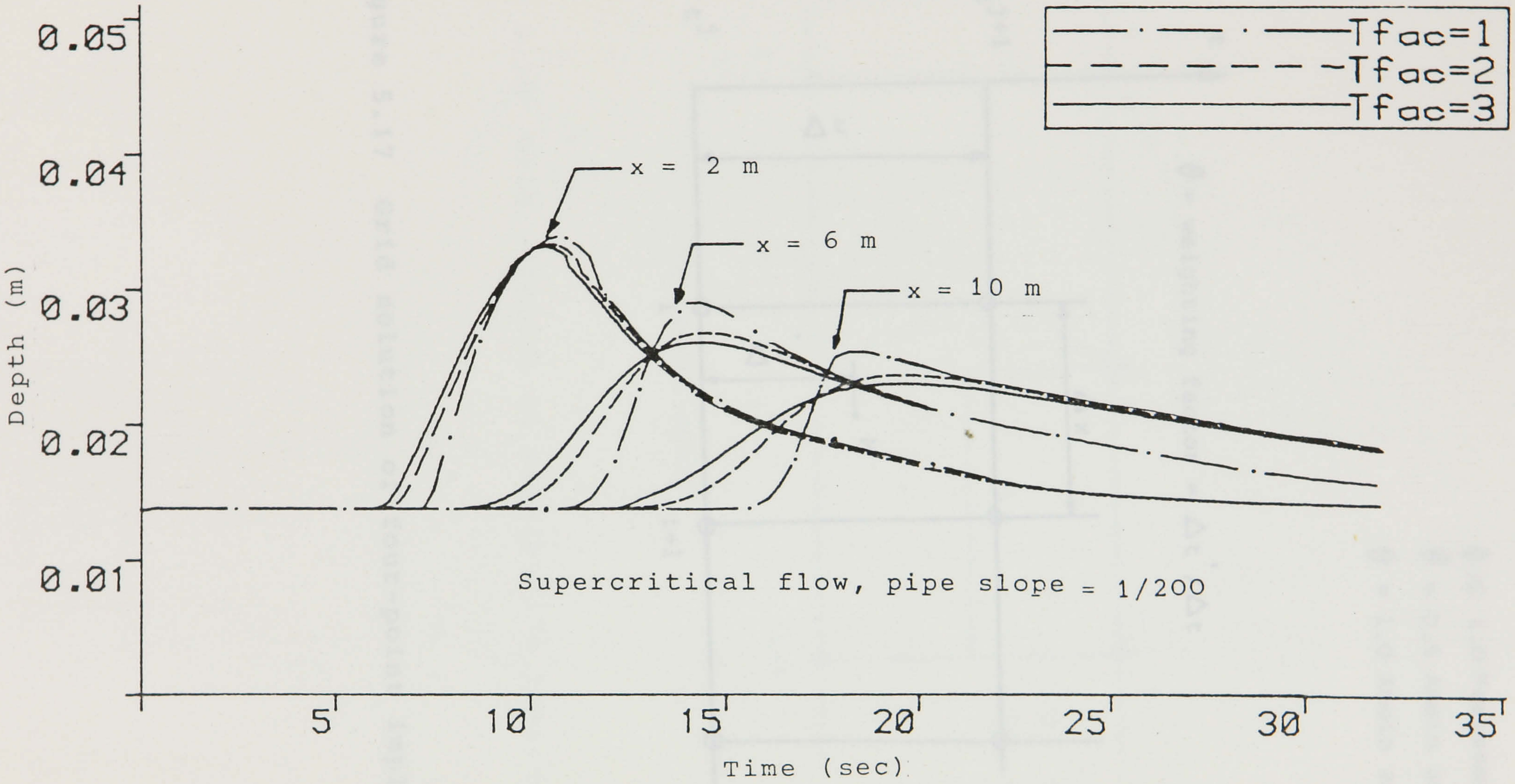

Figure 5.16 Effect of different time steps on the calculated depth hydrographs.

$\theta \leq$ 1.0 Preissman (1960)

θ = 0.5 Amein and Fang (1970)

θ = 1.0 Amein and Chu (1975)

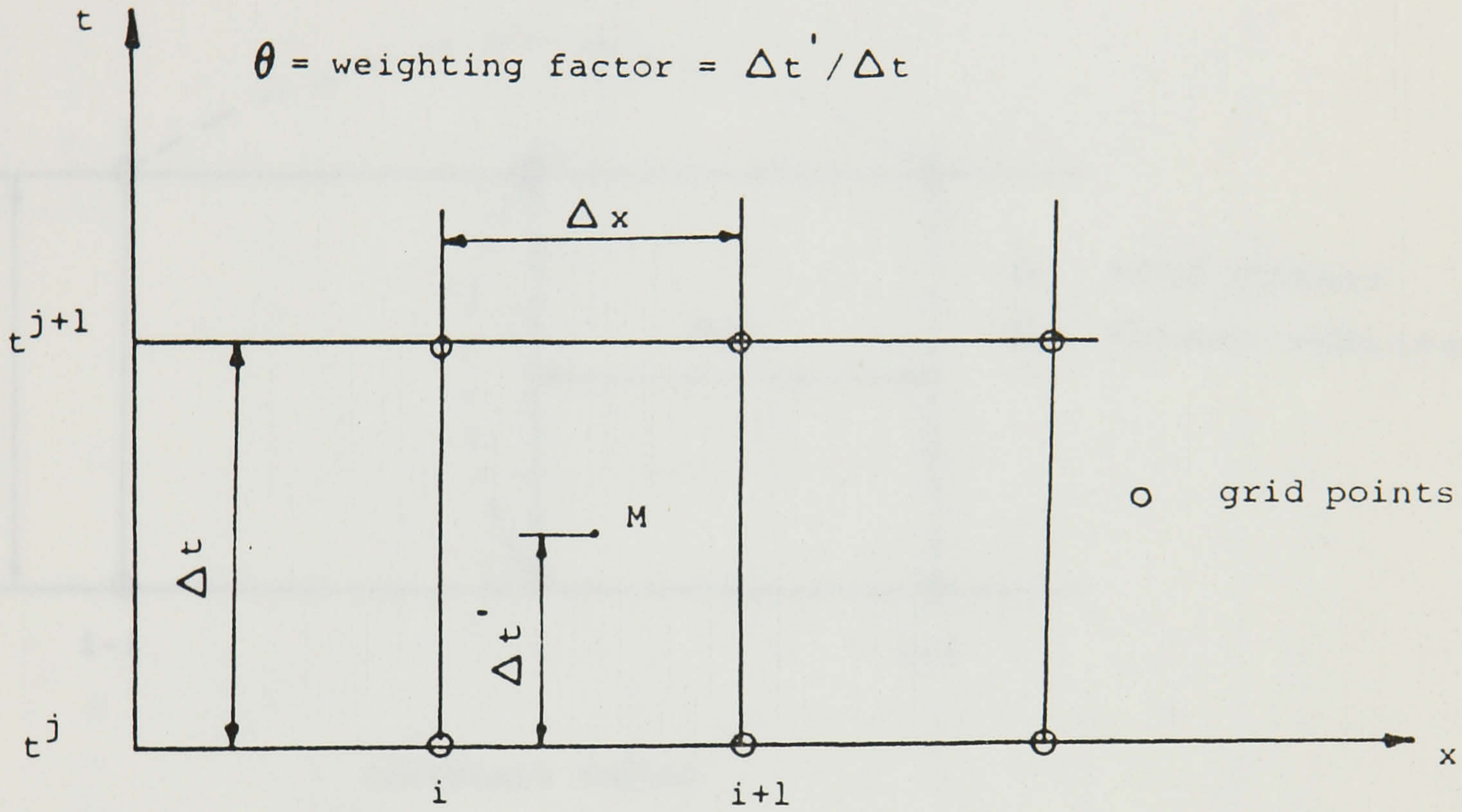

Figure 5.17 Grid solution of four-point implicit method.

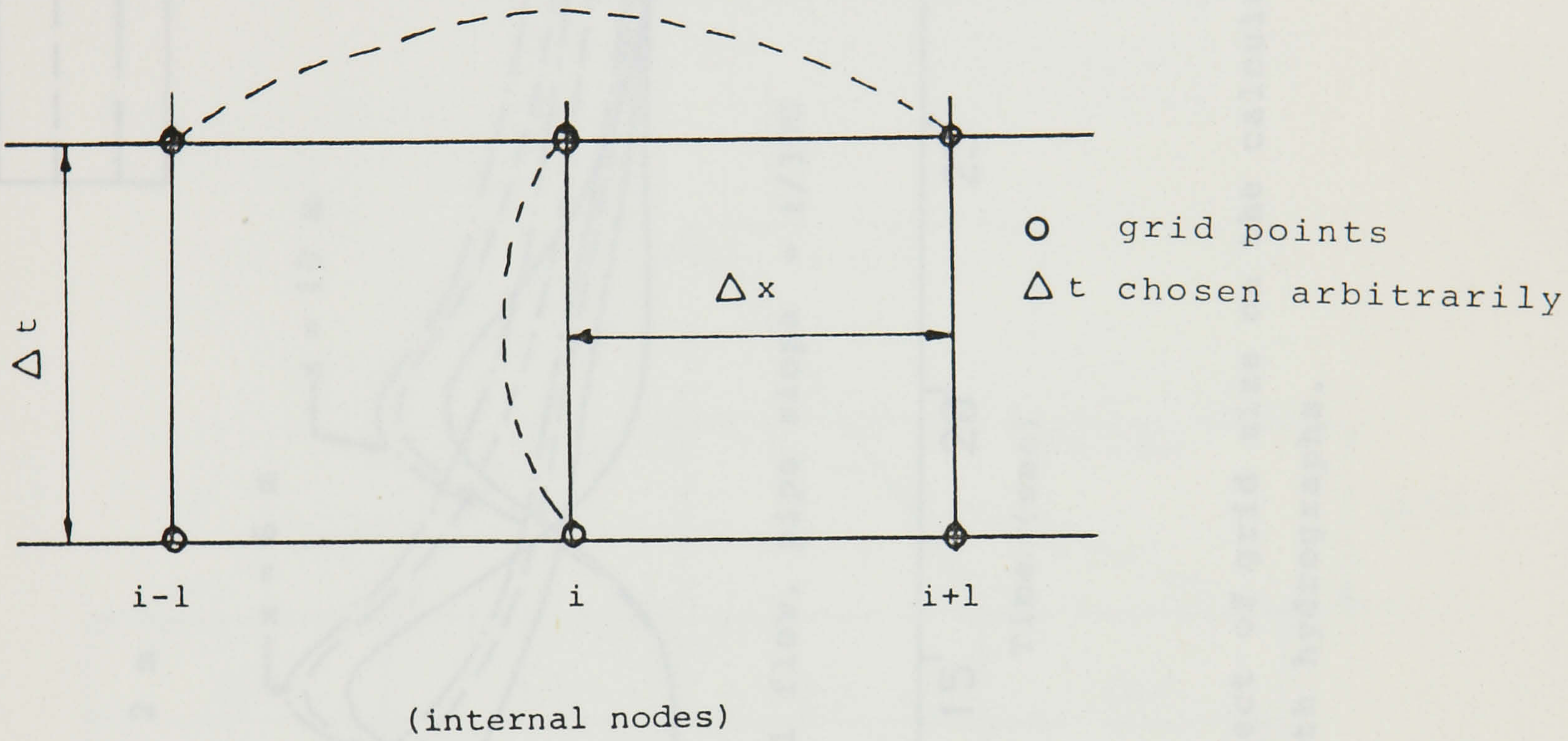

Figure 5.18 Grid solution of Strelkoff's implicit method.

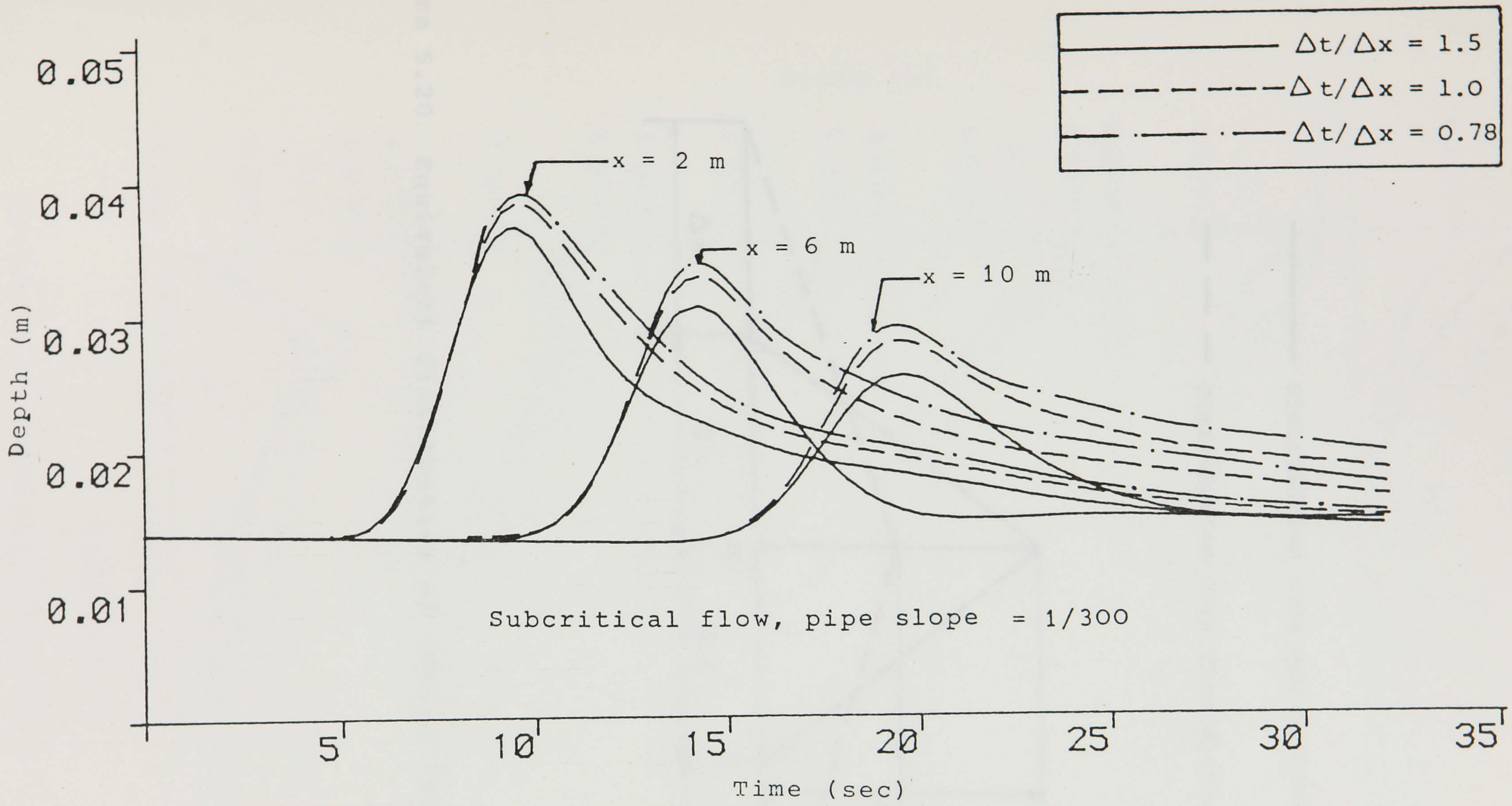

Figure 5.19 Effect of grid size on the calculated depth hydrographs.

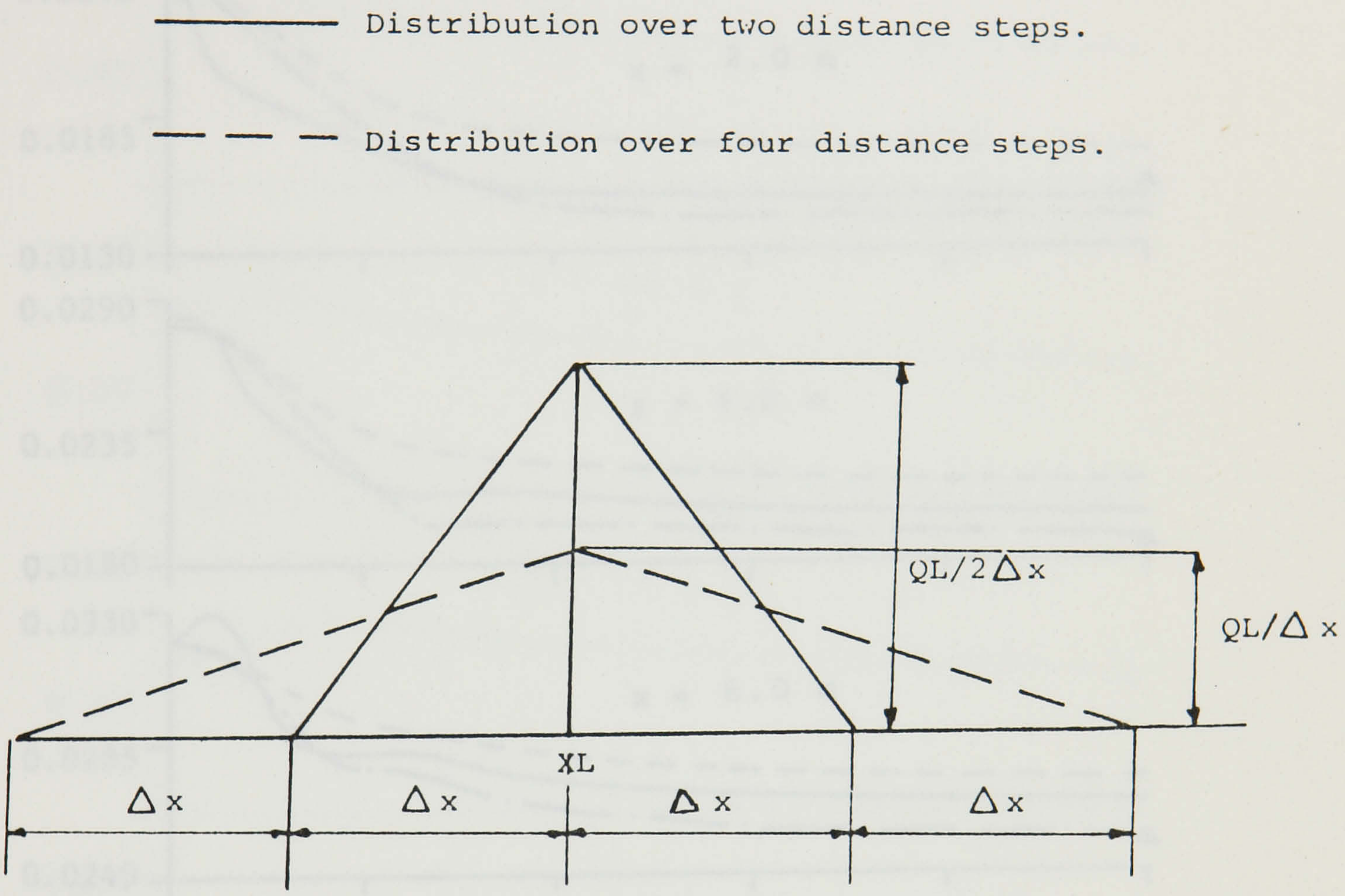

Figure 5.20 Equivalent distribution of concentrated lateral inflow.

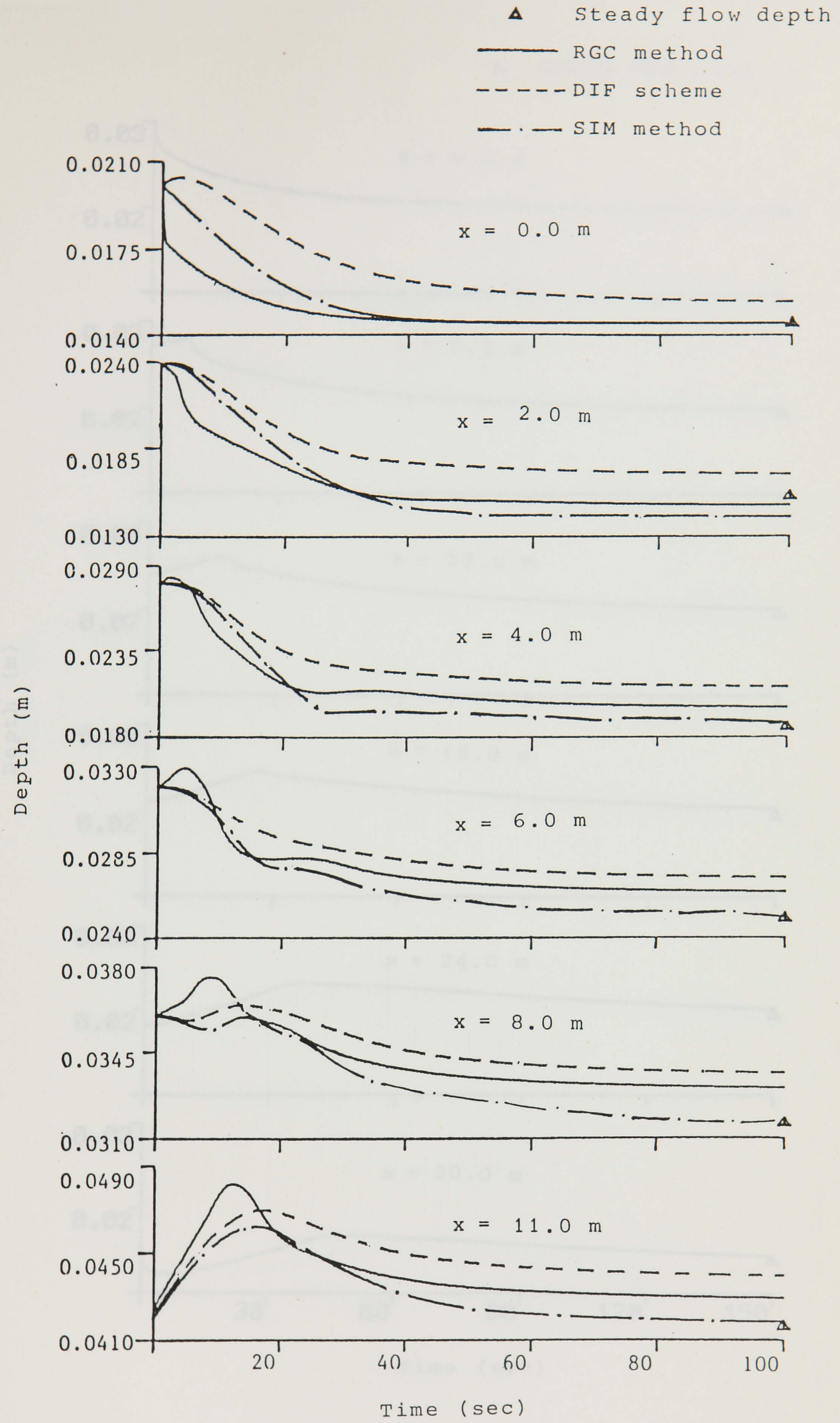

Figure 6.1 Stability test for controlled-outfall boundary condition.

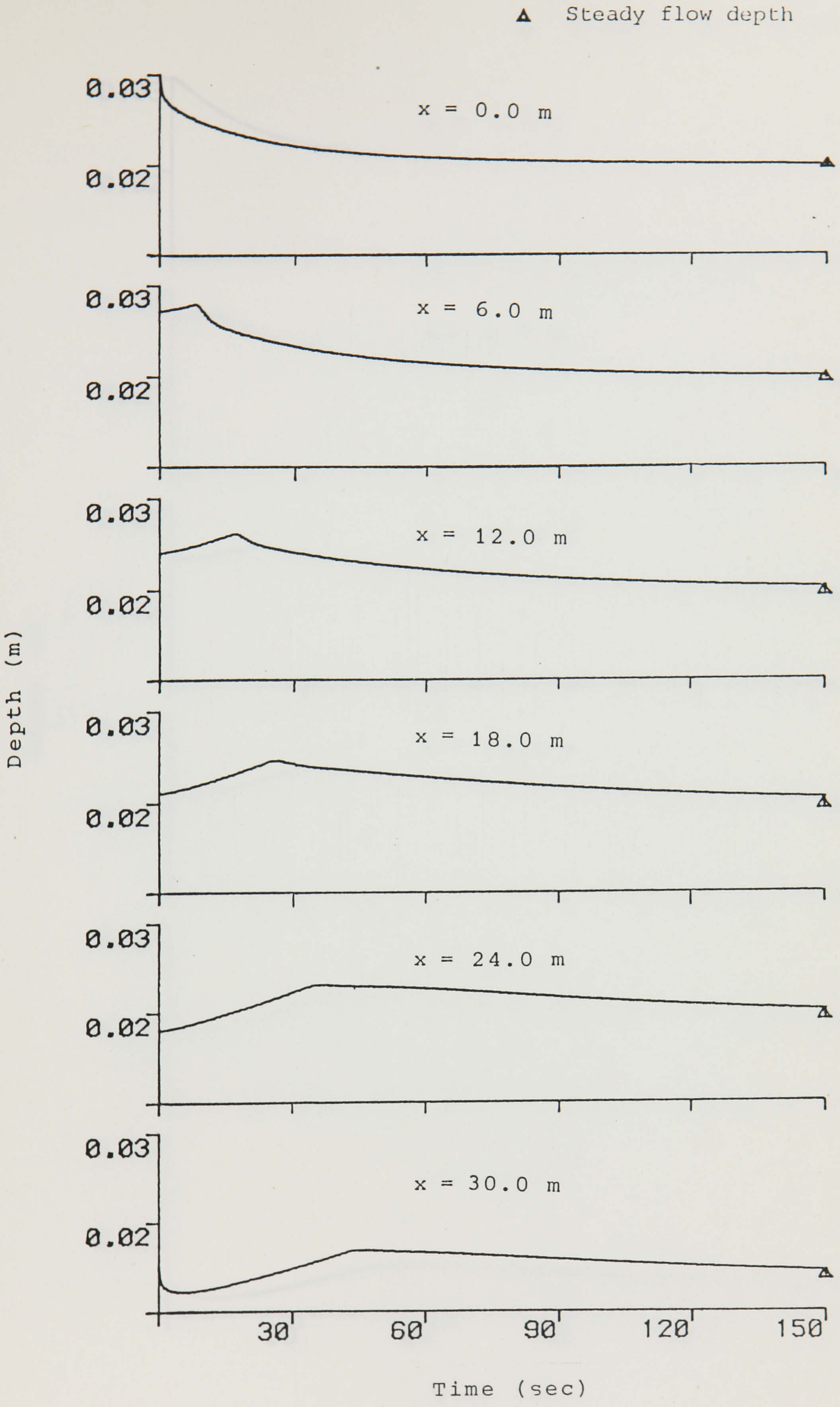

Figure 6.2 Stability test for free-outfall boundary condition, RGC method.

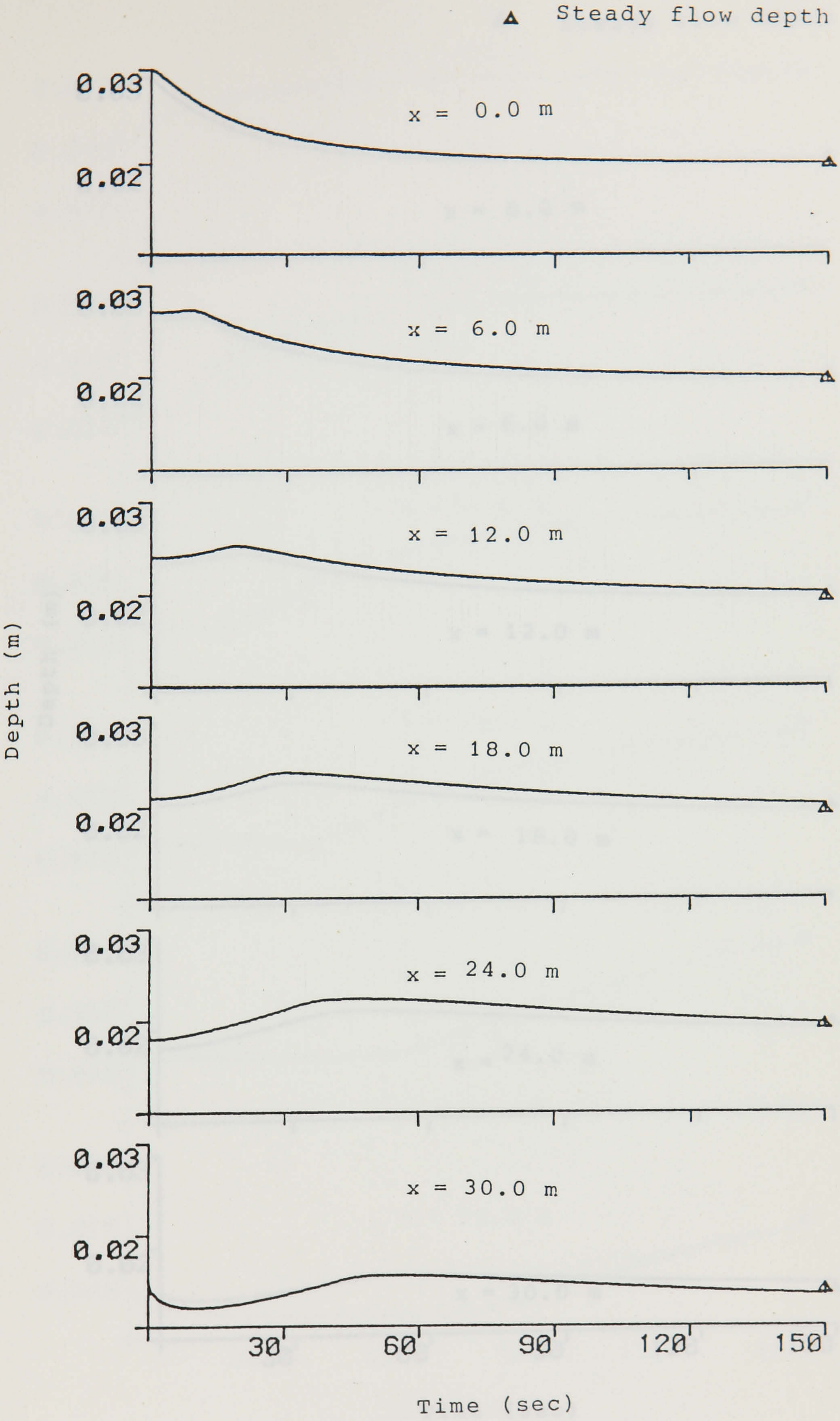

Figure 6.3 Stability test for free-outfall boundary condition, DIF scheme.

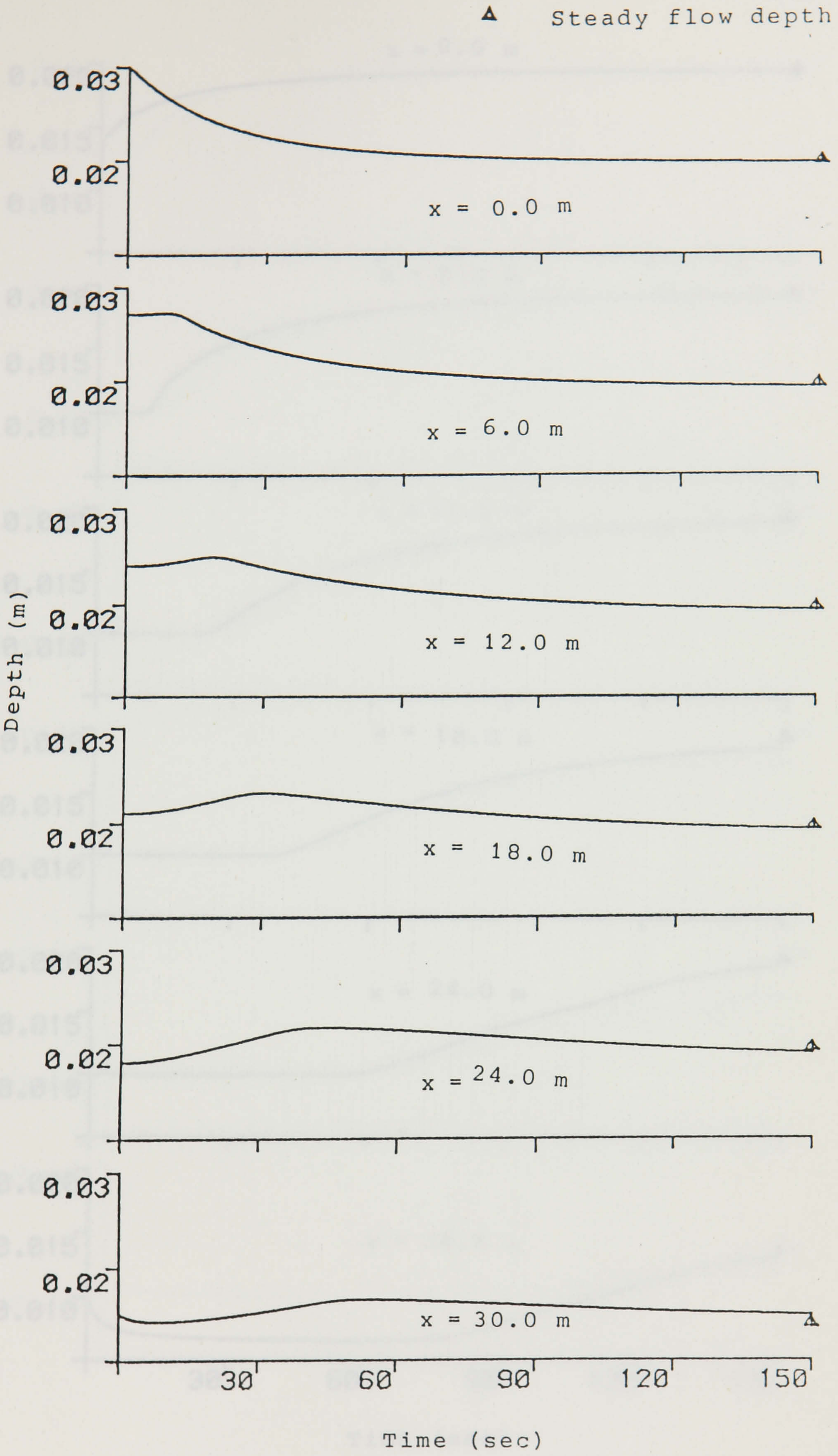

Figure 6.4 Stability test for free-outfall boundary condition, SIM method.

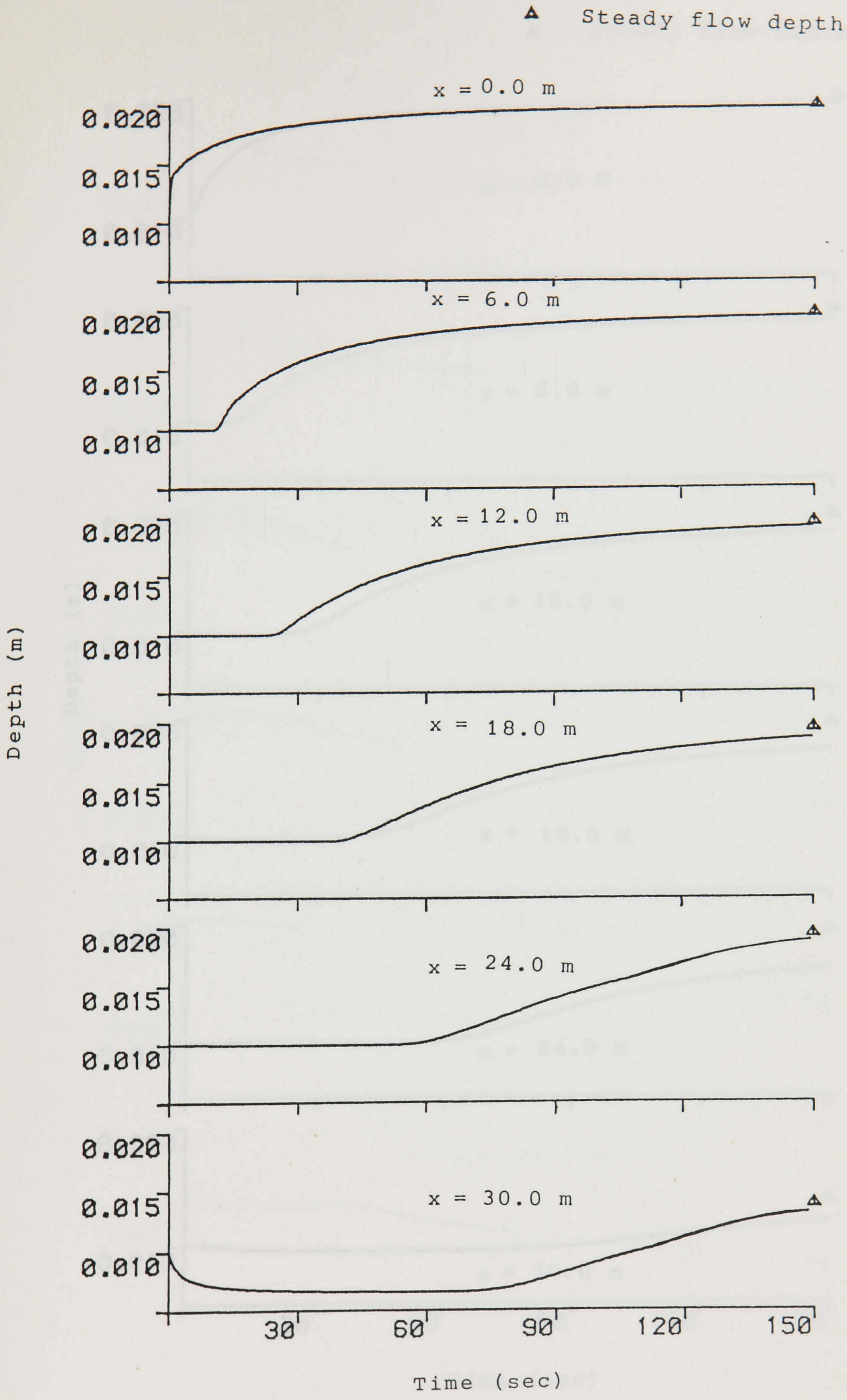

Figure 6.5 Stability test for free-outfall boundary condition, RGC method.

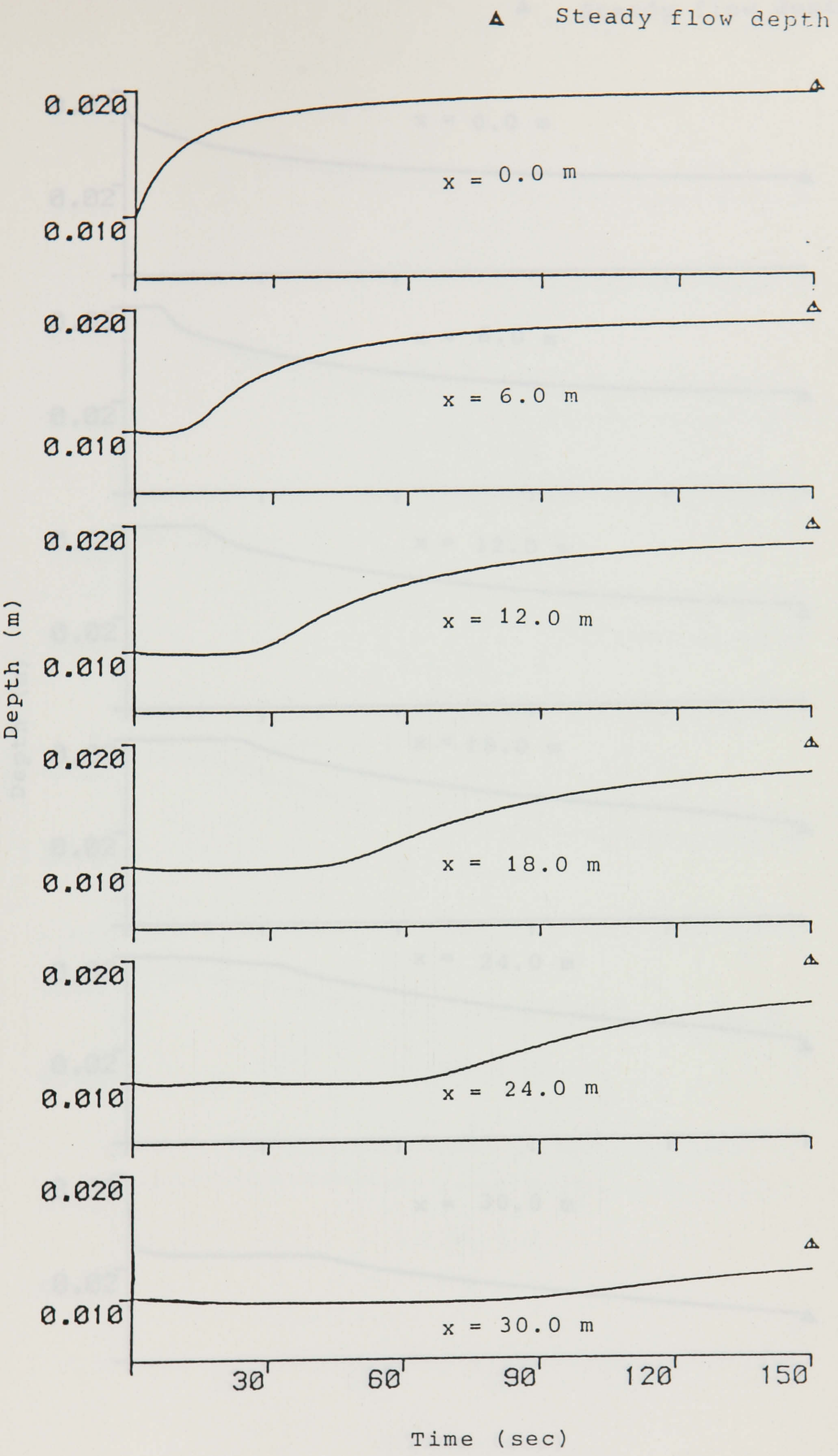

Figure 6.6 Stability test for free-outfall boundary condition, SIM method.

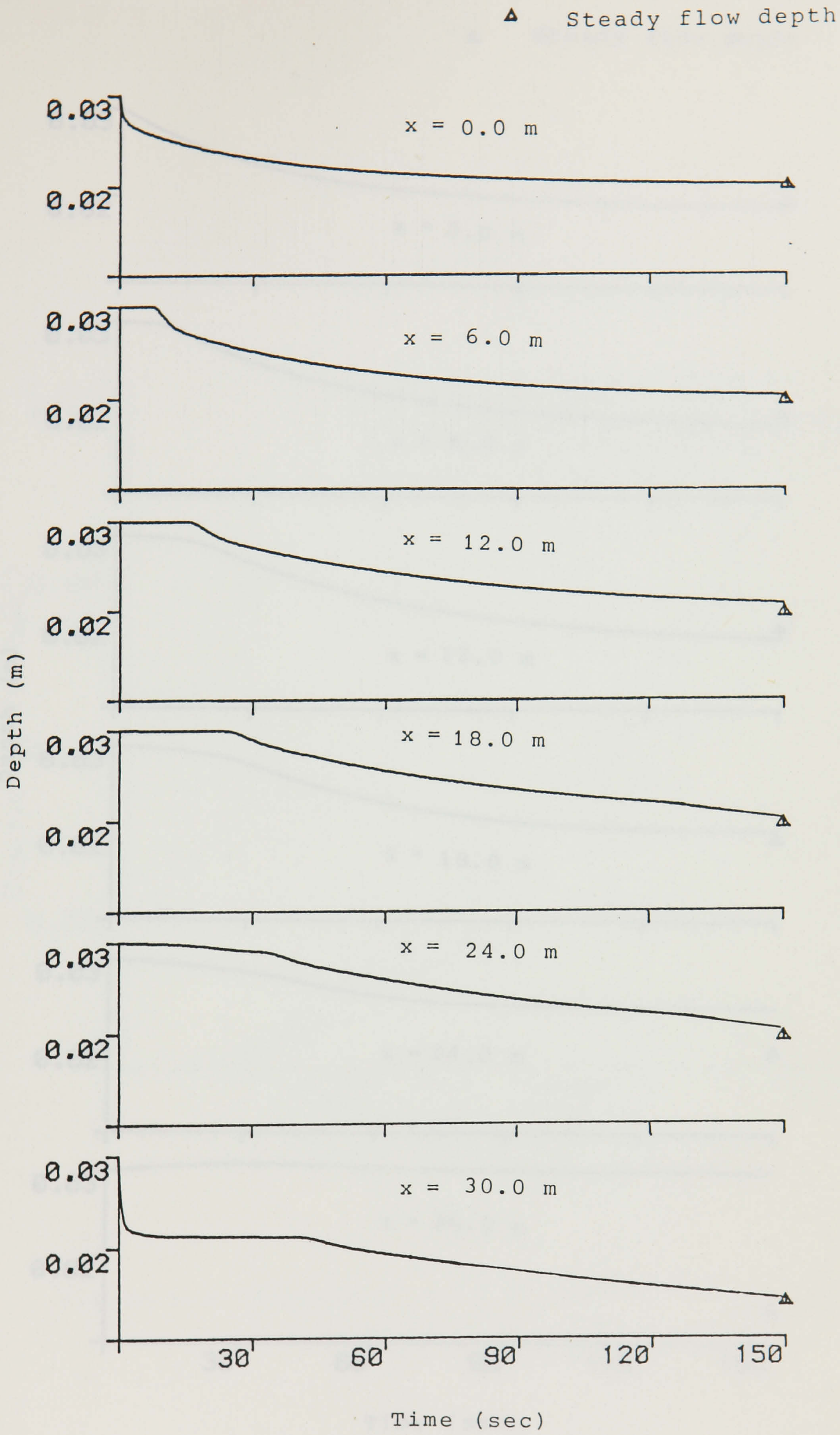

Figure 6.7 Stability test for free-outfall boundary condition, RGC method.

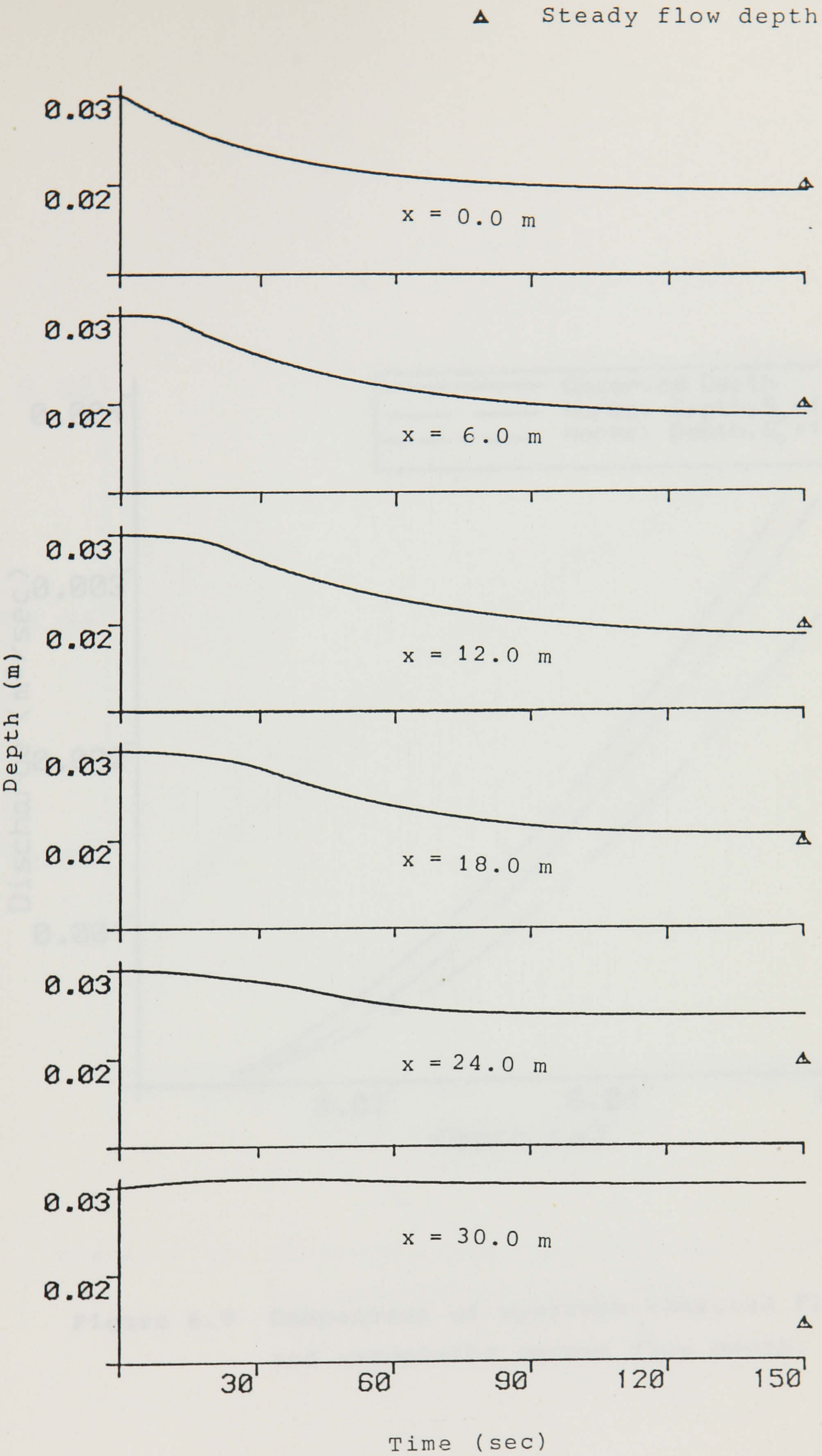

Figure 6.8 Stability test for free-outfall boundary condition, SIM method.

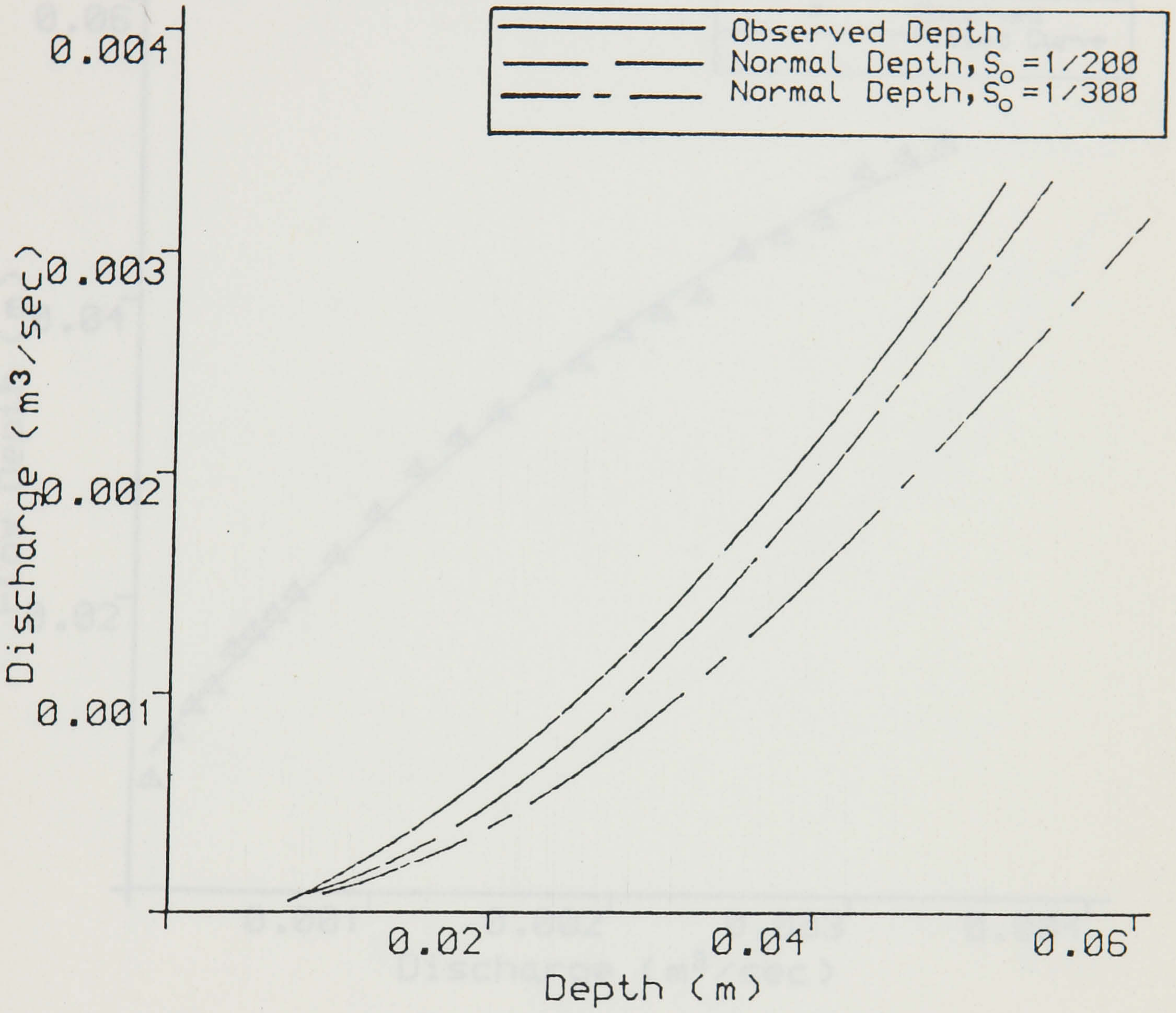

Figure 6.9 Comparison of upstream observed flow depth and calculated normal flow depth.

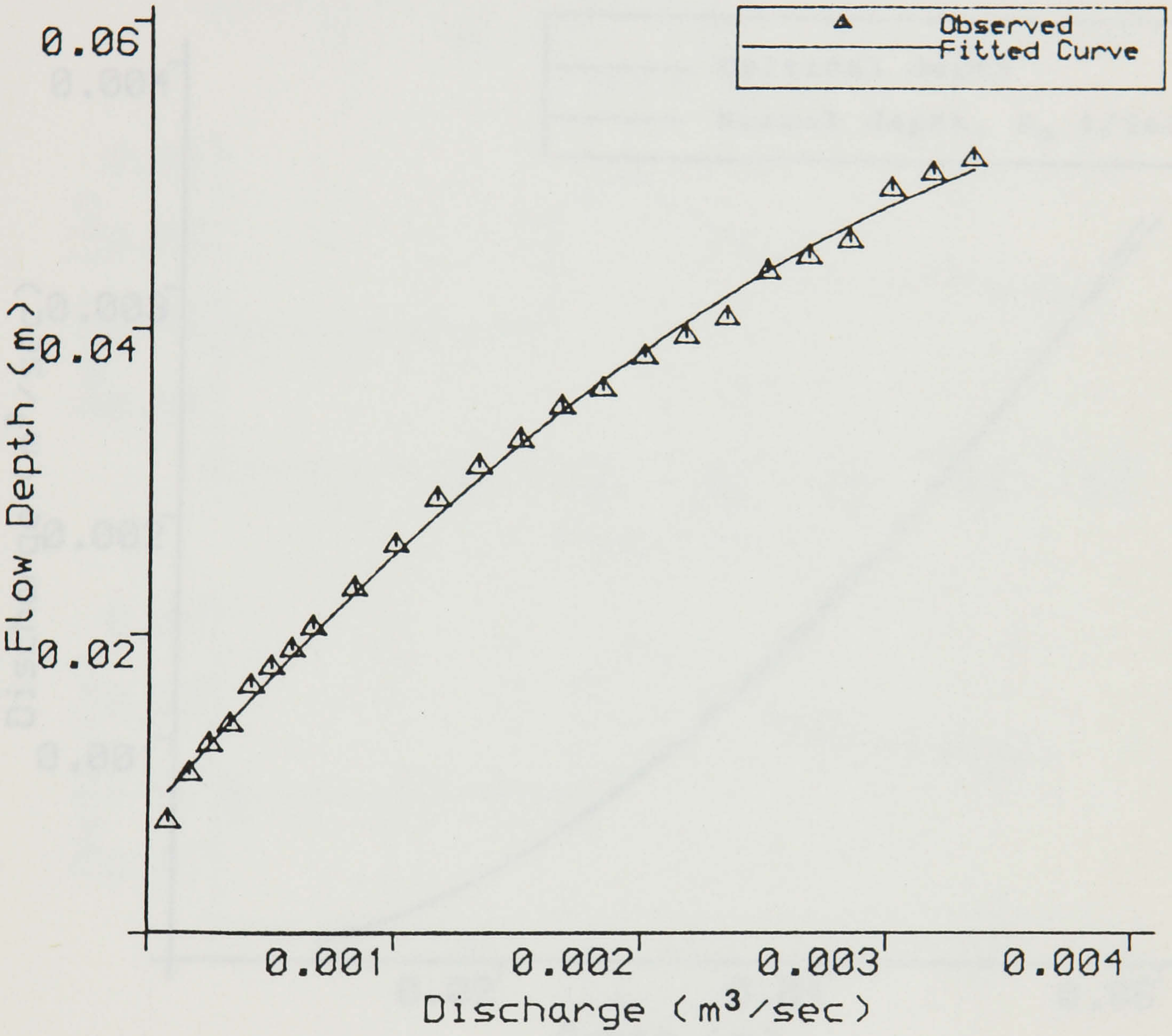

Figure 6.10 Observed discharge-depth relationship at the upstream section, x=0.0.

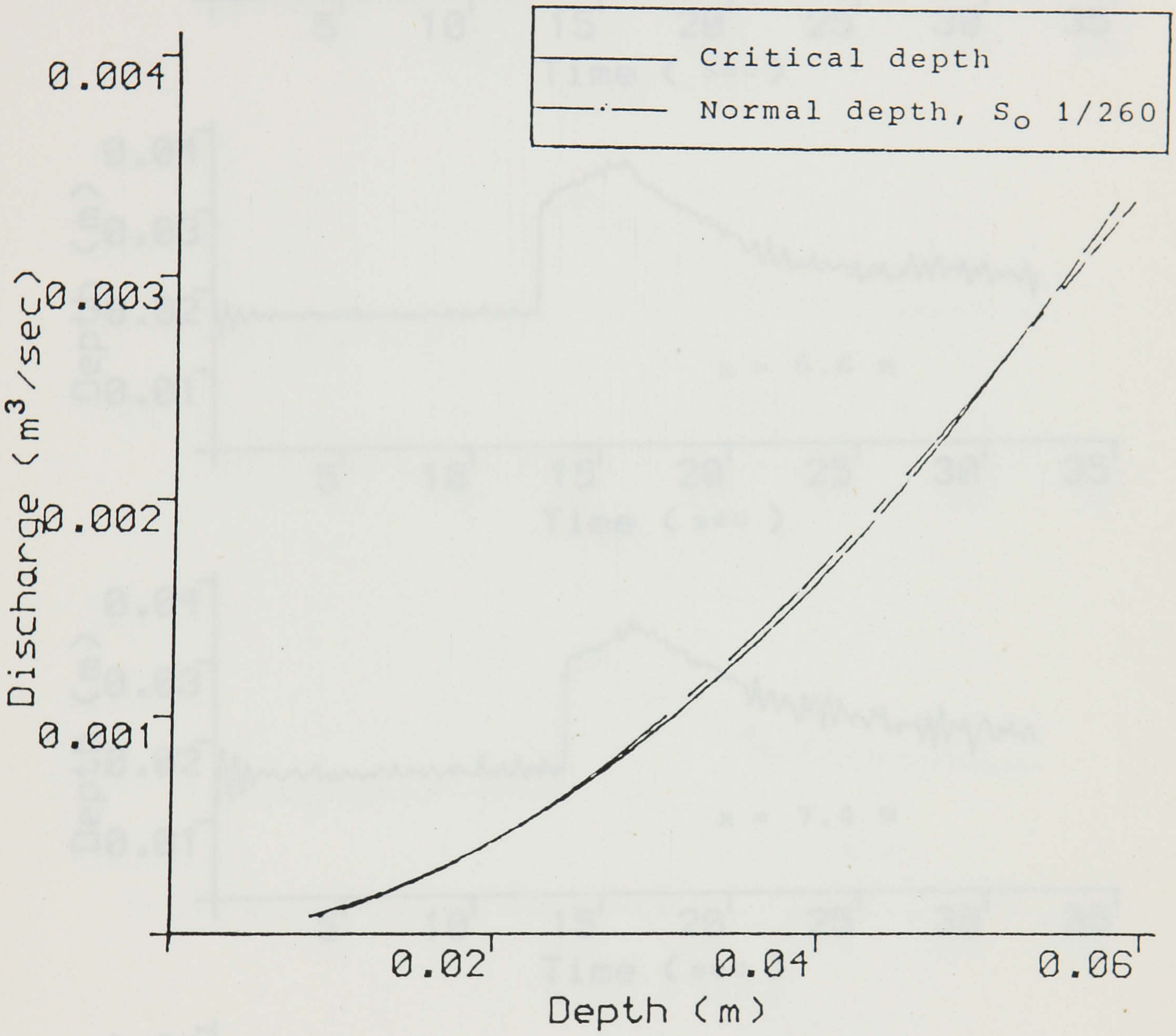

Figure 6.11 Determination of critical pipe slope.

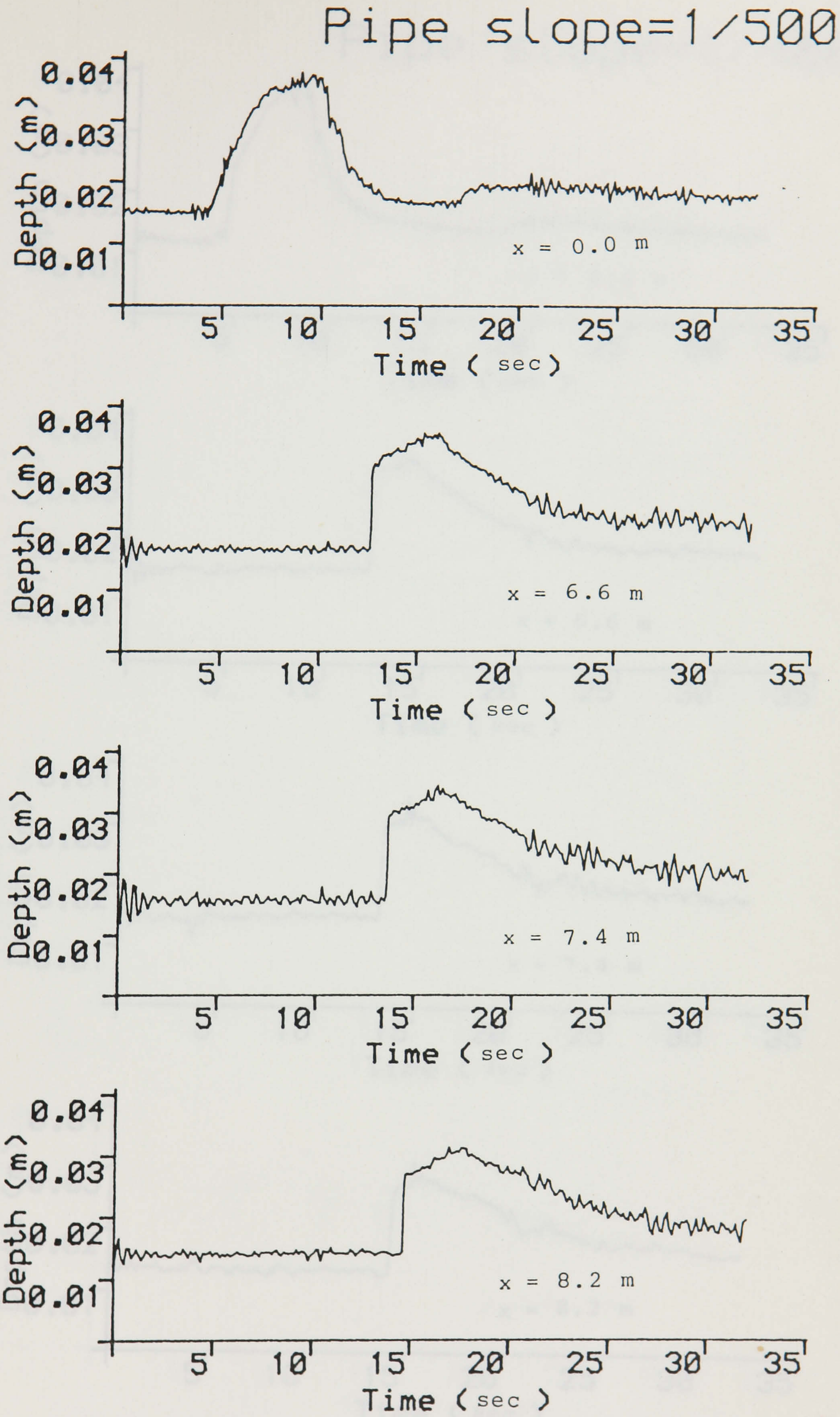

Figure 6.12 Observed depth hydrographs.

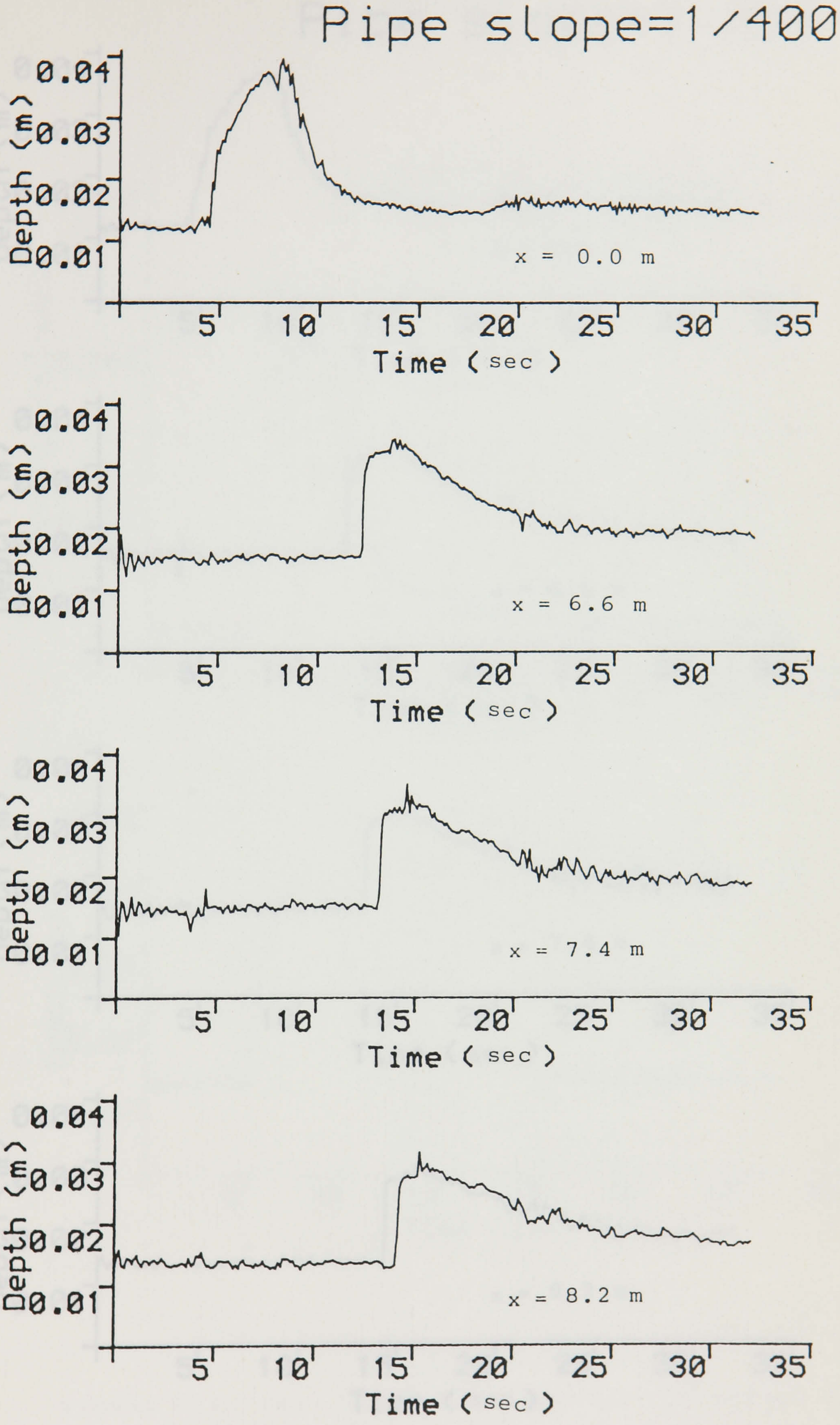

Figure 6.13 Observed depth hydrographs.

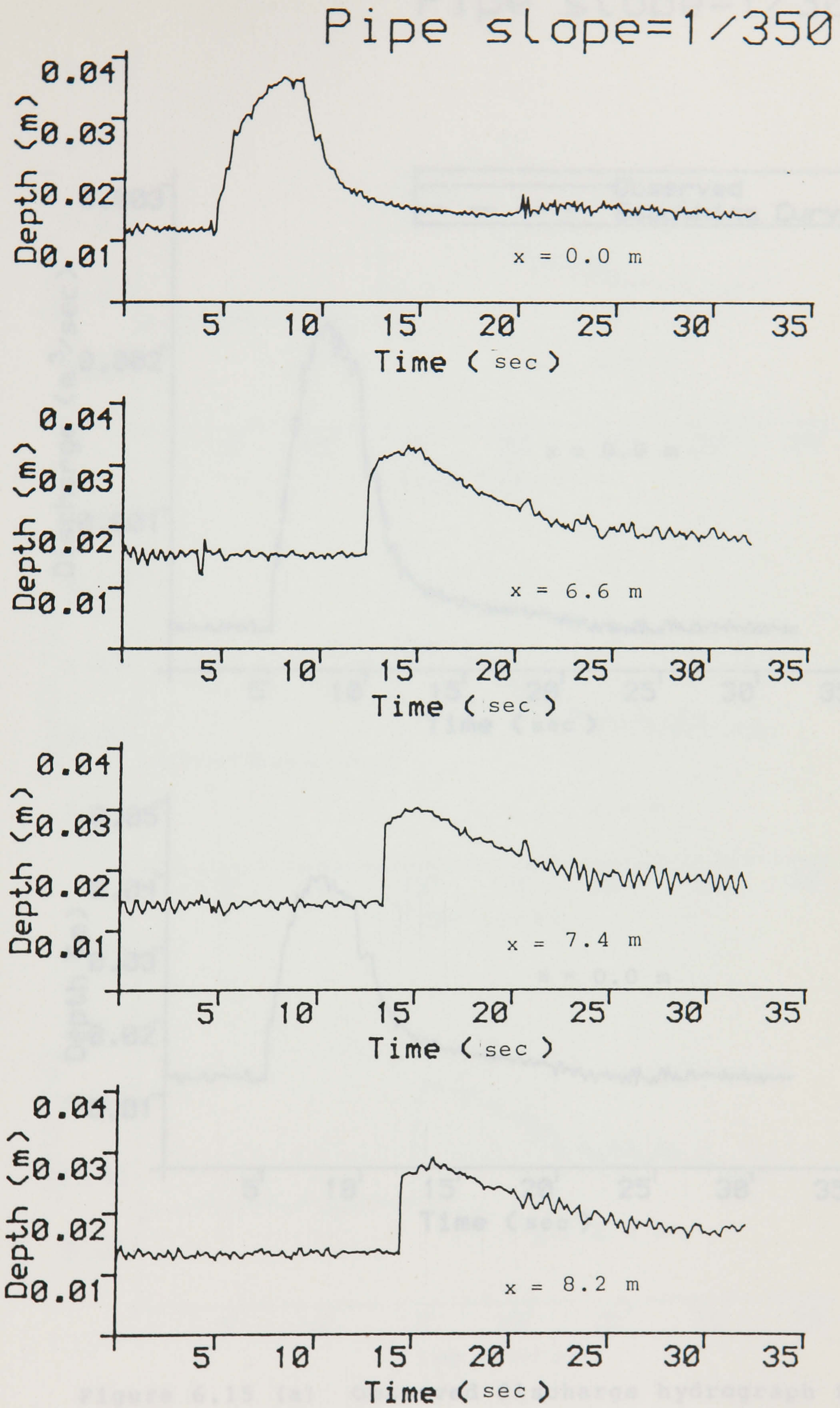

Figure 6.14 Observed depth hydrographs.

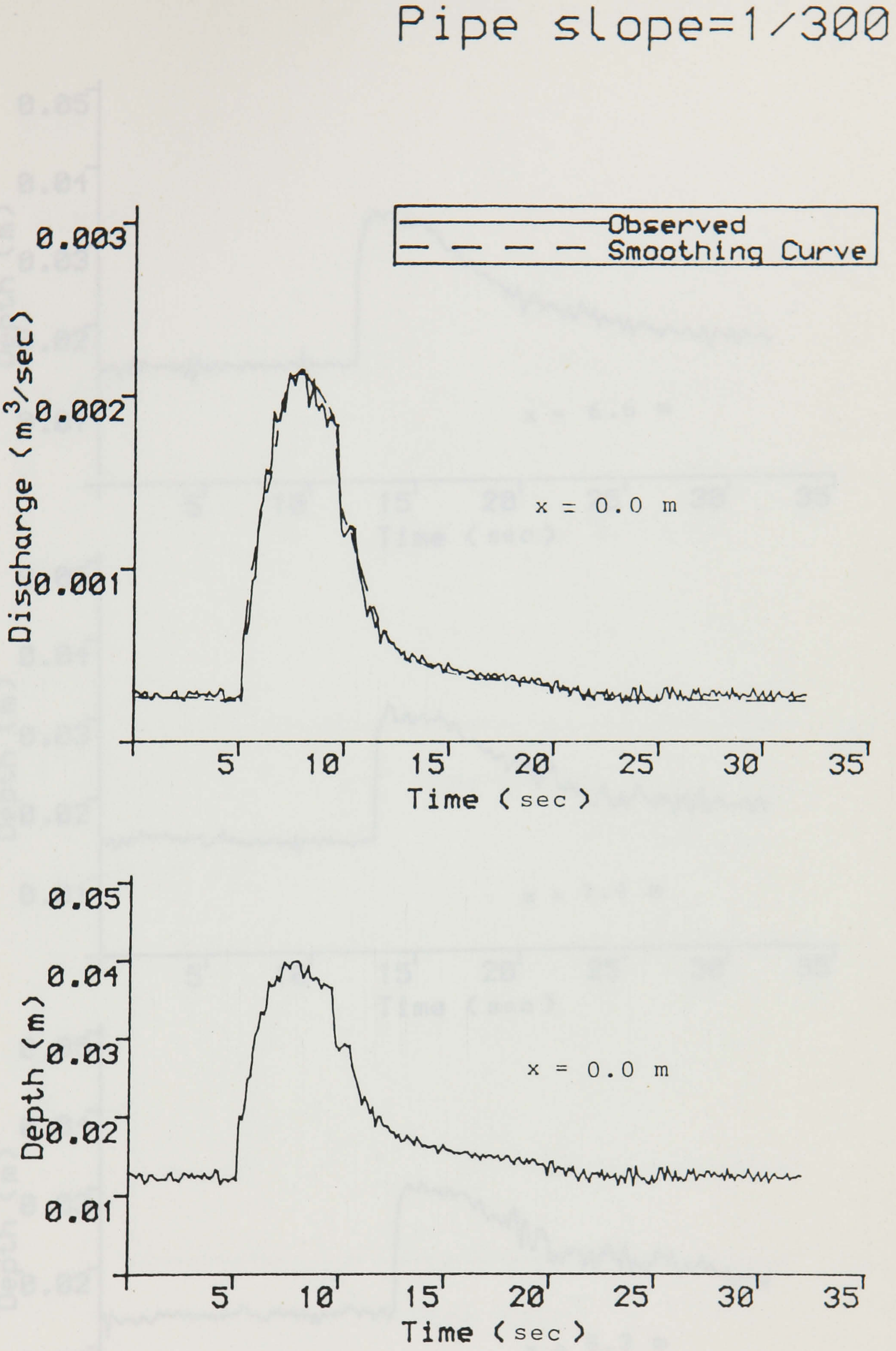

Figure 6.15 (a) Observed discharge hydrograph in the upper graph, depth hydrograph in the lower graph.

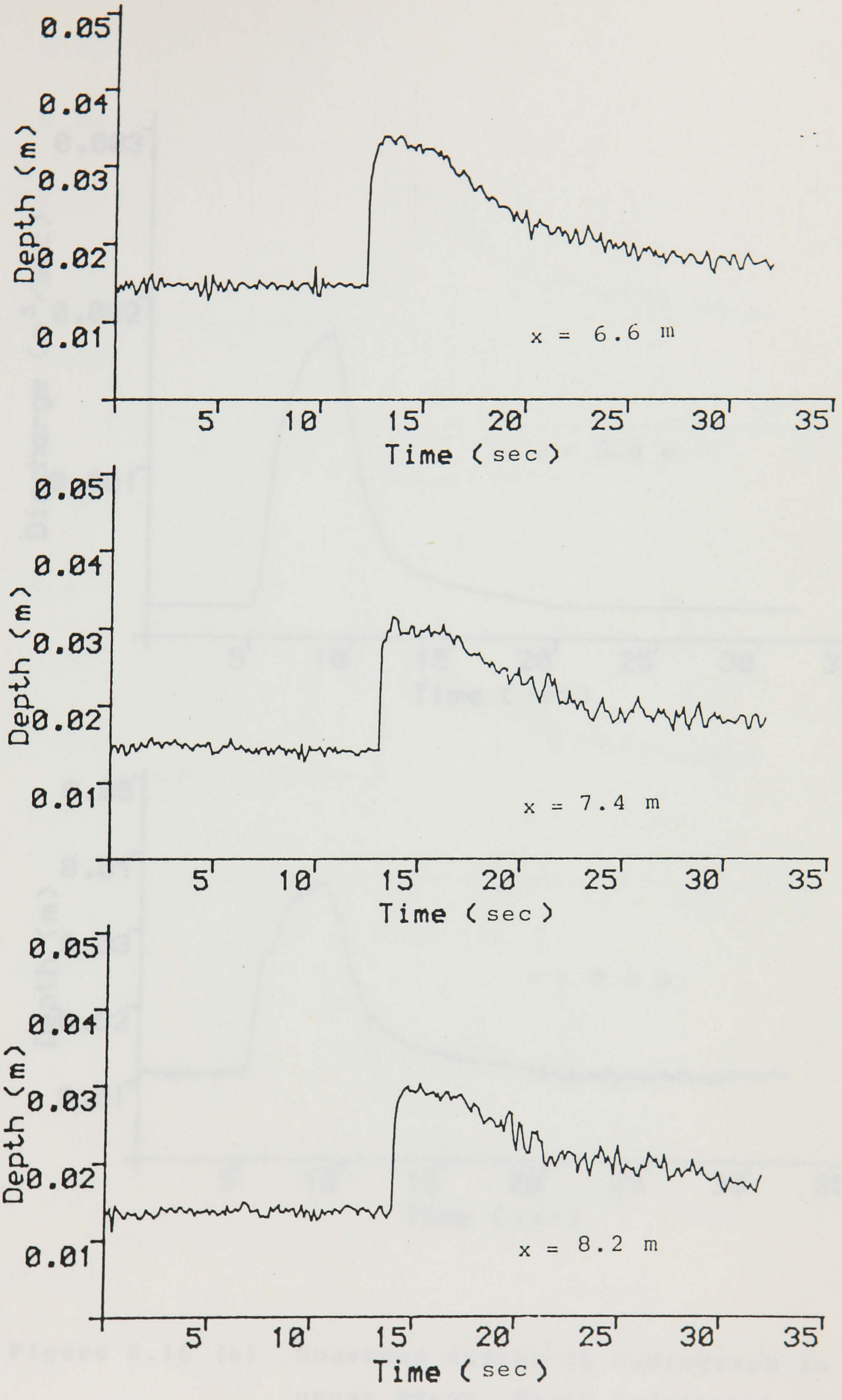

Figure 6.15 (b) Observed depth hydrographs.

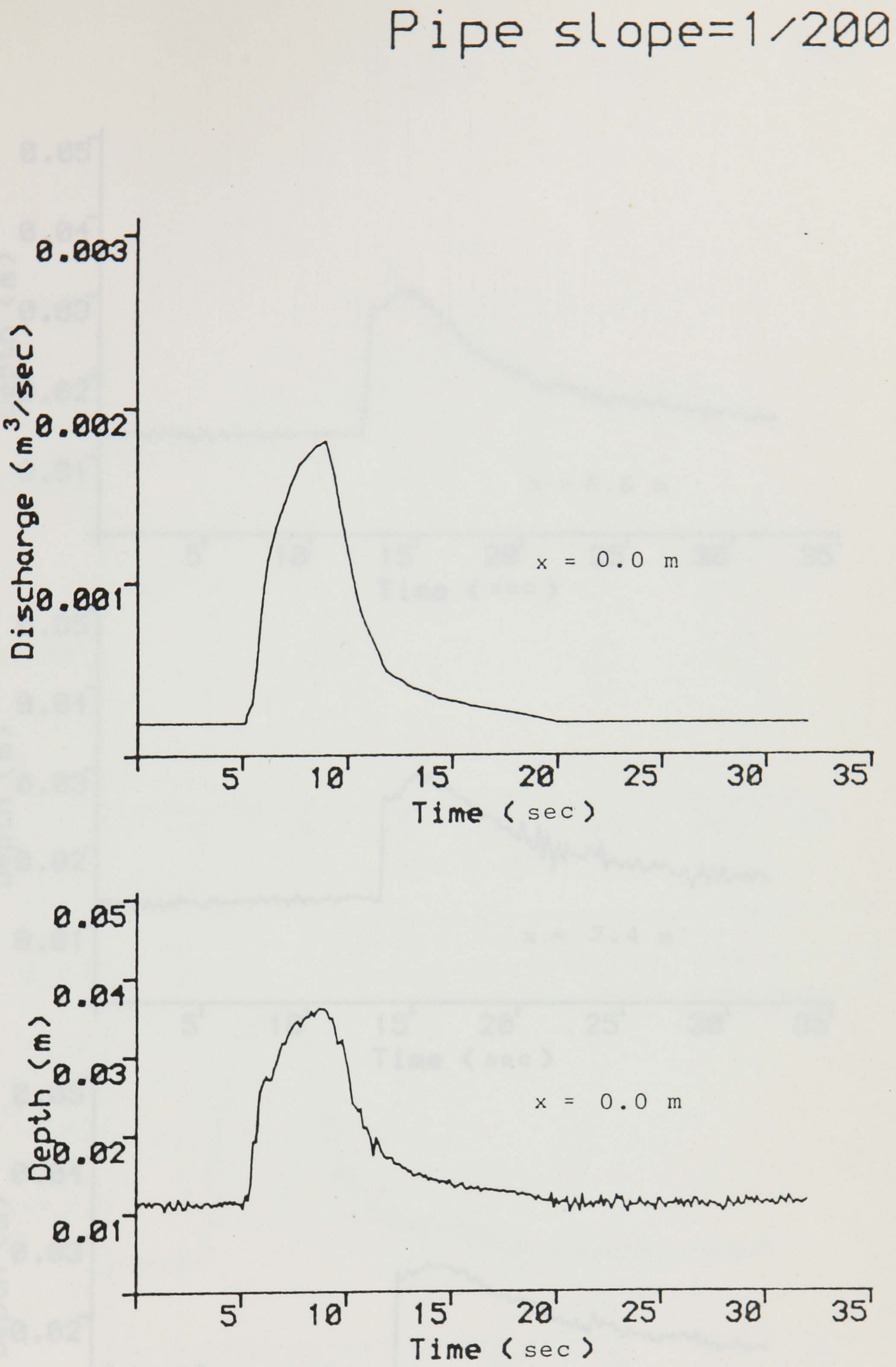

Figure 6.16 (a) Observed discharge hydrograph in the upper graph, depth hydrograph in the lower graph.

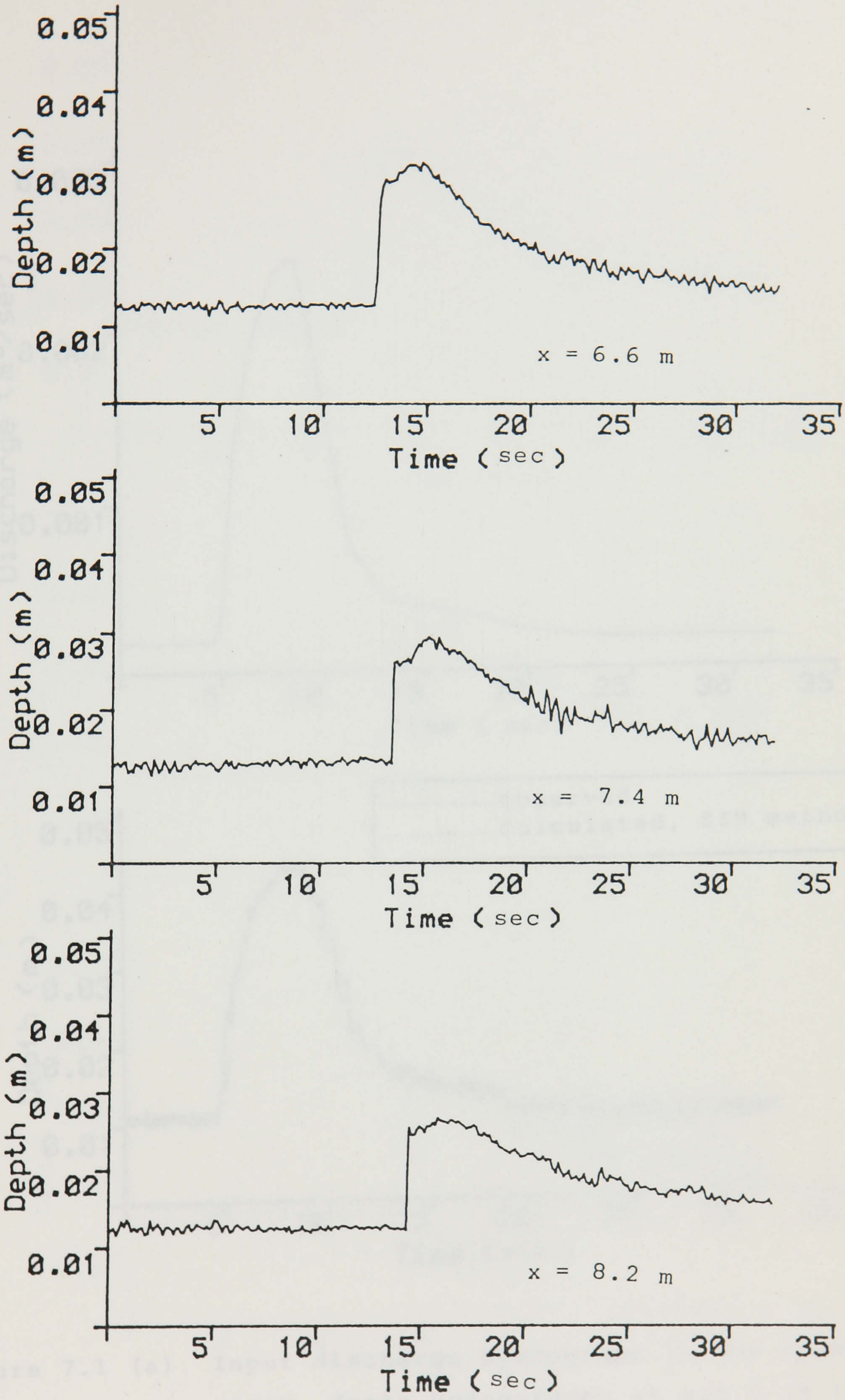

Figure 6.16 (b) Observed depth hydrographs.

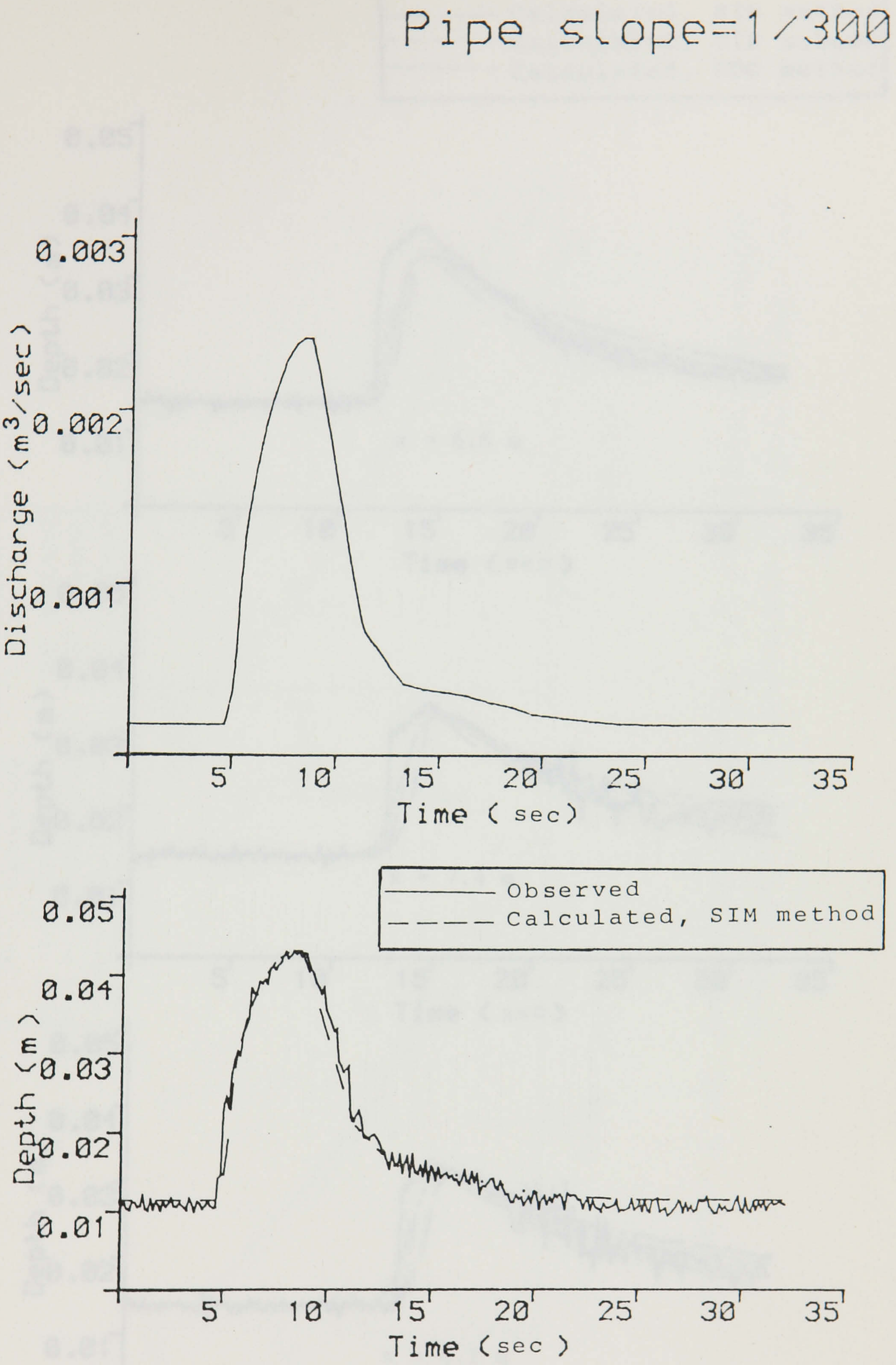

Figure 7.1 (a) Input discharge hydrograph in the upper graph, depth hydrographs at x=0.0 in the lower graph.

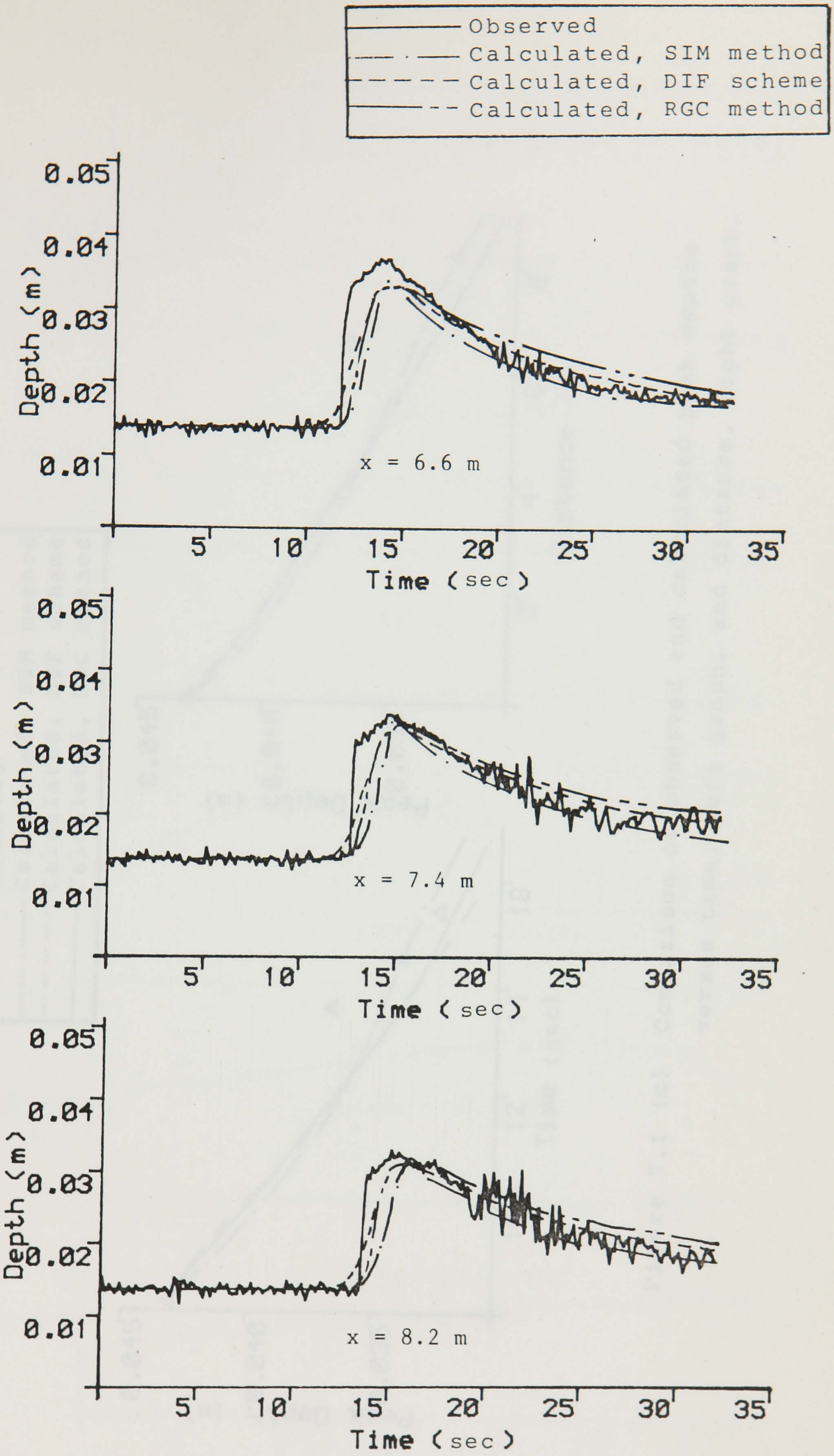

Figure 7.1 (b) Comparison of observed and calculated depth hydrographs.

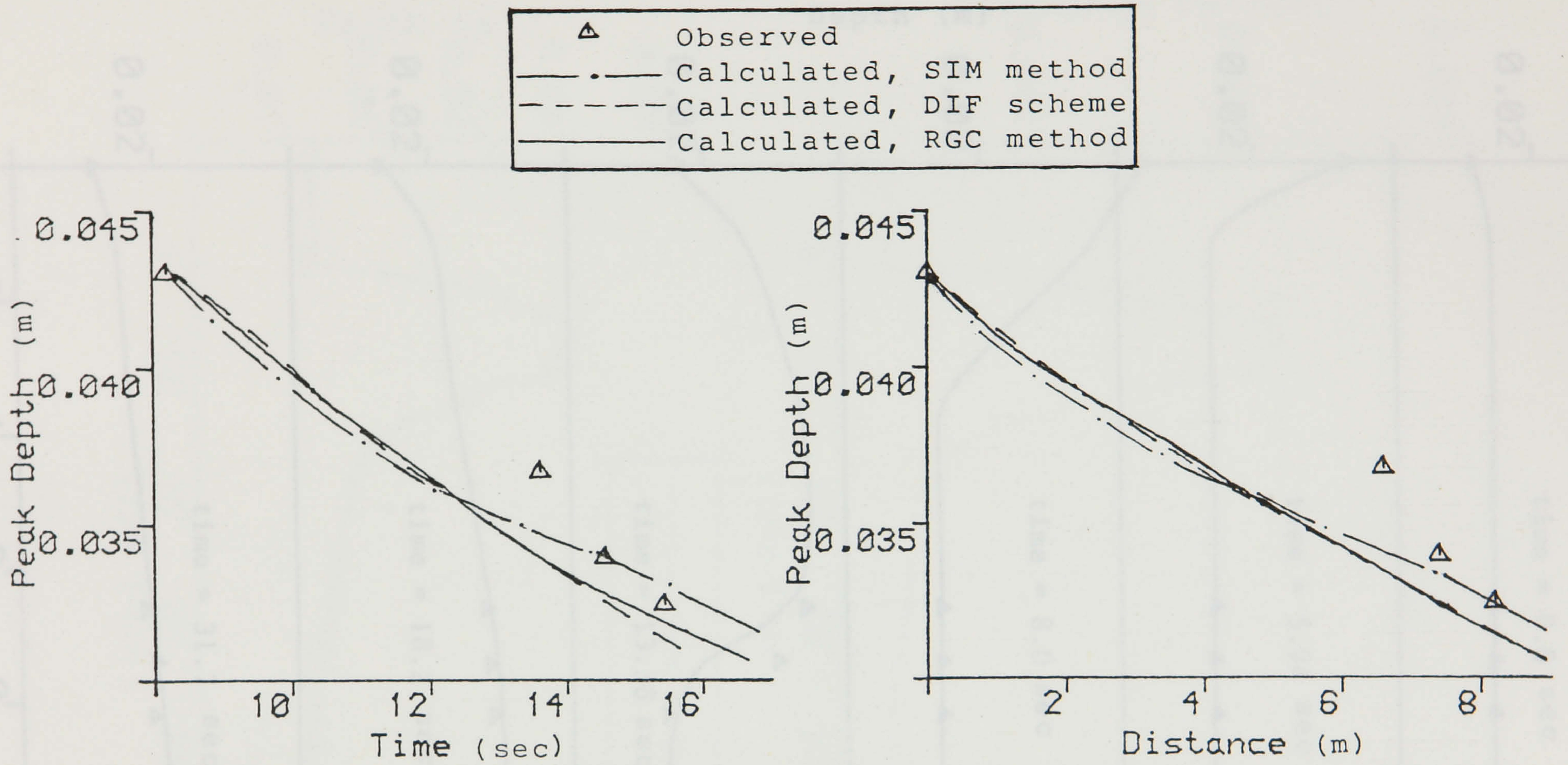

Figure 7.1 (c) Comparison of observed and calculated peak depths versus time, left graph, and distance, right graph.

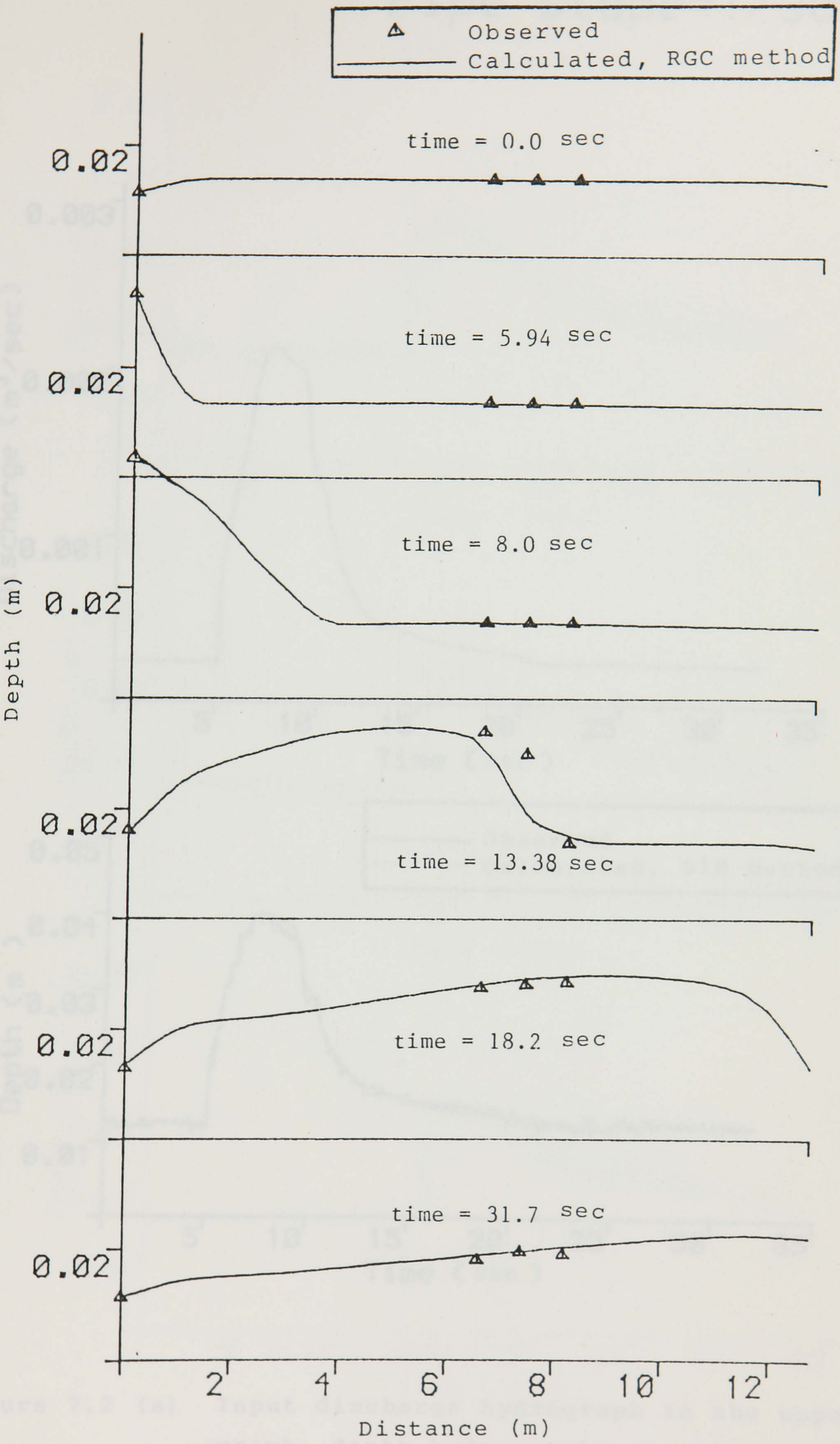

Figure 7.1 (d) Comparison of observed and calculated flow depths along the pipe.

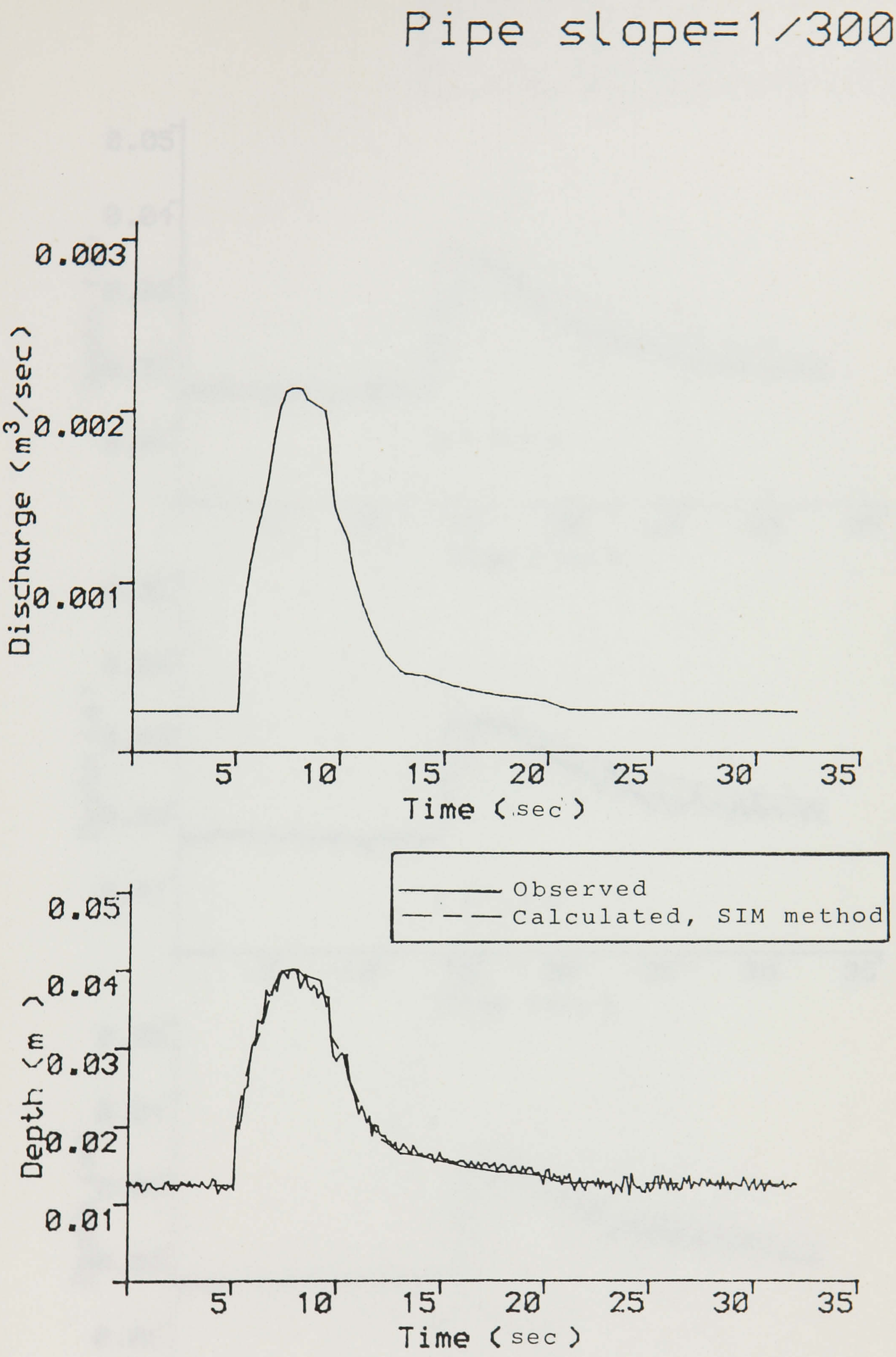

Figure 7.2 (a) Input discharge hydrograph in the upper graph, depth hydrographs at $x=0.0$ in the lower graph.

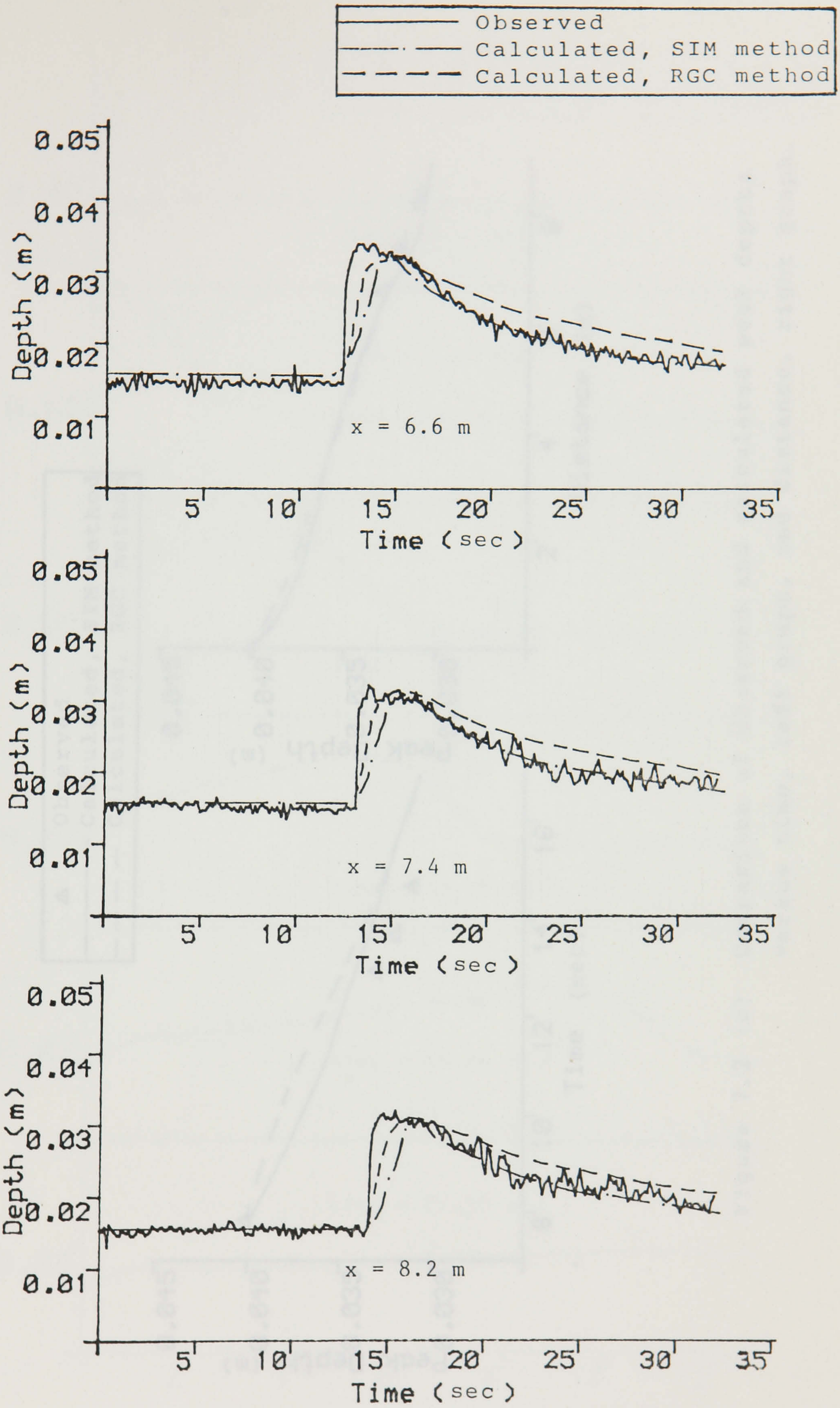

Figure 7.2 (b) Comparison of observed and calculated depth hydrographs.

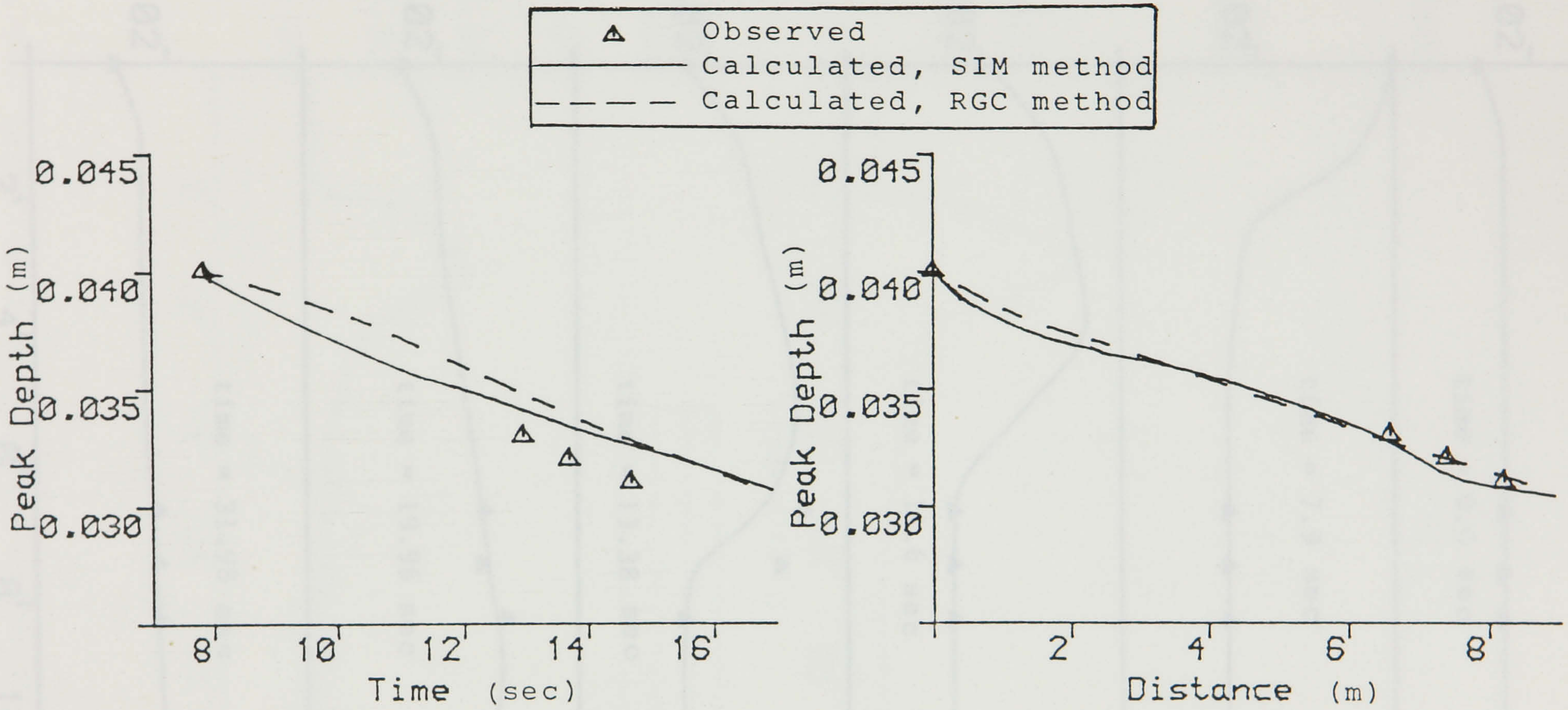

Figure 7.2 (c) Comparison of observed and calculated peak depths versus time, left graph, and distance, right graph.

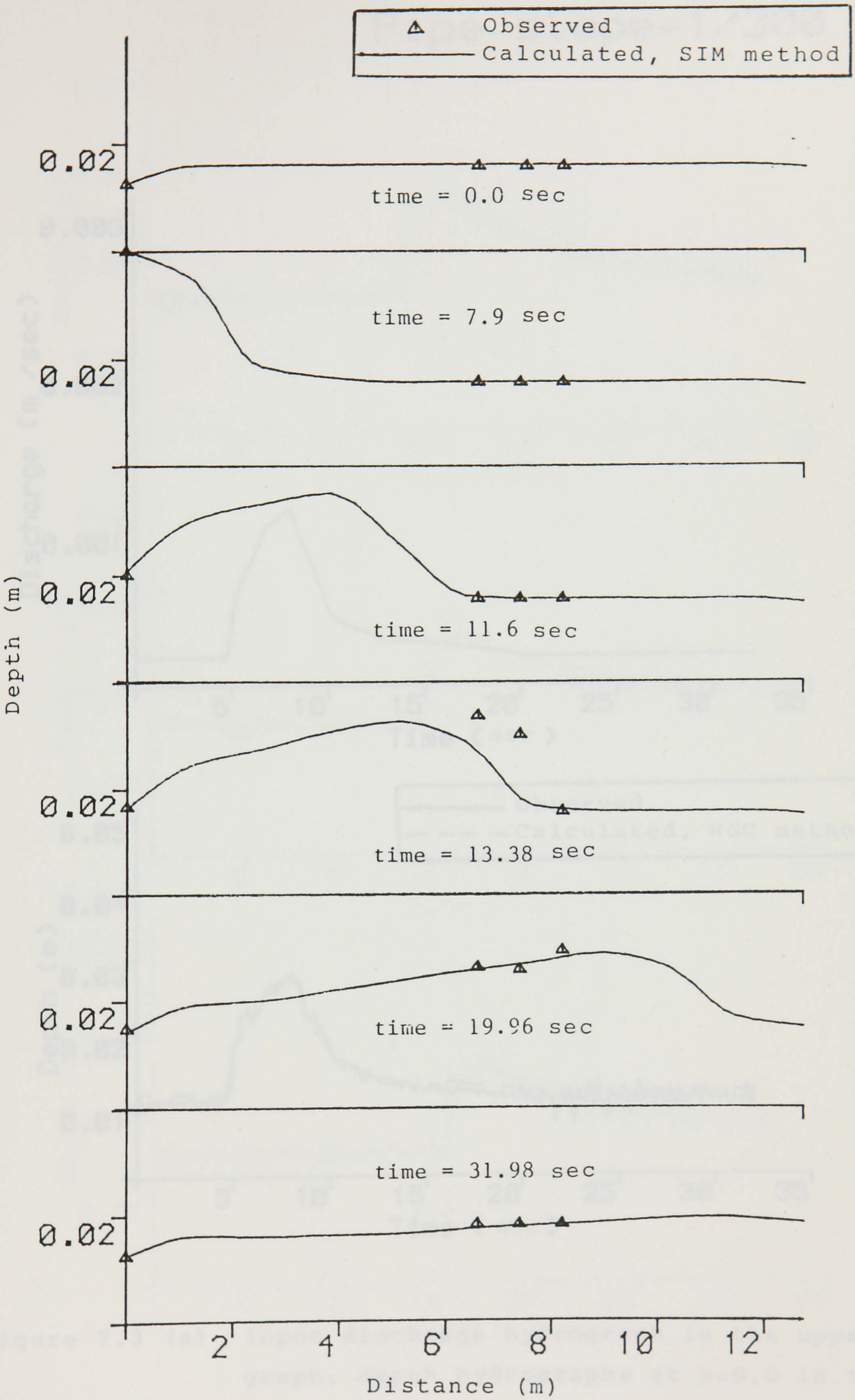

Figure 7.2 (d) Comparison of observed and calculated flow depths along the pipe.

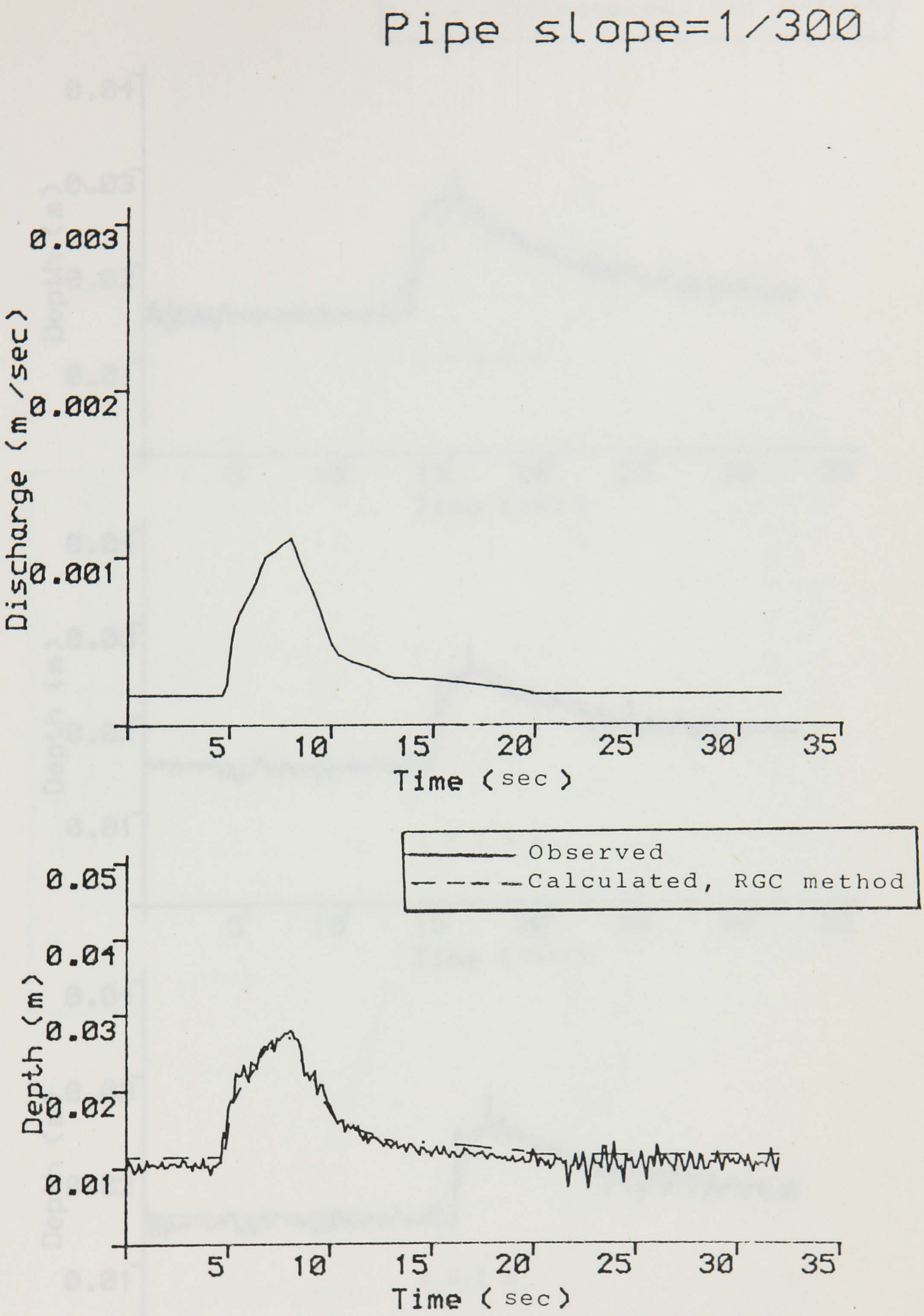

Figure 7.3 (a) Input discharge hydrograph in the upper graph, depth hydrographs at x=0.0 in the lower graph.

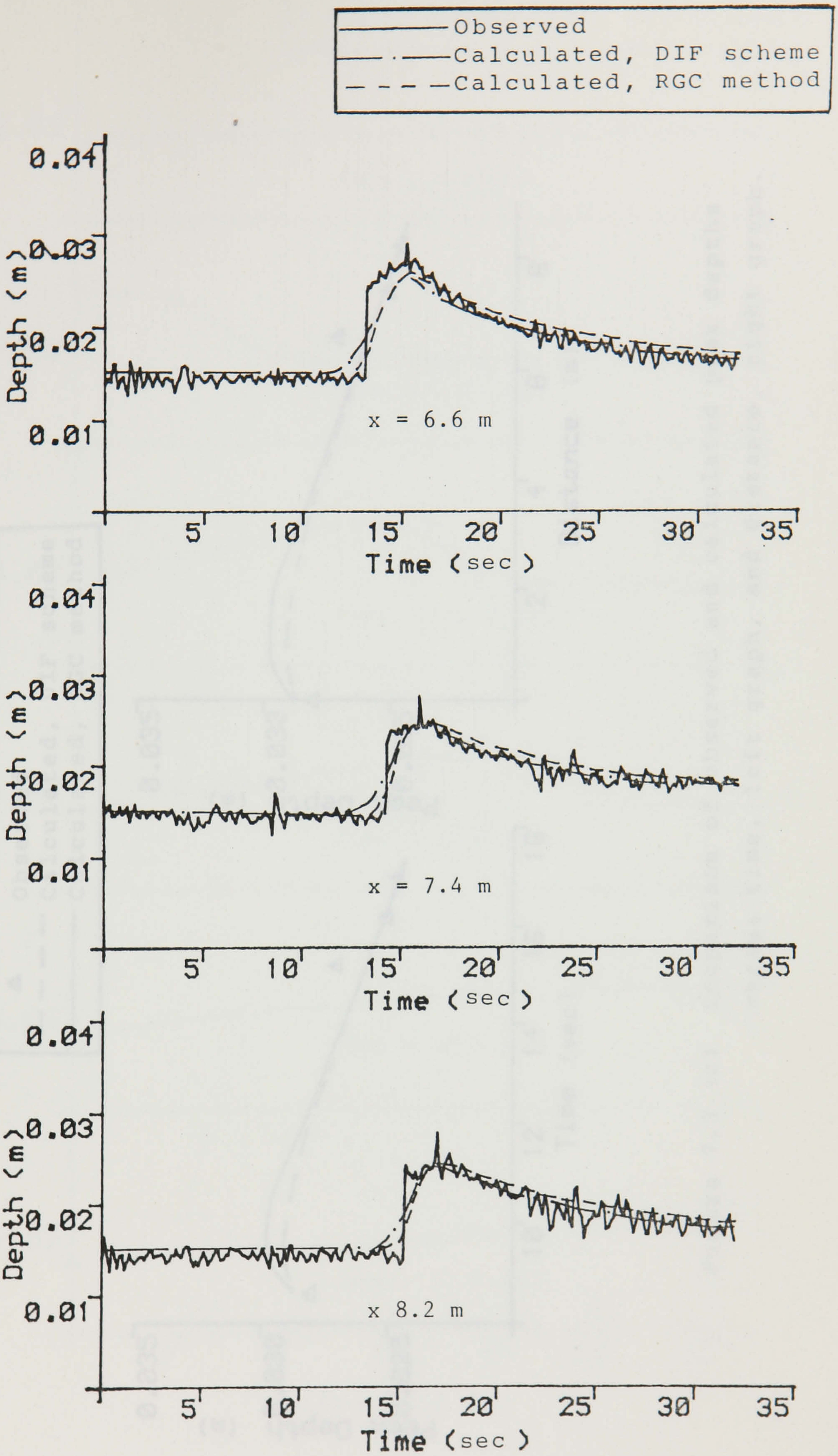

Figure 7.3 (b) Comparison of observed and calculated depth hydrographs.

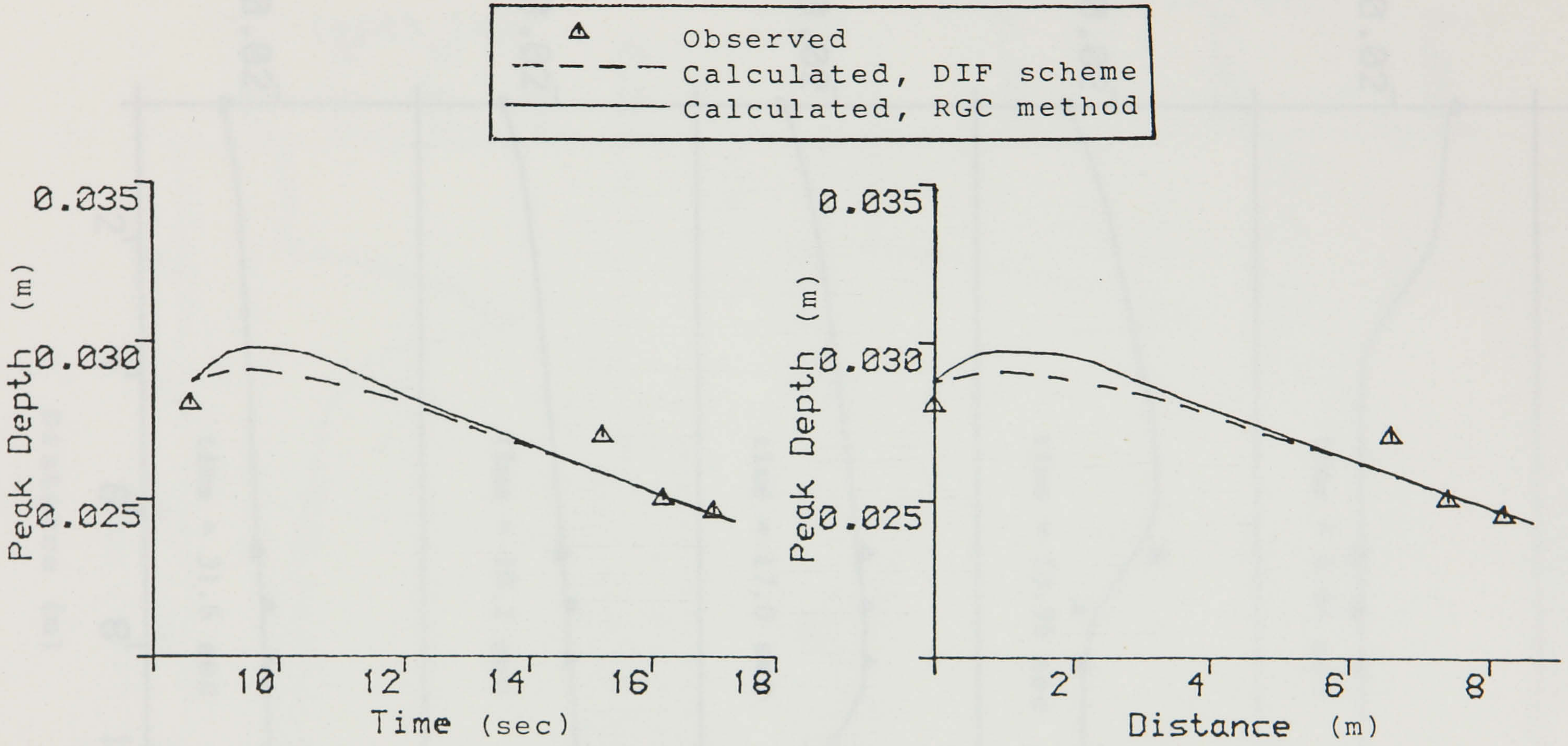

Figure 7.3 (c) Comparison of observed and calculated peak depths versus time, left graph, and distance, right graph.

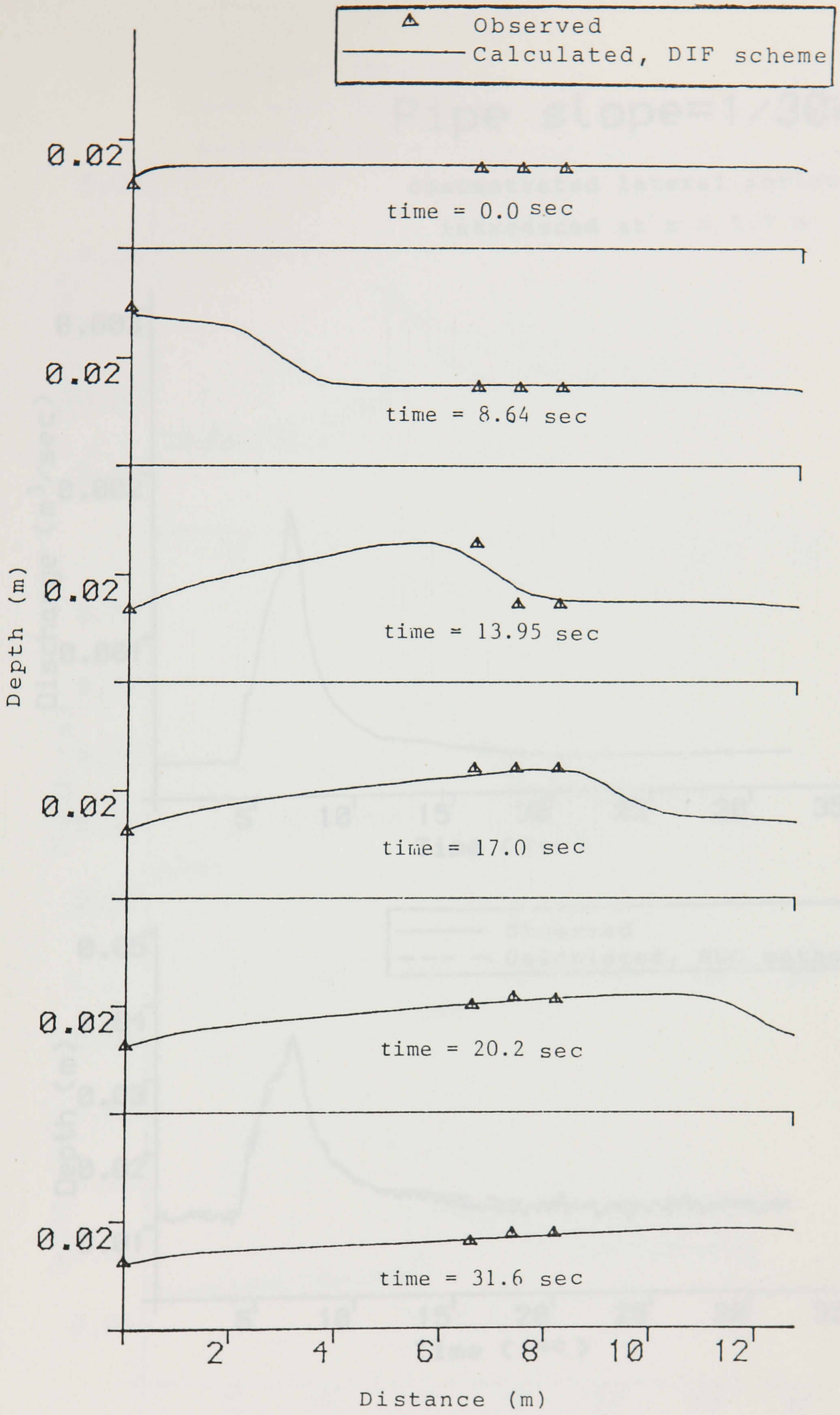

Figure 7.3 (d) Comparison of observed and calculated flow depths along the pipe.

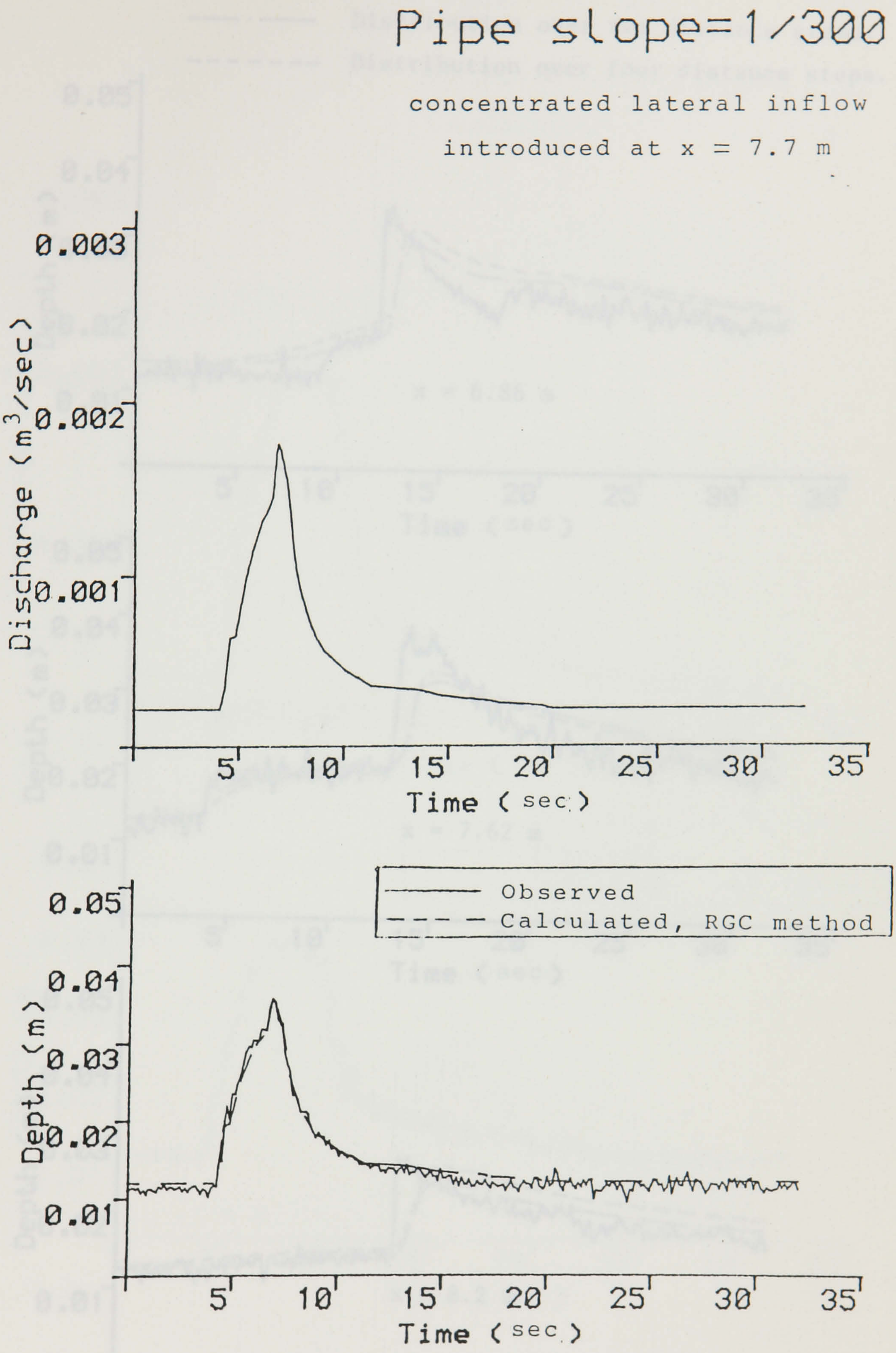

Figure 7.4 (a) Input discharge hydrograph in the upper graph, depth hydrographs at x = 0.0 in the lower graph.

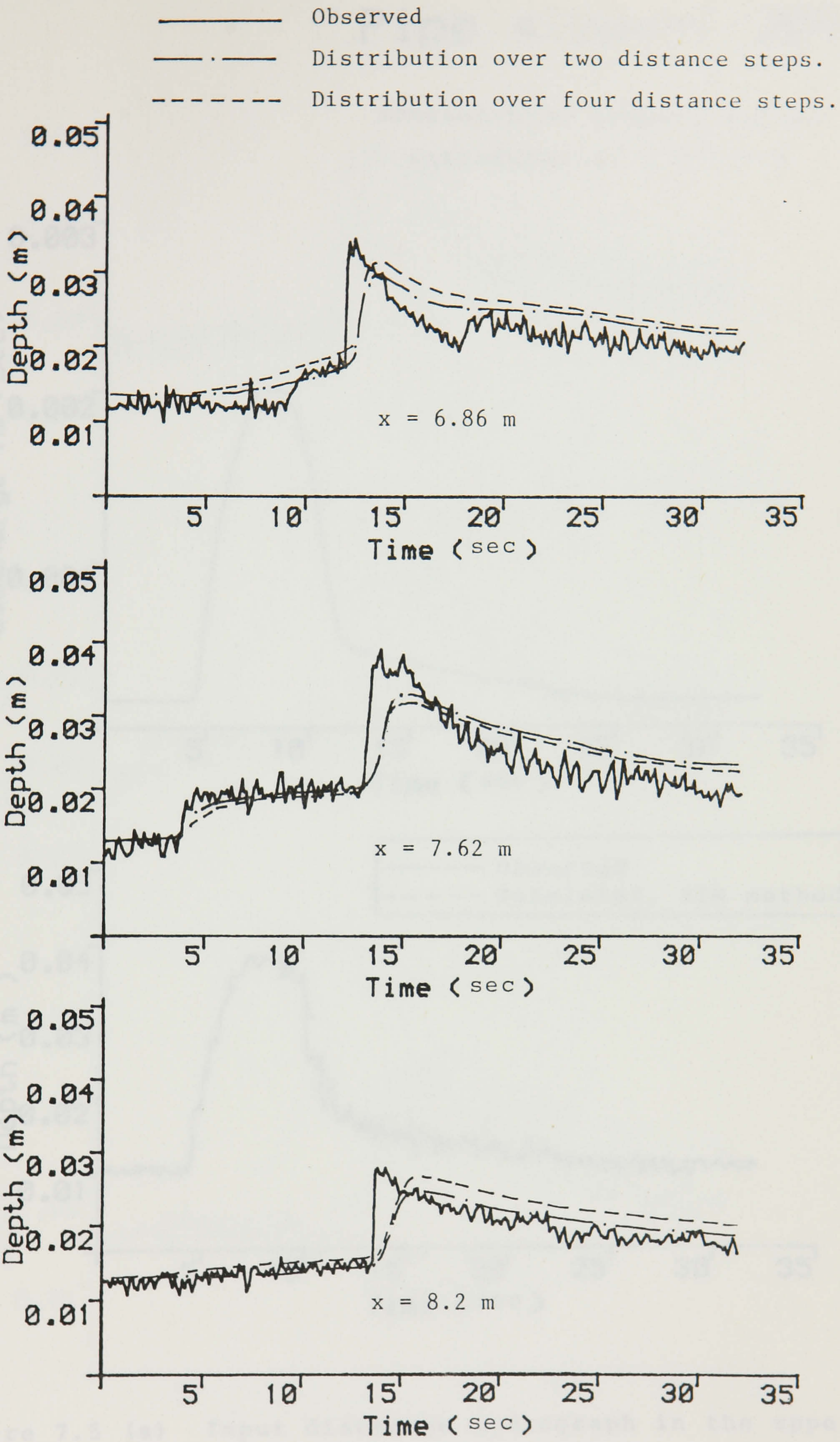

Figure 7.4 (b) Effect of different lateral inflow distributions on the predicted depth hydrographs by the RGC method.

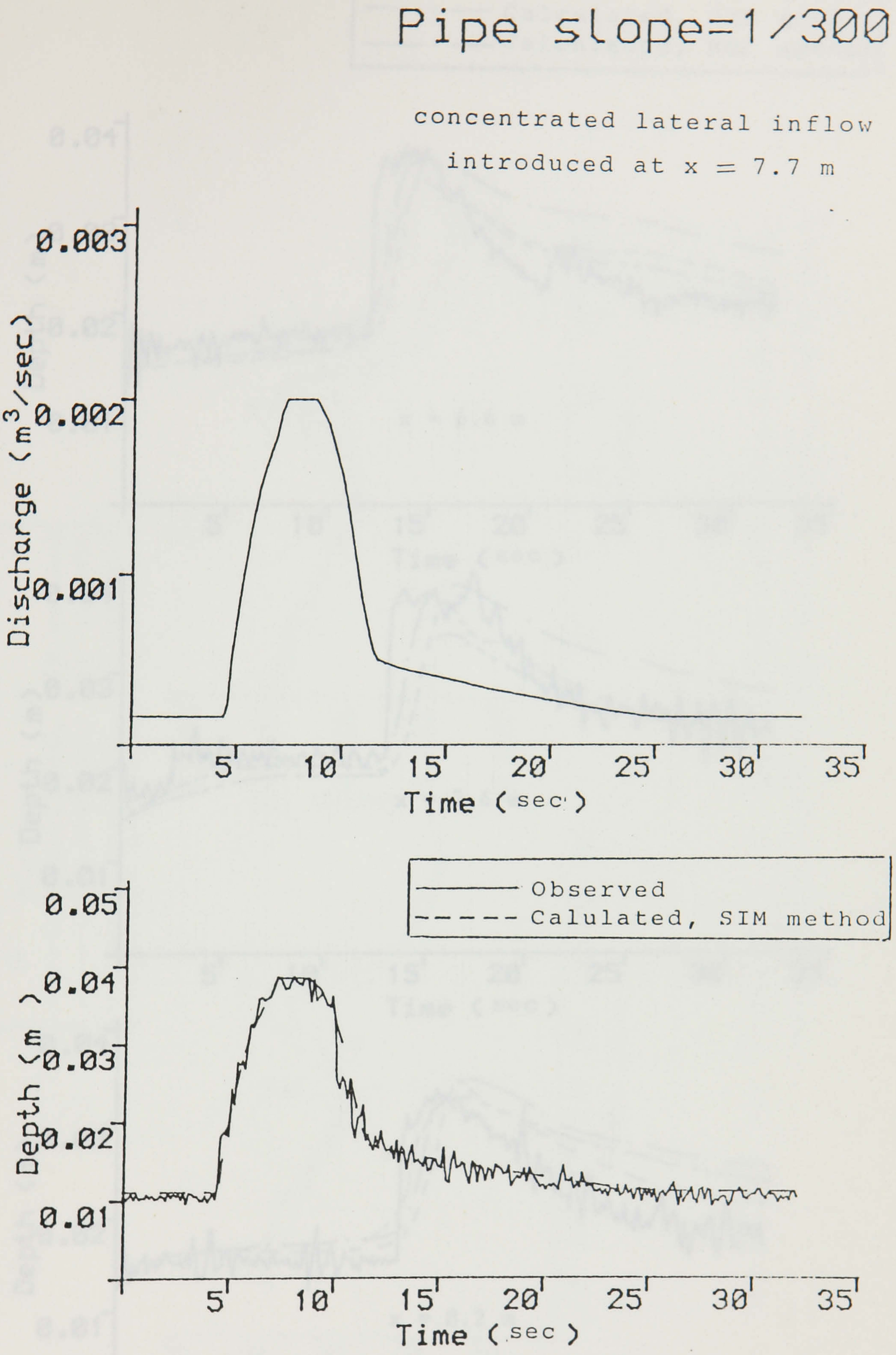

Figure 7.5 (a) Input discharge hydrograph in the upper graph, depth hydrographs at x = 0.0 in the lower graph.

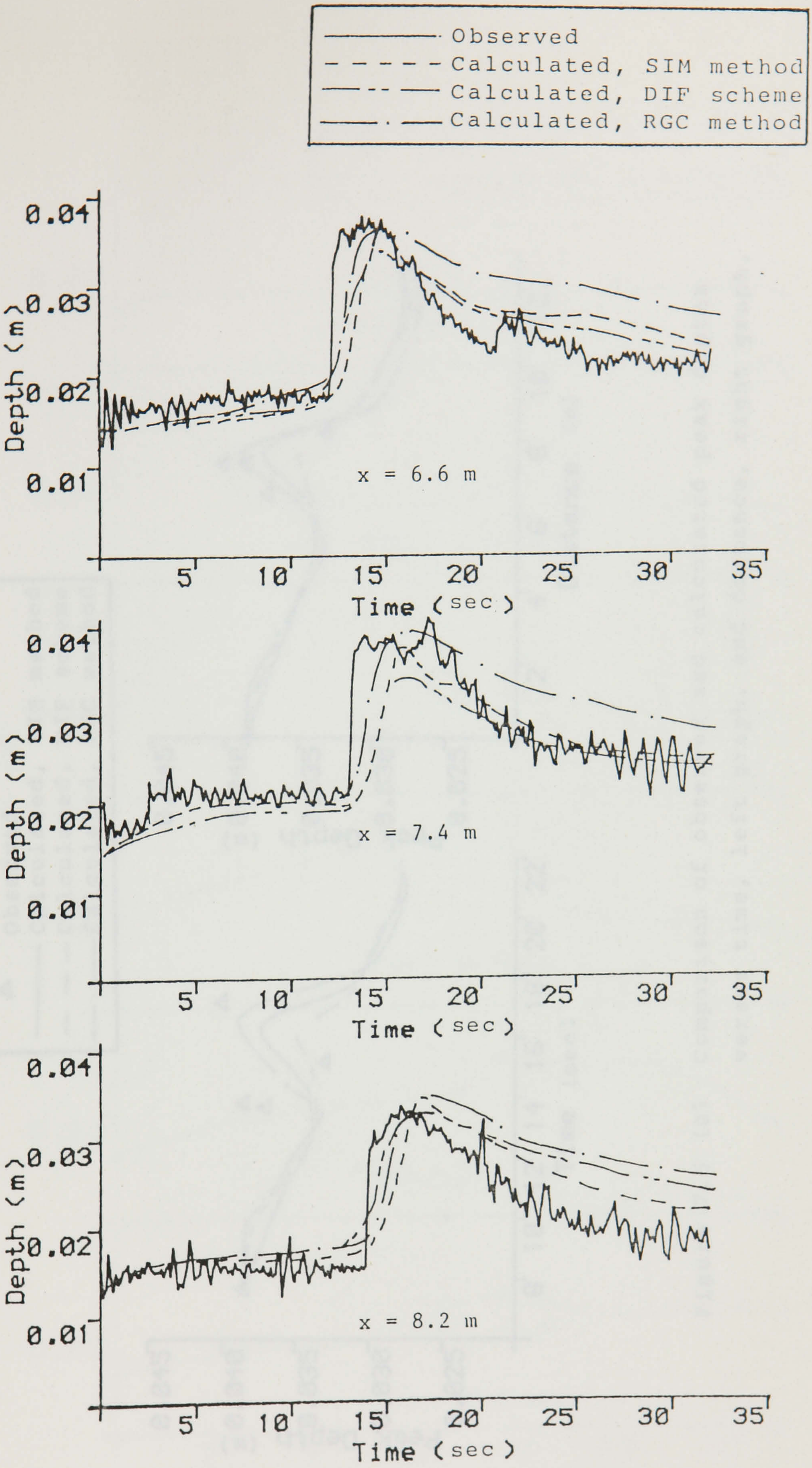

Figure 7.5 (b) Comparison of observed and calculated depth hydrographs.

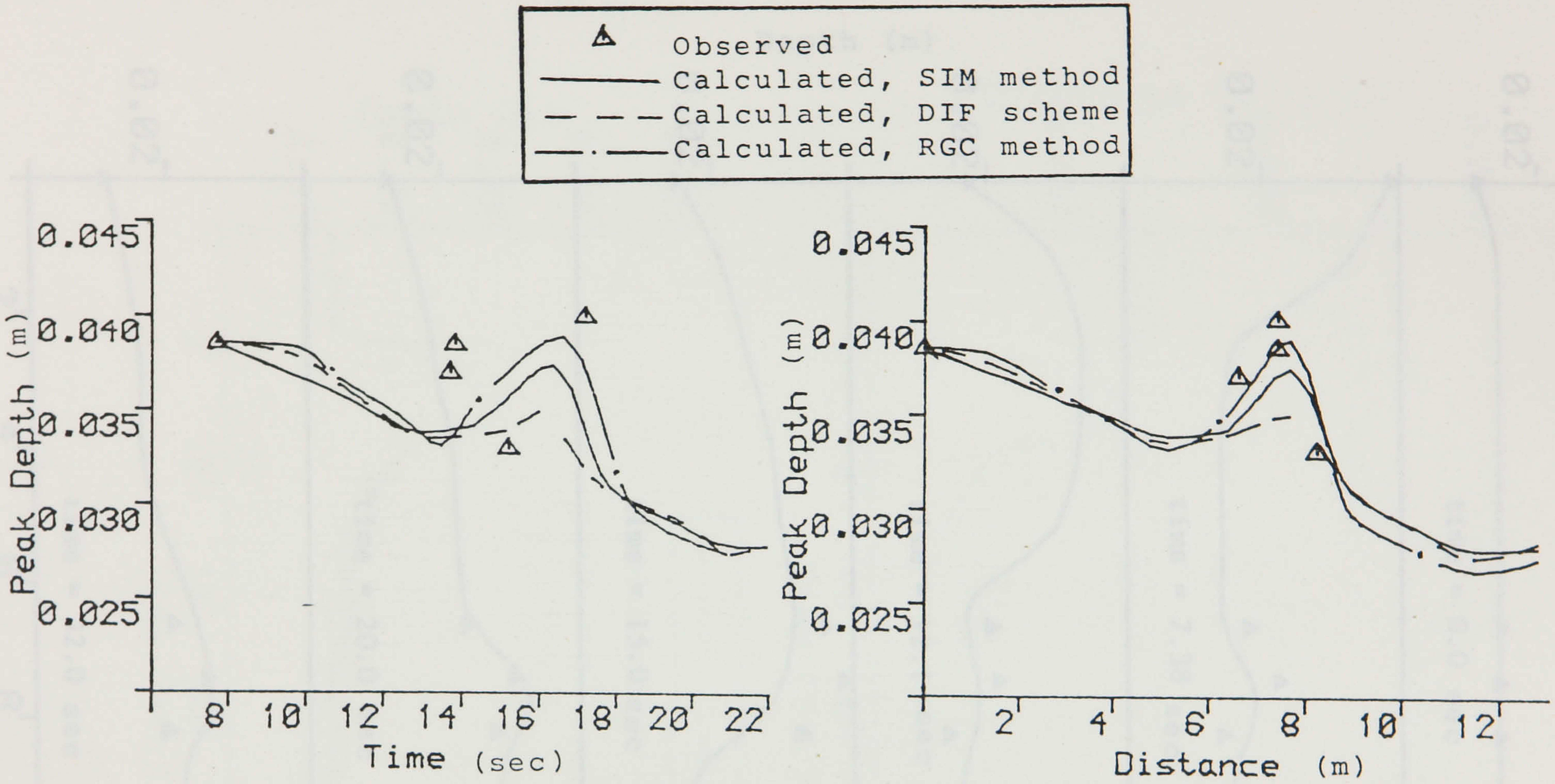

Figure 7.5 (c) Comparison of observed and calculated peak depths versus time, left graph, and distance, right graph.

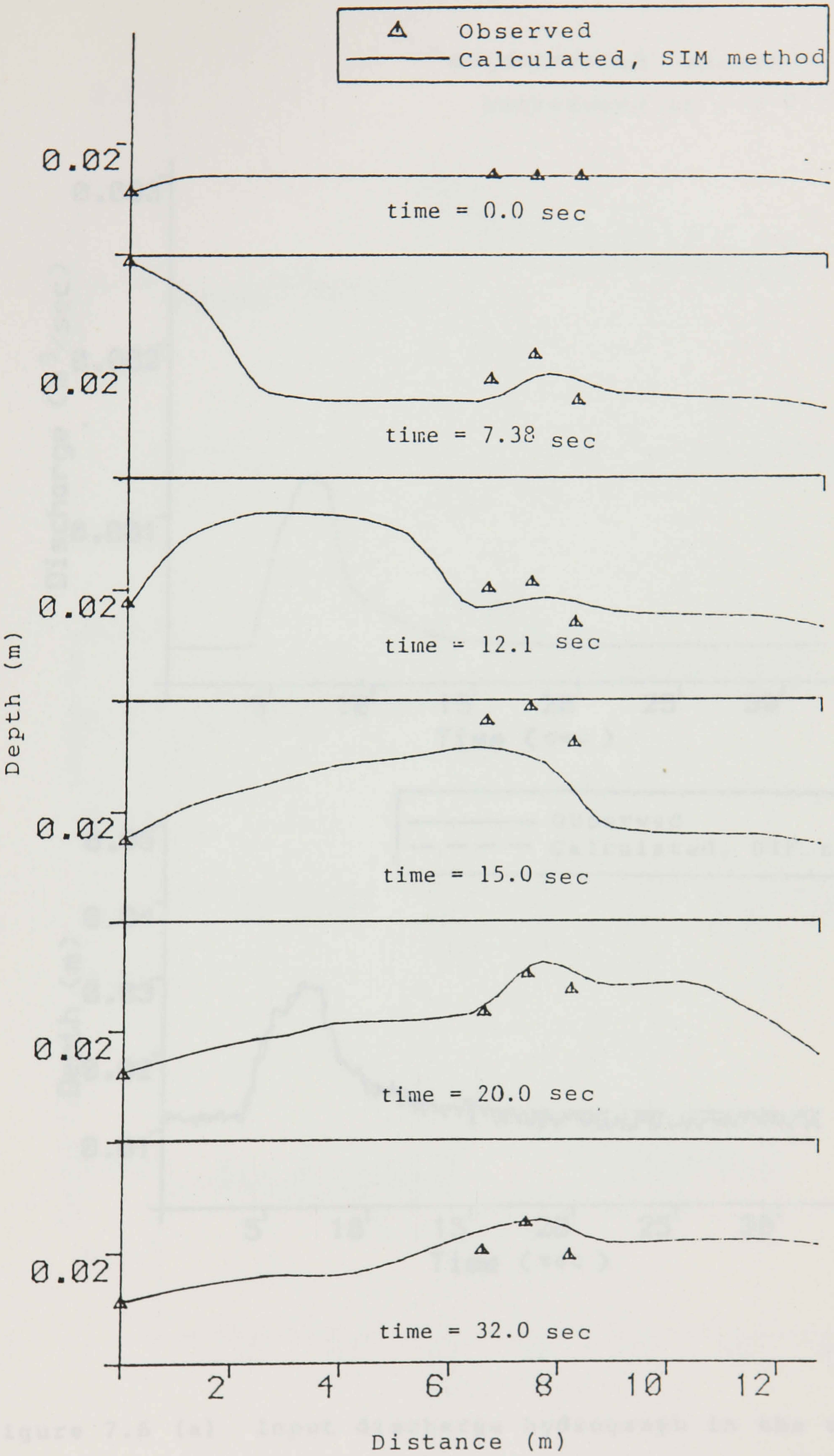

Figure 7.5 (d) Comparison of observed and calculated flow depths along the pipe.

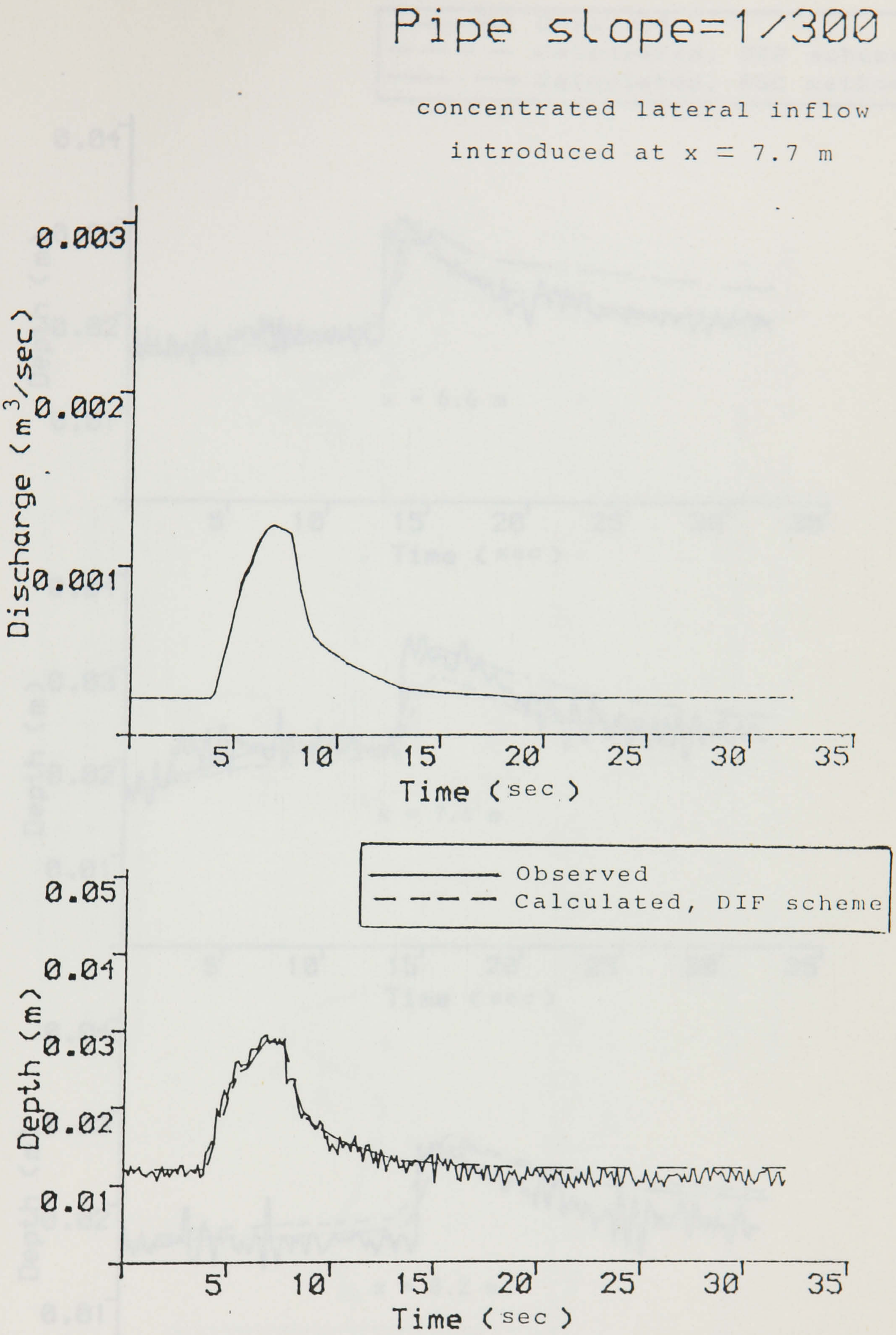

Figure 7.6 (a) Input discharge hydrograph in the upper graph, depth hydrographs at x = 0.0 in the lower graph.

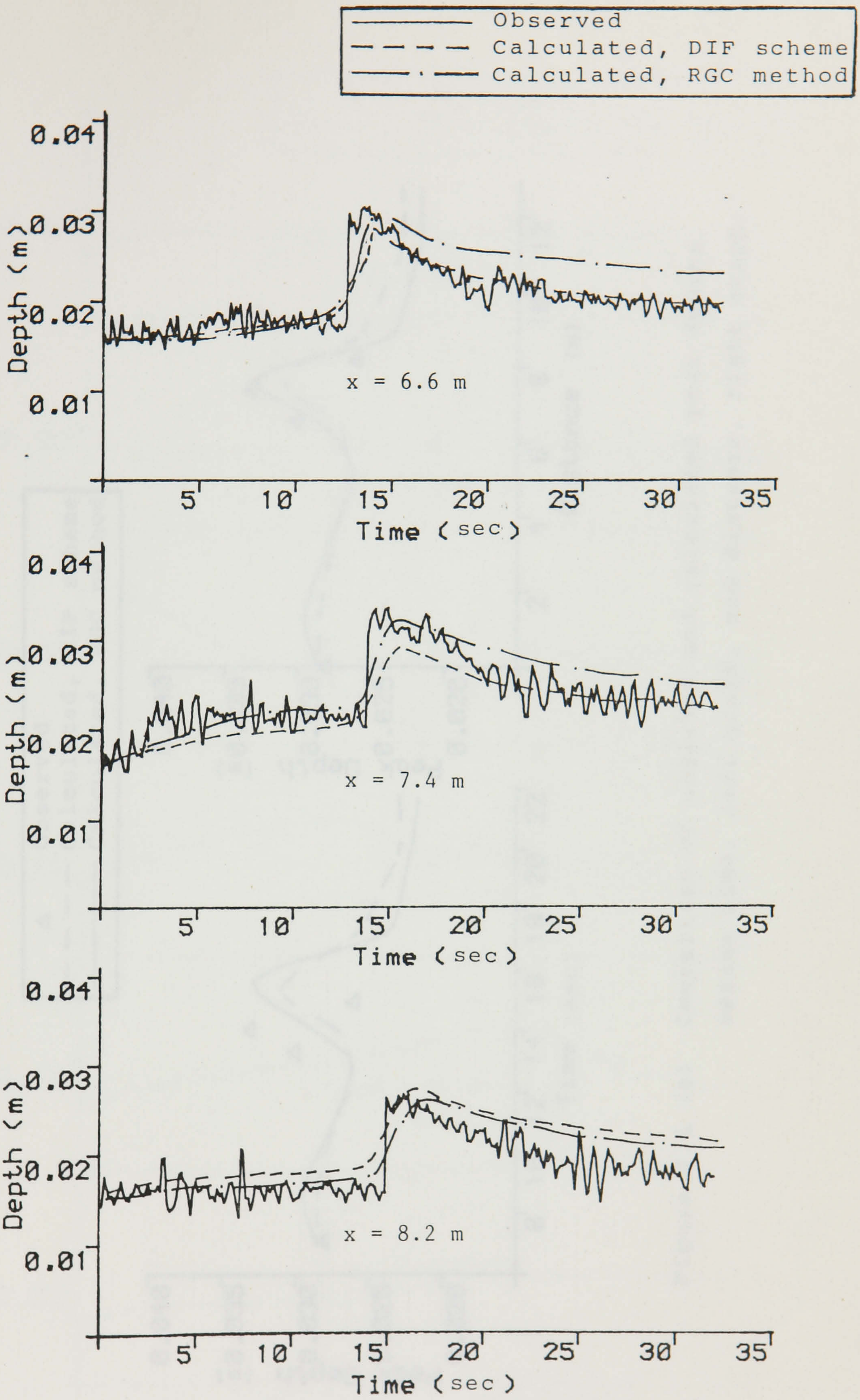

Figure 7.6 (b) Comparison of observed and calculated depth hydrographs.

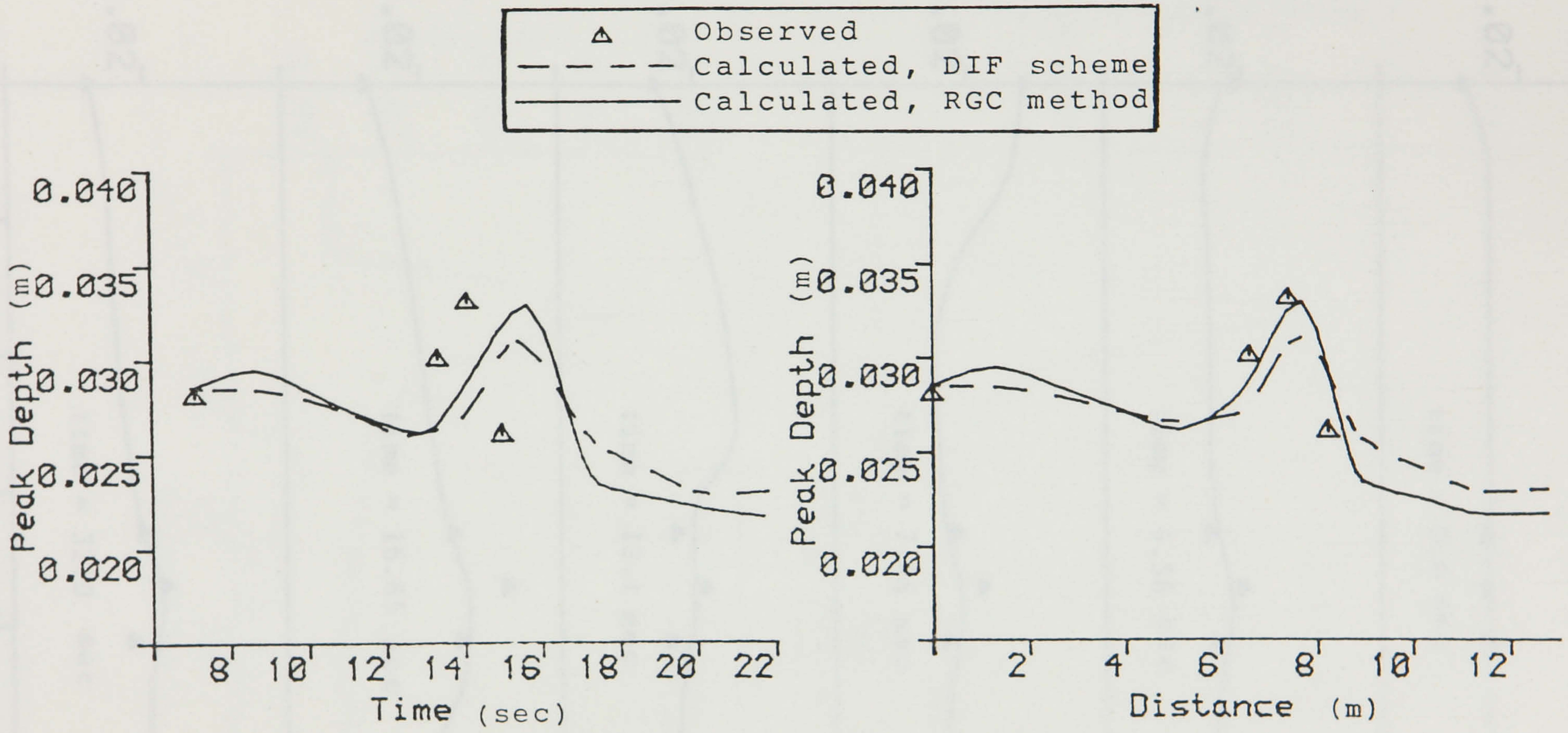

Figure 7.6 (c) Comparison of observed and calculated peak depths versus time, left graph, and distance, right graph.

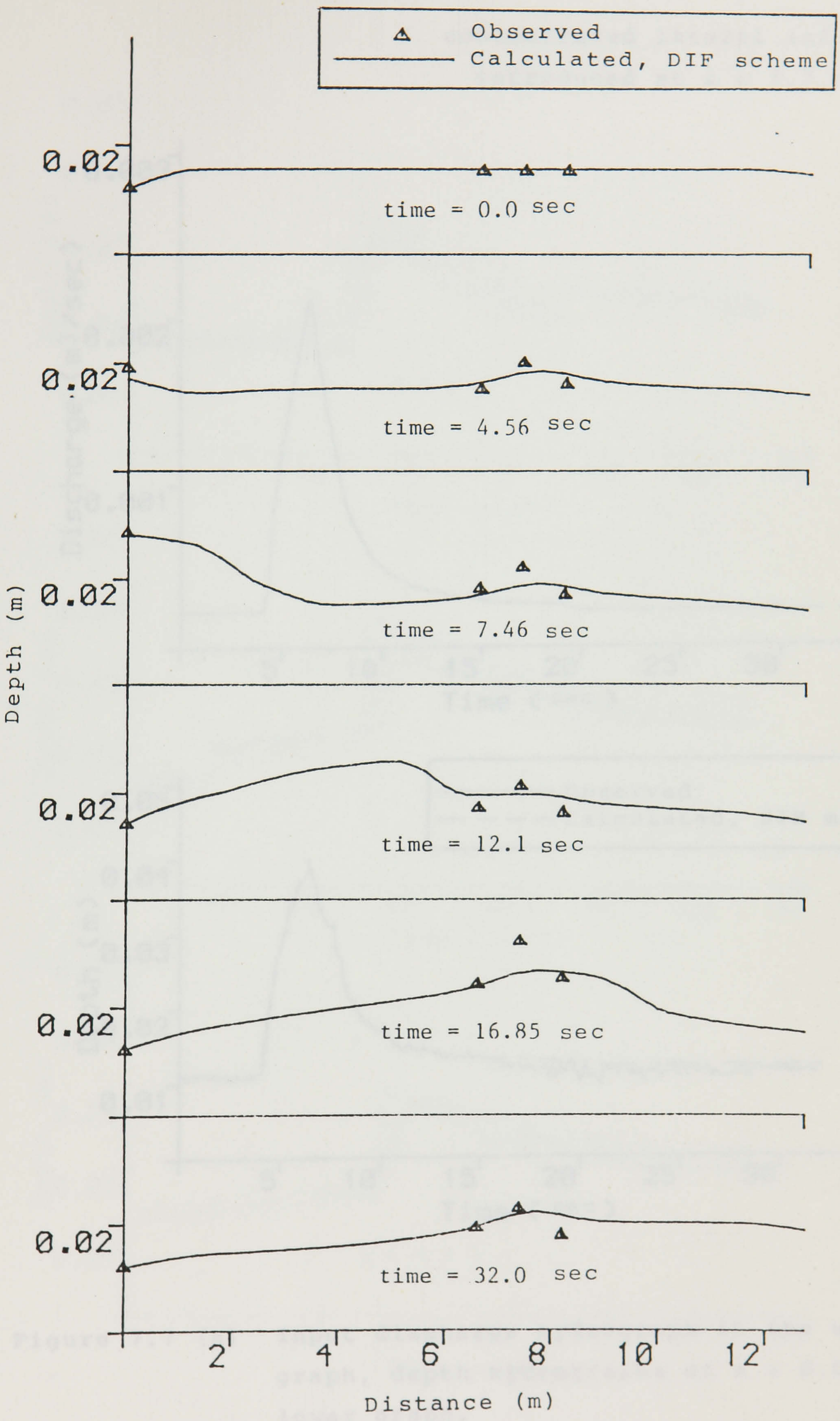

Figure 7.6 (d) Comparison of observed and calculated flow depths along the pipe.

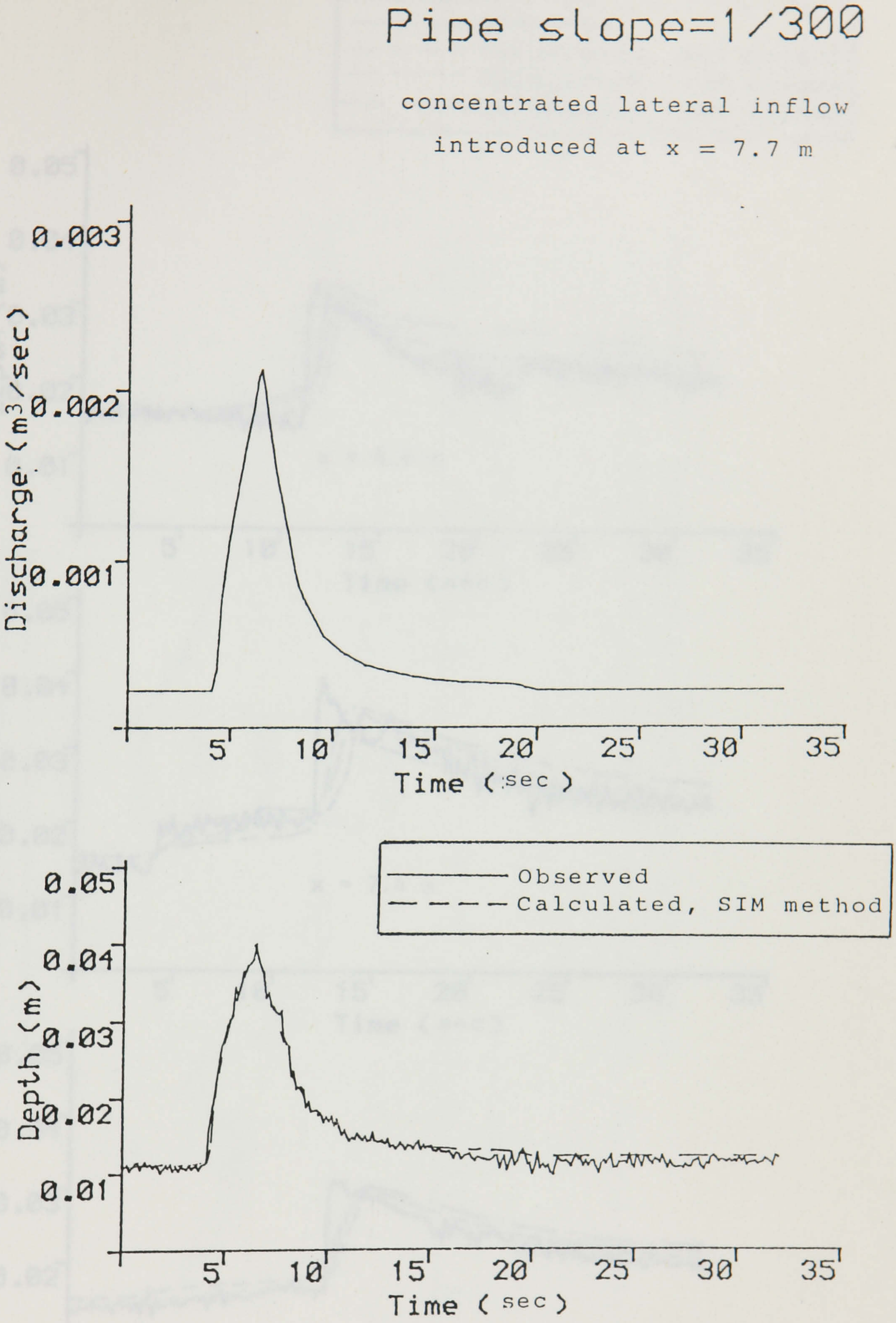

concentrated lateral inflow introduced at x = 7.7 m

Figure 7.7 (a) Input discharge hydrograph in the upper graph, depth hydrographs at x = 0.0 in lower graph.

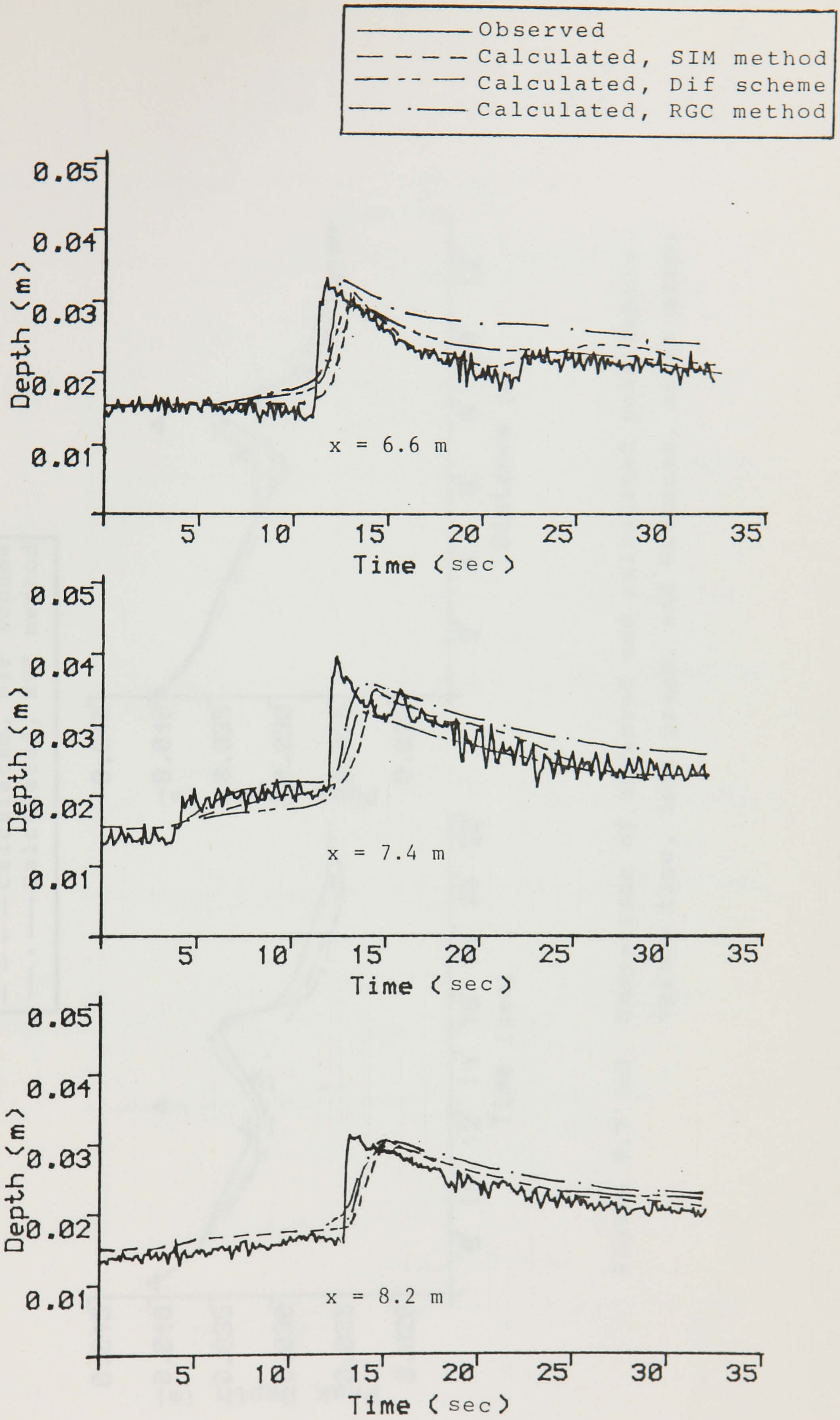

Figure 7.7 (b) Comparison of observed and calculated depth hydrographs.

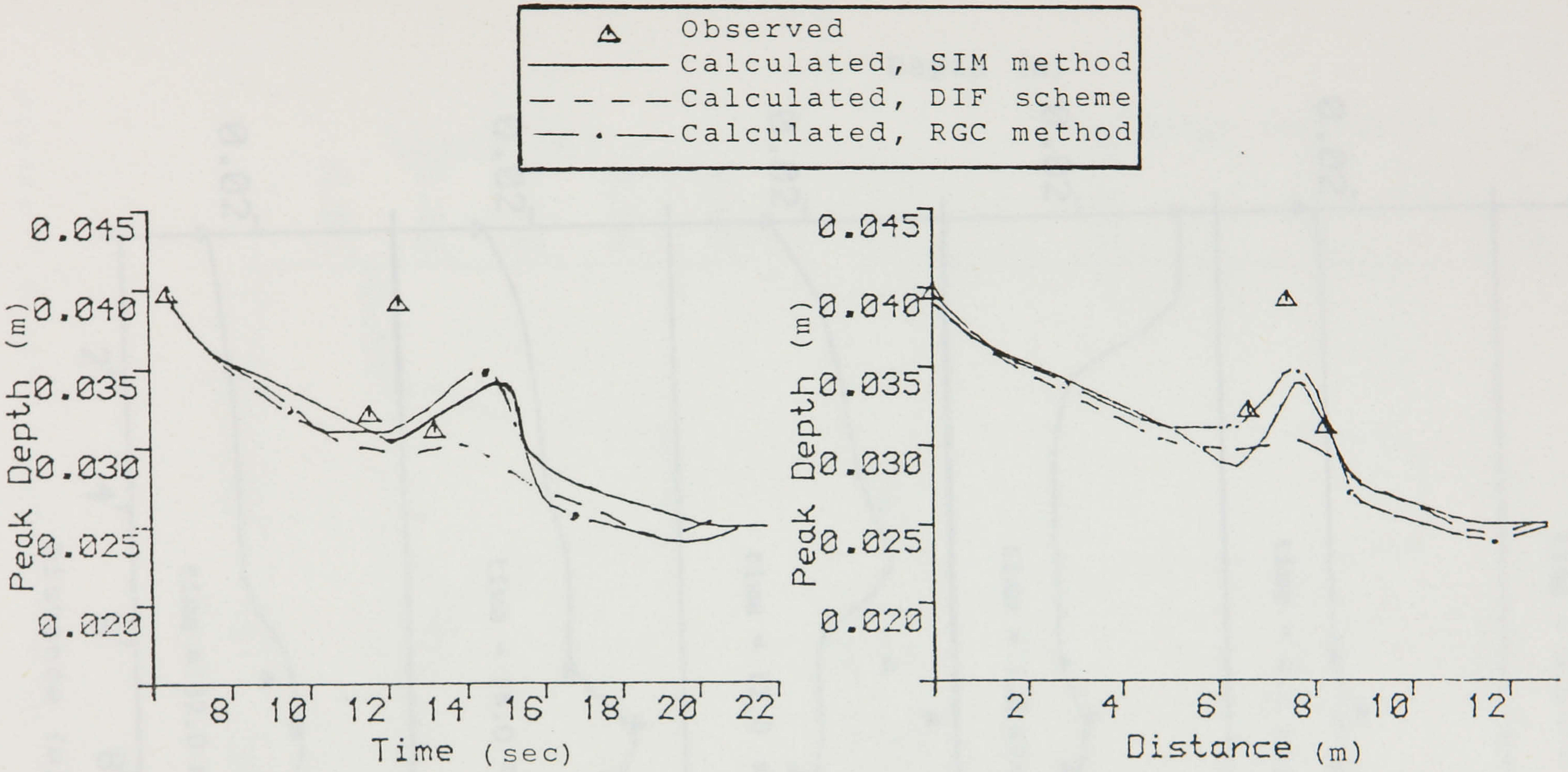

Figure 7.7 (c) Comparison of observed and calculated peak depths versus time, left graph, and distance, right graph.

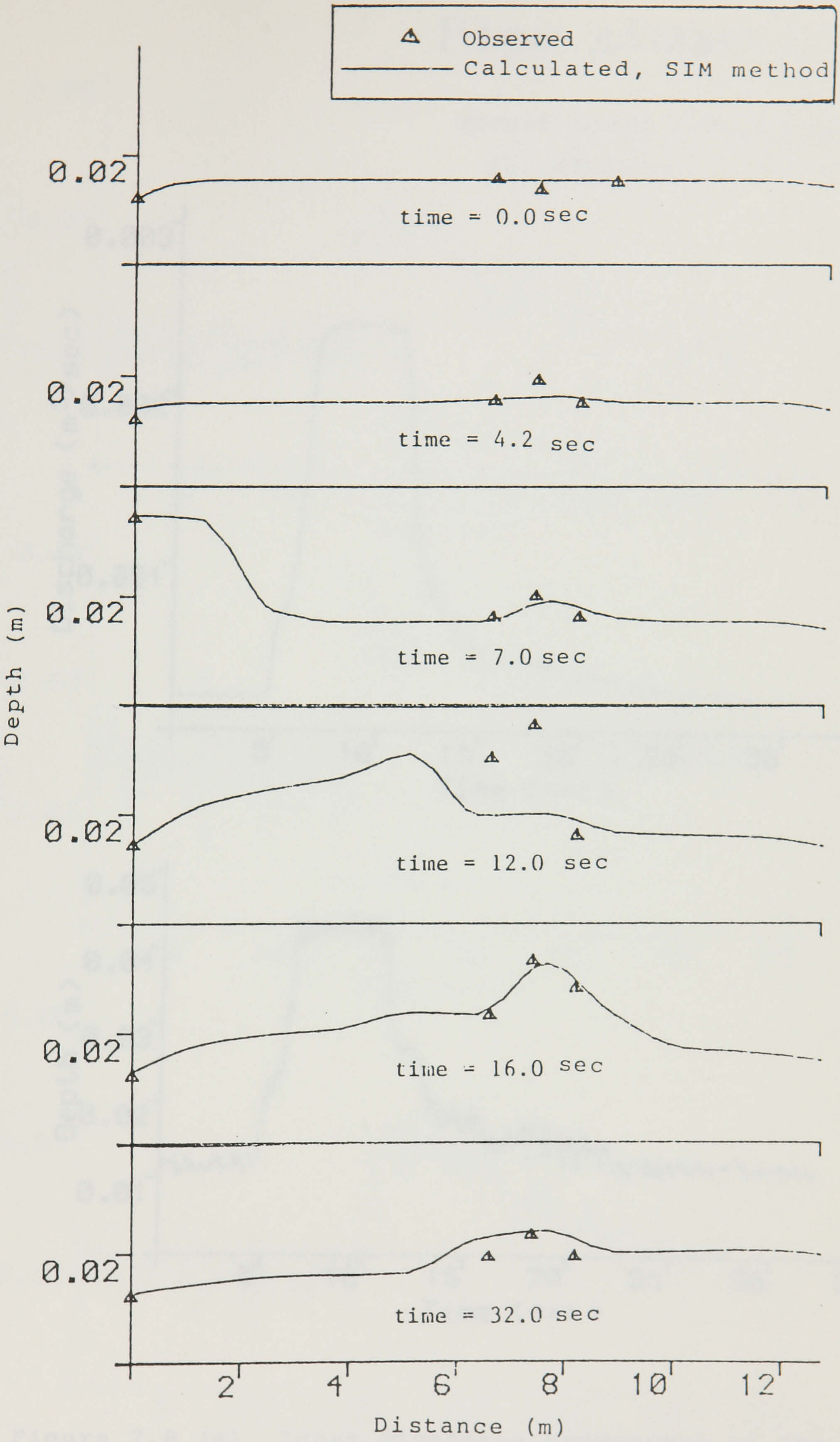

Figure 7.7 (d) Comparison of observed and calculated flow depths along the pipe.

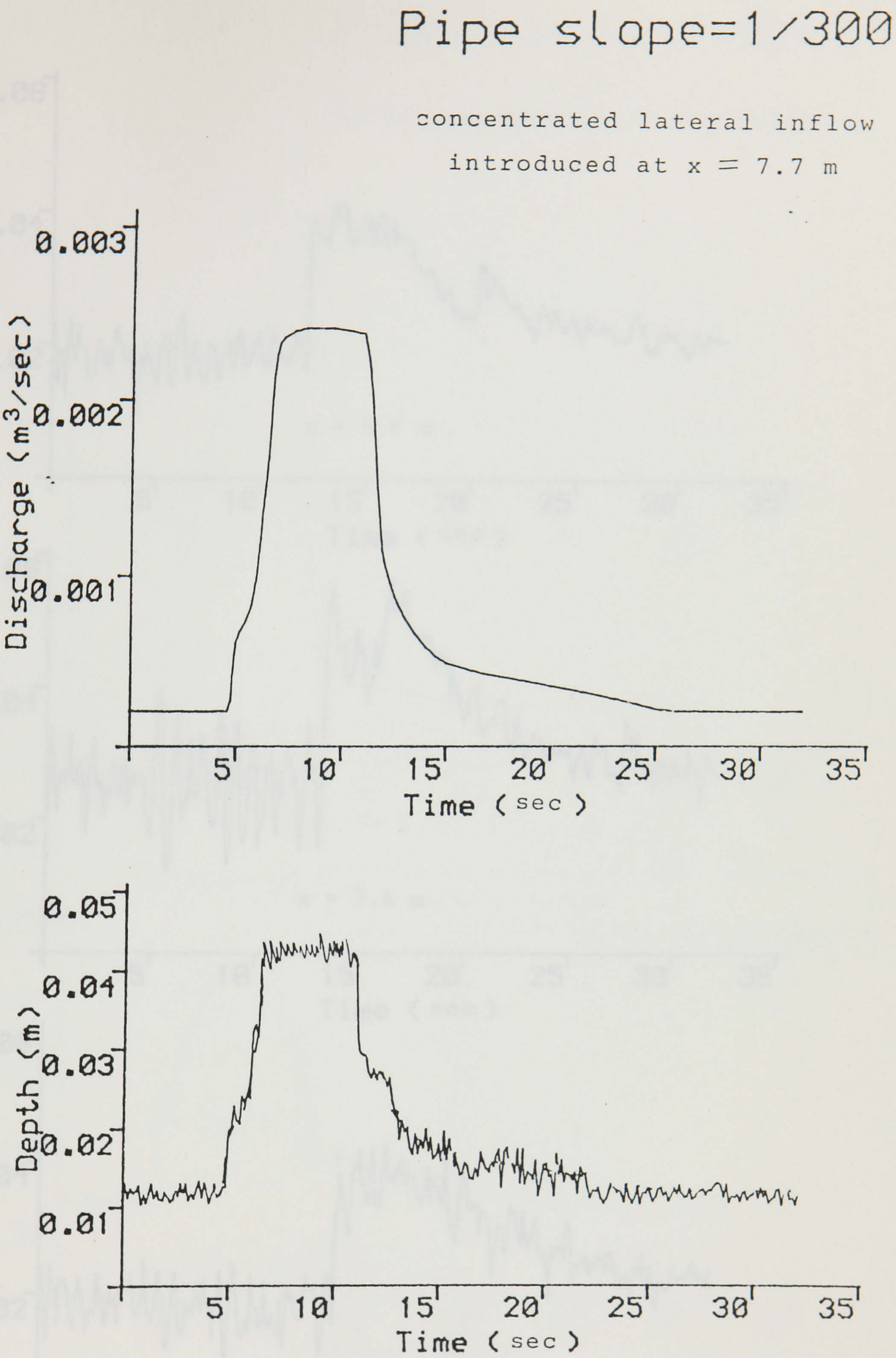

Figure 7.8 (a) Input discharge hydrograph in the upper graph, depth hydrograph at x = 0.0 in the lower graph.

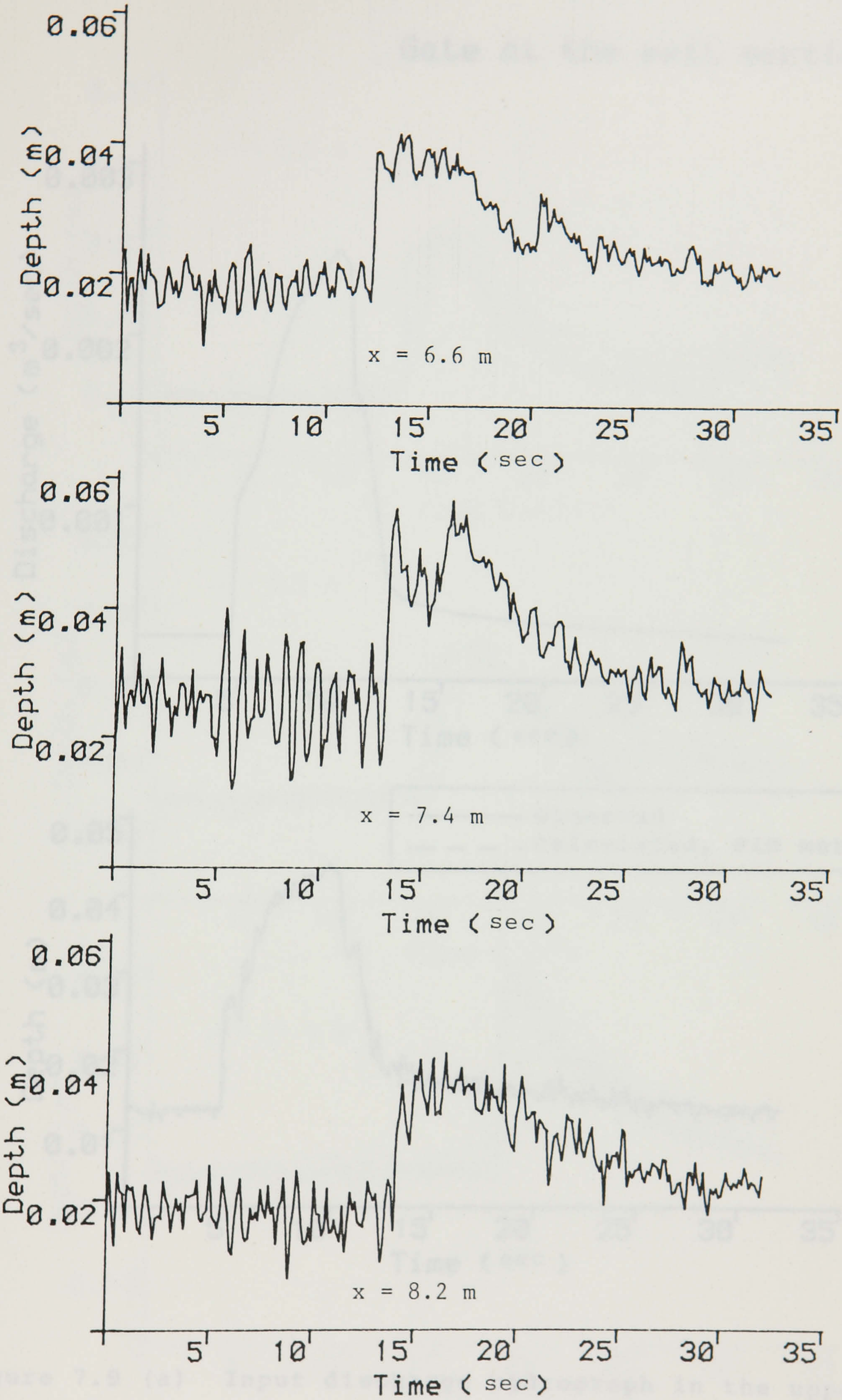

Figure 7.8 (b) Observed depth hydrographs.

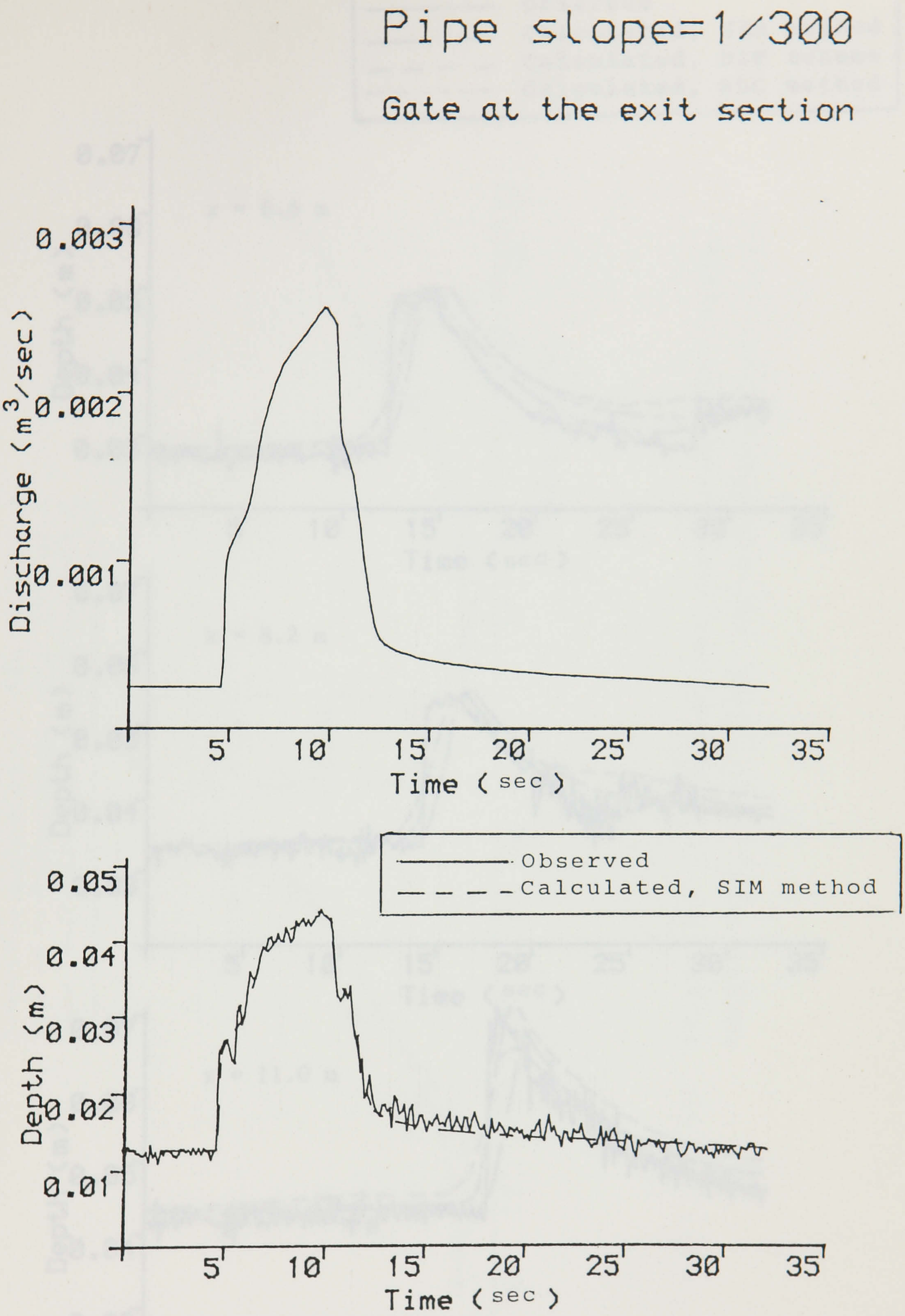

Figure 7.9 (a) Input discharge hydrograph in the upper graph, depth hydrographs at x = 0.0 in the lower graph.

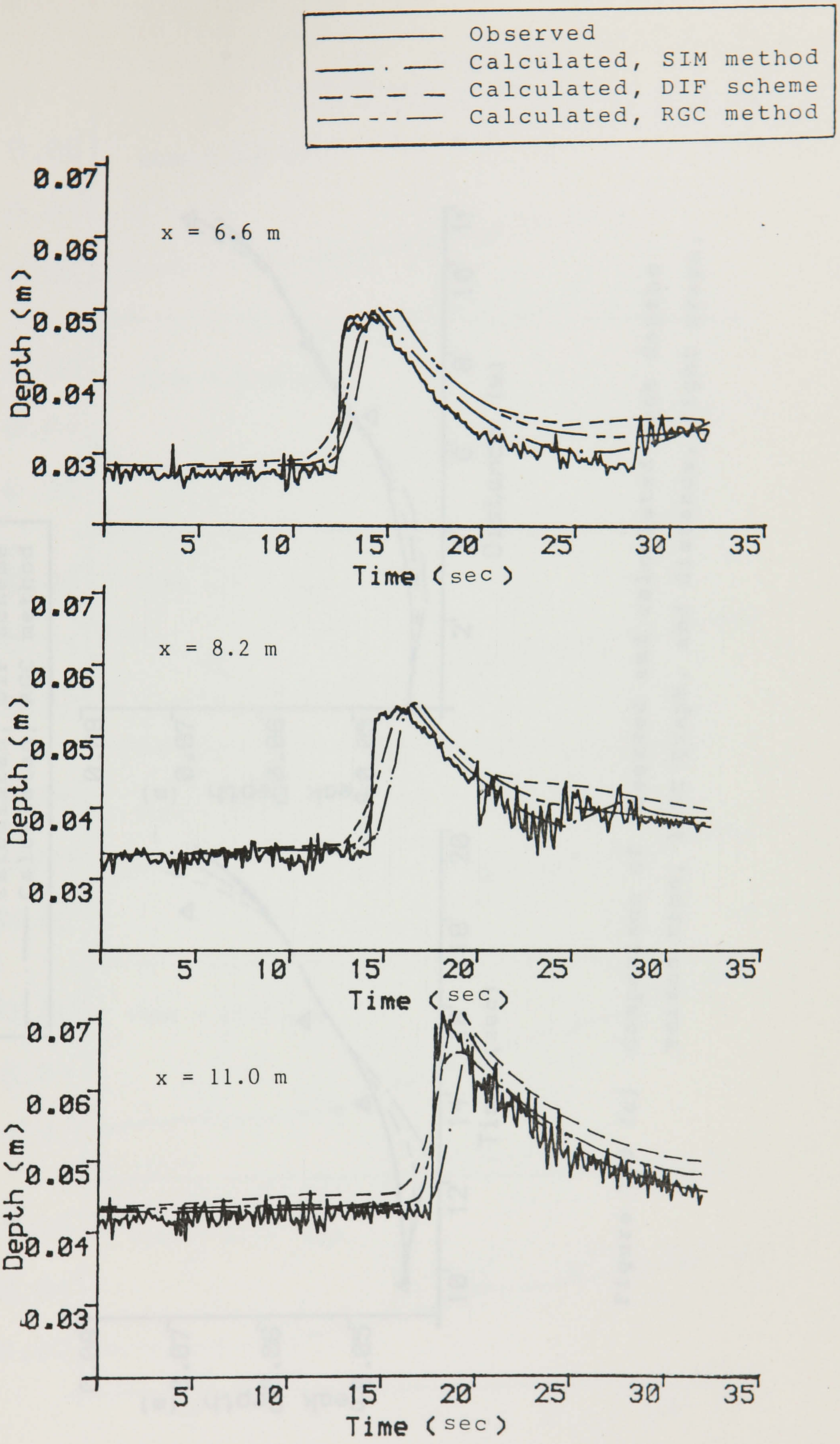

Figure 7.9 (b) Comparison of observed and calculated depth hydrographs.

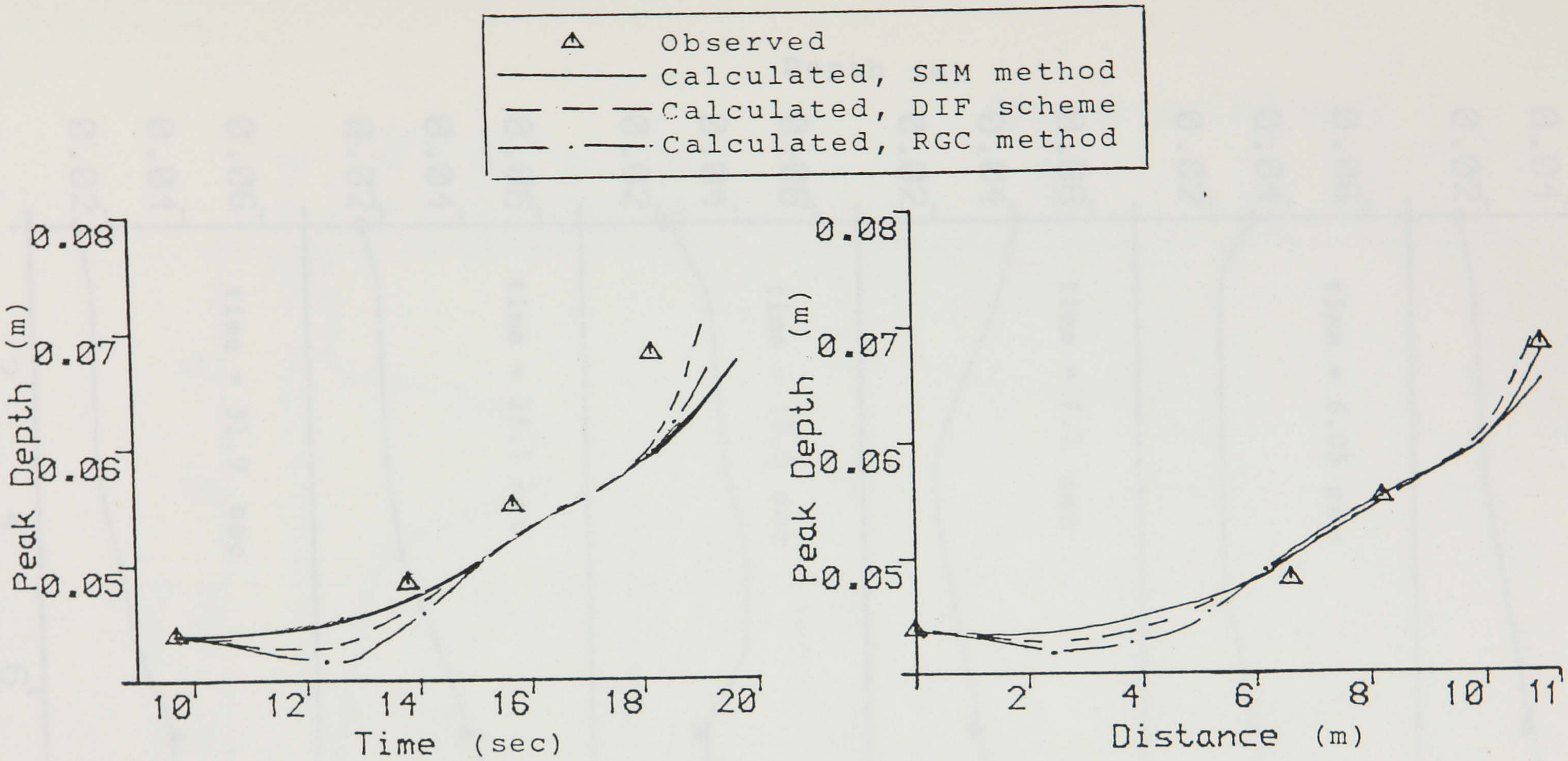

Figure 7.9 (c) Comparison of observed and calculated peak depths versus time, left graph, and distance, right graph.

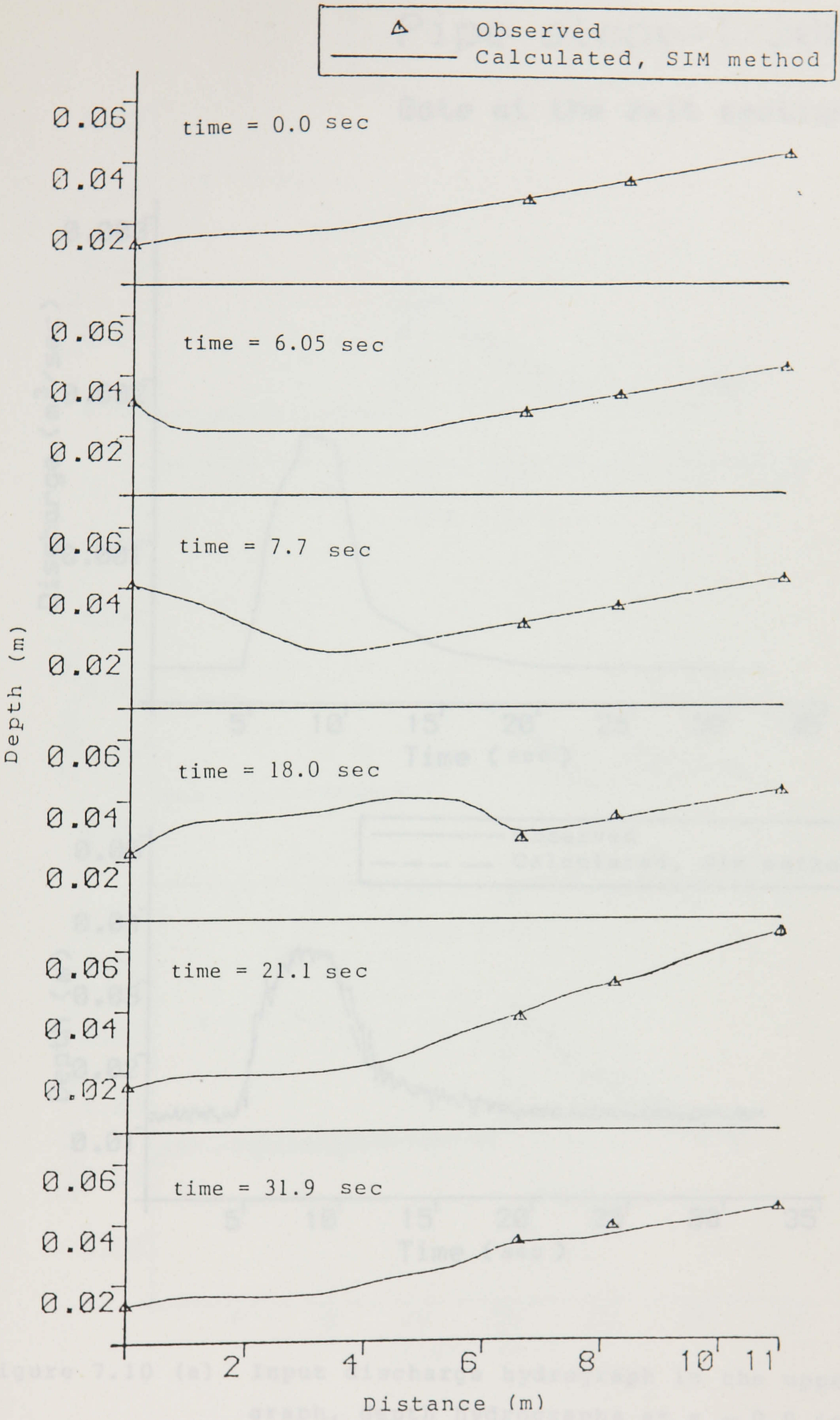

Figure 7.9 (d) Comparison of observed and calculated flow depths along the pipe.

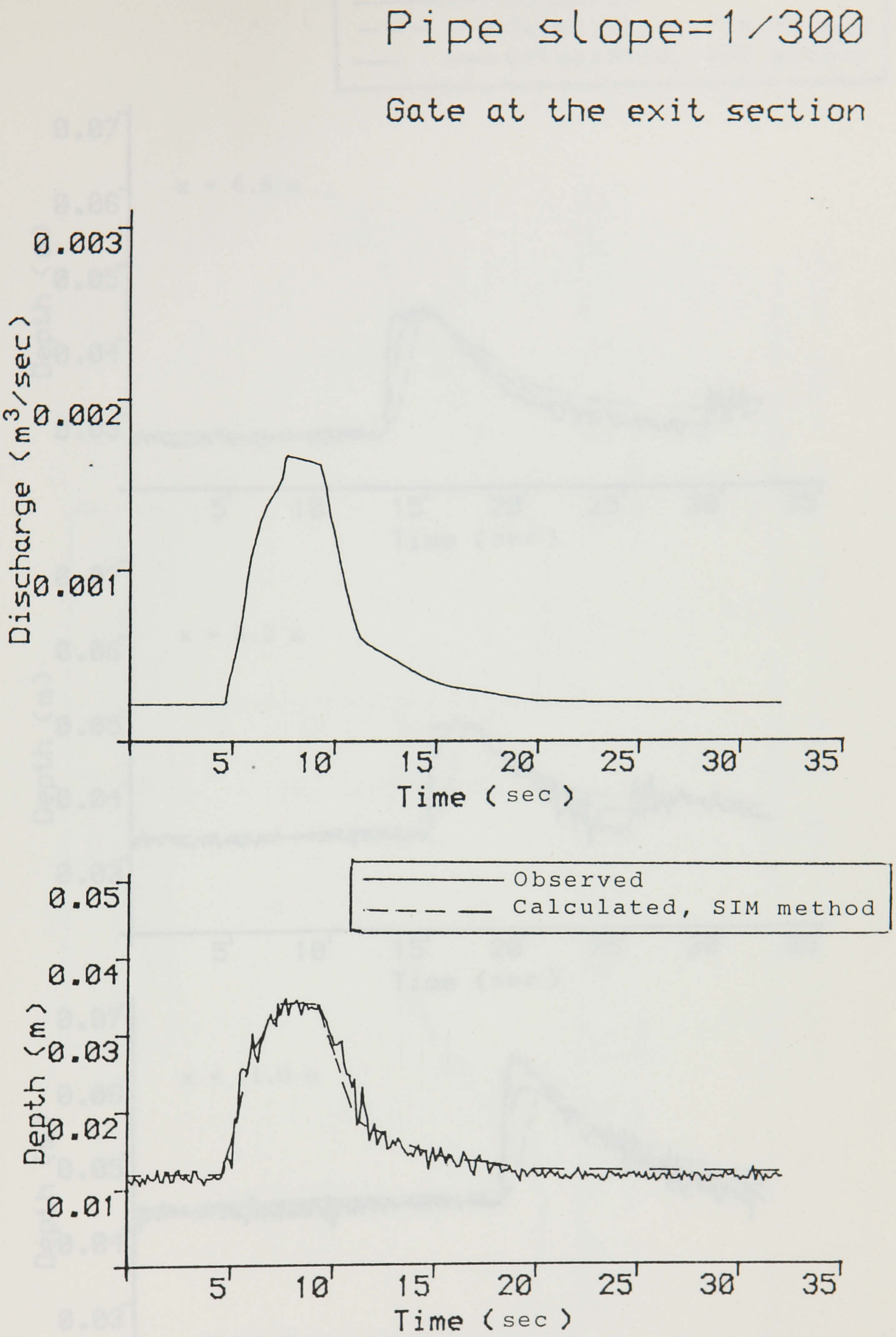

Figure 7.10 (a) Input discharge hydrograph in the upper graph, depth hydrographs at x = 0.0 in the lower graph.

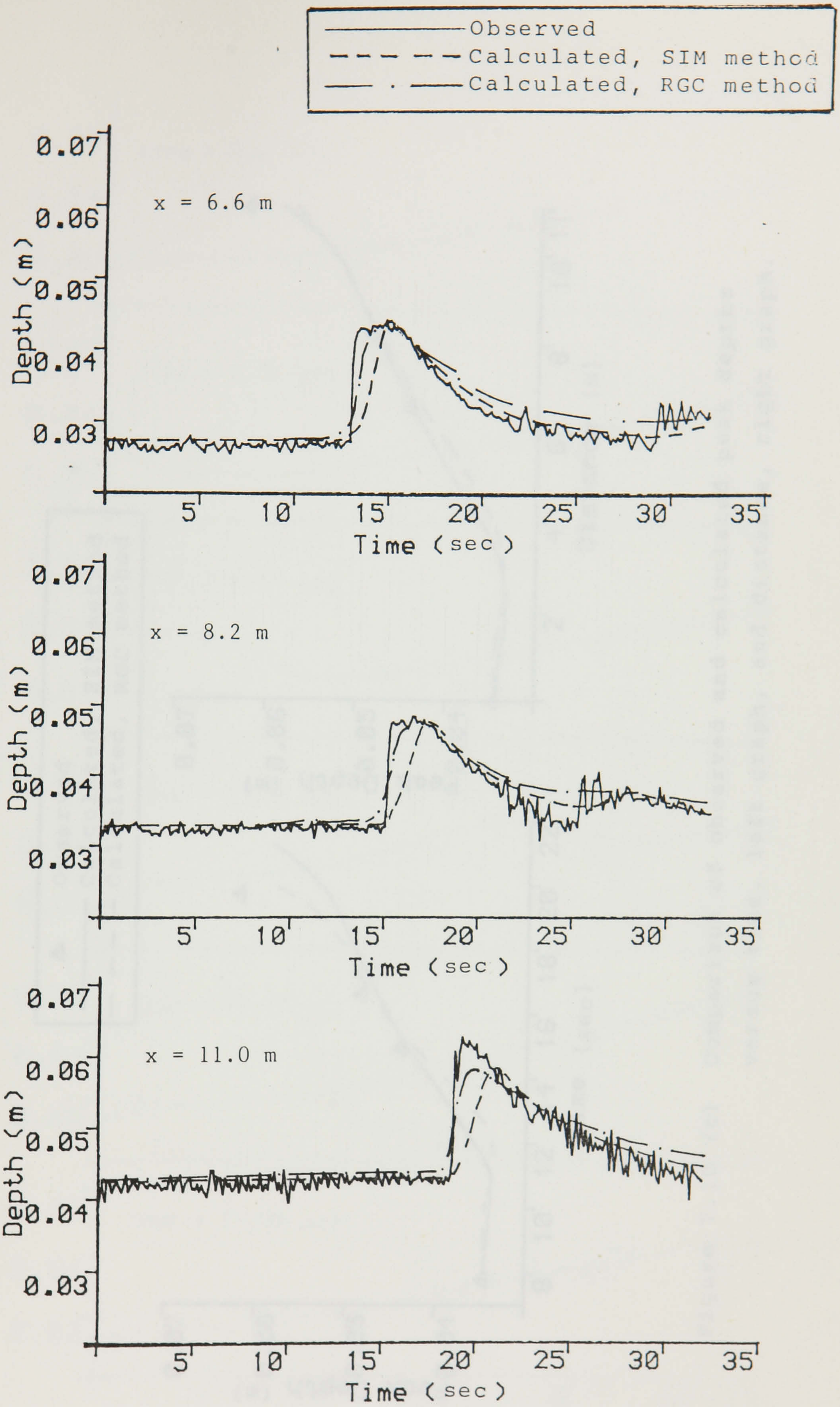

Figure 7.10 (b) Comparison of observed and calculated depth hydrographs.

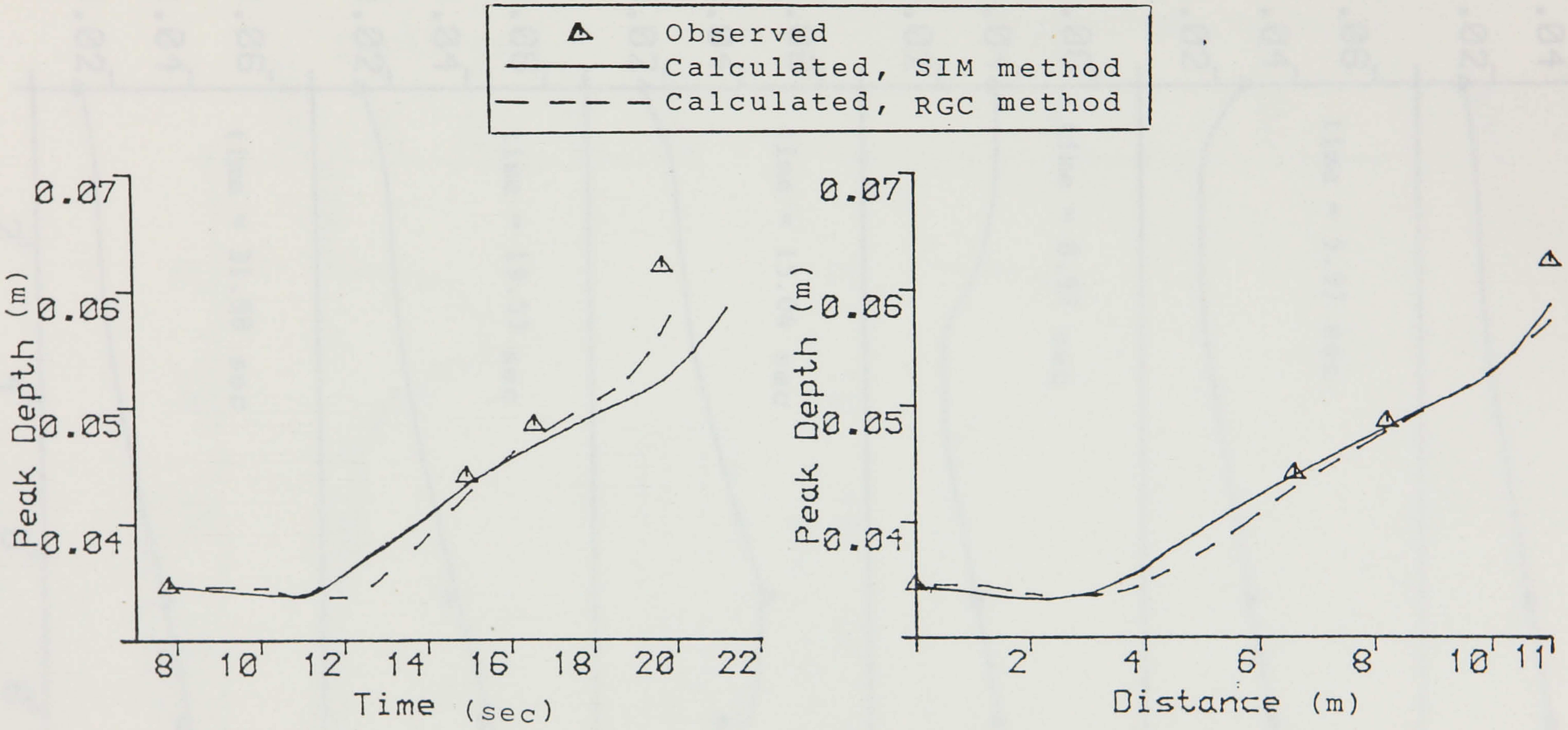

Figure 7.10 (c) Comparison of observed and calculated peak depths versus time, left graph, and distance, right graph.

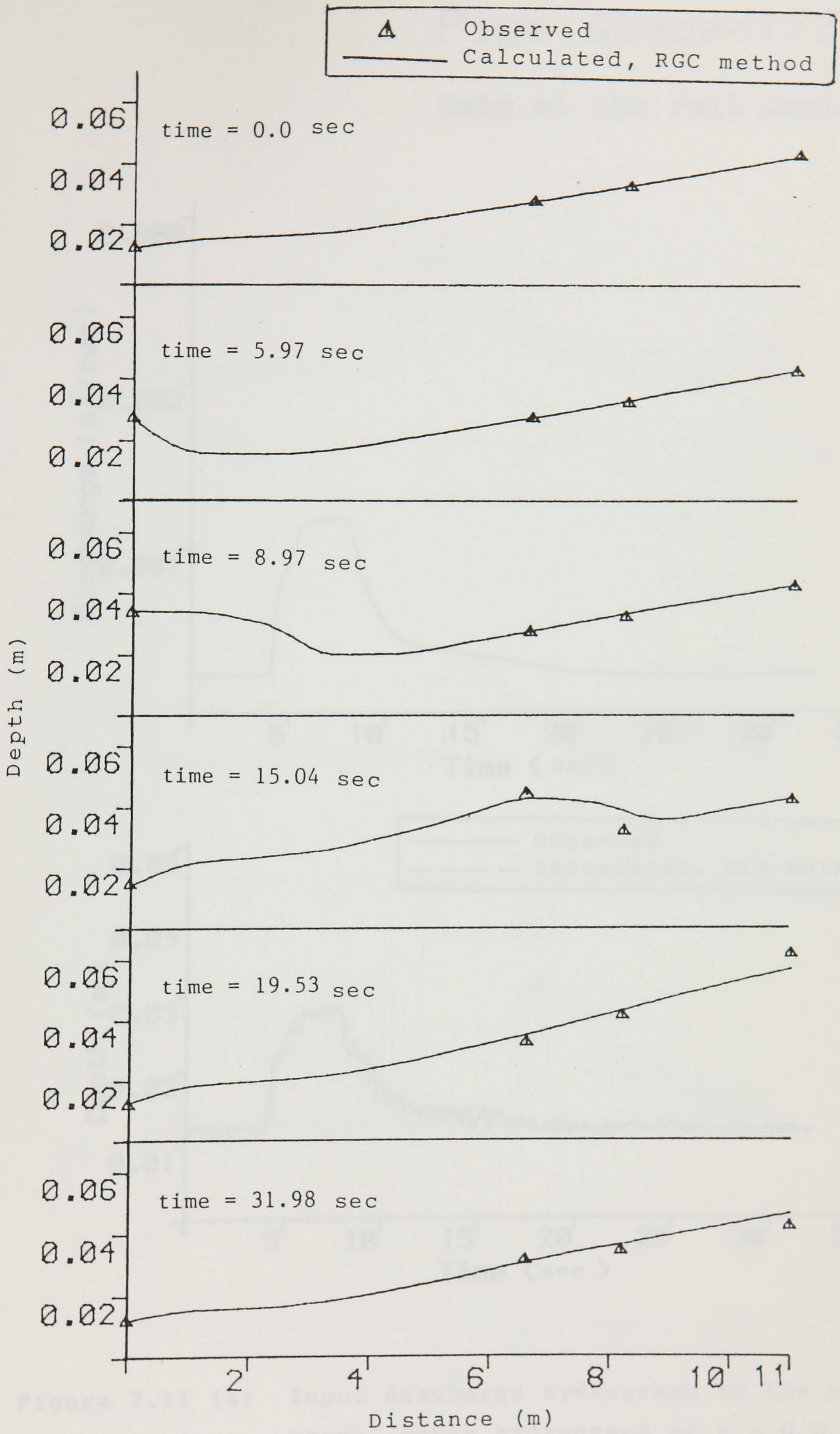

Figure 7.10 (d) Comparison of observed and calculated flow depths along the pipe.

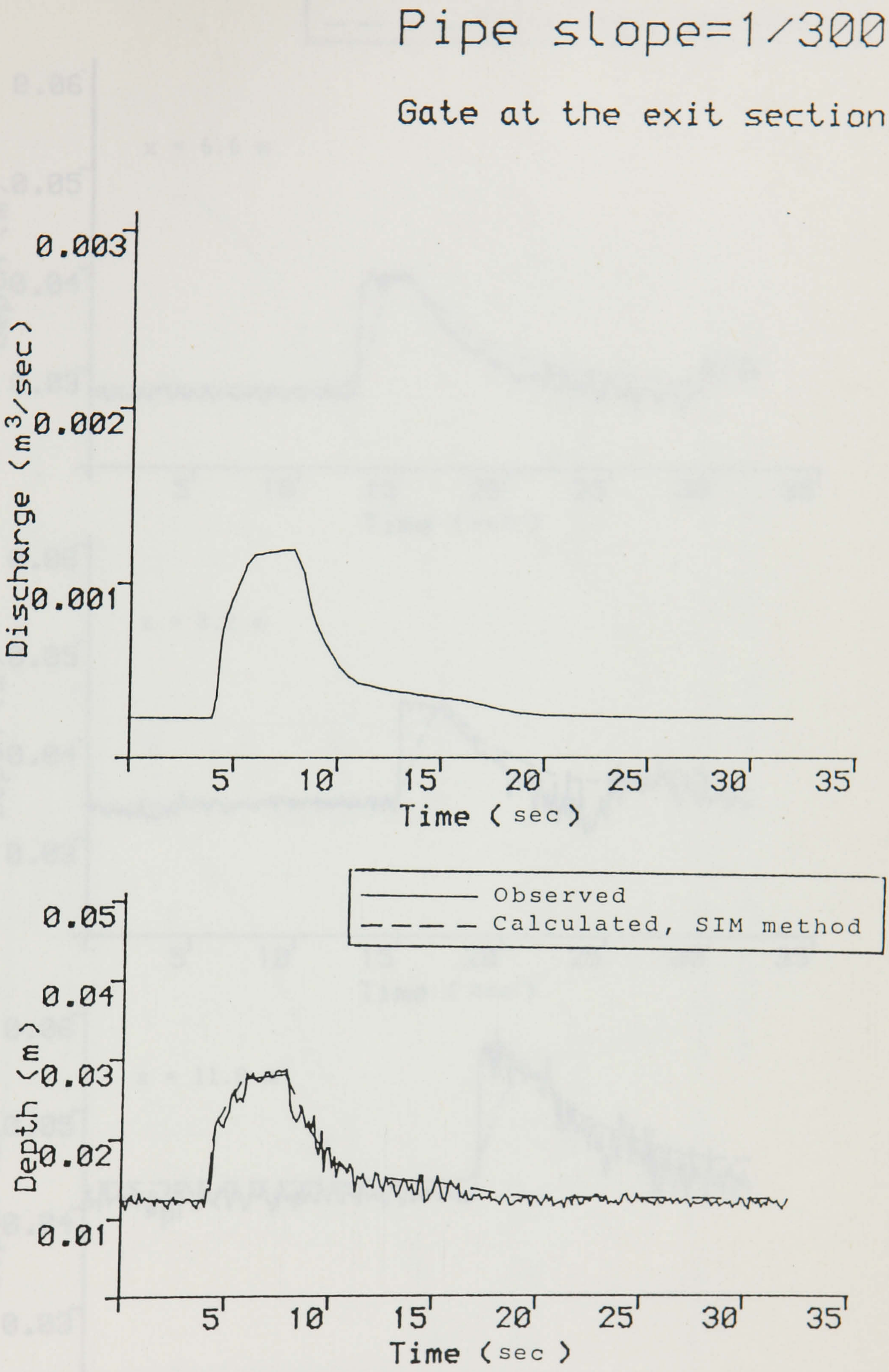

Figure 7.11 (a) Input discharge hydrograph in the upper graph, depth hydrograph at x = 0.0 in the lower graph.

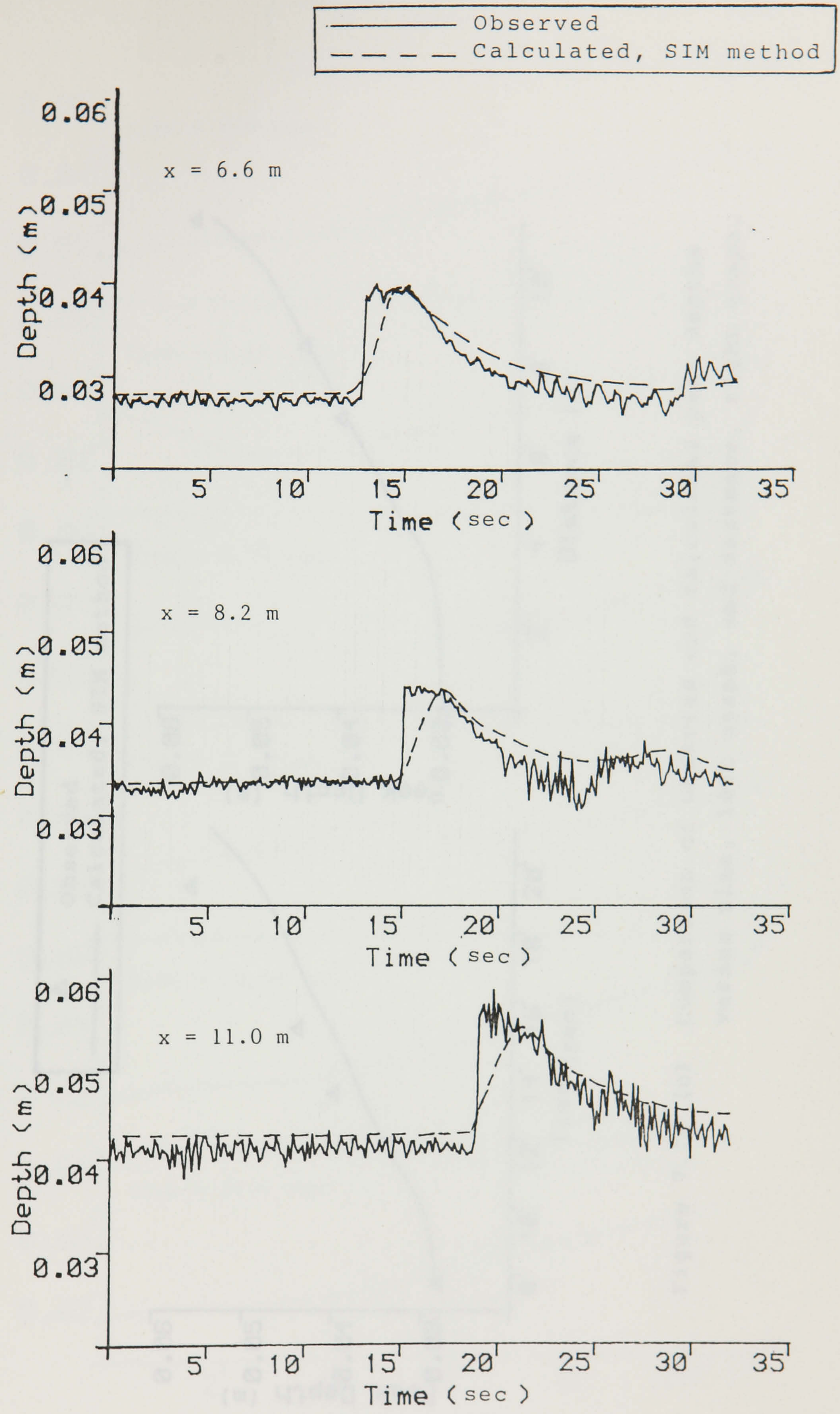

Figure 7.11 (b) Comparison of observed and calculated depth hydrographs.

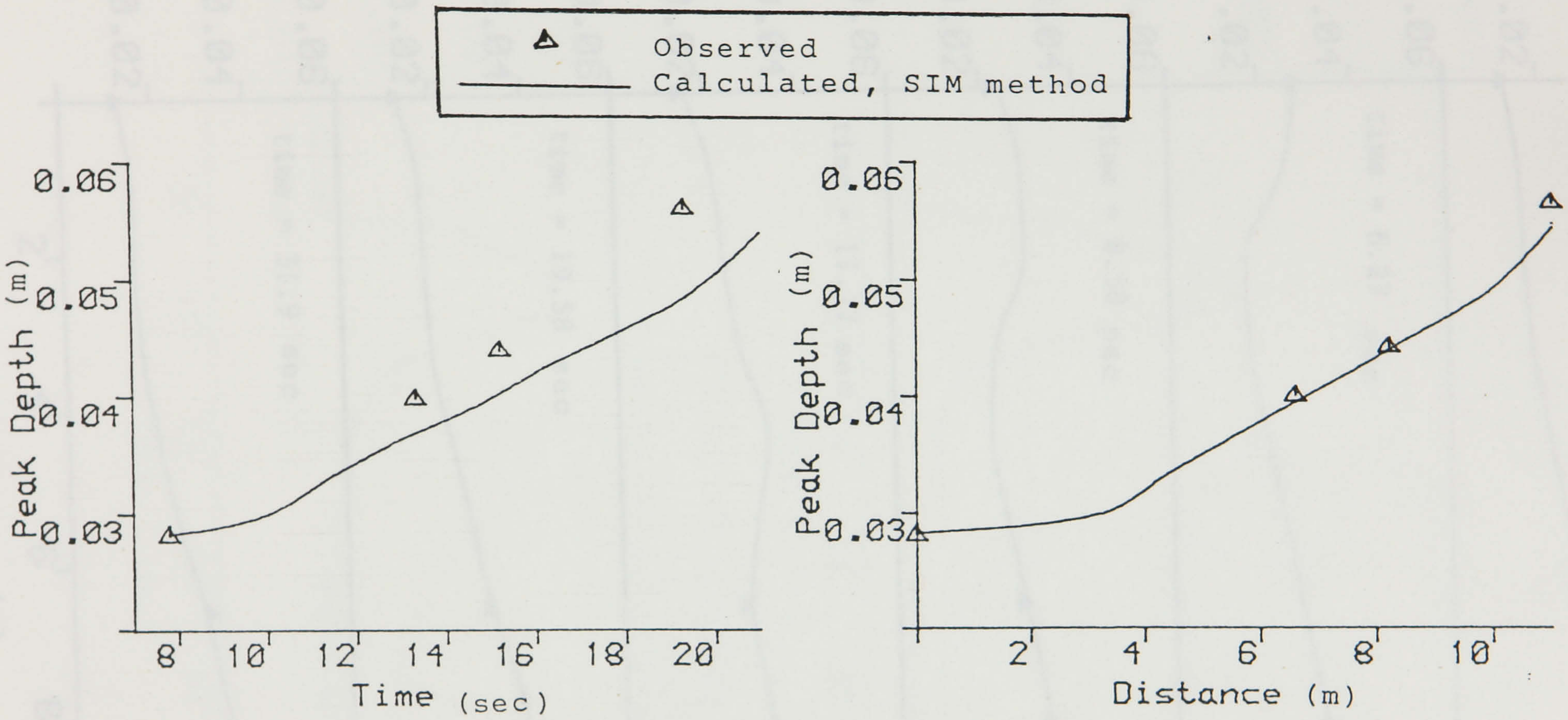

Figure 7.11 (c) Comparison of observed and calculated peak depths versus time, left graph, and distance, right graph.

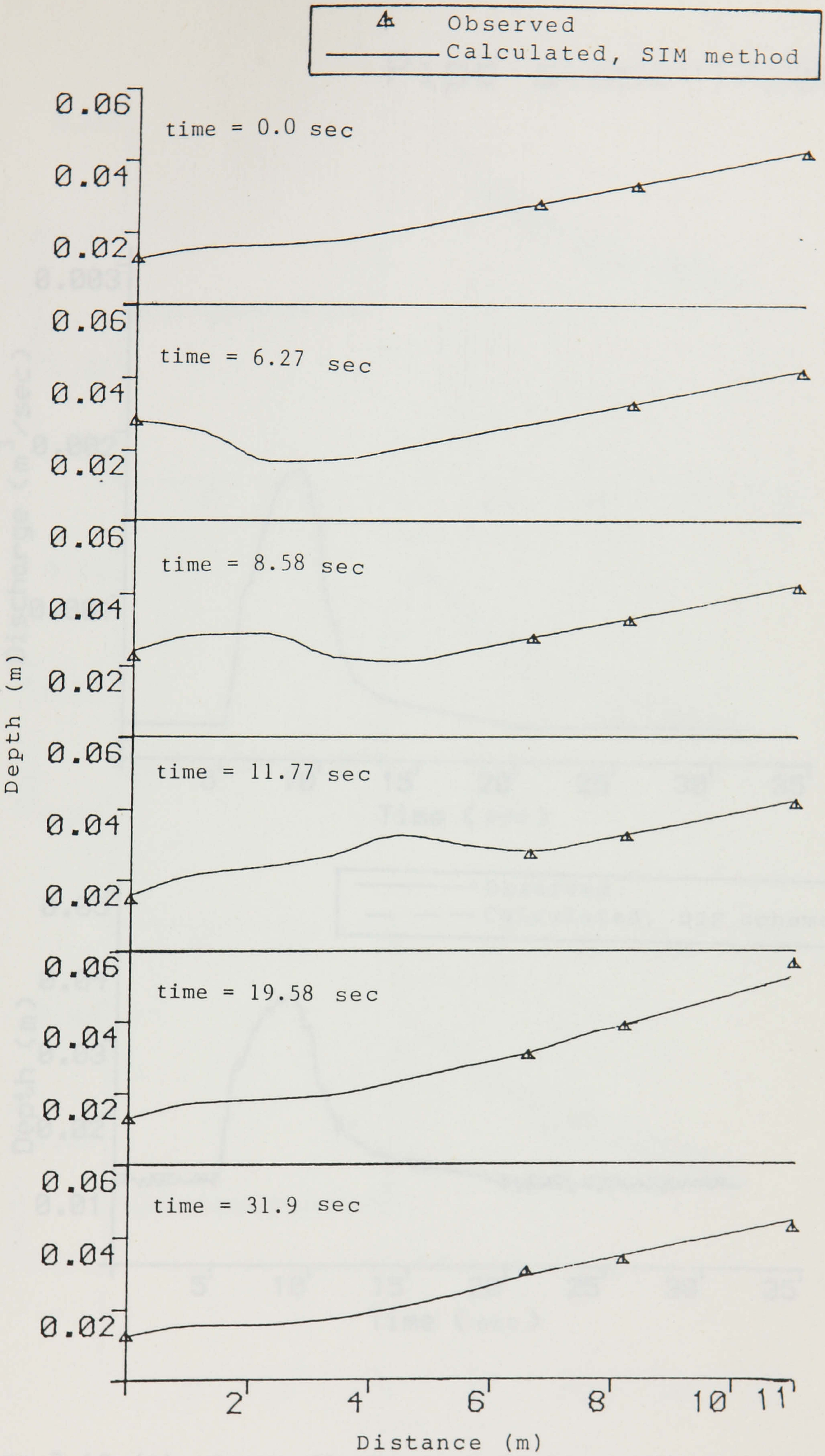

Figure 7.11 (d) Comparison of observed and calculated flow depths along the pipe.

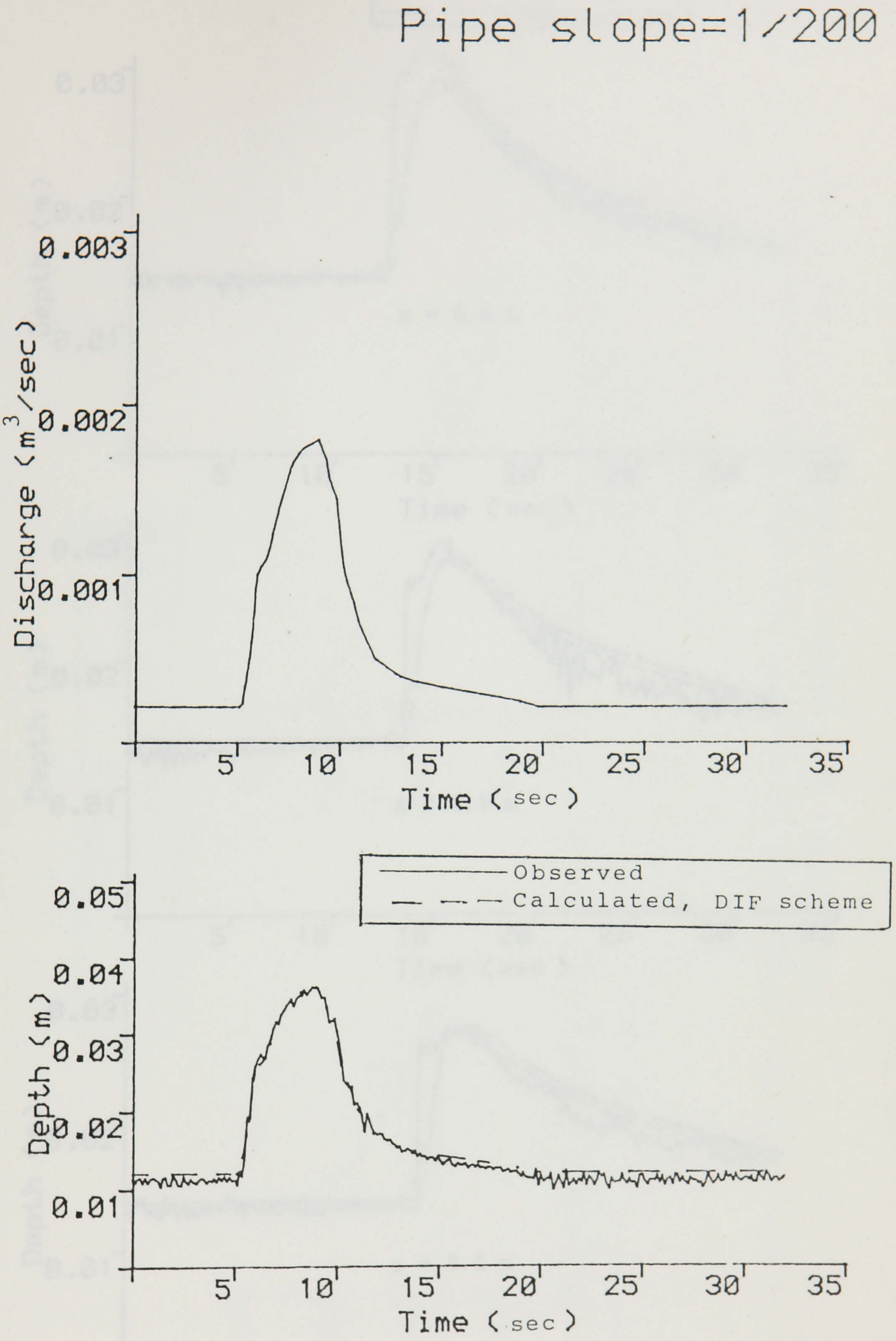

Figure 7.12 (a) Input discharge hydrograph in the upper graph, depth hydrographs at x = 0.0 in the lower graph.

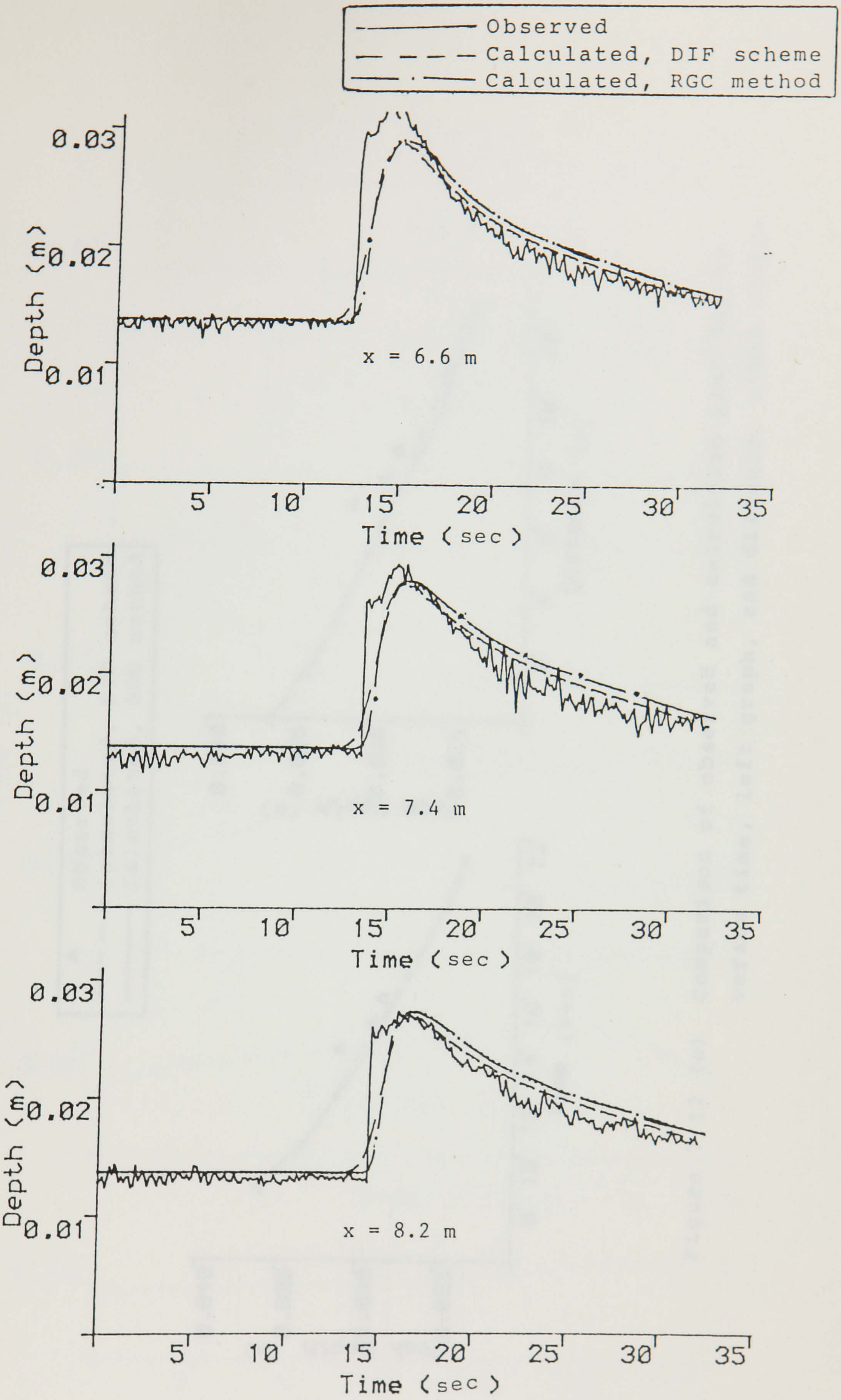

Figure 7.12 (b) Comparison of observed and calculated depth hydrographs.

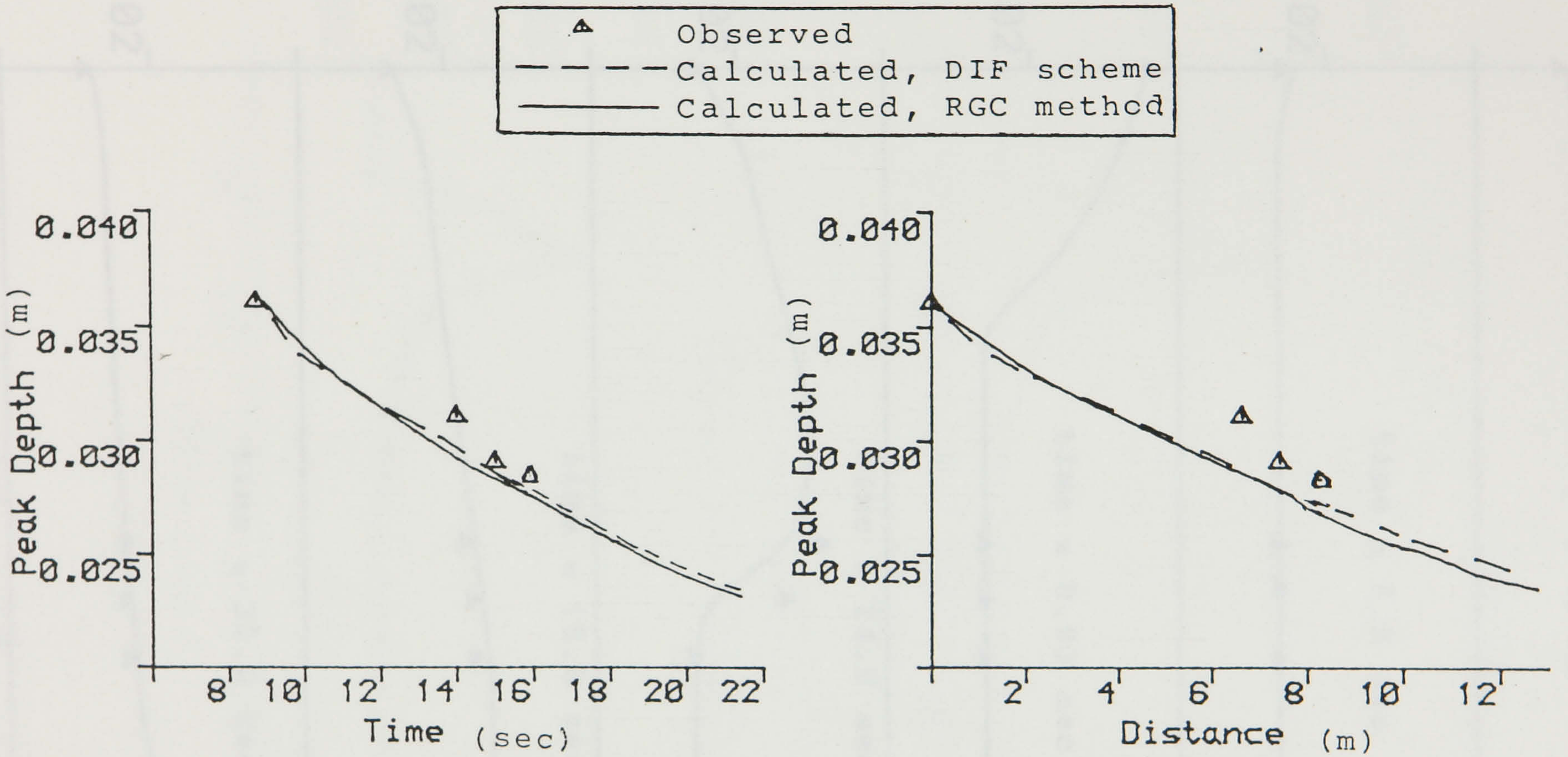

Figure 7.12 (c) Comparison of observed and calculated peak depths versus time, left graph, and distance, right graph.

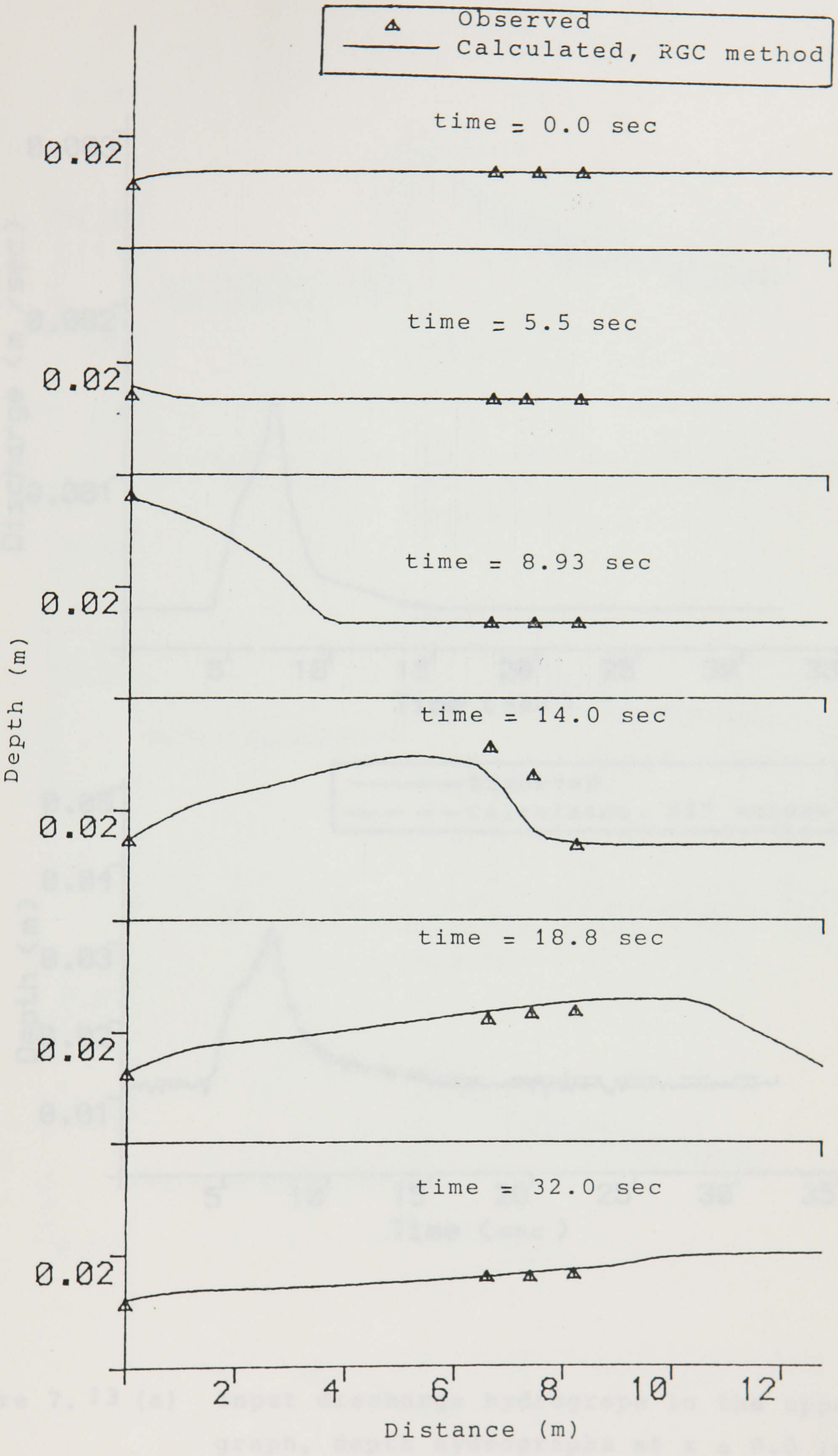

Figure 7.12 (d) Comparison of observed and calculated flow depths along the pipe.

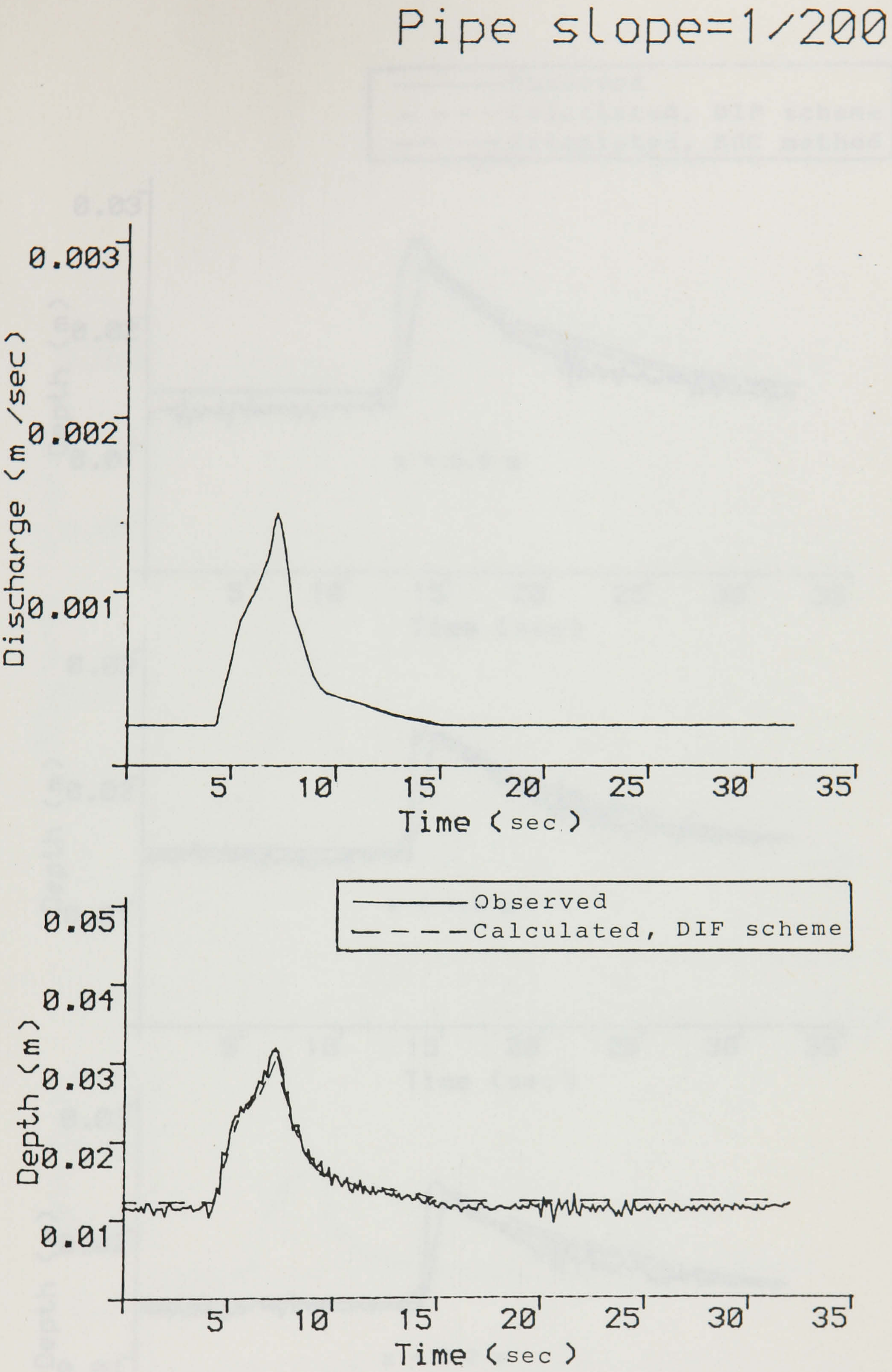

Figure 7.13 (a) Input discharge hydrograph in the upper graph, depth hydrographs at x = 0.0 in the lower graph.

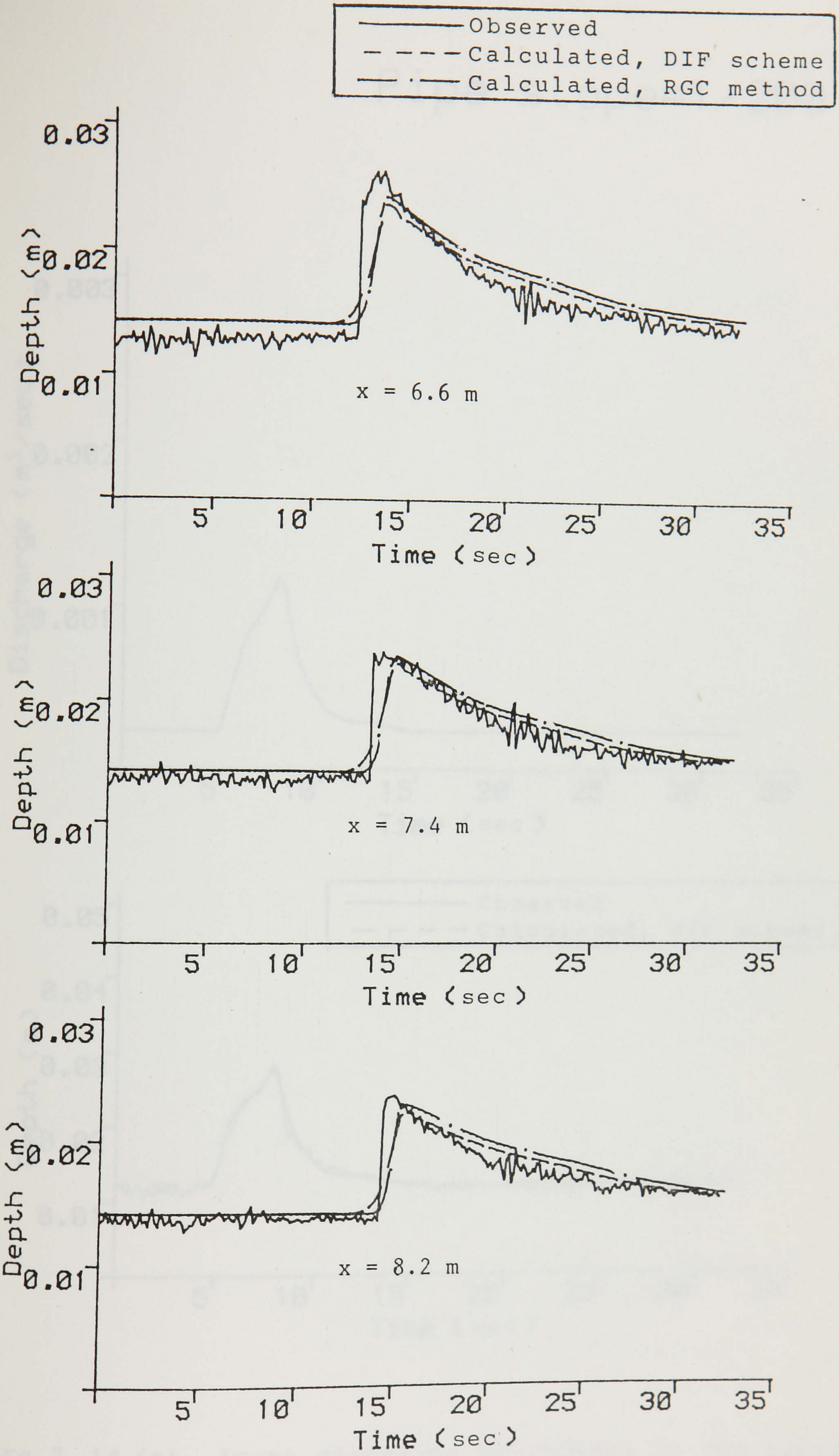

Figure 7.13 (b) Comparison of observed and calculated depth hydrographs.

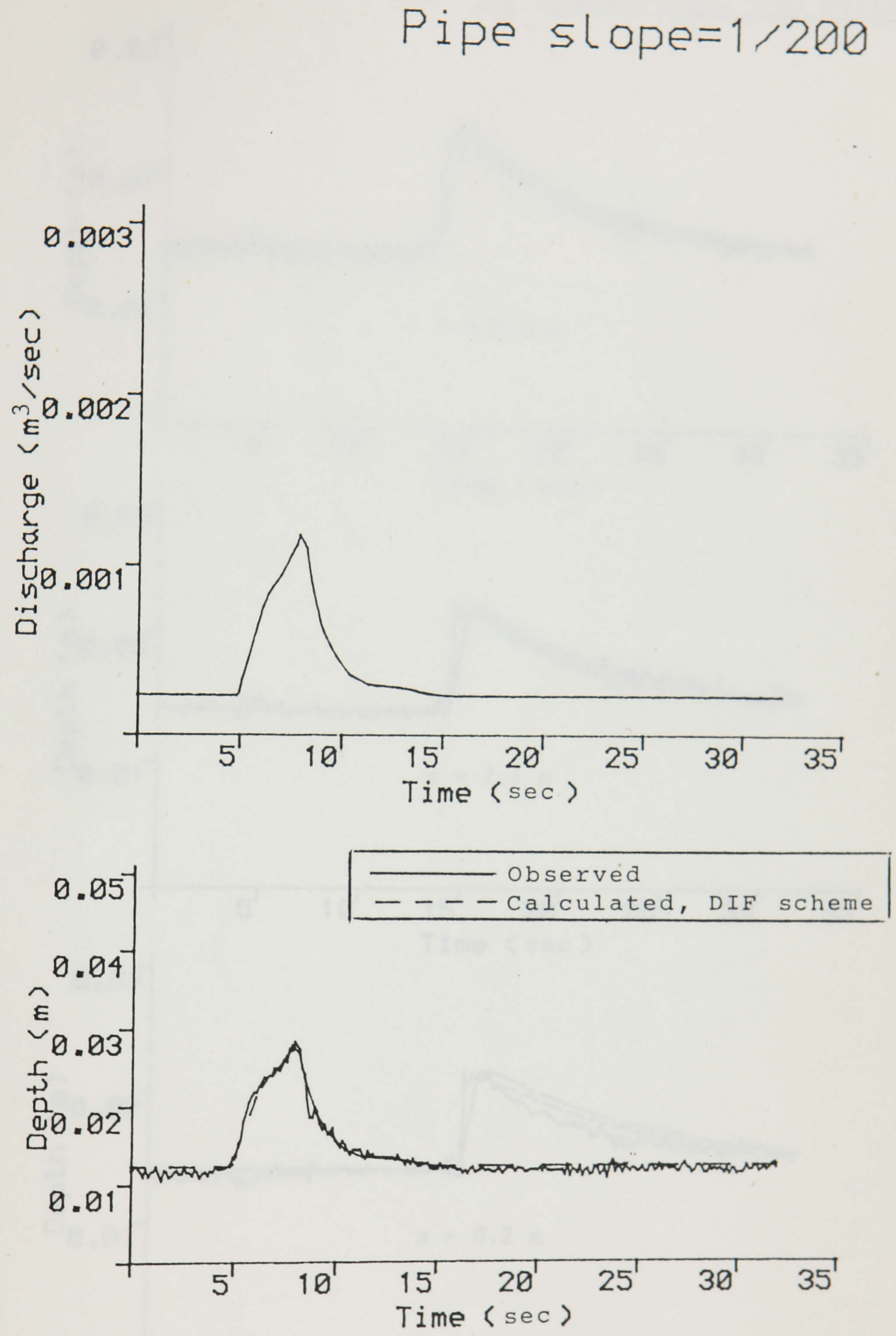

Figure 7. 14 (a) Input discharge hydrograph in the upper graph, depth hydrographs at x - 0.0 in the lower graph.

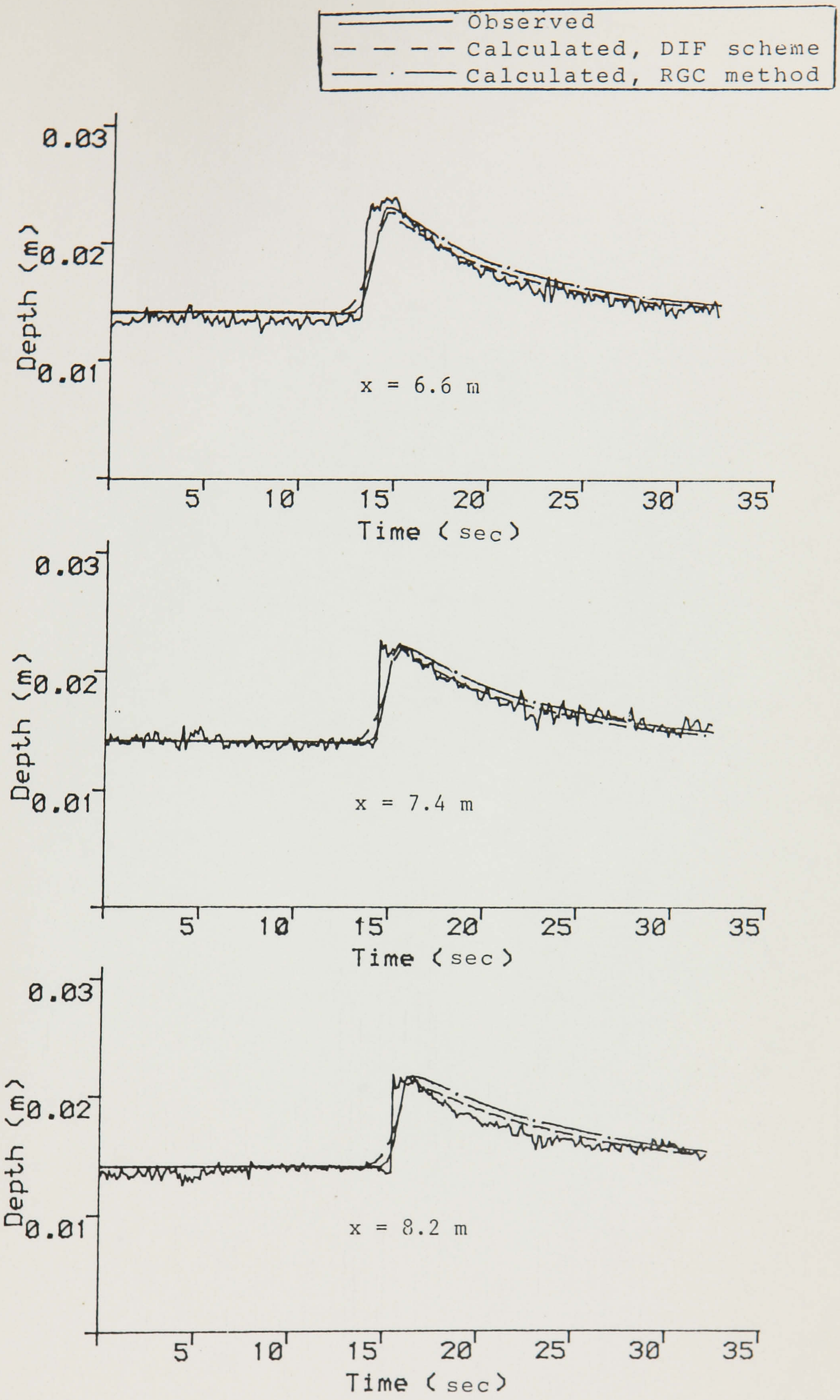

Figure 7.14 (b) Comparison of observed and calculated depth hydrographs.